INORGANIC-ORGANIC HYBRID NANOPOROUS MATERIALS FOR CARBON DIOXIDE CAPTURE

Ph.D. THESIS

by

RAEESH MUHAMMAD

DEPARTMENT OF CHEMISTRY
INDIAN INSTITUTE OF TECHNOLOGY ROORKEE
ROORKEE – 247 667 (INDIA)
MARCH, 2018

INORGANIC-ORGANIC HYBRID NANOPOROUS MATERIALS FOR CARBON DIOXIDE CAPTURE

A THESIS

Submitted in partial fulfilment of the requirements for the award of the degree

of

DOCTOR OF PHILOSOPHY

in

CHEMISTRY

by

RAEESH MUHAMMAD

DEPARTMENT OF CHEMISTRY
INDIAN INSTITUTE OF TECHNOLOGY ROORKEE
ROORKEE – 247 667 (INDIA)
MARCH, 2018

INDIAN INSTITUTE OF TECHNOLOGY ROORKEE
ROORKEE

CANDIDATE'S DECLARATION

I hereby certify that the work which is being presented in the thesis entitled **"INORGANIC-ORGANIC HYBRID NANOPOROUS MATERIALS FOR CARBON DIOXIDE CAPTURE"** in partial fulfilment of the requirements for the award of the Degree of Doctor of Philosophy and submitted in the Department of Chemistry of the Indian Institute of Technology Roorkee, Roorkee is an authentic record of my own work carried out during a period from July, 2013 to March, 2018 under the supervision of Dr. Paritosh Mohanty, Associate Professor, Department of Chemistry, Indian Institute of Technology Roorkee, Roorkee.

The matter presented in this thesis has not been submitted by me for the award of any other degree of this or any other Institute.

(RAEESH MUHAMMAD)

This is to certify that the above statement made by the candidate is correct to the best of my knowledge.

(PARITOSH MOHANTY)
Supervisor

The Ph. D. Viva-Voce Examination of **Raeesh Muhammad**, Research Scholar, has been held on **23 July 2018.**

Chairman, SRC **Signature of External Examiner**

This is to certify that the student has made all the corrections in the thesis.

Signature of Supervisor (s) **Head of the Department**

Date: 23 July 2018

This thesis is dedicated to
my supervisor and my beloved parents,
the two pillars of strength behind my success

ABSTRACT

The looming threat of global warming owing to the unprecedented rise in the environmental CO_2 level that reached as high as 408 ppm in recent times has forced the scientific community to find ways to restrict the use of fossil fuels for energy generation that emit a substantial amount of CO_2 to the environment or find sustainable alternative energy sources. With so much of R&D activities in last decades, the contribution of the later to the total energy generation is not encouraging and hence, the former looks more realistic. Almost 41 billion ton of CO_2 emitted annually into the atmosphere due to the fossil fuel burning, is required to be captured in order to have sustainable energy economy protecting the environment. Traditionally, organic liquid amine solutions have been utilized for tripping off CO_2 from fossil fuel fired flue gas stream with an unacceptable financial burden. Use of the solid adsorbents has emerged as potential alternatives, as it could circumvent some of the disadvantages of the above method such as the ease of regeneration, thermal and hydrothermal stability. Solid adsorbents such as metal oxide, zeolites, activated carbon, amine grafted mesoporous silica, metal organic framework, covalent organic framework, porous aromatic framework have been utilized for the CO_2 capture application with some hope for their potential use to trap the CO_2 in the coal-fired power plants. After having a basic understanding about the principle governing the effective adsorption process, especially for CO_2 capture, in the present research, the adsorbent materials have been synthesized utilizing precursors that could lead to the formation of materials with large and uniform distribution of heteroatoms. Two types of inorganic-organic hybrid nanoporous materials *viz.* (i) non-siliceous and (ii) siliceous hybrid materials have been made. The non-siliceous hybrid materials were synthesized using cyclophosphazene moiety via Schiff base and nucleophilic condensation that yielded materials with the maximum specific surface area of 976 and 1328 $m^2\ g^{-1}$, respectively. The maximum CO_2 capture capacity recorded was 22.8 wt% at 273 K and 1 bar. The siliceous hybrid materials were synthesized by condensation of cyanuric chloride with (3-aminopropyl)triethoxyxilane, *N*-[3-(trimethoxysilyl)propyl]ethylenediamine or N^1-(3-trimethoxysilylpropyl)ethylenetriamine, followed by hydrolysis and polycondensation. The nitrogen content was tuned in these organosilica frameworks by taking pre-determined precursors. Moreover, the textural properties were improved by co-condensing with TEOS. The maximum estimated specific surface area recorded was 1304 $m^2\ g^{-1}$ with a maximum CO_2 uptake of 11.6 wt% at 273 K and 1 bar. All these synthesized materials have been characterized by state-of-the-art analytical techniques.

ACKNOWLEDGEMENTS

The journey of obtaining Ph.D. degree has been challenging and full of joy, and this would not have been possible to do without the guidance, support and encouragement of many individuals. I would like to acknowledge all these individuals for making this journey a memorable and wonderful experience.

At the outset, I would like to express my heartful gratitude to my teacher, philosopher and role model i.e. my honorific supervisor**, Dr. Paritosh Mohanty**, Associate Professor, Department of Chemistry, IIT Roorkee. He has been actively interested and involved in my research that kept me focused on achieving my goal. He has always been there providing his able guidance and heartfelt support. His dedication and enthusiasm towards research, guidance, motivational talk, constructive discussion and vast experience made this research journey a smooth walk. I would also like to thank him for all the freedom to pursue the research, showing the confidence in me and giving me the opportunity to work with him. Without his support and guidance, this thesis would not have been possible. I would take this opportunity to thank **Mrs. Solvia Priyadarshini** for her continued support.

I also appreciate the expert advice of the SRC members **Prof. Anil Kumar** (SRC and DRC chairman, Department of Chemistry), **Prof. R. K. Dutta** (Internal expert, Department of Chemistry) and **Prof. Y. K. Sharma** (External expert, Department of Physics) for advice, suggestions and sharing their valuable experience relevant to my research work.

I owe my sincere gratitude to **Prof. M. R. Maurya**, HOD, Department of Chemistry, IIT Roorkee. I would also like to thank the faculty members of IIT Roorkee for their co-operation and support during this research work. I gratefully acknowledge the support of Department of Chemistry, Department of Applied Science and Engineering and Institute Instrumentation Center towards providing the necessary research and characterization facility. I thank all the staff members of IIT Roorkee for their support throughout my research work.

I sincerely admire the help and contribution of all my past and present lab mates especially Dr. Pawan Rekha, Sudiksha Aggrawal, Nisha Dhiman, Dr. Indu Chauhan, Dr. Vivek Sharma, Monika Chaudhary, Ruchi Sharma, Aseema Bahlwal, Ashish Madhual, Jasasmita Das, Dr. P. V. R. K. Ramacharyulu, Dr. Sunil Dutt, Vicky Varma, Chandrawati Yadav, Jyoti, Nishant Jain and Charu Agarwal for providing a fun filled lab environment, constant help with personal and lab matters.

My time at IIT Roorkee was made enjoyable in large part due to my friends especially Asit Sahoo, Ruchir Priyadarshi, Amit Kumar, Dr. Prerna Chaturvedi, Lovjeet Singh, Md. Zeeshan, Shiv Dutt Purohit and Brahma Praksah Dueby. Thank you, guys for standing by my side in my good and bad times, and always ready with solutions and suggestions whenever there were some problems.

Finally, my parents, siblings and family members deserve special mention here. The successful culmination of my Ph.D. journey is the result of their continued support, unconditional love, affection and encouragement. They have been a constant source of inspiration. Thanks to Stuti and Sthiti for making my thesis and manuscript correction time very enjoyable.

Last, but not least, I thank the almighty God for giving me all the passion, strength, patience, knowledge, ability and opportunity to undertake this research study and to persevere and complete it satisfactorily.

(RAEESH MUHAMMAD)

CONTENTS

LIST OF ABBREVIATIONS

ACs	Activated carbons
APOPs	Aromatic porous organic polymers
APTES	(3-aminopropyl)triethoxyxilane
BET	Brunauer–Emmett–Teller
BILPs	Benzimidazole linked polymers
BLPs	Borazine linked polymers
BTEE	1,2-bis(triethoxysilyl)ethane
BTSE	Bis(triethoxysilyl)ethane
BTSM	Bis(triethoxysilyl)methane
CHNMs	Cyclophosphazene-based hybrid nanoporous materials
CMPs	Conjugated microporous polymers
CNC	Cyanuric chloride
COFs	Covalent organic frameworks
CPMAS	Cross polarization magic angle spinning
CTABr	Cetyltrimethylammonium bromide
DCM	Dichloromethane
DFT	Density functional theory
DMSO	Dimethyl sulfoxide
DOE	Department of Energy
DTG	Differential thermal gravimetry
FESEM	Field emission scanning electron microscopy
FTIR	Fourier transform infrared spectroscopy
HCPs	Hyper crosslinked polymers
HNMs	Hybrid nanoporous materials
IUPAC	International Union of Pure and Applied Chemistry
MHB	*m*-hydroxy benzaldehyde
MOFs	Metal organic frameworks
NETPMOs	Nitrogen enriched triazine bridged mesoporous organosilicas
NMR	Nuclear magnetic resonance spectroscopy
PAFs	Porous aromatic frameworks
PHB	*p*-hydroxy benzaldehyde
PIMs	Polymer of intrinsic porosity

PMOs	Periodic mesoporous organosilicas
PNC	Phosphonitrilic chloride trimer
POPs	Porous organic polymers
PPNs	Porous polymeric networks
PSD	Pore size distribution
Q_{st}	Isosteric heat of adsorption
RT	Room temperature
SA_{BET}	Specific surface area
SAED	Selected area electron diffraction
SAXS	Small angle X-ray scattering
SDA	Structure directing agent
TEOS	Tetraethyl orthosilicate
TEM	Transmission electron microscopy
TGA	Thermogravimetric analysis
THF	Tetrahydrofuran
TMSPD	*N*-[3-(trimethoxysilyl)propyl]ethylenediamine
TMSPT	N^1-(3-trimethoxysilylpropyl)ethylenetriamine
XPS	X-ray photo electron spectroscopy
XRD	X-ray diffraction
ZIFs	Zeolite imidazolate frameworks
δ	Chemical shift

LIST OF PUBLICATIONS

Publications in Journals

1. **R. Muhammad**, M. Chaudhary and P. Mohanty*, Harnessing electron-rich framework in cyclophosphazene derived hybrid nanoporous materials for organocatalytic C-C bond formation and gas sorption applications, *J. CO_2 Util*., 2018, **25**, 302-309.
2. **R. Muhammad** and P. Mohanty*, Cyclophosphazene-based hybrid nanoporous materials as superior metal-free adsorbents for gas sorption applications, *Langmuir*, 2018, **34**, 2926-2932.
3. **R. Muhammad**, Jyoti and P. Mohanty*, Nitrogen enriched triazine bridged mesoporous organosilicas for CO_2 capture and dye adsorption applications, *J. Mol. Liq.*, 2017, **248**, 127-134.
4. **R. Muhammad**, P. Rekha and P. Mohanty*, Aminal linked inorganic-organic hybrid nanoporous materials (HNMs) for CO_2 capture and H_2 storage applications, *RSC Adv.*, 2016, **6**, 17100-17105.
5. **R. Muhammad**, P. Rekha and P. Mohanty*, Facile synthesis of a thermally stable imine and benzimidazole functionalized nanoporous polymer (IBFNP) for CO_2 capture application, *Greenhouse Gas: Sci. Technol*., 2016, **6**, 150-157.
6. PVRK Ramacharyulu, **R. Muhammad**, J. P. Kumar, G. K. Prasad and P. Mohanty*, Iron phthalocyanine modified mesoporous titania nanoparticles for photocatalytic activity and CO_2 capture applications, *Phys. Chem. Chem. Phys*., 2015, **17**, 26456-26462.
7. P. Rekha, **R. Muhammad** and P. Mohanty*, Sonochemical synthesis of cyclophosphazene bridged mesoporous organosilicas and their application in methyl orange, congo red and Cr(VI) removal, *RSC Adv*., 2015, **5**, 67690-67699.
8. P. Rekha, **R. Muhammad**, V. Sharma, M. Ramteke and P. Mohanty*, Unprecedented adsorptive removal of $Cr_2O_7^{2-}$ and methyl orange by using a low surface area organosilica, *J. Mater. Chem. A*, 2016, **4**, 17866-17874.
9. M. Chaudhary, A. K. Nayak, **R. Muhammad**, D. Pradhan and P. Mohanty*, Nitrogen-enriched nanoporous polytriazine for high performance supercapacitor application, *ACS Sustainable Chem. Eng*., 2018, **6**, 5895-5902.

Conference presentations

1. **R. Muhammad** and P. Mohanty*, Triazine bridged mesoporous organosilicas for CO_2 capture application, 2nd national workshop on development of nanomaterials for energy, environment and sustainability (DNEES-2016), Bhubaneswar, India, May 9-10, 2016. [**Best Poster Award**]

2. **R. Muhammad** and P. Mohanty*, Cyclophosphazene based inorganic-organic hybrid high surface area nanoporous solid adsorbents with amine functionality for CO_2 capture and H_2 storage applications, international symposium on functional materials (ISFM-2018), Chandigarh, India, April 13-15, 2018.

CHAPTER-I

INTRODUCTION

1.1. INTRODUCTION

1.1.1. Overview

This chapter contains the comprehensive discussion on available literature related to the synthesis of various high surface area nanoporous materials and their use as solid adsorbents for carbon dioxide (CO_2) capture and hydrogen (H_2) storage.[1-27] Search for the clean and alternative energy sources due to the drastic rise in the atmospheric temperature and depletion of conventional energy sources has been the main point of discussion in almost all scientific and government forum worldwide working on the energy and environment sectors.[27-31] It is almost accepted by the majority of scientist and expert that the excess anthropogenic CO_2 emission led to the global warming.[1-3,5-7,32] To cut this anthropogenic CO_2 emission, several measures have been pursued without any significant gain. Notably, the use of (i) renewable energies such as solar, wind energy, hydroelectric energy and geothermal energy, (ii) carbon-free fuel like H_2, and (iii) use of fossil-based energy source without the release of CO_2 into the atmosphere, are the leading technologies.[33-41] Among these, the fossil-based energy sources are considered as best if CO_2 could be economically separated and utilized.[2,5,21] This was aggressively pursued recently by a large number of research groups throughout the world adopting new and novel approaches.[42,43] However, the technology of using nanoporous high surface area materials to capture and separate CO_2 from the flue gas stream has been in the forefront.[21-23] The detailed discussion pertaining to synthesis and application of the various types of nanoporous materials such as zeolite, mesoporous silica, metal oxide, activated carbon, zeolite imidazolate frameworks (ZIFs), metal organic frameworks (MOFs), covalent organic frameworks (COFs), porous aromatic frameworks (PAFs), borazine linked polymers (BLPs) and hyper crosslinked polymers (HCPs) etc. used for various application has been given in this chapter.[44-73] Moreover, the use of these materials for storage of H_2 has also been studied.[48,51] Based on the thorough study of the related literature, the objectives of the current research work have been outlined.

1.1.2. Statement of the problem

The massive consumption of fossil fuel to satisfy the ever-growing energy demand with the rapid population growth has contributed to the dramatic increase in the emission of CO_2 in the atmosphere that crossed 400 ppm in the recent times.[1-3,74,75] The uncontrolled CO_2 emission has led to rise in the earth's surface temperature at an unusually rapid rate and has risen by 0.83 °C since pre-industrial era.[21,76] If CO_2 emission is not properly handled now or in the near future, several devastating calamities are predicted such as, submerging of many

populous world cities like New York, Mumbai, Tokyo, Paris, Hong Kong, London, and Shanghai, with the rise in the sea level due to the melting of glaciers.[77-79] The melting of the glaciers not only increase the sea level but also facilitate further melting of the glaciers at a faster rate due to lower albedo.[80] Additionally, the increased earth's temperature will cause problems like drought, downpour, and typhoon.[81]

The demand for carbon-based energy sources has been on the rise especially in the developing countries due to the scarcity of alternative and renewable energy sources, without compromising the rate of industrial development and economic growth.[82-84] Various contributors along with their percentage share of CO_2 emission are summarized in ***Figure 1.1***. It can be clearly seen that the point sources such as electricity and heat production, industry and other energy production industries are the major CO_2 emitters.[85-92] The electricity and heat production industries are mainly the coal-fired plants that generate a huge amount of CO_2, which is primarily released to the atmosphere.[93-95] Under current circumstances, where the pace of economic growth and international uncertainty led to a situation, a single proper guideline could not be devised to put a break to the uncontrolled CO_2 emission from these point sources. However, the need of the time is to find the solutions to the problem already created by the excess use of the fossil fuel. A potential solution could be the economical separation of CO_2 from the flue gas stream of these point sources.[96,97]

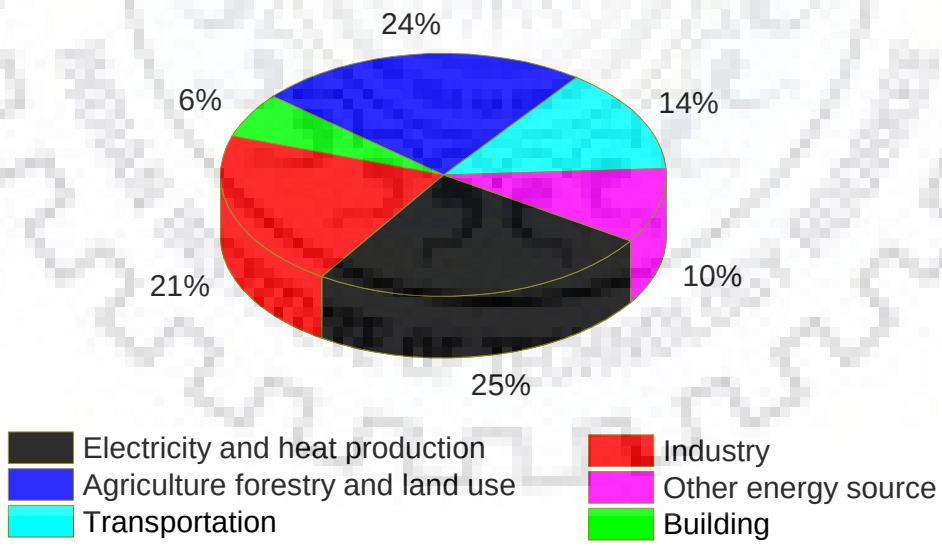

Figure 1.1: The percentage contribution of different CO_2 emitting sources in atmospheric CO_2.[97]

For years, liquid organic alknolamines and their derivatives have been commercially tried for tripping off CO_2 from flue gas stream in the coal-fired power plants without much

success.[1,9,11,12] The amine solutions are very selective towards CO_2 capture due to the various chemical bond formations as shown in ***Scheme 1.1***. The reaction of primary and secondary amine with CO_2 leads to the formation of carbamate whereas, the tertiary amines don't form a carbamate.[1] However, it's reaction with CO_2 in presence of H_2O could lead to the formation of bicarbonate ions as shown in ***Scheme 1.1***. Moreover, the presence of H_2O may also hydrolyze a part of carbamate to form bicarbonate ion.[1] The amount of CO_2 loading for primary and secondary amines is different from tertiary amines. In general, 0.5 to 1 mol of CO_2 could be loaded in 1 mol of primary and secondary amines, whereas, the CO_2 loading in case of the tertiary amine is 1:1.[1,98]

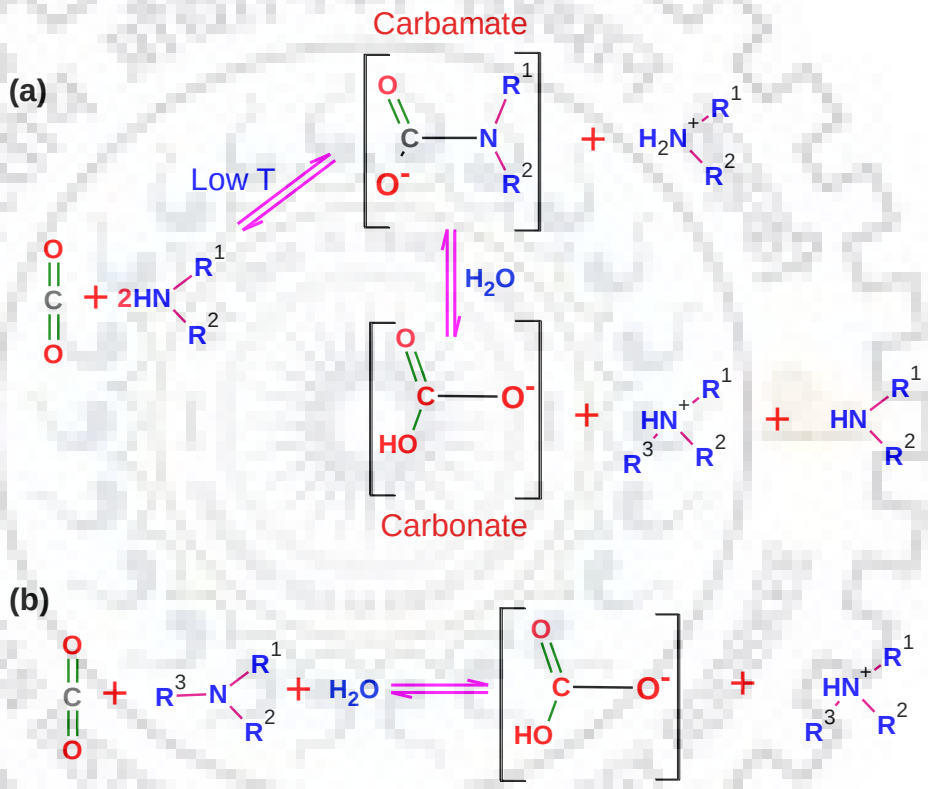

Scheme 1.1: Mechanistic representation of CO_2 capture by chemical absorption using (a) primary or secondary and (b) tertiary amine-containing solvents.[1]

The presence of small amount of primary or secondary amines in tertiary amines solution enhances its rate of adsorption of CO_2.[1] Among these, the regeneration of tertiary amine is less parasitic owing to its lower heat of reaction with CO_2 (320 Cal g^{-1}) as compared to primary (455 Cal g^{-1}) and secondary amines (360 Cal g^{-1}).[99] The higher heat of formation for primary and secondary amine is associated to carbamate formation.[1,99] Moreover, the rate of corrosion for tertiary amine is also least.[99] The rate constant for the reaction of primary, secondary and tertiary amines with CO_2 are 7000, 1200 and 3.5 m^3 s^{-1} $kmol^{-1}$ at 25 °C, respectively.[100] Due to slow reaction kinetics of the tertiary amine, more circulations of

amine solvent are required to remove the CO_2.[99] Among all, the primary amine has highest theoretical CO_2 uptake capacity but due to lower vapor pressure and higher corrosion rate, its upper limit has not been tested.[101] Despite showing very high selectivity and superior uptake capacity, the amine-based technology could not achieve the desired success because of several drawbacks. High regeneration cost, corrosive nature, thermal stability and ease of handling a large quantity of the liquid amine became the bottleneck for the technology.[1,9,11,12]

In order to address some of the problems associated with the use of liquid organic amines as adsorbents for capture and separation of CO_2, the use of solid adsorbents have been recently envisioned.[7,9-11] The textural properties, microstructure, morphologies and the nature of adsorption play a significant role in deciding the adsorbents for adsorption of specific adsorbates.[45,102-104] Among the above-listed parameters, the adsorption processes are classified based on the nature of operative forces between the adsorbate and adsorbent. The adsorption process proceeding via formation of chemical bond (covalent bond or ionic bond) between adsorbate and adsorbent is known as chemisorption with a higher heat of adsorption values, while, the process proceeding via week physical forces like van der Waals interaction and H-bonding with a lower heat of adsorption is known as physisorption.[17,105,106] The chemisorption with higher values of heat of adsorption has several advantages such as higher adsorbate uptake and selectivity among several adsorbates as compared to the physisorption process.[11,17,106] But desorption of the adsorbate takes place by breaking the permanent chemical bond formed would consume more energy.[1] From an application point of view, the regeneration of adsorbent is necessary and hence a trade-off between physisorption and chemisorption could be ideally the best solution. Keeping in mind all the parameters that play leading role in deciding the adsorption process, an ideal adsorbent should have the following characteristics;[17,107]

- Fast reaction kinetic
- High selective uptake
- Facile regeneration of the sorbent at low-energy penalty
- High surface area for adsorption
- Low cost of the sorbent material
- Chemical stability towards other components of the process
- For high temperature application, material should have good thermal stability

Recently, high surface area nanoporous solids adsorbents have emerged the winner for such applications as they satisfy some of the above-mentioned properties owing to their high specific surface area, hierarchical pore structure, large pore volume, and ease of pore wall functionalization.[11,17] The high specific surface area enables the adsorption of a large quantity of adsorbate by comparatively a small quantity of adsorbent.[11,17] The hierarchy in pore structure would facilitate the kinetics of adsorbate movement. The ease of appending the application-driven functionality enables these materials for various desired applications. Especially, for adsorption of small molecules, the presence of desired functionality in the confined space reduces the undesired kinetic and thermodynamic barrier and enhances the van der Waals interaction.[11,108,109] Hence, the regeneration process would be less energy intensive as it does not involve the breaking of the chemical bond.[108] Various types of natural and artificial high surface materials like zeolite, metal oxide, mesoporous silica, activated carbon, porous organic polymer and hybrid framework materials have been recently explored for adsorption application.[44-73] Each of the above-mentioned adsorbents has certain merits and demerits of their own.[110] For example, zeolites are having a high specific surface area and ultra-narrow pore size distribution but are sensitive towards moisture and their regeneration is more energy intensive due to higher heat of adsorption.[1,11] Carbonaceous adsorbents such as activated carbon and composites are cheap, readily available and have high specific surface area but have shown low gas uptake and selectivity.[110] The hybrid adsorbents like MOFs and ZIFs have very high specific surface area along with a high uptake capacity but are sensitive towards moisture and air, while the polymeric adsorbents such as COFs, POPs and PAFs show higher and selective CO_2 uptake, but their low stability has hindered the practical application.[110-112]

In an endeavor of moving towards the green energy sources, use of H_2 in the fuel cell which produces an enormous amount of energy (energy density of 33.3 kWh kg^{-1}) with no greenhouse pollutant like fossils fuels, is considered as the best green energy source.[105,113-115] The gravimetric energy density of H_2 (33.3 kWh kg^{-1}) is higher as compared to gasoline (11.1 kWh kg^{-1}), whereas, it's volumetric energy density is just reverse. The liquid H_2 produces energy of 8 MJ l^{-1} whereas, gasoline produces 32 MJ l^{-1}.[115] Thus, the only possible economical way to utilize the H_2 as fuel is to find a suitable storage system that can have large gravimetric storage capacity. Keeping in mind all the physicochemical properties of H_2 molecule along with the state of the art know-how, the U.S. Department of Energy (DOE) for the year 2017, has set a target of 5.5 wt% gravimetric storage capacity and 40 g l^{-1} volumetric capacity of H_2 by adsorbents at near ambient working condition.[115] However, this target is

way higher than the best-reported hydrogen storage capacity by any solid adsorbent.[24-26,116,117]

The H_2 storage mechanism can broadly be classified into two major categories. The reaction of H_2 with various metals/intermetallic via permanent chemical bond formation produces a series of hydrides with a large uptake of H_2.[105,118] These hydrides could release H_2 at an elevated temperature for the desired applications.[118] This method has been very popular initially but the elevated temperature operation becomes the bottle neck that restricted its wide-scale application.[118] The physical adsorption of H_2 by various high surface area solid adsorbents has been in the forefront of H_2 storage research of late, especially after several breakthrough researches on the development of the high surface area and narrow pore size solid adsorbents made up of lightweight elements with low skeletal density.[24-26,116-119] There was a continued effort to improve the interaction between the H_2 and the adsorbents by manipulating the chemistry of the adsorbent pore surface. The adsorbents such as MOFs, COFs and POPs are in the forefront for H_2 storage research owing to their ultra-high specific surface area with a low skeletal density, and controlled pore structure.[24-26,116-120]

1.2. NANOPOROUS MATERIALS

1.2.1. Historical prospective

As discussed above, for the applications of CO_2 capture or H_2 storage, high surface area nanoporous materials with controlled pore structure and functionality are sought. Discussion of nanoporous materials could never be complete if zeolites, one of the most important and first known nanoporous materials, are not included and discussed. Natural zeolites are formed by occasional volcanic activity.[121-123] These were discovered by the A. F. Cronstedt, a Swedish mineralogist and chemist in the year 1756.[121,122] Since then, many of the natural zeolites have been explored. During 1850s, zeolites were known to show properties like selective adsorption and reversible cation exchange but the real interest towards the utilization of zeolite aroused during 1930s when its sieving ability was discovered.[122] This led to the use of zeolite for the selective separation of gas based on their molecular size and polarity. The zeolites discovered until mid of 19th century were mostly the accumulation of well-arranged crystals of sub centimeter sizes.[124] These were mostly formed with requisite purity under hydrothermal condition of the late stage magmatic solutions but have the disadvantage of exiguity. In an endeavor to find the alternatives for industrial applications of zeolites, a massive exploration work has been carried out during 1950s with great success of finding large deposits of zeolite in the countries like Italy, Japan, and USA etc.[124]

Large abundance and low price have always attracted the industries for wide spread applications, however, the presence of impurities in the natural zeolites have dented their utilization to a greater extent.[124,125] This forced the researchers working towards the development of methodology to replicate the formation of the natural zeolites.[126] Although, the effort has started as early as 1940s, and first synthetic zeolite using hydrothermal synthesis method with low Si to Al ratio was reported.[126] Arrays of synthetic methodologies have been followed with a focus to not only the synthesis procedure but also the control of the structure, microstructure and textural properties.[126] However, the failure to increase the pore size remains a great challenge in the application prospective and limited its glaze in the adsorbents and catalysis community.[124,125] This is followed by the series of discoveries in the area of nanoporous materials that includes the breakthrough work by Mobile researchers, synthesis of MOFs, COFs, POPs, and ZIFs etc.[126-132] Activated carbon, has been known since 1500 BC, and have been used for water purification by ancient Indian societies.[133] The gas sorption properties of it was first time observed by K. W. Scheele in 1773 and after that it has been extensively used for sugar decolorization.[133,134] The large-scale production it for the first time was started in early 20th century in Germany. Thus, a vast research area was created in this processes that needed several controls by the agency such as IUPAC (International Union of Pure and Applied Chemistry). It provides several parameters that define the textural properties in a better way. A comprehensive discussion in this regard is followed.

1.2.2. Definition and classifications of porous materials

Porous material can be defined as the materials having cavities, voids or channels which are deeper than wider. In the Year 1985, IUPAC categorized the porous materials on the basis of pore size into three distinct classes; (i) microporous materials (pore size < 2 nm), (ii) mesoporous materials (pore size between 2 to 50 nm), and (iii) macroporous materials (pore size > 50 nm) as shown in ***Figure 1.2.a***.[135] For simplicity, another terminology "nanoporous materials" was coined that defines the materials with pore size smaller than 100 nm. Based on the pore structure and arrangement, further the porous materials were classified as (i) ordered porous materials where the pores are arranged in regular fashion, and (ii) disordered porous material with random pore arrangement as shown in ***Figure 1.2.b***.[136] With the development of the nanoporous materials field, various other classification schemes have been proposed from time to time by different research groups. In the following section, various families of high surface area nanoporous materials are discussed along with the explored applications and challenges.

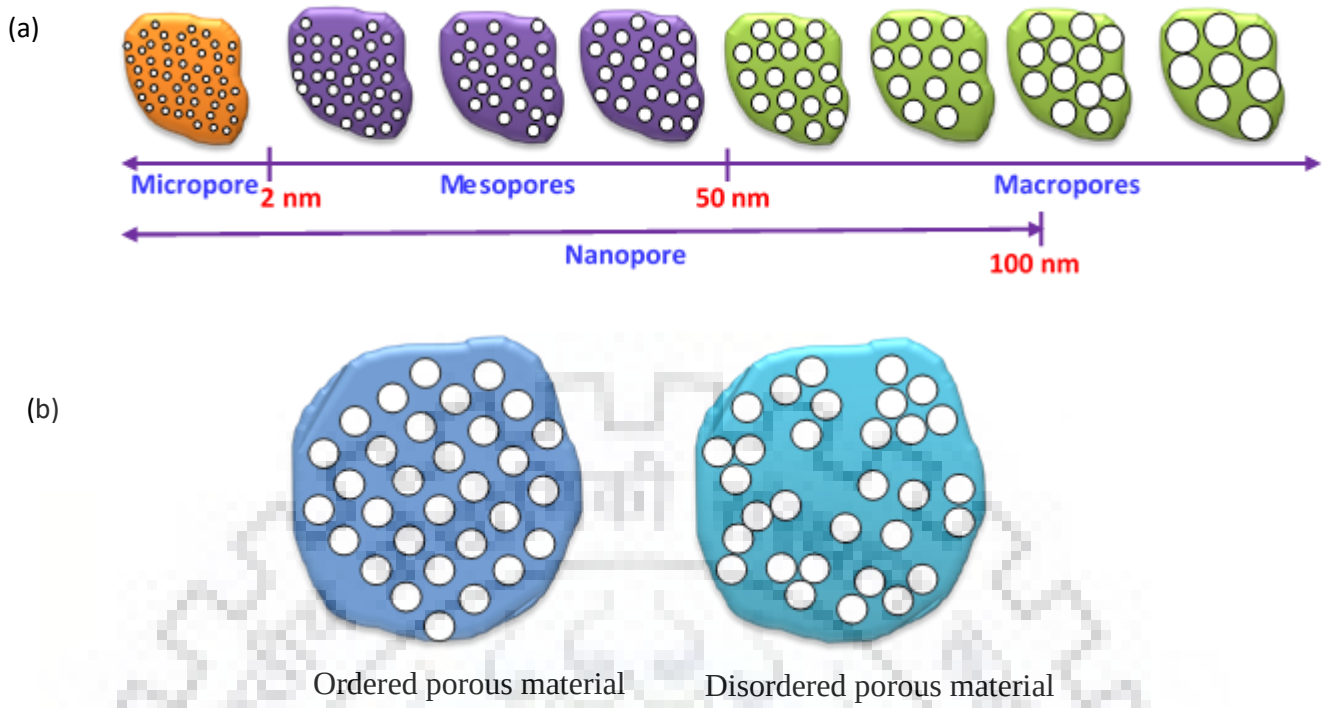

Figure 1.2: Classification schemes of porous materials based on the (a) pore size and (b) pore arrangement.[135,136]

1.2.3. Examples of various classes of nanoporous materials

1.2.3.1. Zeolites

Zeolites are three-dimensional crystalline aluminosilicate frameworks consisting of tetrahedral units TO_4 (T = Si and Al) joined through "O" corner to their four-neighboring groups.[140] The Si to Al ratio varies between 1 and ∞.[137] When the Si:Al ratio lies in the lower side, the zeolite surface becomes more negatively charged and hence show high acidic character.[137] Till date, more than forty natural zeolites have been explored and among these mordenite (MOR) and clinoptilolite (HEU) have extensively been used for agricultural, biological and environmental applications. Most of the natural zeolites have lower Si:Al ratio.[137] Although, the natural zeolite has been discovered more than 200 years ago, the presence of impurities forced to find ways to obtain a comparatively pure form of zeolites for industrial applications.[137] A lot of efforts have been made until the discovery of first synthetic zeolites, zeolites A and X in 1959 by Union Carbide employee "Milton and Breck".[126] This breakthrough invention embarked the new era of zeolite research. This further opens up a horizon where the zeolite framework was not restricted to Al and Si only, but several other ions of B, Ge, P and transition elements (like Co, Fe, Mn, and Zn) have been incorporated into frameworks.[127,137,138] In 1964, Breck reported the synthesis of zeolite Y with the Si:Al ratio in the range of 1.5 to 3.8.[136] Before that the synthetic zeolites were made with low

Si:Al ratio. This improvement in the Si:Al ratio proved instrumental in enhancing the thermal and acid stabilities.[137] To further improve the characteristic properties of the zeolites the researchers at Mobil research corporation synthesized zeolites with a higher Si:Al ratio in the range of 10 to 100 and even higher.[137]

Despite substantial efforts on the development of the synthetic methodologies, the application of zeolite was mostly limited to small molecules owing to their narrow pore size.[138] The application involving the larger molecules mostly suffered due to the pore clogging. To overcome this, the novel work by Ryoo and co-workers employing amphiphilic organosilane as structure directing agent to synthesize zeolites with larger pores become instrumental to pursue the applications involving larger molecules.[139] Similarly, Xiao *et al.* introduced hierarchy in the pore structure of the zeolite framework by employing the mixture of mesoscale cationic polymers and small molecules as structure directing agents.[140] However, the thermal and hydrothermal stability of these mesoporous zeolites are inferior in comparison to the microporous zeolites due to the amorphous nature of the mesopore channel walls.[141] The size and shape of the structure directing agent (SDA) have a profound role in the framework structure and pore architecture.[142] For example, the use of SDA-2 with four chiral centers, as shown in ***Figure 1.3.a***, resulted in the formation of chiral zeolites ITQ-37 with large open pores as shown in ***Figure 1.3.b***.

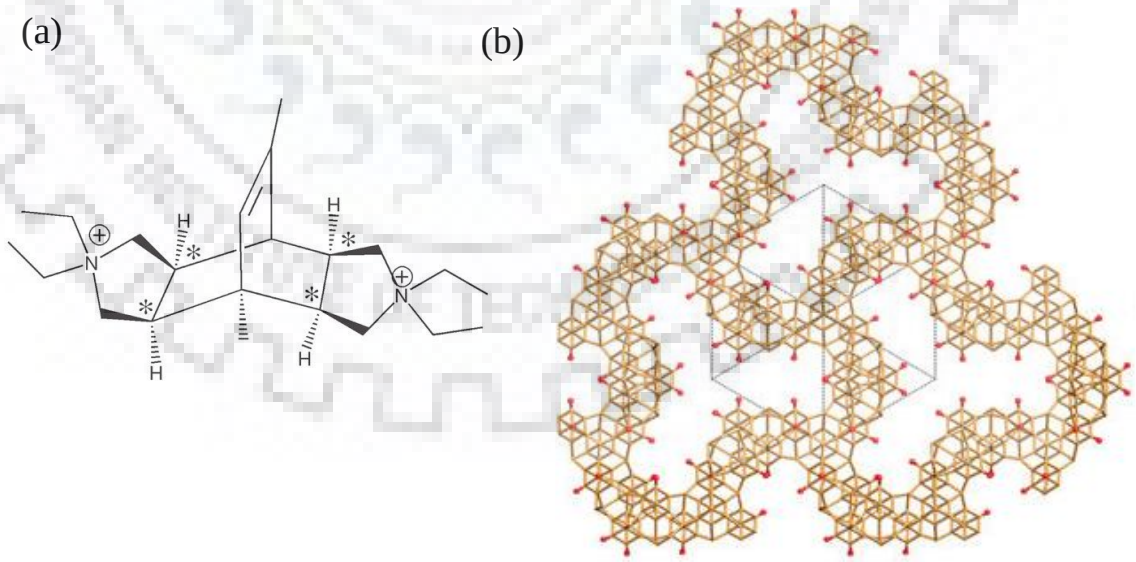

Figure 1.3: Effect of size and shape of structure directing agent on the pore architecture and framework structure of zeolite; (a) structure of SDA-2 and (b) framework structure and pore geometry of ITQ-37 zeolite.[Reprinted with permission from ref. 142 © 2009 Springer Nature]

1.2.3.2. Mesoporous silicas

The limitation of pore size in the zeolites has forced the researchers working in the catalysis, separation science and adsorption areas to look for the alternatives with a better control over the pore size distribution.[127,143] To this, the historic discovery of Mobil researchers Beck and Virtuli in 1992 on the synthesis of mesoporous silicates designated as MCMs with pore size centers in the range of 2-10 nm using hexadecyltrimethylammonium ammonium salt as SAD, stands out.[144] The MCM-41 consists of interconnected SiO_4 tetrahedral units and possesses three-dimensional framework structure with high surface area.[145] Following this discovery a series of mesoporous silica materials have been synthesized by changing various experimental parameters, precursors and SDA.[145-149] The commonly used SDA are CTABr and triblock polymers like Pluronic P-123 and F-127.[150] Most of the high surface area inorganic silica materials are synthesized by hydrothermal hydrolysis followed by polycondensation of TEOS using soft templates.[151] In next few years a large number of research articles and patents published focusing the applications of these over-hyped materials. Despite having a greater control over the pore size distribution, pore geometry and pore architecture, the mesoporous silica materials have found limited industrial applications owing to the lack of pore functionalities and hydrothermal stability.[151]

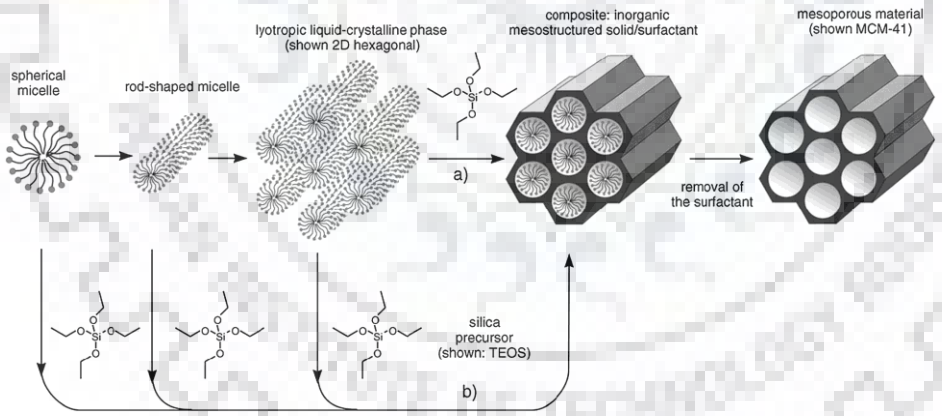

Figure 1.4: Formation of mesoporous materials by structure-directing agents: a) true liquid-crystal template mechanism, b) cooperative liquid-crystal template mechanism. [Reprinted with permission from ref. 151 © 2006 John Wiley & Sons, Inc.]

1.2.3.3. Activated carbons

Activated carbons (ACs) are one of the oldest and most used porous materials for myriad of application owing to their low cost, availability of raw materials, ease of synthesis and high surface area.[152-154] These are predominantly being used in adsorption and selective separation of pollutants from air and water.[152-160] One of the major applications of the ACs

lies as the support materials for various metal and metal oxide catalysts.[156,161-163] Moreover, these are also extensively used as electrode materials in energy storage devices.[164-168] The different carbon nanostructures like carbon nanotube, graphene etc. are widely used for aforementioned application.[153,165] In general, the ACs are synthesized by two methods, (i) physical method and (ii) chemical method. In physical method, ACs are synthesized by low temperature carbonization followed by high temperature activation in presence of CO_2 or steam flow.[167,168] The chemical method involves the carbonization in presence of activating agent such as $ZnCl_2$ or KOH etc. Lignocellulose, coal, bio-waste and agriculture wastes are major raw materials used for the production of ACs.[167] The specific surface area of ACs is very high and could reach as high as 3300 m^2 g^{-1}. Efforts are being made to further improve it by utilization of hard templates. Masika *et al.* and Cai *et al.* reported the synthesis of ACs, ZTC and 10Xc-70 with specific surface area of 3332 and 3331 m^2 g^{-1}, respectively.[159,169] These records breaking high surface area ACs ZTC and 10Xc-70 were synthesized using 13X and 10X zeolite as a templates, respectively. Further, Kuchta *et al.* have predicted a theoretical specific surface area of 6500 m^2 g^{-1} for ACs as shown in ***Figure 1.5.*** that can further store a record amount of hydrogen of 100-260 g kg^{-1} at 77 K and 100 bar pressure.[170]

Figure 1.5: Hypothetical three dimensional open framework structures of carbon.[Reprinted with permission from ref. 170 © 2012 ACS Publisher]

In order to further tune the physical and chemical properties of ACs, doping of various heteroatoms such as N, P, S and B are explored.[171-175] The incorporation of heteroatoms in ACs was performed using post-synthesis modification of carbon by high energy consuming amination, nitration, acid and base treatments or carbonization of heteroatom functionalized agro/bio-waste or synthetic polymer.[168] These heteroatom doped ACs have shown promising application in adsorption and separation of harmful pollutants from air and water, gas storage, energy storage and heterogeneous catalysis.[158, 171-176] Cao *et al.* modified the commercial AC by nitration and amination, and modified AC have shown enhanced catalytic activity

towards ozonation of oxalic acid. [177] Similarly, Ashourirad *et al.* have used benzimidazole-linked polymers as a N containing precursor for synthesis of CPC-550 with specific surface area of 1630 m^2 g^{-1} and highest ever reported CO_2 uptake of 36.7 wt% at 273 K and 1 bar, for any reported carbonaceous materials.[178] Although, the research on the ACs are promising and their application in industry is wide spread, the selectivity and capture capacity of various adsorbents has limited its use as gas storage and separation instrument.[179]

1.2.3.4. Metal organic frameworks (MOFs) and Zeolite imidazolate frameworks (ZIFs)

Metal organic frameworks (MOFs) are three dimensional crystalline porous frameworks and consist of multivalent metal ion linked to organic ligands via coordinate bonds.[128-130] MOFs have been in public domain for several decades but the term MOFs was first coined by Yaghi and Kitagwa in late 1990's.[128,129,180] These are synthesized by conventional modular synthesis strategy and possess very high specific surface area.[128-130,180] The highest ever reported specific surface area of 7010 and 7140 m^2 g^{-1} was reported by Farha *et al.* for a super critical CO_2 activated paddlewheel connected MOFs having hexacarboxylated organic linkers designated as NU-109 and NU-110, respectively, as shown in ***Figure 1.6.(a) and (b).***[116] They further predicted a theoretical maximum achievable specific surface area of 14,400 m^2 g^{-1}.[116]

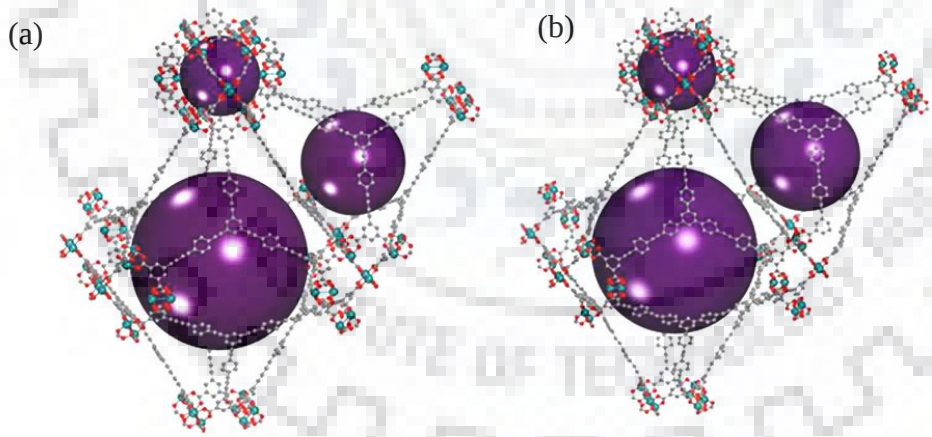

Figure 1.6: Schematic representations of (a) NU-109 and (b) NU-110. (O= red, C= grey, Cu= teal. Purple sphere represents three types of cages. To remove the ambiguity hydrogen and solvent molecules are excluded. [Reprinted with permission from ref. 116 © 2012 ACS Publisher]

The MOFs are the most studied nanoporous material after natural porous materials such as zeolites and carbon, owing to their interesting structural and compositional feature.[181] They have been utilized for myriad of applications such as gas sorption and separation,

catalysis, energy storage, sensing, light emission and drug delivery owing to their high specific surface areas, hierarchical pore size distribution and large pore volumes.[128-130,180-185] Despite having interesting physicochemical properties, the application of MOFs is limited to moisture free environment due to their susceptibility towards moisture.[186] In presence of moisture, the moisture susceptive oxygen bonds in MOFs lead to phase transformation which results in framework decomposition.[186] In general, the stability of MOFs depends upon the strength of coordinate bond between metal ion and bridging organic ligand as well as the protection of the coordination sites by bulkier functional groups.[186] In this endeavor, organic bridging ligand functionalized with hydrophobic groups such as methyl, ethyl, 2,5-dimethyl, phosphate and carboxylate have been used.[187,188] Moreover, the group-IV elements have strong affinity towards organic linkers and form strong bonds which result better stability of MOFs even in humid environment.[189] Recently, Zheng *et al.* reported Ni-MOF-74 a pore engineered MOF with adjustable pore size as shown in ***Figure 1.7*** that has shown excellent water and fluorocarbon adsorption capacities.[190]

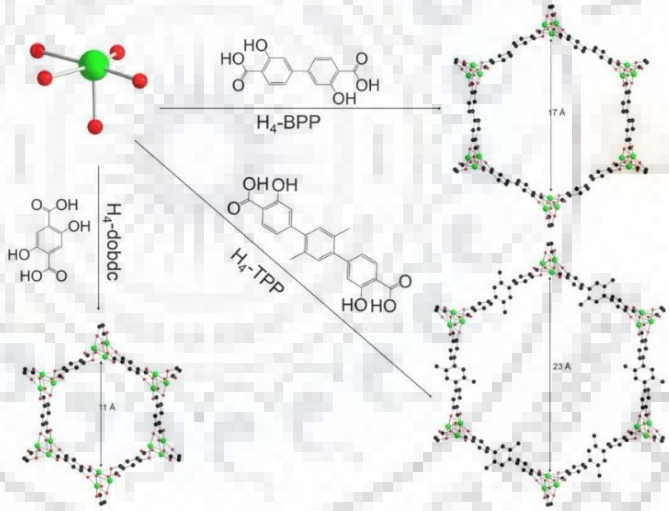

Figure 1.7: Reaction scheme for the synthesis of Ni-MOF-74, a water stable MOF. Black, red green spheres represent C, O and Ni atoms, respectively. [Reprinted with permission from ref. 190 © 2017 ACS Publisher]

Another subclass of nanoporous materials, zeolite imidazolate frameworks (ZIFs) that possess very high specific surface area, were also invented by Yaghi and co-workers.[191] The ZIFs are new type of framework materials having structural feature similar to zeolite and composed of tetrahedral transition metal ions like Zn^{2+} or Co^{2+} coordinated with imidazolate linker through O^{2-} ions.[191-193] Traditionally, ZIFs have been prepared by hydrothermal or solvothermal method under varying reaction conditions.[191] The synthesis of ZIFs has also been extended to solvent-free synthesis methodology. Recently, several non-conventional

synthesis methods have been adopted to synthesize ZIFs with application-driven functionalities.[194] Till now more than 150 ZIFs have been reported with their applications spanning in different areas such as adsorption, catalysis, sensing and electronic devices, permeation membrane as well as drug delivery agents.[194,195] The supremacy of ZIFs over MOFs lies in their permanent porosity and robust thermal and chemical stability.[196-199] The interaction in ZIFs is more strong in comparison to MOFs owing to the higher basicity of imidazolate linkers as compared to carboxylate linkers.[196-199] Despite having very high surface area and well-defined pore structure, MOFs and ZIFs both are not suitable for application under humid environment due to moisture susceptible coordinate bond present between metal and bridging ligands.[196-199]

1.2.3.5. Porous organic polymers (POPs)

In the quest for improving the bonding between the atoms that form the porous framework structure, rigid covalent bond with robust stability are preferred over the coordinate bond that very often lack the much needed thermal and hydrothermal stability.[130,199-202] There could not be anything better than using the earth's most abundant elements such as C, H, N, O and S for the above-mentioned purpose.[130,202] This encouraged the research in the field of metal-free nanoporous materials which garnered much attention of late.[202-216] Several types of covalently bonded metal free porous organic polymers (POPs) like covalent organic frameworks (COFs), porous aromatic frameworks (PAFs), polymer of intrinsic porosity (PIMs), hyper crosslinked polymers (HCPs), porous polymeric networks (PPNs) and conjugated microporous polymers (CMPs) etc. have been reported.[9,17,21,34,65-73,202-206] The POPs are porous frameworks consisting of light weight elements mainly from the first two row of the periodic table (H, B, C, N, O and S), and possess high specific surface area.[130,201] Broadly, POPs are divided into two classes: (i) crystalline POPs formed by thermodynamic controlled reversible reaction e.g. COFs, and (ii) amorphous POPs which are formed by irreversible kinetic controlled reaction e.g. PAFs, PIMs, HCPs, PPNs etc.[202,206-208] Due to reversible nature of thermodynamic controlled reaction in COFs synthesis, it has features like "proof reading and error checking" that leads to the formation of periodic pore ordering in COFs.[202,208] The diversity in synthetic approach and development of analytical techniques enabled to incorporate various heteroatom-based building block like pyrrole, indole capable of performing stimuli-responsive behavior, which in general is not seen in other categories of nanoporous materials like carbon, zeolite and mesoporous silica.[209,211,217,218]

During the last decade or so, the POPs have extensively been utilized (***Figure 1.8***) in gas sorption, drug delivery, sensors, catalysis, energy storage, proton conduction, light emission and many more owing to the availability of possible synthesis methodology, vast library of available organic building blocks, light weight, rigid framework structure, high surface area and tuneable pore functionality.[201-208,210] The high specific surface area has always been one of the most sought characteristic and maximum specific surface area reported for POPs is 5640 m^2 g^{-1}.[214] The pore size can be tuned either by using templating or non-templating routes.[215] The pore wall of the POPs could be functionalized by either post-synthesis modification as well as *in-situ* methods and among these *in-situ* method has been more popular.[168] For example, Timur *et al.* have tuned the binding affinity of benzimidazole linked polymers (BILPs) by combination of pre- and post-synthesis modifications to improve the CO_2 adsorption and reported the capture capacity of 24.48 wt%.[168] The maximum reported CO_2 uptake for POPs was 27.7 wt% at 273 K and 1 bar for the hexaphenylene based triazine framework (HAT-CTF-450/600).[216] Cooper *et al.* reported high surface area materials with extended π conjugation known as conjugated microporous polymers (CMPs), these are electrically conducting in nature.[219] Furthermore, polymers of intrinsic microporosity (PIMs) is another subclass of POPs with intrinsic microporosity that have been studied for selective uptake of CO_2, catalysis and hydrogen storage.[220]

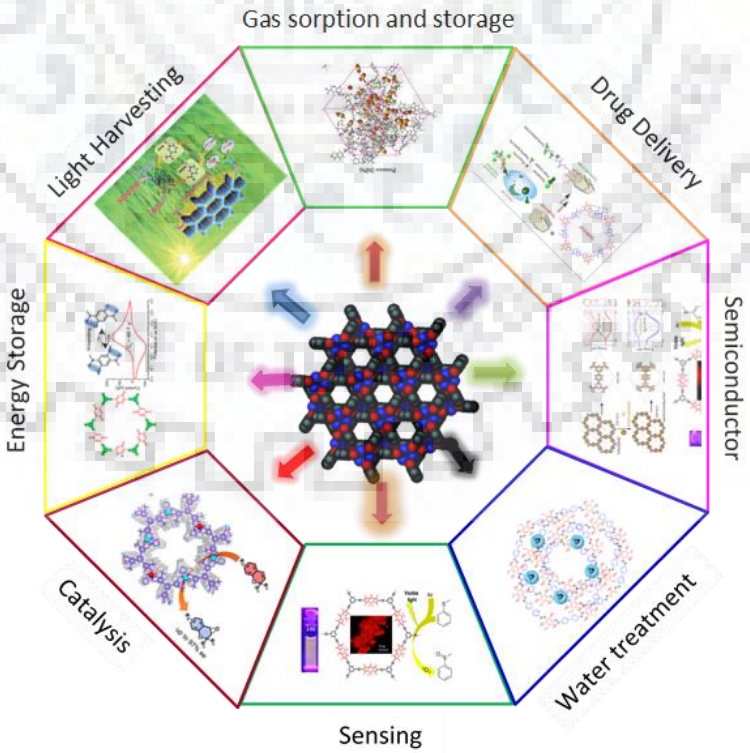

Figure 1.8: Applications of high surface area POPs in different fields.

1.3. INORGANIC-ORGANIC HYBRID MATERIALS

Inorganic-organic hybrid materials are the materials obtained after the molecular or materials interaction between the organic and inorganic moieties.[221] These materials possess the properties of both inorganic as well as organic components and additionally some novel properties could also be envisioned.[221-226] The evolution of inorganic-organic hybrid materials have made significant contribution towards the advancement of functional nanomaterials and garnered the attention of people from wide scientific field from biology and chemistry to physics and materials science.[223-228] The organic moieties provides the toughness, elasticity, chemical functionality and optical properties whereas, the inorganic components impart the much needed thermal and hydrothermal stability and modulus strength to the resultant hybrid materials.[221] Due to the above mentioned characteristics hybrid materials have been explored for myriad of application in the field of energy, environment, catalysis, optics and electronics etc.[229-232]

1.3.1. Historical perspective

The term "hybrid" was originated from the Latin word "*hybrida*," meaning mixed-breed.[229] These have been in public domain since 8th century. During this period a clay organic pigment called Maya Blue was used by Maya civilization in Mesoamerica during pre-Spanish era.[230-232] This nanostructured material is very stable and its color has not faded by the continuous exposure of harsh condition for more than twelve centuries.[231,232] Moreover, Maya blue has shown exceptional stability towards strong mineral acids such as aqua regia and temperature up to 250 °C (***Figure 1.9.)***.[231-233]

Figure 1.9: Painting of Mayan warrior Maya Blue pigments. [Reprinted with permission from ref. 233 © 2005 RSC Publisher]

To know the scientific fact about the exceptional stability and color persistence of Maya blue even when it is exposed to harsh chemical environment, scientific community took the

help of various analytical techniques.[230] The observations revealed that Maya blue is neither a pure organic dye nor any inorganic mineral and its exceptional resistivity towards the harsh environmental conditions is the result of its hybrid chemical composition, where organic dye molecules "indigo" is protected within superlattice of inorganic clay palygorskite crystal, $(MgAl)_2Si_4O_{10}(OH)\cdot 4H_2O$.[231-233] These findings led to a conclusion that the blending of inorganic and organic moieties leads to the creation of a very interesting materials with exceptional properties.[231,232] In the last century, the discovery of sol-gel process for silicone rubber synthesis using silicone oxide gave major impetus towards the development of inorganic-organic hybrid materials.[221] Very recently, owing to the better understanding of science of hybrid materials and fundamentals of interaction between the moieties, well-established hybrid materials for advanced application have been developed.[221-226]

1.3.2. Classes of inorganic-organic hybrid materials

The inorganic-organic hybrid materials have been classified into two major classes; *class-I* and *class-II*, based on the interaction between inorganic and organic building blocks.[221,223] In *class-I* hybrid materials, weak interactive forces such as hydrogen bonding, van der Waals or weak electrostatic interaction operate between the inorganic and organic units.[231,233] These are primarily the mixing of inorganic and organic materials with defined microstructure. Due to weak interaction between different components, the *class-I* hybrid materials are unstable and undergo leaching, aggregation and phase separation.[221,233] The examples of *class-I* hybrid materials includes the composites of metal nanoparticle and polymer membrane.[221,229,233] In *class-II* hybrid materials, the inorganic and organic components are held together by strong chemical bonds like covalent bond.[221,229,233] The examples of *class-II* hybrid materials are ZIFs, MOFs and periodic mesoporous silicas (PMOs) where blending of organic and inorganic component is at molecular scale. Due to strong chemical bonds, *class-II* hybrid materials possess high stability. The interactions between the inorganic and organic components in both classes of the hybrid materials are shown schematically in ***Figure 1.10***.[229]

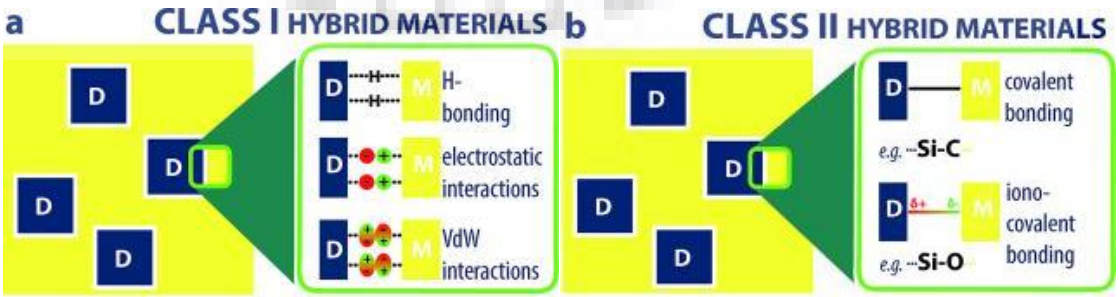

Figure 1.10: Different categories of interaction present between inorganic and organic moieties in hybrid materials. [Reprinted with permission from ref. 229 © 2016 John Wiley & Sons, Inc.]

1.3.3. Inorganic-organic hybrid nanoporous materials

Inorganic-organic hybrid nanoporous materials have been one of the fast-growing fields in the material science and engineering discipline and attracted much attention of scientists due to the ease of synthesis, high specific surface area, tunable pore functionality, high mechanical strength, low density, and thermal and hydrothermal stability.[49-51,58-63,116,181-188] With increasing demand of smart functional materials, tremendous efforts have been put towards the development of inorganic-organic hybrid nanoporous materials having some exciting features and functionality.[58-63,181-188] To meet the current materials demand, there is an utmost need to modify the synthesis approaches to introduce the tailor-made application driven functionality.[58-63,181-188,234]

Inorganic-organic hybrid nanoporous materials can be further subdivided in two categories: (i) siliceous materials and (ii) non-siliceous materials.[49-51,58-63] The materials like PMOs where silicon atoms are connected with carbon and oxygen atoms forming framework structures are known as siliceous hybrid materials, while materials such as MOFs and ZIFs which are made up of metal ions bridged with organic linkers are in the non-siliceous hybrid materials category.[49-51,58-63] Recently, phosphonate based MOFs came into existence where metal ions are linked with organophosphonic linkages instead of carboxylate linkages.[235,236] Most of the siliceous hybrid materials are synthesized by template-assisted method using various precursors to control the porosity.[233,234]

1.4. CYCLOPHOSPHAZENE AND ITS DERIVATIVES

The chemistry of polyphosphazene and its various aspects related to synthesis and design have been extensively investigated by Allcock and co-workers at Pennsylvania State University, USA.[237-241] Polyphosphazene has –P(R,R')=N- repeating unit with single and double bond at alternate position in the polymer skeleton (***Figure 1.11***), and considered as one of the largest inorganic macromolecule.[237-241] The polyphosphazene chain may contain the same or different substituents as side groups attached to phosphorous as shown in ***Figure 1.12***.[242] The side groups present in polyphosphazene skeleton play an important role in tuning the properties and applications.[242] For example, a thermal stability up to 300 °C can be observed for the conventional polyphosphazene chain containing chloride as side group functionality.[240,241] However, the polyphosphazene chain readily undergoes hydrolysis in humid condition due to the presence of moisture susceptible -P-Cl bond.[237-241] To enhance the hydrolytic stability, attempts were made to substitute the chloride with hydrophobic organic

functionalities.[243-245] Even, in some instances, the phosphorous atom has been replaced by carbon or sulfur atom in polyphosphazene skeleton to impart this characteristic.[242]

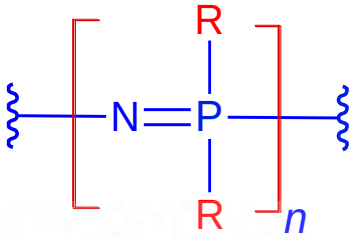

Figure 1.11: General chemical structure of polyphosphazene.[242]

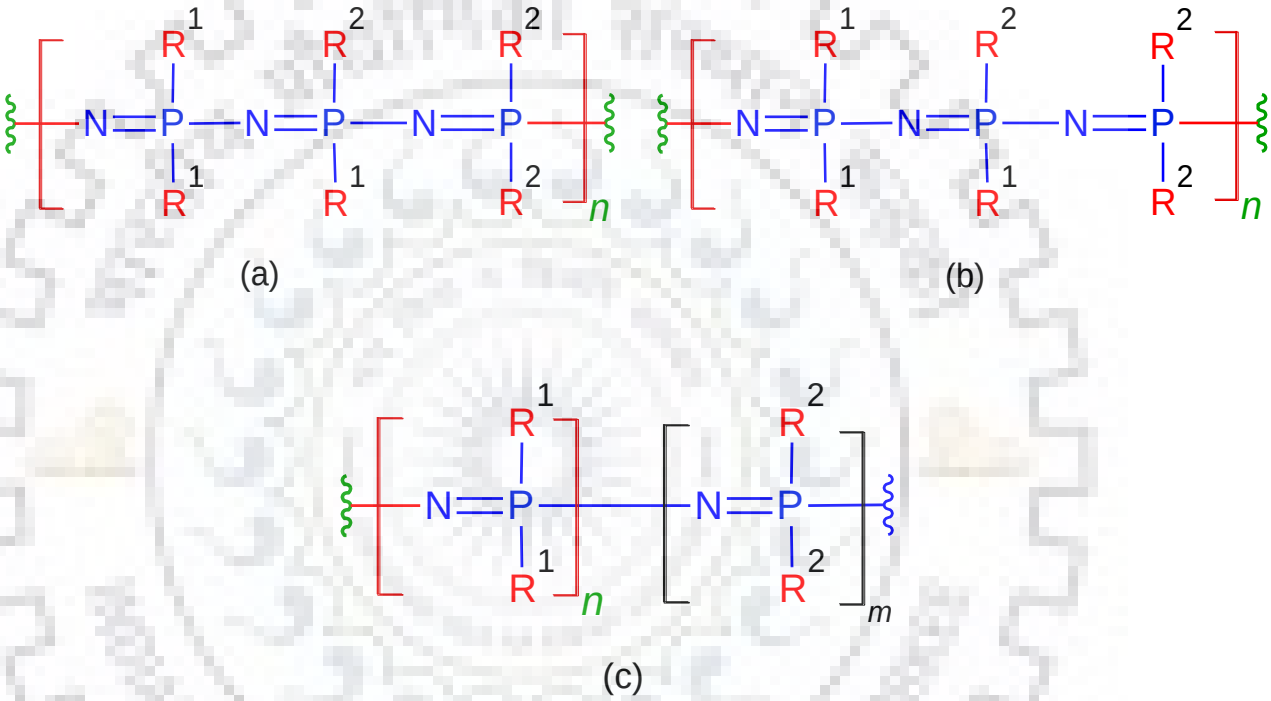

Figure 1.12: (a) Random distribution, (b) non-geminal disubstitution, and (c) diblock distribution of side groups in polyphosphazene chain.[242]

In 1897, H. N. Stokes proposed that polyphosphazene can attain cyclic structure and named this compound as "cyclophosphazene".[243] Cyclophosphazene like its predecessor polyphosphazene consists of phosphorous and nitrogen at the alternate position, and chloride group as side functionality attached with phosphorous atom.[243] Moreover, the cyclic structure of cyclophosphazene like polyphosphazene has alternate single and double bonds. The first reported cyclophosphazene as shown in ***Figure 1.13.a.*** is hexachlorocyclotriphosphazene ($N_3P_3Cl_6$), commonly known as phosphonitrilic chloride trimer (PNC). Another eight-membered ring of cyclophosphazene, octachlorotetracyclophosphazene ($N_4P_4Cl_8$), as shown in ***Figure 1.13.b.*** is also reported.[242] The six-membered cyclic compound PNC is more rigid as compared to eight-membered ring compound.[242] The PNC has an interesting paddle wheel

structure.[246] Due to the rigidity of the ring and paddle wheel structure, the six-membered cyclophosphazene derivatives could impart permanent porosity.[110,246-250] Heating of PNC beyond 250 °C leads to ring opening and forming an important class of polymer known as "inorganic rubber".[251]

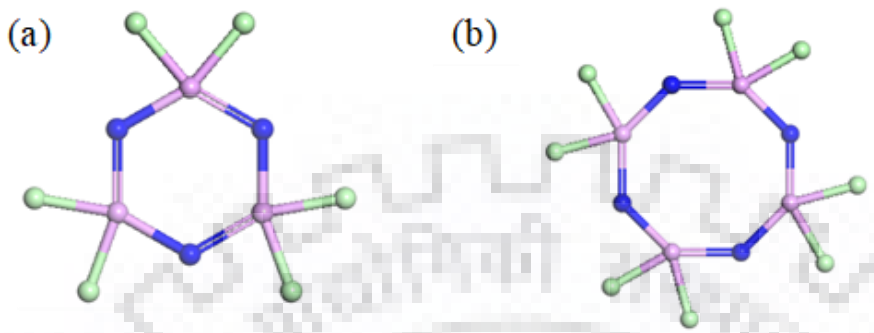

Figure 1.13: The stick and ball model of (a) Hexachlorotricyclophosphazene and (b) octachlorotetracyclophosphazene.[251]

The PNC consists of six easily replaceable chloride groups that can be substituted by appropriate functionality and this method is widely used for the formation of three-dimensional framework structures.[243,246-250] Recently, various functional materials like dendrimers, macromolecule and inorganic-organic hybrid framework have been synthesized utilizing this concept.[252-260] The inorganic-organic hybrid materials having cyclophosphazene moieties in its frameworks have been utilized for myriad of applications owing to their flame retardant property, thermal stability and biodegradability.[253-255,260] The sensitivity of polyphosphazene chain towards water resulted in the synthesis of many of the water-soluble polyphosphazene polyelectrolytes that have been utilized as hydrogel materials, microencapsulating agents, active components of vaccine formulations, and environmentally responsive polymers.[257-260] Andrianov *et al.* have prepared controlled size hydrogel microspheres using polyphosphazene for protein and vaccine delivery application.[257] As the constituent elements of cyclophosphazene, phosphorus and nitrogen, possess high limiting oxygen index, its derivatives have exclusively been used to enhance the flame retardant properties.[253-255,260] In this direction, Shin *et al.* reported the flame retardant properties of the phenol and catechol functionalized derivatives of cyclophosphazene.[254,255] Similarly, Gall *et al.* immobilized allyl-functionalized polyphosphazene in cotton fabric to improve its flame retardant properties.[254] The cyclophosphazene derivatives have also been used for detection of nitroaromatic explosive like picric acid. It also found its application as fuel cell membrane.[251] Recently, our research group has exploited the paddle wheel structure of the

cyclophosphazene to synthesize high surface area mesoporous silica materials bridged with cyclophosphazene moieties.[110,248-250]

1.5. SCHIFF BASE CONDENSATION

The classical Schiff base condensation was discovered by German chemist "Hugo Schiff" in 1864.[261] It has traditionally been used for the formation of imine and aminal linkages by condensation of carbonyl functional group with different amines.[262,263] In general, the imine double bond is formed, however, primary amines may subsequently attack the imine bond resulting in aminal linkages.[264] Schiff base condensation undergoes in acidic or basic medium; the mechanism has thoroughly been investigated and involves a number of reversible steps.[263] In the first step, amine reacts with aldehyde group via nucleophilic condensation forming a hydroxyl compound which undergoes dehydration in the presence of acid or base to yield an imine bond (Schiff base) as shown in ***Scheme 1.2***.[263,264]

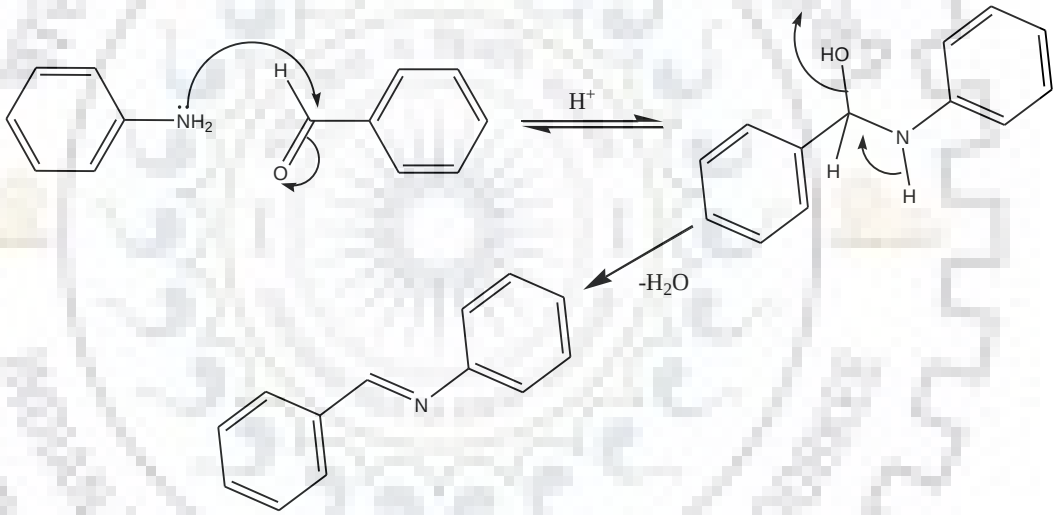

Scheme 1.2: Schiff base mechanism for the formation of imine bond.

1.5.1. Application of Schiff base condensation to synthesize nanoporous materials

Schiff base condensation reaction was very recently used for the synthesis of high surface area nanoporous materials. The formation of the imine and aminal linkages have been exploited to synthesize various polymers with imine, amine and imidazole linkages.[202-204,211-213] The Schiff base condensation is one of the highly used organic reactions for the synthesis of amorphous POPs like PAFs, PPNs, BILPs etc. as well as crystalline POPs like COFs.[168,202-204,208-213,265-268] The nanoporous materials synthesized through Schiff base condensation with aromatic rings have extended conjugation and hence, display robust stability towards moisture in comparison to the aliphatic polymers.[211-213] Although, initially Schiff based nanoporous materials have extensively been used for gas storage, but later on the incorporation

of various functionalities led to their applications in catalysis, energy storage, sensor, drug delivery, solar and optoelectronic devices.[202-204,208-213] The most important selling point of this method is that it does not need any metal-based catalyst and possess self-correction feature under thermodynamic condition owing to reversibility of imine bond.[202] Recently, *Yaghi and coworkers* have reported several two and three-dimensional COFs such as COF-42, COF-43 and COF-300 in presence of acetic acid, as shown in ***Figure 1.14.,*** using planar and three-dimensional building block.[265,266]

Although, most of the framework synthesis needed acid as catalyst but precursor with higher basicity such as melamine undergoes Schiff base condensation without any catalyst.[267] As shown below in ***Figure 1.15***, Schwab *et al.* condensed melamine with terephthaldehyde in a catalyst-free reaction condition using DMSO as solvent at 180 °C.[267] Similarly, Song *et al.* utilized an identical methodology for the synthesis of nitrogen rich aromatic porous organic polymers (APOPs) by condensation of melamine and its derivatives with different aldehydes.[268] The APOPs have demonstrated excellent selective CO_2 uptake of 19.8 wt% at 273 K and appreciable hydrogen storage capacity of 1.8 wt% at 77 K and 1 bar pressure. El-Kaderi and coworkers used the Schiff base chemistry for the synthesis of BILPs for gas sorption application.[168,203]

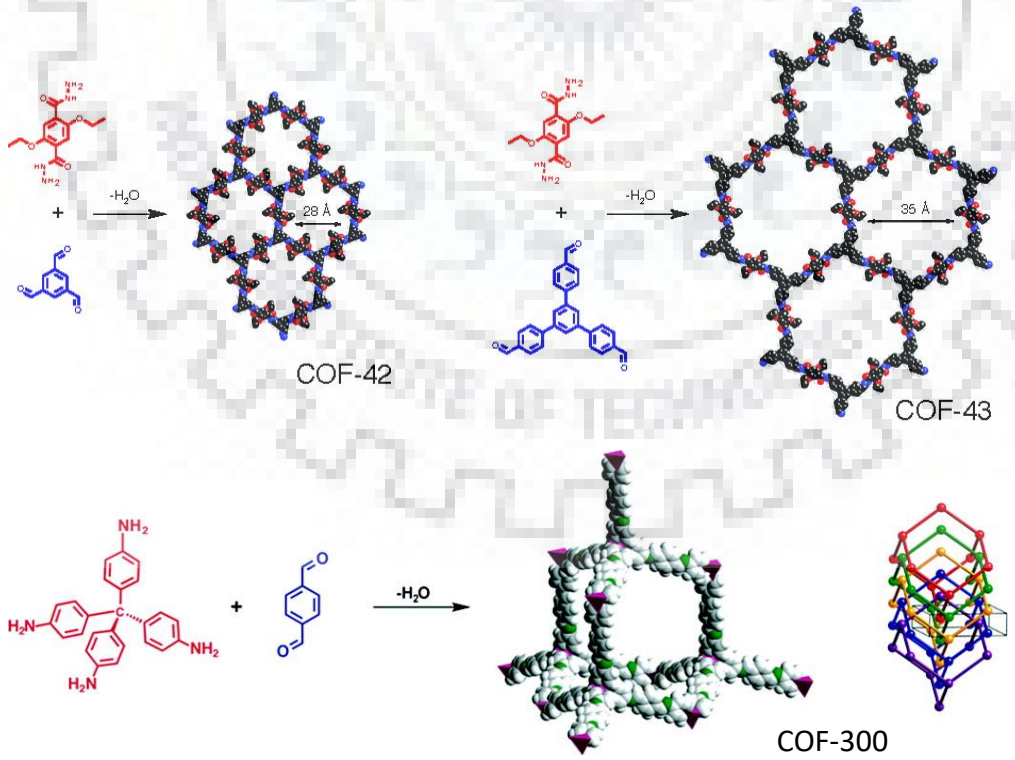

Figure 1.14: Synthesis of crystalline POPs (COFs) using Schiff-base condensation in presence of acetic acid as a catalyst. [Reprinted with permission from ref. 265, 266 © 2011 and 2009, respectively, ACS Publisher]

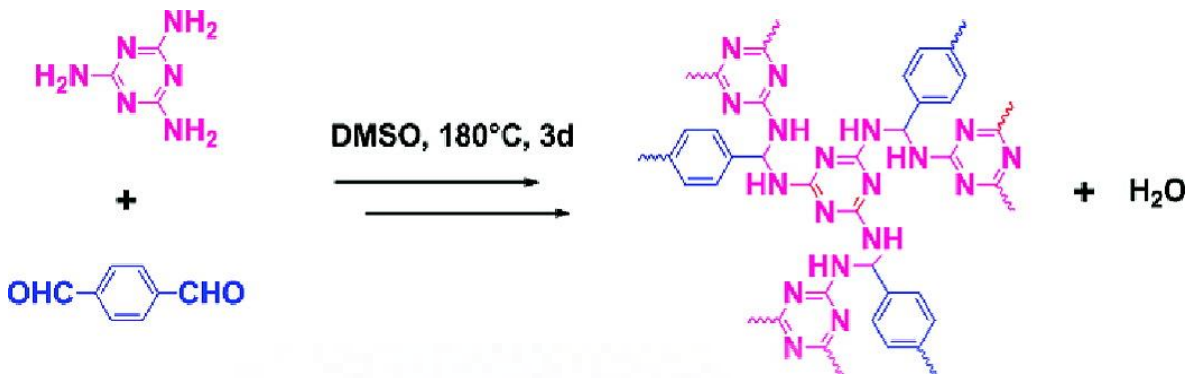

Figure 1.15: Synthesis of amorphous POP (SNW-1) by Schiff base condensation of terephthaldehyde and melamine under catalyst-free condition. [Reprinted with permission from ref. 267 © 2009 ACS Publisher]

1.6. MESOPOROUS ORGANOSILICAS

1.6.1. Overview

The development of mesoporous silicas such as MCMs, SBAs, CMKs etc. have received the most attention for almost a decade from their first report in 1992.[144,269-271] Manipulating the specific surface area, pore size distribution, pore volume and synthesizing the mesoporous silicas in various pore symmetries have got all the focus during this period of time.[272,273] A large number of publications citing the success story of these mesoporous silicas have brought a great hope for their uses. Despite having all the requirements that could make these, materials of the century, the lack of pore functionalities has limited their industrial applications.[273] To address this issue, efforts were made to incorporate the application-oriented functionality in the pore wall of silica framework.[273] For this, the post-synthesis functionalization of the pore surface found a great deal of attention because of its simplicity and versatility.[274] However, the lower and non-homogeneous loading of functional groups coupled with the occasional pore blocking affected adversely the performance of the functionalized mesoporous silica materials.[151]

The historic discovery by three independent research groups in 1999 on the formation of Si-C bond in the mesoporous siliceous framework to synthesize a new class of nanoporous material popularly known as PMOs has further developed a renewed hope in the research field of catalysis, adsorption, separation, drug delivery, sensing, chromatography, electronic industries, energy and environment. Many of the short-comings of post-synthesis modification method were resolved by this *in-situ* incorporation of organic moieties into the porous siliceous frameworks.[274-281] Soon after, a large number of functionalities have been incorporated into the pore walls of siliceous frameworks suitable for different applications.[275,277,282]

1.6.2. Organosilicas with different functionalities

The simple organic moieties such as methylene, ethylene and vinylene groups that were incorporated at the beginning by choosing precursors such as bis(triethoxysilyl)methane (BTSM), 1,2-bis(triethoxysilyl)ethane (BTEE) and bis(triethoxysilyl)ethane (BTSE) were replaced by a large numbers of other functionalities.[283-286] The incorporation of ethene functionality in PMOs garnered much attention due to its potential for further functionalization of its double bond as shown in ***Figure 1.16***.[281] The first ordered ethene bridged PMO having semicrystal like structure was synthesized by Xia *et al.*[287]

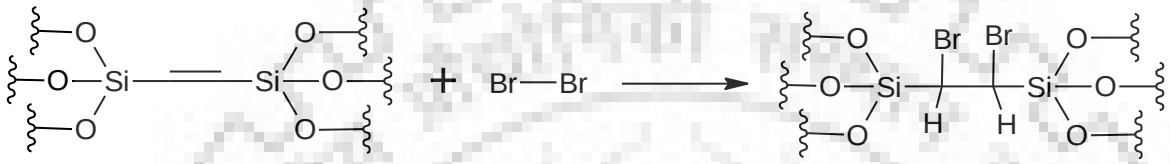

Figure 1.16: (a) Schematic representation of functionalization of ethylene bridged PMO by bromination reaction.[281]

Some of the notable functionalities that provided the room for exploring various applications are diacetylene, amine, amidoxime, porphyrin, vinyl, thiol, carboxylic acid, phosphonic acid and sulphonic acid.[273,288] All these functionalization made the PMOs as one of the most sought materials among the nanoporous materials.[273,288] Further, with the development of synthetic methodology and analytical techniques, complex functionalities were also incorporated into the PMO frameworks.[289] Li *et al.* synthesized a light responsive PMO by appending porphyrin, a visible light absorbing organic moiety with extended π conjugation, into PMO pore wall as shown in ***Figure 1.17a***.[289] Similarly, Olkhovyk *et al*. incorporated heterocyclic organic moiety (***Figure 1.17b***) having affinity for heavy metal ions like Hg.[290]

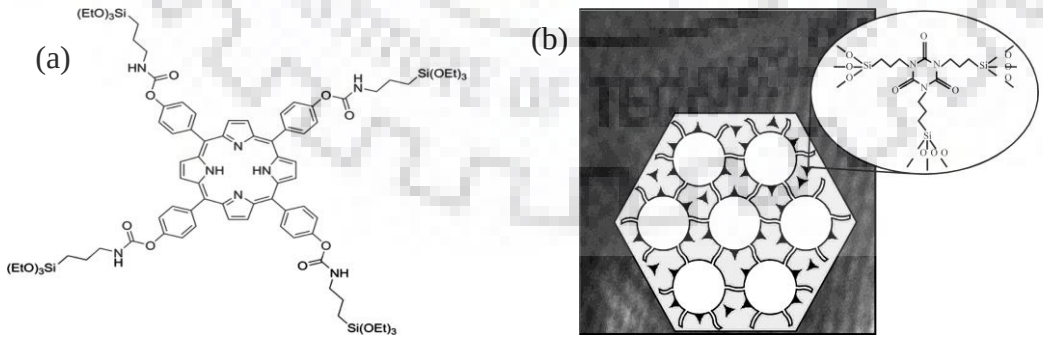

Figure 1.17: (a) Light responsive PMO synthesized by appending porphyrin and (b) PMOs functionalized with tris[3-(trimethoxysilyl)propyl]isocyanurate heterocyclic organic moiety having affinity towards heavy metal ion. [Reprinted with permission from ref. 289, 290 © 2013 and 2005, respectively, ACS Publisher]

Recently, the focus has been shifted towards the inclusion of electron-rich nitrogen enriched moieties especially triazine like moieties into the PMOs frameworks. Triazine, with alternative carbon and nitrogen in the hexagonal planar ring is one of the nitrogen enriched moieties because of its high electron density and aromatic character.[64,216,268] Its presence in various high surface area microporous organic polymers have shown extraordinary properties and applications and hence, is considered as an important organic moieties to be incorporated in the PMOs.[291-293] Several triazine functionalized PMOs as well as non-siliceous materials have shown much improved performance in catalysis, gas adsorption, energy storage and electrocatalysis applications.[64,216,268,269] In this regard, Ibrahim *et al.* [292], have synthesized triazine incorporated membrane and investigated the water desalination applications. Furthermore, Lin *et al.* have synthesized triazine bridged polysilsesquioxanes containing lanthanide ions for luminescence application.[291] Further, Prasetyanto *et al.* reported the synthesis of nitrogen rich triazine bridged PMOs in presence of Pluronic P123 (triblock polymer), as shown in ***Figure 1.18.,*** and used it for catalytic activation of CO_2 under metal-free condition.[293]

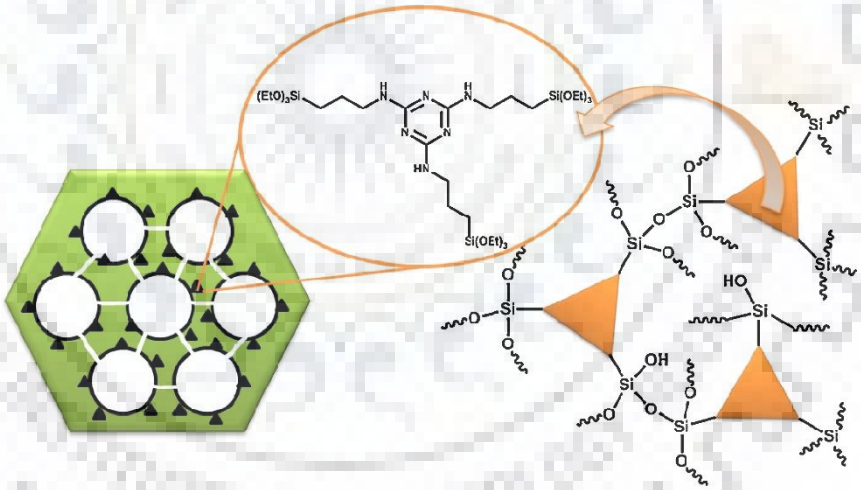

Figure 1.18: Illustration of nitrogen rich triazine bridged PMO synthesized in presence of SDA. [Reprinted with permission from ref. 293 © 2010 Elsevier Ltd.]

1.7. MOTIVATION AND OBJECTIVES

The thorough literature studies on the recent developments of high surface area nanoporous materials used for the CO_2 capture applications has provided the much-needed direction to chalk out a plan for the present research. In this direction, it was found that the presence of heteroatoms such as nitrogen, oxygen and phosphorus in the framework of these nanoporous materials have improved the adsorbent-adsorbate interaction. The CO_2, being a Lewis acidic gas has a stronger interaction to the Lewis basic frameworks resulting in the thermodynamically favorable adsorption process. Moreover, as documented in many of the literature, controlling the textural properties favors the kinetics of the adsorption. Hierarchical pore structures with a majority of the pores in the micropore region help in the improved adsorption capacity reinforced by the presence of mesopores that helps in the mass transfer. Thus, based on the above know-how, the objectives of the present research were defined to take forward the research in a direction one step closer to the realization of a sustainable CO_2 capture system.

The main objectives of present research work are;

- To synthesize inorganic-organic hybrid nanoporous materials by choosing appropriate inorganic and organic precursors
- To control the experimental conditions in such a way that, it could lead to the formation of materials with high specific surface area, narrow pore size distribution, hierarchical pore structure and homogeneous distribution of large numbers of heteroatoms
- To characterize the synthesized inorganic-organic hybrid nanoporous materials by the state-of-the-art analytical techniques such as, FT-IR, NMR, CHNS(O), XPS, TGA, XRD, FE-SEM, TEM and N_2 sorption
- To investigate the CO_2 sorption performance of the selected high surface area inorganic-organic hybrid nanoporous materials
- To investigate the performance of selected materials for H_2 and CH_4 storage applications

1.8. THESIS OUTLINE

The thesis is organized into six chapters;

Chapter-I

- Comprehensive literature studies on various high surface area nanoporous materials along with their synthesis and applications in various fields.
- Detailed discussion on the synthesis and applications of various inorganic-organic hybrid nanoporous materials.
- The chemistry of cyclophosphazene moieties and its role in the synthesis of various functional materials has been discussed.
- The use of Schiff base condensation for the synthesis of nanoporous materials has been discussed.
- Nanoporous high surface area siliceous materials with various functionalities are discussed.
- Incorporation of tirazine moiety in siliceous frameworks has been discussed.
- Use of solid adsorbents for CO_2 capture and H_2 storage are discussed.

Chapter-II

- Detailed account of the synthetic approaches utilized to prepare various inorganic-organic hybrid nanoporous materials investigated for gas sorption studies has been given.
- Synthesis methodology adopted for the synthesis of precursors and their further utilization for making the hybrid frameworks have been discussed.
- Non-siliceous hybrid nanoporous materials were synthesized by Schiff base condensation and nucleophilic condensation reaction.
- The synthesis of siliceous hybrid nanoporous materials and the systematic nitrogen enrichments have been included.
- Basic working principle of analytical techniques used in this research such as FT-IR, NMR, CHNS/O, XPS, TGA, XRD, SAXS, FE-SEM, TEM, and gas sorption were given in detail.

Chapter-III

- The use of Schiff base condensation to synthesize non-siliceous inorganic-organic hybrid nanoporous materials (HNMs) by simple condensation method has been discussed.
- Detailed characterization of both the synthesized precursors as well as the hybrid materials have been carried out by the analytical techniques.

- Based on the use of precursors for synthesis, the structure of HNMs was proposed and confirmed by the outcome of the analytical methods.
- The gas sorption study of HNMs has been investigated and discussed in details by comparing with the existing literature.

Chapter-IV

- Detailed synthesis and characterization of cyclophosphazene based hybrid nanoporous materials (CHNMs) via solvothermal method have been given.
- The proposed structure of CHNMs was confirmed using state-of-the-art analytical techniques.
- The CO_2 capture and H_2 storage behavior of CHNMs have been accessed and further compared with the recently reported solid adsorbents.

Chapter-V

- Detailed synthesis and characterization of the siliceous hybrid materials designated as NETPMOs using the condensation products of CNC with APTES, TMSPD or TMSPT, followed by hydrolysis and polycondensation have been given.
- Systematic nitrogen enrichment in the siliceous framework has been conducted by choosing appropriate precursors.
- The co-condensation with TEOS for the improvement of textural properties has been performed.
- The role of nitrogen enrichments in CO_2 sorption behavior of NETPMOs has been investigated.

Chapter-VI

- Summary of the hybrid materials synthesized by various methods has been discussed.
- The control of textural properties and gas sorption performance of different materials has been compared and discussed in this chapter.
- The achieved milestones have been summarized.
- The challenges faced in conducting the present research has been noted
- The future prospects of the current research were outlined

References

1. D. M. D'Alessandro, B. Smit and J. R. Long, Carbon dioxide capture: Prospects for new materials, *Angew. Chem. Int. Ed.*, 2010, **49**, 6058−6082.
2. J. Yu, L. H. Xie, J. R. Li, Y. Ma, J. M. Seminario and P. B. Balbuena, CO_2 capture and separations using MOFs: Computational and experimental studies, *Chem. Rev.*, 2017, **117**, 9674−9754.
3. S. Zeng, X. Zhang, L. Bai, X. Zhang, H. Wang, J. Wang, D. Bao, M. Li, X. Liu and S. Zhang, Ionic-liquid-based CO_2 capture systems: Structure, interaction and process, *Chem. Rev.*, 2017, **117**, 9625−9673.
4. E. D. Bates, R. D. Mayton, I. Ntai and J. H. D. Jr, CO_2 capture by a task-specific ionic liquid, *J. Am. Chem. Soc.*, 2002, **124**, 926–927.
5. Q. Wang, J. Luo, Z. Zhong and A. Borgna, CO_2 capture by solid adsorbents and their applications: Current status and new trends, *Energy Environ. Sci.*, 2011, **4**, 42–55.
6. H. Yang, Z. Xu, M. Fan, R. Gupta, R. B. Slimane, A. E. Bland and I. Wright, Progress in carbon dioxide separation and capture: A review, *J. Environ. Sci.*, 2008, **20**, 14–27.
7. A. Samanta, A. Zhao, G. K. H. Shimizu, P. Sarkar and R. Gupta, Post-combustion CO_2 capture using solid sorbents: A review, *Ind. Eng. Chem. Res.*, 2012, **51**, 1438–1463.
8. F. Geyer, C. Schönecker, H. J. Butt and D. Vollmer, Enhancing CO_2 capture using robust super omniphobic membranes, *Adv. Mater.*, 2017, **29**, 1603524−1603529.
9. L. Zou, Y. Sun, S. Che, X. Yang, X. Wang, M. Bosch, Q. Wang, H. Li, M. Smith, S. Yuan, Z. Perry and H. C. Zhou, Porous organic polymers for post-combustion carbon capture, *Adv. Mater.*, 2017, **29**, 1700229−1700263.
10. A. Darabi, P. G. Jessop and M. F. Cunningham, CO_2-responsive polymeric materials: Synthesis, self-assembly, and functional applications, *Chem. Soc. Rev.*, 2016, **45**, 4391−4436.
11. J. Wang, L. Huang, R. Yang, Z. Zhang, J. Wu, Y. Gao, Q. Wang, D. O'Hareb and Z. Zhong, Recent advances in solid sorbents for CO_2 capture and new development trends, *Energy Environ. Sci.*, 2014, **7**, 3478−3518.
12. D. P. Hanak, E. J. Anthony and V. Manovic, A review of developments in pilot-plant testing and modelling of calcium looping process for CO_2 capture from power generation systems, *Energy Environ. Sci*., 2015, **8**, 2199−2249.
13. Y. Tang and K. Landskron, CO_2-sorption properties of organosilicas with bridging amine functionalities inside the framework, *J. Phys. Chem. C*, 2010, **114**, 2494−2498.
14. A. Goeppert, M. Czaun, J. P. Jones, G. K. S. Prakash and G. A. Olah, Recycling of carbon dioxide to methanol and derived products–closing the loop, *Chem. Soc. Rev.*, 2014, **43**, 7995−8048.
15. S. R. Venna and M. A. Carreon, Metal organic framework membranes for carbon dioxide separation, *Chem. Eng. Sci.*, 2015, **124**, 3–19.
16. P. Carraro, V. Elías, A. García Blanco, K. Sapag, S. Moreno, M. Oliva and G. Eimer, Synthesis and multi-technique characterization of nickel loaded MCM-41 as potential hydrogen-storage materials, *Micropor. Mesopor. Mater.*, 2014, **191**, 103–111.
17. R. T. Woodward, L. A. Stevens, R. Dawson, M. Vijayaraghavan, T. Hasell, I. P. Silverwood, A. V. Ewing, T. Ratvijitvech, J. D. Exley, S. Y. Chong, F. Blanc, D. J. Adams, S. G. Kazarian, C. E. Snape, T. C. Drage and A. I. Cooper, Swellable, water- and acid-tolerant polymer sponges for chemoselective carbon dioxide capture, *J. Am. Chem. Soc.*, 2014, **136**, 9028–9035.
18. H. Li, Q. Pan, Y. Ma, X. Guan, M. Xue, Q. Fang, Y. Yan, V. Valtchev and S. Qiu, Three-dimensional covalent organic frameworks with dual linkages for bifunctional cascade catalysis, *J. Am. Chem. Soc.*, 2016, **138**, 14783–14788.
19. Z. J. Lin, J. Lu, L. Li, H. F. Li and R. Cao, Defect porous organic frameworks (dPOFs) as a platform for chiral organocatalysis, *J. Catal.*, 2017, **355**, 131–138.
20. K. P. Rao, Y. K. Devi, J. Suryachandram, R. P. Rao and J. N. Behera, A dense I^1O^3 hybrid superhydrophobic network, Pb(H-BTMB), exhibits selectivity toward CO_2 gas sorption, *Inorg. Chem.*, 2017, **56**, 11184–11189.
21. H. A. Patel, J. Byun and C. T. Yavuz, Carbon dioxide capture adsorbents: Chemistry and methods, *ChemSusChem*, 2017, **10**, 1303–1317.

22. A. Goeppert, M. Czaun, G. K. S. Prakash and G. A. Olah, Air as the renewable carbon source of the future: An overview of CO_2 capture from the atmosphere, *Energy Environ. Sci.*, 2012, **5,** 7833–7853.
23. J. Wang, S. Wang, Q. Xin and Y. Li, Perspectives on water-facilitated CO_2 capture materials, *J. Mater. Chem. A*, 2017, **5**, 6794–6816.
24. A. C. Dillon and M. J. Heben, Hydrogen storage using carbon adsorbents: Past, present and future, *Appl. Phys. A*, 2001, **72**, 133–142.
25. L. Schlapbach and A. Züttel, Hydrogen-storage materials for mobile applications, *Nature*, 2001, **414**, 353–358.
26. M. G. Nijkamp, J. E. M. J. Raaymakers, A. J. Dillen and K. P. Jong, Hydrogen storage using physisorption–materials demands, *Appl. Phys. A*, 2001, **72**, 619–623.
27. S. R. Marri, S. Ratha, C. Sekhar Rout and J. N. Behera, 3D cuboidal vanadium diselenide embedded reduced graphene oxide hybrid structures with enhanced supercapacitor properties, *Chem. Commun*., 2017, **53**, 228–231.
28. C. W. Kim, S. J. Yeob, H. M. Cheng and Y. S. Kang, A selectively exposed crystal facet-engineered TiO_2 thin film photoanode for the higher performance of the photoelectrochemical water splitting reaction, *Energy Environ. Sci.*, 2015, **8**, 3646–3653.
29. A. K. Nayak, Y. Sohn and D. Pradhan, Facile green synthesis of $WO_3{\cdot}H_2O$ nanoplates and WO_3 nanowires with enhanced photoelectrochemical performance, *Cryst. Growth Des.*, 2017, **17**, 4949−4957.
30. A. Maitra, S. K. Karan, S. Paria, A. K. Das, R. Bera, L. Halder, S. K. Si, A. Bera and B. B. Khatua, Fast charging self-powered wearable and flexible asymmetric supercapacitor power cell with fish swim bladder as an efficient natural bio-piezoelectric separator, *Nano Energy*, 2017, **40**, 633–645.
31. D. Mohapatra, S. Parida, S. Badrayyana and B. K. Singh, High performance flexible asymmetric CNO-ZnO//ZnO supercapacitor with an operating voltage of 1.8 V in aqueous medium, *Appl. Mater. Today*, 2017, **7**, 212–221.
32. C. W. Kim, M. J. Kang, S. Ji and Y. S. Kang, Artificial photosynthesis for formaldehyde production with 85% of faradaic efficiency by tuning the reduction potential, *ACS Catal.*, 2018, **8**, 968−974.
33. S. Huang, Y. Meng, S. He, A. Goswami, Q. Wu, J. Li, S. Tong, T. Asefa and M. Wu, N-, O-, and S-tridoped carbon-encapsulated Co_9S_8 nanomaterials: Efficient bifunctional electrocatalysts for overall water splitting, *Adv. Funct. Mater.*, 2017, **27**, 1606585–1606595.
34. S. Nandi, J. Rother, D. Chakraborty, R. Maity, U. W. Zwanziger and R. Vaidhyanathan, Exceptionally stable bakelite-type polymers for efficient pre-combustion CO_2 capture and H_2 purification, *J. Mater. Chem. A*, 2017, **5**, 8431–8439.
35. Z. R. Herm, J. A. Swisher, B. Smit, R. Krishna and J. R. Long, Metal-organic frameworks as adsorbents for hydrogen purification and precombustion carbon dioxide capture, *J. Am. Chem. Soc*., 2011, **133**, 5664–5667.
36. P. R. Deshmukh, Y. Sohn and W. G. Shin, Flexible solid-state symmetric supercapacitor based on $(Fe,Cr)_2O_3$ oxide layer developed on the stainless steel mesh, *ACS Sustainable Chem. Eng.*, 2018, **6**, 300-310.
37. G. Sneddon, A. Greenaway and H. H. P. Yiu, The potential applications of nanoporous materials for the adsorption, separation, and catalytic conversion of carbon dioxide, *Adv. Energy Mater.*, 2014, **4**, 1301873–1301891.
38. H. L. Tuller, Solar to fuels conversion technologies: A perspective, *Mater Renew Sustain Energy*, 2017, **6**, DOI: 10.1007/s40243-017-0088-2.
39. M. Bastos-Neto, C. Patzschke, M. Lange, J. Möllmer, A. Möller, S. Fichtner, C. Schrage, D. Lässig, J. Lincke, R. Staudt, H. Krautscheid and R Gläser, Assessment of hydrogen storage by physisorption in porous materials, *Energy Environ. Sci.*, 2012, **5**, 8294–8303.
40. A. U. Pawar, C. W. Kim, M. J. Kang and Y. S. Kang, Crystal facet engineering of ZnO photoanode for higher water splitting efficiency with proton transferable nafion film, *Nano Energy*, 2016, **20,** 156–167.
41. S. Maiti, S. K. Karan, J. Lee, A. K. Mishra, B. B. Khatua and J. K. Kim, Bio-waste onion skin as an innovative nature-driven piezoelectric material with high energy conversion efficiency, *Nano Energy*, 2017, **42**, 282−293.

42. Z. Xie, M. Zhu, A. Nambo, J. B. Jasinski and M. A. Carreon, Microwave-assisted synthesized SAPO-56 as a catalyst in the conversion of CO_2 to cyclic carbonates, *Dalton Trans.*, 2013, **42**, 6732−6735.
43. Y. Sohn, W. Huang and F. Taghipour, Recent progress and perspectives in the photocatalytic CO_2 reduction of Ti-oxide-based nanomaterials, *Appl. Surf. Sci.*, 2017, **396**, 1696–1711.
44. J. C. Fisher, R. V. Siriwardane and R. W. S. Jr., Zeolite-based process for CO_2 capture from high-pressure, moderate-temperature gas streams, *Ind. Eng. Chem. Res.*, 2011, **50**, 13962–13968.
45. T. H. Pham, B. K. Lee, J. Kim and C. H. Lee, Enhancement of CO_2 capture by using synthesized nano-zeolite, *J. Taiwan Inst. Chem. Eng.*, 2016, **64**, 220–226.
46. E. M. Gallego, M. T. Portilla, C. Paris, A. L. Escamilla, M. Boronat, M. Moliner and A. Corma, Ab initio" Synthesis of zeolites for pre-established catalytic reactions, *Science*, 2017, **355**, 1051–1054.
47. Z. Yang, Y. Xia and R. Mokaya, Enhanced hydrogen storage capacity of high surface area zeolite-like carbon materials, *J. Am. Chem. Soc.*, 2007, **129**, 1673–1679.
48. S. Zheng, F. Fang, G. Zhou, G. Chen, L. Ouyang, M. Zhu and D. Sun, Hydrogen storage properties of space-confined $NaAlH_4$ nanoparticles in ordered mesoporous silica, *Chem. Mater.*, 2008, **20**, 3954–3958.
49. W. Chaikittisilp, R. Khunsupat, T. T. Chen and C. W. Jones, Poly(allylamine)–mesoporous silica composite materials for CO_2 capture from simulated flue gas or ambient air, *Ind. Eng. Chem. Res.*, 2011, **50**, 14203–14210.
50. M. Niu, H. Yang, X. Zhang, Y. Wang and A. Tang, Amine-impregnated mesoporous silica nanotube as an emerging nanocomposite for CO_2 capture, *ACS Appl. Mater. Interfaces*, 2016, **8**, 17312–17320.
51. K. Mori, S. Masuda, H. Tanaka, K. Yoshizawa, M. Chee and H. Yamashita, Phenylamine-functionalized mesoporous silica supported PdAg nanoparticles: A dual heterogeneous catalyst for formic acid/CO_2-mediated chemical hydrogen delivery/storage, *Chem. Commun.*, 2017, **53**, 4677–4680.
52. S. Wang, S. Yan, X. Ma and J. Gong, Recent advances in capture of carbon dioxide using alkali-metal-based oxides, *Energy Environ. Sci.*, 2011, **4**, 3805–3819.
53. P. Li, W. Liu, J. S. Dennis and H. C. Zeng, Synthetic architecture of MgO/C nanocomposite from hierarchical-structured coordination polymer toward enhanced CO_2 capture, *ACS Appl. Mater. Interfaces*, 2017, **9**, 9592–9602.
54. B. K. Singh, A. Shaikh, S. Badrayyana, D. Mohapatra, R. O Dusane and S. Parida, Nanoporous gold–copper oxide based all-solid-state micro-supercapacitors, *RSC Adv.*, 2016, **6**, 100467-100475
55. J. Hea, J. Tob, J. Meib, Z. Baob and J. Wilcox, Facile synthesis of nitrogen-doped porous carbon for selective CO_2 capture, *Energy Procedia*, 2014, **63**, 2144–2151.
56. D. Cazorla-Amorós, J. Alcañiz-Monge, and A. Linares-Solano, Characterization of activated carbon fibers by CO_2 adsorption, *Langmuir*, 1996, **12**, 2820–2824.
57. S. Ratha, S. R. Marri, J. N. Behera and C. S. Rout, High-energy-density supercapacitors based on patronite/single-walled carbon nanotubes/reduced graphene oxide hybrids, *Eur. J. Inorg. Chem.*, 2016, 259–265.
58. Y. Guana, J. Shi, M. Xia, J. Zhang, Z. Pang, A. Marchetti, X. Wang, J. Cai and X. Kong, Monodispersed ZIF-8 particles with enhanced performance for CO_2 adsorption and heterogeneous catalysis, *Appl. Surf. Sci.*, 2017, **423**, 349–353.
59. L. Zhang, G. Wu and J. Jiang, Adsorption and diffusion of CO_2 and CH_4 in zeolitic imidazolate framework-8: effect of structural flexibility, *J. Phys. Chem. C*, 2014, **118**, 8788−8794.
60. A. A. Niya, G. Birkett, Z. Zhu and T. E. Rufford, Gate opening effect of zeolitic imidazolate framework ZIF-7 for adsorption of CH_4 and CO_2 from N_2, *J. Mater. Chem. A*, 2017, **5**, 21389−21399.
61. A. Verma, D. De, K. Tomar and P. K. Bharadwaj, An amine functionalized metal−organic framework as an effective catalyst for conversion of CO_2 and Biginelli reactions, *Inorg. Chem.*, 2017, **56**, 9765−9771.
62. S. Nandi, S. Collins, D. Chakraborty, D. Banerjee, P. K. Thallapally, T. K. Woo and R. Vaidhyanathan, Ultralow parasitic energy for postcombustion CO_2 capture realized in a nickel

isonicotinate metal−organic framework with excellent moisture stability, *J. Am. Chem. Soc.*, 2017, **139**, 1734−1737.
63. R. K. Tiwaria and J. N. Behera, Organic–inorganic hybrid three-dimensional metal sulfite-oxalates with honeycomb-like structures, *Dalton Trans.*, 2017, **46**, 5911–5917.
64. O. Buyukcakir, S. H. Je, S. N. Talapaneni, D. Kim and A. Coskun, Charged covalent triazine frameworks for CO_2 capture and conversion, *ACS Appl. Mater. Interfaces*, 2017, **9**, 7209−7216.
65. X. Han, Q. Xia, J. Huang, Y. Liu, C. Tan and Y. Cui, Chiral covalent organic frameworks with high chemical stability for heterogeneous asymmetric catalysis, *J. Am. Chem. Soc.*, 2017, **139**, 8693–8697.
66. L. Zhai, N. Huang, H. Xu, Q. Chen and D. Jiang, A backbone design principle for covalent organic frameworks: The impact of weakly interacting units on CO_2 adsorption, *Chem. Commun.*, 2017, **53**, 4242–4245.
67. Y. Liao, Z. Cheng, W. Zuo, A. Thomas and C. F. J. Faul, Nitrogen-rich conjugated microporous polymers: Facile synthesis, efficient gas storage, and heterogeneous catalysis, *ACS Appl. Mater. Interfaces*, 2017, DOI: 10.1021/acsami.7b09553.
68. T. E. Reich, S. Behera, K. T. Jackson, P. Jena and H. M. El-Kaderi, Highly selective CO_2/CH_4 gas uptake by a halogen-decorated borazine-linked polymer, *J. Mater. Chem.*, 2012, **22**, 13524–13528.
69. M. G. Rabbani, T. Islamoglu and H. M. El-Kaderi, Benzothiazole- and benzoxazole-linked porous polymers for carbon dioxide storage and separation, *J. Mater. Chem. A*, 2017, **5**, 258–265.
70. A. R. Antonangelo, C. G. Bezzu, S. S. Mughal, T. Malewschik, N. B. McKeown and S. Nakagaki, A porphyrin-based microporous network polymer that acts as an efficient catalyst for cyclooctene and cyclohexane oxidation under mild conditions, *Catal. Commun.*, 2017, **99**, 100–104.
71. L. Tan and B. Tan, Hypercrosslinked porous polymer materials: Design, synthesis, and applications, *Chem. Soc. Rev*., 2017, **46**, 3322–3356.
72. H. Li, B. Meng, S. H. Chai, H. Liu and S. Dai, Hyper-crosslinked β-cyclodextrin porous polymer: An adsorption-facilitated molecular catalyst support for transformation of water-soluble aromatic molecules, *Chem. Sci.*, 2016, **7**, 905–909.
73. Z. Jia, J. Pan and D. Yuan, High Gas uptake and selectivity in hyper-crosslinked porous polymers knitted by various nitrogen-containing linkers, *ChemistryOpen*, 2017, **6**, 554–561.
74. P. R. Deshmukh, Y. Sohn and W. G. Shin, Chemical synthesis of ZnO nanorods: Investigations of electrochemical performance and photo-electrochemical water splitting applications, *J. Alloys Compd.*, 2017, **711**, 573–580.
75. A. Tyagi, K. M. Tripathi and R. K. Gupta, Recent progress in micro-scale energy storage devices and future aspects, *J. Mater. Chem. A*, 2015, **3**, 22507–22541.
76. https://www.co2.earth/ accessed august 2017.
77. Y. Feng and Y. Liu, Scenario prediction of emerging coastal city using CA modeling under different environmental conditions: A case study of Lingang New City, China, *Environ. Monit. Assess.*, 2016, **188**, DOI: 10.1007/s10661–016–5558–y.
78. S. Jevrejeva, L. P. Jackson, R. E. M. Riva, A. Grinsted and J. C. Moore, Coastal sea level rise with warming above 2° C, *Proc. Natl. Acad. Sci.*, 2016, **113**, 13342–13347.
79. Z. Juncheng, Y. Yiqiu, Z. Jianli, C. Meixiang and X. Qing, Prediction of China's submerged coastal areas by sea level rise due to climate change, *J. Ocean Univ. China*, 2013, **12**, 327–334.
80. D. J. Erickson, B. Sulzberger, R. G. Zepp and A. T. Austin, Effects of stratospheric ozone depletion, solar UV radiation, and climate change on biogeochemical cycling: Interactions and feedbacks, *Photochem. Photobiol. Sci.*, 2015, **14**, 127–148.
81. J. E. Thornes and F. D. Pope, *Geoengineering of the climate system*, RSC, UK, 2014.
82. A. K. Shukla, K. Sudhakar and P. Baredar, Renewable energy resources in south asian countries: Challenges, policy and recommendations, *Resource-Efficient Technol.*, 2017, **3**, 342–346.
83. D. Momodu, A. Bello, K. Oyedotun, F. Ochai-Ejeh, J. Dangbegnon, M. Madito and N. Manyala, Enhanced electrochemical response of activated carbon nanostructures from tree-bark biomass waste in polymer-gel active electrolytes, *RSC Adv.*, 2017, **7**, 37286–37295.
84. S. Styring, Artificial photosynthesis for solar fuels, *Faraday Discuss.*, 2012, **155**, 357–376.

85. http://www.esrl.noaa.gov/gmd/ccgg/trends/.
86. B. Metz, O. Davidson, H. D. Coninck, M. Loos and L. Meyer, *IPCC (International Panel on Climate Change)*, Cambridge University Press, UK, 2005.
87. J. Davison, Performance and costs of power plants with capture and storage of CO_2, *Energy*, 2007, **32**, 1163–1176.
88. D. Schrag, Preparing to capture carbon, *Science*, 2007, **315**, 812–813.
89. EPRI (Electric Power Research Institute), *Advanced coal power systems with CO_2 capture: EPRI's coal fleet for tomorrow vision-2011 update*,1023468, 2011.
90. A. N. Hildebrand and H. J. Herzog, Optimization of carbon capture percentage for technical and economic impact of near-term CCS implementation at coal-fired power plants, *Energy Procedia*, 2009, **1**, 4135–4142.
91. NETL (National Energy Technology Laboratory) "*Coal-fired power plants in the United States; Examination of the costs of retrofitting with CO_2 capture technology"*, Revision 3, DOE/NETL-402/102309, 2011.
92. N. Stern, *Stern review on the economics of climate change*, Cambridge University Press, Cambridge, UK, 2006.
93. R. Kneer, D. Toporov, M. Forster, D. Christ, C. Broeckmann, E. Pfaff, M. Zwick, S. Engels and M. Modigell, OXYCOAL-AC: Towards an integrated coal-fired power plant process with ion transport membrane-based oxygen supply, *Energy Environ. Sci*., 2010, **3**, 198–207.
94. K. Wellner, T. Marx-Schubach and G. Schmitz, Dynamic behavior of coal-fired power plants with post combustion CO_2 capture, *Ind. Eng. Chem. Res*., 2016, **55**, 12038–12045.
95. B. C. Sempuga, B. Patel, D. Hildebrandt and D. Glasser, Efficient combustion: A process synthesis approach to improve the efficiency of coal-fired power stations, *Ind. Eng. Chem. Res.*, 2012, **51**, 9061–9077.
96. R. S. Haszeldine, Carbon capture and storage: How green can black be?, *Science*, 2009, **325**, 1647–1652.
97. https://www.epa.gov/ghgemissions/global-greenhouse-gas-emissions-data.
98. J. A. Mason, T. M. McDonald, T. H. Bae, J. E. Bachman, K. Sumida, J. J. Dutton, S. S. Kaye and J. R. Long, Application of a high-throughput analyzer in evaluating solid adsorbents for post-combustion carbon capture via multicomponent adsorption of CO_2, N_2 and H_2O, *J. Am. Chem. Soc.*, 2015, **137**, 4787−4803.
99. https://hub.globalccsinstitute.com/publications/building-capacity-co2-capture-and-storage-apec-region-training-manual-policy-makers-and-practitioners/module-2-co2-capture-post-combustion-flue-gas-separation.
100. C. H. Yu, C. H. Huang and C. S. Tan, A review of CO_2 capture by absorption and adsorption, *Aerosol and Air Quality Research*, 2012, **12**, 745–769.
101. S. Wong and R. Bioletti, *Carbon dioxide separation technologies, Carbon & Energy Management*, Alberta Research Council Inc., Edmonton, Alberta, 2002.
102. S. Prodinger, R. S. Vemuri, T. Varga, B. P. McGrail, R. K. Motkuri and M. A. Derewinski Impact of chabazite SSZ-13 textural properties and chemical composition on CO_2 adsorption applications, *New J. Chem.*, 2016, **40**, 4375–4385.
103. D. Kang, X. Yu and M. Ge, Morphology-dependent properties and adsorption performance of CeO_2 for fluoride removal, *Chem. Eng. J.*, 2017, **330**, 36–43.
104. H. Pan, Y. Yi, Q. Lin, G. Xiang, Y. Zhang and F. Liu, Effect of surface chemistry and textural properties of activated carbons for CH_4 selective adsorption through low-concentration coal bed methane, *J. Chem. Eng. Data*, 2016, **61**, 2120−2127.
105. K. Vetter, S. Proch, G. F. Gantefor, S. Behera and P. Jena, Hydrogen mimicking the properties of coinage metal atoms in Cu and Ag monohydride clusters, *Phys. Chem. Chem. Phys*., 2013, **15**, 21007−21015.
106. J. A. A. Gibson, E. Mangano, E. Shiko, A. G. Greenaway, A. V. Gromov, M. M. Lozinska, D. Friedrich, E. E. B. Campbell, P. A. Wright and S. Brandani, Adsorption materials and processes for carbon capture from gas fired power plants: AMPGas, *Ind. Eng. Chem. Res.*, 2016, **55**, 3840−3851.
107. S. J. J. Titinchi, M. Piet, H. S. Abbo, O. Bolland and W. Schwieger, Chemically modified solid adsorbents for CO_2 capture, *Energy Procedia*, 2014, **63**, 8153 – 8160.

108. K. V. Kumar, K. Preuss, L. Lu, Z. X. Guo and M. M. Titirici, Effect of nitrogen doping on the CO_2 adsorption behavior in nanoporous carbon structures: A molecular simulation study, *J. Phys. Chem. C*, 2015, **119**, 22310–22321.
109. M. Sevilla, J. B. Parra and A. B. Fuertes, Assessment of the role of micropore size and N-doping in CO_2 capture by porous carbons, *ACS Appl. Mater. Interfaces*, 2013, **5**, 6360–6368.
110. P. Rekha, U. Sahoo and P. Mohanty, Click-based porous inorganic–organic hybrid material (PHM) containing cyclophosphazene unit and their application in carbon dioxide capture, *RSC Adv.*, 2014, **4**, 34860–34863.
111. H. Xu, J. Gao and D. Jiang, Stable, crystalline, porous, covalent organic frameworks as a platform for chiral organocatalysts, *Nat. Chem.*, 2015, **7**, 905–912.
112. Z. Li, X. Feng, Y. Zou, Y. Zhang, H. Xia, X. Liu and Y. Mu, A 2D azine-linked covalent organic framework for gas storage applications, *Chem. Commun.*, 2014, **50**, 13825–13828.
113. A. K. Nayak, M. Verma, Y. Sohn, P. A. Deshpande and D. Pradhan, Highly active tungsten oxide nanoplate electrocatalysts for the hydrogen evolution reaction in acidic and near neutral electrolytes, *ACS Omega*, 2017, **2**, 7039–7047.
114. Y. Basdogana and S. Keskin, Simulation and modelling of MOFs for hydrogen storage, *CrystEngComm*, 2015, **17**, 261–275.
115. M. P. Suh, H. J. Park, T. K. Prasad and D. W. Lim, Hydrogen storage in metal–organic frameworks, *Chem. Rev.*, 2012, **112**, 782–835.
116. O. K. Farha, I. Eryazici, N. C. Jeong, B. G. Hauser, C. E. Wilmer, A. A. Sarjeant, R. Q. Snurr, S. T. Nguyen, A. O. Yazaydın and J. T. Hupp, Metal-organic framework materials with ultrahigh surface areas: Is the sky the limit?, *J. Am. Chem. Soc.*, 2012, **134**, 15016–15021.
117. H. Furukawa, N. Ko, Y. B. Go, N. Aratani, S. B. Choi, E. Choi, A. O. Yazaydin, R. Q. Snurr, M. O'Keeffe, J. Kim and O. M. Yaghi, Ultrahigh porosity in metal-organic frameworks, *Science*, 2010, **329**, 424–428.
118. K. L. Lim, H. Kazemian, Z. Yaako and W. R. W. Daud, Solid-state materials and methods for hydrogen storage: a critical review, *Chem. Eng. Technol.*, 2010, **33**, 213–226.
119. X. Wu, R. Wang, H. Yang, W. Wang, W. Cai and Q. Li, Ultrahigh hydrogen storage capacity of novel porous aromatic frameworks, *J. Mater. Chem. A*, 2015, **3**, 10724–10729.
120. S. S. Han, H. Furukawa, O. M. Yaghi and W. A. Goddard, Covalent organic frameworks as exceptional hydrogen storage materials, *J. Am. Chem. Soc.*, 2008, **130**, 11580–11581.
121. M. Moshoeshoe, M. S. N. Tabbiruka and V. Obuseng, A review of the chemistry, structure, properties and applications of zeolites, *A. Journ. Mater. Sci.*, 2017, **7**, 196–221.
122. C. Colella, Storie di zeoliti sul declinare del secolo dei lumi. La supremazia della Svezia e della Francia (In Italian. *Transl*: Histories of zeolites in the declining of the age of enlightenment. the supremacy of sweden and france). *Bollettino AIZ (Bulettin of the Italian Zeolite Association)*, 2009, **34**, 10–32.
123. C. Colella, The fascinating story of porous materials, *Curr. Physical Chem.*, 2012, **2**, 126–135.
124. K. Stocker, M. Ellersdorfer, M. Lehner and J. G. Raith, Characterization and utilization of natural zeolites in technical applications, *BHM*, 2017, **162,** 142–147.
125. J. Weitkamp, Zeolites and catalysis, *Solid State Ionics*, 2000, **131**, 175–188.
126. C. S. Cundy, The hydrothermal synthesis of zeolites: History and development from the earliest days to the present time, *Chem. Rev.*, 2003, **103**, 663−701.
127. E. T. C. Vogt and B. M. Weckhuysen, Fluid catalytic cracking: recent developments on the grand old lady of zeolite catalysis, *Chem. Soc. Rev.*, 2015, **44**, 7342–7370.
128. O. M. Yaghi and H. L. Li, Hydrothermal synthesis of a metal-organic framework containing large rectangular channels, *J. Am. Chem. Soc.*, 1995, **117**, 10401–10402.
129. O. M. Yaghi, G. Li and H. Li, Selective binding and removal of guests in a microporous metal-organic framework, *Nature*, 1995, **378**, 703–706.
130. A. P. Cote, A. I. Benin, N. W. Ockwig, M. O'Keeffe, A. J. Matzger and O. M. Yaghi, Porous, crystalline, covalent organic frameworks, *Science*, **2005**, *310*, 1166–1170.
131. R. Dawson, E. Stocke, J. R. Holst, D. J. Adams and A. I. Cooper, Microporous organic polymers for carbon dioxide capture, *Energy Environ. Sci.*, 2011, **4**, 4239–4245.
132. Y.-Q. Tian, Z.-X. Chen, L.-H. Weng, H.-B. Guo, S. Gao and D.-Y. Zhao, Two polymorphs of cobalt(II) imidazolate polymers synthesized solvothermally by using one organic template N, N-dimethylacetamide, *Inorg. Chem.*, 2004, **43**, 4631–4635.

133. P. J. Rangari and P. Chavan, A Review on Preparation of activated carbon from coconut shell, *IJIRSET*, 2017, **6**, 5829–5849.
134. W. A. Helbig, Activated Carbon, *J. Chem. Educ.*, 1946, **23**, 98–102.
135. M. Thommes, K. Kaneko, A. V. Neimark, J. P. Olivier, F. Rodriguez-Reinoso, J. Rouquerol and K. S.W. Sing, Physisorption of gases, with special reference to the evaluation of surface area and pore size distribution (IUPAC technical report), *Pure Appl. Chem*. 2015, DOI 10.1515/pac-2014-1117.
136. F. Rouquerol, J. Rouquerol and K. Sing, *Adsorption by powders and porous solids: Principle, methodology and applications*, Academic press, London, UK, 1999.
137. P. Payra and P. K. Dutta, Zeolites: A primer. *In the handbook of zeolite science and technology*; Auerbach, S. M., Carrado, K. A., Dutta, P. K., Eds.; CRC Press: London, 2003.
138. V. H. Bekkum and H. W, Kouwenhoven, Progress in the use of zeolites in organic synthesis. In *Introduction to Zeolite Science and Practice*; J. Cejka, H. V. Bekkum, A. Corma, F. E. Schüth, Elsevier: London, 2007.
139. M. Choi, H. S. Cho, R. Srivastava, C. Venkatesan, D. H. Choi and R. Ryoo, Amphiphilic organosilane directed synthesis of crystalline zeolite with tunable mesoporosity, *Nat. Mater.*, 2006, **5**, 718–723.
140. F. S. Xiao, L. Wang, C. Yin, K. Lin, Y. Di, J. Li, R. Xu, D. S. Su, R. Schlogl, T. Yokoi and T. Tatsumi, Catalytic properties of hierarchical mesoporous zeolites templated with a mixture of small organic ammonium salts and mesoscale cationic polymers, *Angew. Chem. Int. Ed.*, 2006, **45**, 3090–3093.
141. C.-M. Song A. J. Jiang and A. Z. Yan, Synthesis and characterization of MCM-41-type composite materials prepared from ZSM-5 zeolite, *J. Porous Mater.*, 2008, **15**, 205–211.
142. J. Sun, C. Bonneau, A. Cantın, A. Corma, M. J. Dıaz-Cabanas, M. Moliner, D. Zhang, M. Li and X. Zou, The ITQ-37 mesoporous chiral zeolite, *Nature*, 2009, **458**, 1154–1157.
143. C. Perego and R. Millini, Porous materials in catalysis: Challenges for mesoporous materials, *Chem. Soc. Rev.*, 2013, **42**, 3956–3976
144. C. T. Kresge, M. E. Leonowicz, W. J. Roth and J. C. Vartuli, Ordered mesoporous molecular sieves synthesized by a liquid crystal template mechanism, *Nature*, 1992, **359**, 710–712.
145. Z. A. Alothman, A review: Fundamental aspects of silicate mesoporous materials, *Materials*, 2012, **5**, 2874–2902.
146. D. Sachdev, G. R. Wilson, N. M. Srivastava and A. Dubey, Debenzylation of vanillic acid over sulfosuccinic acid functionalized mesoporous silica nanocomposites, *Catal. Commun.*, 2014, **51**, 90–94.
147. T. Asefa, M. J. Maclachlan, H. Grondey, N. Coombs and G. A. Ozin, Metamorphic channels in periodic mesoporous methylenesilica, *Angew. Chem. Int. Ed.*, 2000, **39**, 1808–1811.
148. K. Landskron and G. A. Ozin, Periodic mesoporous organosilicas: Self-assembly from bridged cyclic silsesquioxane precursors, *Angew. Chem. Int. Ed.*, 2005, **44**, 2107–2109.
149. C. W. Kim, U. Pal, S. Park, J. Kim and Y. S. Kang, Synthesis of multifunctional metal- and metal oxide core@mesoporous silica shell structures by using a wet chemical approach, *Chem. Eur. J.*, 2012, 12314–12321.
150. M. E. Mohanty, V. J. Rao and A. K. Mishra, A fluorescence study on the interaction of telmisartan in triblock polymers pluronic P123 and F127, *Spectrochim. Acta Part A: Mol. and Biomol. Spectrosc.*, 2014, **112**, 330-338.
151. F. Hoffmann, M. Cornelius, J. Morell, and M. Froba, Silica-based mesoporous organic–inorganic hybrid materials, *Angew. Chem. Int. Ed.*, 2006, **45**, 3216–3251.
152. A. Tyagi, K. M. Tripathi, N. Singh, S. Choudhary and R. K. Gupta, Green synthesis of carbon quantum dots from lemon peel waste: Applications in sensing and photocatalysis, *RSC Adv.*, 2016, **6**, 72423–72432.
153. L. L. Zhang and X. S. Zhao, Carbon-based materials as supercapacitor electrodes, *Chem. Soc. Rev.*, 2009, **38**, 2520–2531.
154. D. Mohan and C. U.P. Jr, Activated carbons and low-cost adsorbents for remediation of tri- and hexavalent chromium from water, *J. Hazard. Mater.*, 2006, **137**, 762–811.
155. M. S. Shafeeyan, W. M. A. W. Daud, A. Houshmand and A. Shamiri, A review on surface modification of activated carbon for carbon dioxide adsorption, *J. Anal. Appl. Pyrol.*, 2010, **89**, 143–151.

156. Y. Chen, Y. Zhu, Z. Wang, Y. Li, L. Wang, L. Ding, X. Gao, Y. Ma and Y. Guo, Application studies of activated carbon derived from rice husks produced by chemical-thermal process-a review, *Adv. Colloid. Interfac.*, 2011, **163**, 39–52.
157. T. L. Silva, A. L. Cazetta, P. S. C. Souza, T. Zhang, T. Asefa, V. C. Almeida, Mesoporous activated carbon fibers synthesized from denim fabric waste: Efficient adsorbents for removal of textile dye from aqueous solutions, *J. Clean. Prod.*, 2018, **171**, 482–490.
158. C. Y. Yin, M. K. Aroua and W. M. A. W. Daud, Review of modifications of activated carbon for enhancing contaminant uptakes from aqueous solutions, *Sep. Purif. Technol.*, 2007, **52**, 403–415.
159. E. Masika and R. Mokaya, Preparation of ultrahigh surface area porous carbons templated using zeolite 13X for enhanced hydrogen storage, *Prog. Nat. Sci.: Mater. Int.*, 2013, **23**, 308–316.
160. K. M. Tripathi, A. Tyagi, M. Ashfaqa and R. K. Gupta, Temperature dependent, shape variant synthesis of photoluminescent and biocompatible carbon nanostructures from almond husk for applications in dye removal, *RSC Adv.*, 2016, **6**, 29545–29553.
161. A. Shaikh and S. Parida, Facile sonochemical synthesis of highly dispersed ultrafine Pd nanoparticle decorated carbon nanoonions with high metal loading and enhanced electrocatalytic activity, *RSC Adv*., 2016, **6**, 83711–83719.
162. H. Jüntgen, Activated carbon as catalyst support: A review of new research results, *Fuel*, 1986, **65**, 1436–1446.
163. A. Shaikh, S. Parida, and S. Bohm, One step eco-friendly synthesis of Ag–reduced graphene oxide nanocomposite by phytoreduction for sensitive nitrite determination, *RSC Adv.*, 2016, **6**, 100383–100391.
164. Z. Xie, Z. He, X. Feng, W. Xu, X. Cui, J. Zhang, C. Yan, M. A. Carreon, Z. Liu and Y. Wang, Hierarchical sandwich-like structure of ultrafine N-rich porous carbon nanospheres grown on graphene sheets as superior lithium-ion battery anodes, *ACS Appl. Mater. Interfaces*, 2016, **8**, 10324−10333.
165. S. Ratha, S. R. Marri, N. A. Lanzillo, S. Moshkalev, S. K. Nayak, J. N. Behera and C. S. Rout, Supercapacitors based on patronite–reduced graphene oxide hybrids: experimental and theoretical insights, *J. Mater. Chem. A*, 2015, **3**, 18874–18881.
166. D. Mohapatra, S. Badrayyana and S. Parida, Designing binder-free, flexible electrodes for high performance, supercapacitors based on pristine carbon nano-onions and their composite with CuO nanoparticles, *RSC Adv.*, 2016, **6**, 14720–14729.
167. A. Tyagi and R. K. Gupta, *Carbon Nanostructures from Biomass Waste for Supercapacitor Applications, Nanomaterials: A Guide to Fabrication and Applications*, CRC Press, India. 2016.
168. T. Islamoglu, S. Behera, Z. Kahveci, T. D. Tessema, P. Jena and H. M. El-Kaderi, Enhanced carbon dioxide capture from landfill gas using bifunctionalized benzimidazole-linked polymers, *ACS Appl. Mater. Interfaces*, 2016, **8**, 14648–14655.
169. J. Cai, L. Li, X. Lv, C. Yang and X. Zhao, Large surface area ordered porous carbons via nanocasting zeolite 10X and high performance for hydrogen storage application, *ACS Appl. Mater. Interfaces*, 2014, **6**, 167–175.
170. B. Kuchta, L. Firlej, A. Mohammadhosseini, P. Boulet, M. Beckner, J. Romanos and P. Pfeifer, Hypothetical high-surface-area carbons with exceptional hydrogen storage capacities: Open carbon frameworks, *J. Am. Chem. Soc*., 2012, **134**, 15130–15137.
171. A. Mulyadi, Z. Zhang, M. Dutzer, W. Liu and Y. Deng, Facile approach for synthesis of doped carbon electrocatalyst from cellulose nanofibrils toward high-performance metal-free oxygen reduction and hydrogen evolution, *Nano Energy*, 2017, **32**, 336–346.
172. Y. Zheng, Y. Jiao, L. H. Li, T. Xing, Y. Chen, M. Jaroniec and S. Z. Qiao, Toward design of synergistically active carbon-based catalysts for electrocatalytic hydrogen evolution, *ACS Nano*, 2014, **5**, 5290–5296.
173. Z. Zhang, Z. Yi, J. Wang, X. Tian, P. Xu, G. Shib and S. Wang, Nitrogen-enriched polydopamine analogue-derived defect-rich porous carbon as a bifunctional metal-free electrocatalyst for highly efficient overall water splitting, *J. Mater. Chem. A*, 2017, **5**, 17064–17072.

174. G. Hasegawa, T. Deguchi, K. Kanamori, Y. Kobayashi, H. Kageyama, T. Abe and K. Nakanishi, High-level doping of nitrogen, phosphorus, and sulfur into activated carbon monoliths and their electrochemical capacitances, *Chem. Mater.*, 2015, **27**, 4703–4712.
175. Y. Gong, H. Fei, X. Zou, W. Zhou, S. Yang, G. Ye, Z. Liu, Z. Peng, J. Lou, R. Vajtai, B. I. Yakobson, J. M. Tour and P. M. Ajayan, Boron- and Nitrogen-substituted graphene nanoribbons as efficient catalysts for oxygen reduction reaction, *Chem. Mater.*, 2015, **27**, 1181–1186.
176. A. L. Cazetta, T. Zhang, T. L. Silva, V. C. Almeida and T. Asefa, Bone char-derived metal-free N- and S-co-doped nanoporous carbon and its efficient electrocatalytic activity for hydrazine oxidation, *Appl. Catal. B: Environ.*, 2018, **225**, 30–39.
177. H. Cao, L. Xinga, G. Wu, Y. Xiea, S. Shia, Y. Zhanga, D. Minakatad and J. C. Crittenden, Promoting effect of nitration modification on activated carbon in the catalytic ozonation of oxalic acid, *Appl.Catal. B: Environ.*, 2014, **146**, 169–176.
178. B. Ashourirad, P. Arab, T. Islamoglu, K. A Cychosz, M. Thommes and H. M El-Kaderi, A cost-effective synthesis of heteroatom-doped porous carbons as efficient CO_2 sorbents, *J. Mater. Chem. A*, 2016, **4**, 14693–14702.
179. M. Oschatz and M. Antonietti, A search for selectivity to enable CO_2 capture with porous adsorbents, *Energy Environ. Sci.*, 2018, DOI: 10.1039/C7EE02110K.
180. M. Kondo, T. Yoshitomi, K. Seki, H. Matsuzaka and S. Kitagawa, Three-dimensional framework with channeling cavities for small molecules:$\{[M_2(4, 4'\text{-bpy})_3 (NO_3)_4]\cdot xH_2O\}_n$ (M= Co, Ni, Zn), *Angew. Chem., Int. Ed. Engl.*, 1997, **36**, 1725–1727.
181. J. Jiao, D. Jiang, F. Chen, D. Bai and Y. He, A porous metal–organic framework based on an asymmetric angular diisophthalate for selective adsorption of C_2H_2 and CO_2 over CH_4, *Dalton Trans.*, 2017, **46**, 7813–7820.
182. B. Liu, W. P. Wu, L. Hou and Y. Y. Wang, Four uncommon nanocage-based Ln-MOFs: Highly selective luminescent sensing for Cu^{2+} ions and selective CO_2 capture, *Chem. Commun.*, 2014, **50**, 8731–8734.
183. P. Horcajada, T. Chalati, C. Serre, B. Gillet, C. Sebrie, T. Baati, J. F. Eubank, D. Heurtaux, P. Clayette, C. Kreuz, J.-S. Chang, Y. K. Hwang, V. Marsaud, P.-N. Bories, L. Cynober, S. Gil, G. Férey, P. Couvreur and R. Gref, Porous metal–organic-framework nanoscale carriers as a potential platform for drug delivery and imaging, *Nature Mater.*, 2010, **9**, 172–178.
184. W. Xia, A. Mahmood, R. Zou and Q. Xu, Metal–organic frameworks and their derived nanostructures for electrochemical energy storage and conversion, *Energy Environ. Sci.*, 2015, **8**, 1837–1866.
185. H.-C. J. Zhou and S. Kitagawa, Metal–organic frameworks (MOFs), *Chem. Soc. Rev.*, 2014, **43**, 5415–5418.
186. N. C. Burtch, H. Jasuja and K. S. Walton, Water stability and adsorption in metal-organic frameworks, *Chem. Rev.*, 2014, **114**, 10575–10612.
187. H. Li, M. Eddaoudi, M. O'Keeffe and O. M. Yaghi, Design and synthesis of an exceptionally stable and highly porous metal-organic framework, *Nature*, 1999, **402**, 276–279.
188. T. Wu, L. Shen, M. Luebbers, C. Hu, Q. Chen, Z. Ni and R. I. Masel, Enhancing the stability of metal-organic frameworks in humid air by incorporating water repellent functional groups, *Chem. Commun.*, 2010, **46**, 6120–6122.
189. J. H. Cavka, S. Jakobsen, U. Olsbye, N. Guillou, C. Lamberti, S. Bordiga and K. P. Lillerud, A new zirconium inorganic building brick forming metal organic frameworks with exceptional stability, *J. Am. Chem. Soc.*, 2008, **130**, 13850–13851.
190. J. Zheng, R. S. Vemuri, L. Estevez, P. K. Koech, T. Varga, D. M. Camaioni, T. A. Blake, B. P. McGrail and R. K. Motkuri, Pore-engineered metal–organic frameworks with excellent adsorption of water and fluorocarbon refrigerant for cooling applications, *J. Am. Chem. Soc.*, 2017, **139**, 10601–10604.
191. W. Morris, B. Leung, H. Furukawa, O. K. Yaghi, N. He, H. Hayashi, Y. Houndonougbo, M. Asta, B. B. Laird and O. M. Yaghi, A combined experimental-computational investigation of carbon dioxide capture in a series of isoreticular zeolitic imidazolate frameworks, *J. Am. Chem. Soc.*, 2010, **132**, 11006–11008.
192. X. Feng and M. A. Carreon, Kinetics of transformation on ZIF-67 crystals, *J. Cryst. Growth*, 2015, **148**, 158-162

193. L. Dinga and A. O. Yazaydin, The effect of SO_2 on CO_2 capture in zeolitic imidazolate frameworks, *Phys. Chem. Chem. Phys.*, 2013, **15**, 11856–11861.
194. B. Chen, Z. Yang, Y. Zhu and Y. Xia, Zeolitic imidazolate framework materials: Recent progress in synthesis and applications, *J. Mater. Chem. A*, 2014, **2**, 16811–16831.
195. G. Perot and M. Guisnet, Advantages and disadvantages of zeolites as catalysts in organic chemistry, *J. Mol. Catal.*, 1990, **61**, 173–196.
196. A. Phan, C. J. Doonan, F. J. U. Romo, C. B. Knobler, M. O'keeffe and O. M. Yaghi, Synthesis, structure, and carbon dioxide capture properties of zeolitic imidazolate frameworks, *Accounts Chem. Res.*, 2010, **43**, 58–67.
197. D. Ge and H. K. Lee, Water stability of zeolite imidazolate framework 8 and application to porous membrane-protected micro-solid-phase extraction of polycyclic aromatic hydrocarbons from environmental water samples, *J. Chromatogr. A*, 2011, **1218**, 8490–8495.
198. K. S. Park, Z. Ni, A. P. Cote, J. Y. Choi, R. Huang, F. J. U. Romo, H. K. Chae, M. O'Keeffe and O. M. Yaghi, Exceptional chemical and thermal stability of zeolitic imidazolate frameworks, *Proc. Natl. Acad. Sci. USA*, 2006, **103**, 10186–10191.
199. Y. Grosu, S. Gomes, G. Renaudin, J. P. E. Grolier, V. Eroshenko and J. M. Nedelec, Stability of zeolitic imidazolate frameworks: Effect of forced water intrusion and framework flexibility dynamics, *RSC Adv.*, 2015, **5**, 89498–89502.
200. G. N. Lewis, The atom and the molecule, *J. Am. Chem. Soc.*, 1916, **38**, 762–785.
201. O. M. Yaghi, M. O'Keeffe, N. W. Ockwig, H. K. Chae, M. Eddaoudi and J. Kim, Reticular synthesis and the design of new materials, *Nature*, 2003, **423**, 705–714.
202. J. L. Segura, M. J. Mancheno and F. Zamora, Covalent organic frameworks based on Schiff-base chemistry: Synthesis, properties and potential applications, *Chem. Soc. Rev.*, 2016, **45**, 5635–5671.
203. H. Yang, Y. Du, S. Wan, G. D. Trahan, Y. Jin and W. Zhang, Mesoporous 2D covalent organic frameworks based on shape-persistent arylene-ethynylene macrocycles, *Chem. Sci.*, 2015, **6**, 4049–4053.
204. S. Y. Ding and W. Wang, Covalent organic frameworks (COFs): From design to applications, *Chem. Soc. Rev.*, 2013, **42**, 548–568.
205. H. Furukawa and O. M. Yaghi, Storage of hydrogen, methane, and carbon dioxide in highly porous covalent organic frameworks for clean energy applications, *J. Am. Chem. Soc.*, 2009, **131**, 8875–8883.
206. H. M. El-Kaderi, J. R. Hunt, J. L. M. Cortes, A. P. Cote, R. E. Taylor, M. O'Keeffe and O. M. Yaghi, Designed synthesis of 3D covalent organic frameworks, *Science*, 2007, **316**, 268–272.
207. H. Bildirir, V. G. Gregoriou, A. Avgeropoulos, U. Scherf and C. L. Chochos, Porous organic polymers as emerging new materials for organic photovoltaic applications: Current status and future challenges, *Mater. Horiz.*, 2017, **4**, 546–556.
208. S. Das, P. Heasman, T. Ben and S. Qiu, Porous organic materials: Strategic design and structure−function correlation, *Chem. Rev.*, 2017, **117**, 1515−1563.
209. S. Bhunia, S. K. Das, R. Jana, S. C Peter, S. Bhattacharya, M. Addicoat, A. Bhaumik and A. Pradhan, Electrochemical stimuli-driven facile metal-free hydrogen evolution from pyrene-porphyrin-based crystalline covalent organic framework, *ACS Appl. Mater. Interfaces*, 2017, **9**, 23843–23851.
210. P. Z. Li and Y. Zhao, Nitrogen-rich porous adsorbents for CO_2 capture and storage, *Chem. Asian J.*, 2013, **8**, 1680–1691.
211. B. P. Biswal, S. Chandra, S. Kandambeth, B. Lukose, T. Heine and R. Banerjee, Mechanochemical synthesis of chemically stable isoreticular covalent organic frameworks, *J. Am. Chem. Soc.*, 2013, **135**, 5328−5331.
212. P. Bhanja, S. K. Das, K. Bhunia, D. Pradhan, T. Hayashi, Y. Hijikata, S. Irle and A. Bhaumik, A new porous polymer for highly efficient capacitive energy storage, *ACS Sustainable Chem. Eng.*, 2018, **6**, 202–209.
213. B. C. Patra, S. Khilari, L. Satyanarayana, D. Pradhan and A. Bhaumik, A new benzimidazole based covalent organic polymer having high energy storage capacity, *Chem. Commun.*, 2016, **52**, 7592–7595

214. T. Ben, H. Ren, S. Ma, D. Cao, J. Lan, X. Jing, W. Wang, J. Xu, F. Deng, J. M. Simmons, S. Qiu and G. Zhu, Targeted synthesis of a porous aromatic framework with high stability and exceptionally high surface area, *Angew. Chem.*, 2009, **121**, 9621–9624.
215. Y. Li, Z. Zhang, B. Ge, X. Men and Q. Xue, One-pot, template-free synthesis of a robust superhydrophobic polymer monolith with an adjustable hierarchical porous structure, *Green Chem.*, 2016, **18**, 5266–5272.
216. X. Zhu, C. Tian, G. M. Veith, C. W. Abney, J. Dehaudt and S. Dai, *In situ* doping strategy for the preparation of conjugated triazine frameworks displaying efficient CO_2 capture performance, *J. Am. Chem. Soc*., 2016, **138**, 11497–11500.
217. N. Venkatesan, V. Singh, P. Rajakumar and A. K. Mishra, Isobenzotriazolophanes: A new class of fluorescent cyclophanes as sensors for aromatic nitro explosives – picric acid, *RSC Adv.*, 2014, **4**, 53484–53489.
218. T. L. Thomas and A. K. Mishra, ANS fluorescence as a tool to monitor cross-linking polymerization of acrylamide, *Eur. Polym. J.*, 2002, **38**, 1805–1810.
219. A. I. Cooper, Conjugated microporous polymers, *Adv. Mater.*, 2009, **21**, 1291–1295.
220. N. B. McKeown and P. M. Budd, Polymers of intrinsic microporosity (PIMs): Organic materials for membrane separations, heterogeneous catalysis and hydrogen storage, *Chem. Soc. Rev.*, 2006, **35**, 675–683.
221. G. Kickelbick, *Hybrid materials. Synthesis, characterization, and applications*, Wiley-VCH Verlag GmbH & Co. KGaA, Weinheim, Germany, 2007.
222. A. Sharma, A Dubey, Surface modified mesoporous silica polymer nanocomposites for adsorption of dyes from aqueous solution, *J Porous Mater.*, 2017, 24, 429–435.
223. C. Sanchez, K. J. Shea and S. Kitagawa, Recent progress in hybrid materials science, *Chem. Soc. Rev*., 2011, **40**, 471–472.
224. G. Ferey, C. Serre, T. Devic, G. Maurin, H. Jobic, P. L. Llewellyn, G. D. Weireld, A. Vimont, M. Daturi and J. S. Chang, Why hybrid porous solids capture greenhouse gases?, *Chem. Soc. Rev*., 2011, **40**, 550–562.
225. M. V. Regi, M. Colilla and B. Gonzalez, Medical applications of organic-inorganic hybrid materials within the field of silica-based bioceramics, *Chem. Soc. Rev.*, 2011, **40**, 596–607.
226. P. Judeinstein and C. Sanchez, Hybrid organic-inorganic materials: A land of multidisciplinarity, *J. Mater. Chem.*, 1996, **6**, 511–525.
227. N. Artzi, B. B. Khatua, R. Tchoudakov, M. Narkis, A. Berner, A. Siegmann and J. M. Lagaron, Physical and chemical interactions in melt mixed nylon-6/EVOH blends, *J. Macromol. Sci., Part B–Phys.*, 2004, **43**, 605–624.
228. N. Artzi, B. B. Khatua, M. Narkis and A. Siegmann, Studies on Nylon-6/EVOH/clay ternary composites, *Polym. Comp*., 2006, **27**, 15–23.
229. M. M. Unterlass, Green synthesis of inorganic–organic hybrid materials: State of the art and future perspectives, *Eur. J. Inorg. Chem*., 2016, 1135–1156.
230. M. L. V. Á. Pascual, M. T. D. Carbóa and A. D. Carbó, Characterization of Maya Blue pigment in pre-classic and classic monumental architecture of the ancient pre-Columbian city of Calakmul (Campeche, Mexico), *J. Cultur. Herit.*, 2011, **12**, 140–148.
231. H. V. Olphen, Maya Blue: A clay-organic pigment? *Science*, 1966, **154**, 645-646.
232. M. J. Yacaman, L. Rendon, J. Arenas and M. C. S. Puche, Maya Blue paint: An ancient nanostructured material, *Science*, 1996, **273**, 223–225.
233. P. G. Romero and C. Sanchez, Hybrid materials. Functional properties. From Maya Blue to 21st century materials, *New J. Chem*., 2005, **29**, 57–58.
234. G. R. Wilson and A. Dubey, Synthesis and characterization of trichloroisocyanouric acid functionalized mesoporous silica nanocomposite (SBA/TCCA) for the acylation of indole, *J Chem Sci*., 2016, **128**, 1285–1290.
235. A. Clearfield, Recent advances in metal phosphonate chemistry, *Curr. Opin. Solid State Mater. Sci.*, 1996, **1**, 268–278.
236. K. J. Gagnon, H. P. Perry and A. Clearfield, Conventional and unconventional metal-organic frameworks based on phosphonate ligands: MOFs and UMOFs, *Chem. Rev*., 2012, **112**, 1034–1054.

237. H. R. Allcock and R. J. Best, Phosphonitrilic compounds Part I. The mechanism of phosphonitrilic chloride polymerization capacitance, conductance, and electron-spin resonance studies, *Can. J. Chem.*, 1964, **42**, 447–455.
238. H. R. Allcock and R. L. Kugel, Synthesis of high polymeric alkoxy and aryloxyphosphonitriles, *J. Am. Chem. Soc.*, 1965, **87**, 4216–4217.
239. H. R. Allcock, R. L. Kugel and K. J. Valan, Phosphonitrilic compounds. V1, High molecular weight poly(alkoxy- and aryloxyphosphazenes), *Inorg. Chem.*, 1966, **5**, 1709–1715.
240. H. R. Allcock and R. L. Kugel, Phosphonitrilic high molecular compounds. VII, Weight poly(diaminophosphazenes), *Inorg. Chem.*, 1966, **5**, 1716–1718.
241. H. R. Allcock, A perspective of polyphosphazene research, *J. Inorg. Organomet. Polym. Mater.*, 2006, **16**, 277–294.
242. J. E. Mark, H. R. Allcock and R. West, *Inorganic polymers*, Oxford University Press, 2nd edn., USA, 2005.
243. G. Tesi, and C. M. Douglas, Synthesis of Bis-(perfluoroalky1)-phosphonitriles, *J. Am. Chem. Soc.*,1962, **84**, 549–551.
244. F. Goldschmidt and B. Dishon, Polymeric phosphonitrilic esters: A new type of inorganic organic plastics, *J. Polymer Sci.*, 1948, **3**, 481–486.
245. H. N. Stokes, About the chloronitride phosphoric acid, *Am. Chem. J.*, 1897, **19**, 782–796.
246. H. R. Allcock, *Chemistry and applications of polyphosphazenes*, Wiley, New Jersey, USA, 2002.
247. P. Mohanty, L. D. Kull and K. Landskron, Porous covalent electron-rich organonitridic frameworks as highly selective sorbents for methane and carbon dioxide, *Nat. Commun.*, 2011, **2**, DOI:10.1038/ncomms1405.
248. P. Rekha, R. Muhammad, V. Sharma, M. Ramteke and P. Mohanty, Unprecedented adsorptive removal of $Cr_2O_7^{2-}$ and methyl orange by using a low surface area organosilica, *J. Mater. Chem. A*, 2016, **4**, 17866–17874.
249. P. Rekha, R. Muhammad and P. Mohanty, Sonochemical synthesis of cyclophosphazene bridged mesoporous organosilicas and their application in methyl orange, congo red and Cr(VI) removal, *RSC Adv.*, 2015, **5**, 67690–67699.
250. P. Rekha V. Sharma and P. Mohanty, Synthesis of cyclophosphazene bridged mesoporous organosilicas for CO_2 capture and Cr(VI) removal, *Micropor. Mesopor. Mater.*, 2016, **19**, 93–102.
251. H. Allcock and S. E. Kuharick, Hybrid phosphazene-organosilicon polymers: II. High-polymer and materials synthesis and properties, *J. Inorg. Organomet. Poly.*, 1996, **6**, 1–41.
252. C. Diaz, M. Barbosa and Z. Godoy, Monobranched and hyperbranched dendrimers based on cyclophosphazene containing nitrile and phosphine donors and their Fe and Ru organometallic derivatives, *Polyhedron*, 2004, **23**, 1027–1035
253. T. Zhang, Q. Cai, D. Z. Wu and R. G. Jin, Phosphazene cyclomatrix network polymers: Some aspects of the synthesis, characterization, and flame-retardant mechanisms of polymer, *J. Appl. Polym. Sci.*, 2005, **95**, 880–889.
254. T. M. Gall, D. Knittel, J. S. Gutmann and K. Opwis, Permanent flame-retardant finishing of textiles by allyl- functionalized polyphosphazenes, *ACS Appl. Mater. Interfaces*, 2015, **7**, 9349–9363.
255. Y. J. Shin, Y. R. Ham, S. H. Kim, D. H. Lee, S. B. Kim, C. S. Park, Y. M. Yoo, J. G. Kim, S. H. Kwon and J. S. Shin, Application of cyclophosphazene derivatives as flame retardants for ABS, *J. Ind. Eng. Chem.*, 2010, **16**, 364–367.
256. A. K. Andrianov, Y. Y. Svirkin and M. P. Legolvan, Synthesis and biologically relevant properties of polyphosphazene polyacids, *Biomacromolecules*, 2004, **5**, 1999–2006.
257. A. K. Andrianov, A. Marin and J. Chen, Synthesis, properties, and biological activity of poly[di(sodium carboxylatoethylphenoxy)phosphazene], *Biomacromolecules*, 2006, **7**, 394–399.
258. A. K. Andrianov, J. Chen and L. G. Payne, Preparation of hydrogel microspheres by coacervation of aqueous polyphosphazene solutions, *Biomaterials*, 1998, **19**, 109–115.
259. A. K. Andrianov, J. Chen and M. P. Legolvan, Poly(dichlorophosphazene) as a precursor for biologically active polyphosphazenes: Synthesis, characterization, and stabilization, *Macromolecules*, 2004, **37**, 414–420.

260. B. Edwards, S. Rudolf, P. Hauser and A. El-Shafei, Preparation, polymerization, and performance evaluation of halogen-free radiation curable flame-retardant monomers for cotton substrates, *Ind Eng. Chem. Res.*, 2015, **54**, 577–584.
261. H. Schiff, Mittheilungen aus dem Universitätslaboratorium in Pisa: Eine neue Reihe organischer Basen, *Justus Liebigs Ann. Chem*., 1864, **131**, 118–119.
262. N. E. Borisova, M. D. Reshetova and Y. A. Ustynyuk, Metal-free methods in the synthesis of macrocyclic Schiff bases, *Chem. Rev*., 2007, **107**, 46–79.
263. L. S. M. Forlani and P. E. Todesco, Condensation reactions between aromatic aldehydes and some heterocyclic aromatic amines, *Gazz. Chim. Ital*., 1986, **116**, 229–232.
264. S. J. Rowan and J. F. Stoddart, Thermodynamic synthesis of rotaxanes by imine exchange, *Org. Lett.*, 1999, **1**, 1913–1916.
265. F. J. Uribe-Romo, C. J. Doonan, H. Furukawa, K. Oisaki and O. M. Yaghi, Crystalline covalent organic frameworks with hydrazone linkages, *J. Am. Chem. Soc*., 2011, **133**, 11478–11481.
266. F. J. Uribe-Romo, J. R. Hunt, H. Furukawa, C. Klock, M. O'Keeffe and O. M. Yaghi, A crystalline imine-linked 3-D porous covalent organic framework, *J. Am. Chem. Soc.*, 2009, **131**, 4570–4571.
267. M. G. Schwab, B. Fassbender, H. W. Spiess, A. Thomas, X. Feng and K. Mullen, Catalyst-free preparation of melamine-based microporous polymer networks through Schiff base chemistry, *J. Am. Chem. Soc*., 2009, **131**, 7216–7217.
268. W. C. Song, X. K. Xu, Q. Chen, Z. Z. Zhuang and X. H. Bu, Nitrogen-rich diaminotriazine-based porous organic polymers for small gas storage and selective uptake, *Polym. Chem*., 2013, **4**, 4690–4696.
269. H. Tuysuz, C. W. Lehmann, H. Bongard, B. Tesche, R. Schmidt and F. Schuth, Direct imaging of surface topology and pore system of ordered mesoporous silica (MCM-41, SBA-15, and KIT-6) and nanocast metal oxides by high resolution scanning electron microscopy, *J. Am. Chem. Soc*., 2008, **130**, 11510–11517.
270. S. Jun, S. H. Joo, R. Ryoo, M. Kruk, M. Jaroniec, Z. Liu, T. Ohsuna and O. Terasak, Synthesis of new, nanoporous carbon with hexagonally ordered mesostructure, *J. Am. Chem. Soc*., 2000, **122**, 10712–10713.
271. C. Sanchez, P. Belleville, M. Popall and L. Nicole, Applications of advanced hybrid organic–inorganic nanomaterials: from laboratory to market, *Chem. Soc. Rev*., 2011, **40**, 696–753.
272. A. Sayari and S. Hamoudi, Periodic mesoporous silica-based organic-inorganic nanocomposite materials, *Chem. Mater*., 2001, **13**, 3151–3168.
273. S. S. Park, M. S. Moorthy and C. S. Ha, Periodic mesoporous organosilicas for advanced Applications, *NPG Asia Mater.*, 2014, **6**, DOI:10.1038/am.2014.13.
274. D. Sachdev, P. H. Maheshwari and A. Dubey, Piperazine functionalized mesoporous silica for selective and sensitive detection of ascorbic acid, *J. Porous Mater.*, 2016, **23**, 123-129.
275. T. Asefa, M. J. MacLachlan, N. Coombs and G. A. Ozin, Periodic mesoporous organosilicas with organic groups inside the channel walls, *Nature*, 1999, **402**, 867–871.
276. B. D. Hatton, K. Landskron, W. Whitnall, D. Perovic and G. A. Ozin, Past, present and future of periodic mesoporous organosilicas, *Acc. Chem. Res.*, 2005, **38**, 305–312.
277. N. Lu, Y. Tian, W. Tian, P. Huang, Y. Liu, Y. Tang, C. Wang, S. Wang, Y. Su, Y. Zhang, J. Pan, Z. Teng and G. Lu, Smart cancer cell targeting imaging and drug delivery system by systematically engineering periodic mesoporous organosilica nanoparticles, *ACS Appl. Mater. Interfaces*, 2016, **8**, 2985−2993.
278. J. Croissant, X. Cattoën, M. W. C. Man, A. Gallud, L. Raehm, P. Trens, M. Maynadier and J. O. Durand, Biodegradable ethylene-bis (propyl) disulfide-based periodic mesoporous organosilica nanorods and nanospheres for efficient in-vitro drug delivery, *Adv. Mater.*, 2014, **26**, 6174–6180.
279. X. Qiu, S. Han, Y. Hu, M. Gao and H. Wanga, Periodic mesoporous organosilicas for ultra-high selective copper (II) detection and sensing mechanism, *J. Mater. Chem. A*, 2014, **2**, 1493–1501.
280. J. Du, J. C. Wechsler, J. M. Lobez, H. P. Loock and C. M. Crudden, Periodic mesoporous organosilica films: key components of fiber-optic-based heavy-metal sensors, *Small*, 2010, **6**, 1168–1172.
281. B. J. Melde, B. T. Holland, C. F. Blanford and A. Stein, Mesoporous sieves with unified hybrid inorganic/organic frameworks, *Chem. Mater.*, 1999, **11**, 3302–3308.

282. K. Landskron, B. D. Hatton, D. D. Perovic, G. A. Ozin, Periodic mesoporous organosilicas containing inter-connected [Si(CH2)]3 rings, *Science*, 2003, **302**, 266–275.
283. P. V. D. Voort, D. Esquivel, E. D. Canck, F. Goethals, I. V. Driessche and F. J. R. Salguero, Periodic mesoporous organosilicas: From simple to complex bridges; a comprehensive overview of functions, morphologies and applications, *Chem. Soc. Rev.*, 2013, **42**, 3913–3955.
284. P. Mohanty and K. Landskron, Periodic mesoporous organosilica nanorice, *Nanoscale Res. Lett.*, 2009, **4**, 169-172.
285. P. Mohanty, N. M. K. Linn and K. Landskron, Ultrafast sonochemical synthesis of methane and ethane bridged periodic mesoporous organosilicas, *Langmuir*, 2010, **26**, 1147–1151.
286. B. D. Hatton, K. Landskron, W. Whitnall, D. D. Perovic and G. A. Ozin, Spin-coated periodic mesoporous organosilica thin films: Towards a new generation of low-k materials, *Adv. Funct. Mater.*, 2005, **15**, 823–829.
287. Y. Xia, W. Wang and R. Mokaya, Bifunctional hybrid mesoporous organoaluminosilicates with molecularly ordered ethylene groups, *J. Am. Chem. Soc.*, 2005, **127**, 790–798.
288. S. Sadjadi and M. M. Heravi, Current advances in the utility of functionalized SBA mesoporous silica for developing encapsulated nanocatalysts: State of the art, *RSC Adv.*, 2017, **7**, 30815–30838.
289. Y. Li, F. Auras, F. Lobermann, M. Doblinger, J. Schuster, L. Peter, D. Trauner and T. Bein, A photoactive porphyrin based periodic mesoporous organosilica thin film, *J. Am. Chem. Soc.*, 2013, **135**, 18513–18519.
290. O. Olkhovyk and M. Jaroniec, Periodic mesoporous organosilica with large heterocyclic bridging groups, *J. Am. Chem. Soc.*, 2005, **127**, 60–61.
291. N. Lin, H. Li, Y. Wang, Y. Feng, D. Qin, Q. Gan and S. Chen, Luminescent triazine-containing bridged polysilsesquioxanes activated by lanthanide ions, *Eur. J. Inorg. Chem.*, 2008, 4781–4785.
292. S. M. Ibrahim, R. Xu, H. Nagasawa, A. Naka, J. Ohshita, T. Yoshioka, M. Kanezashia and T. Tsuru, Insight into the pore tuning of triazine-based nitrogen-rich organoalkoxysilane membranes for use in water desalination, *RSC Adv.*, 2014, **4**, 23759–23769.
293. E. A. Prasetyanto, M. B. Ansari, B. H. Min and S. E. Park, Melamine tri-silsesquioxane bridged periodic mesoporous organosilica as an efficient metal-free catalyst for CO_2 activation, *Catal. Today*, 2010, **158**, 252–257.

CHAPTER-II

MATERIALS AND METHODS

2.1. INTRODUCTION

The comprehensive experimental procedures employed for the synthesis and characterization of inorganic-organic hybrid nanoporous high surface area materials are presented in this chapter. In the present research work, two categories of inorganic-organic hybrid materials *viz*. non-siliceous and siliceous hybrid materials have been synthesized. The non-siliceous hybrid materials involve the use of cyclophosphazene moiety, which has a unique three-dimensional peddle wheel structure that gets condensed with various small organic molecules. The siliceous hybrid materials involve the hydrolysis and polycondensation of organosilane precursors with appropriate functionalities followed by the co-condensation with varied amount of tetraethyl orthosilicate (TEOS). The synthesized high surface area nanoporous hybrid materials have been employed for various gas sorption applications. The detailed experimental methods used for the gas sorption applications have also been included in this chapter. Finally, the working principle and experimental procedure of all the analytical techniques that have been used for the structural characterizations and application of all the synthesized materials in this research work have been documented.

2.2. EXPERIMENTAL DETAILS

2.2.1. Materials

The following reagents and solvents have been procured from various sources as mentioned below and are used as-received without any further purification unless otherwise mentioned. Phosphonitrilic chloride trimer (PNC) (99%, Sigma Aldrich, UK), *p*-hydroxy benzaldehyde (PHB, 98%, Sigma Aldrich, China), *m*-hydroxy benzaldehyde (MHB, 99%, Sigma Aldrich, USA), Melamine (99%, Sigma Aldrich, USA), Pyrrole (99%, SRL, India), Cyanuric chloride (CNC, 99%, Sigma Aldrich, Switzerland), (3-aminopropyl)triethoxysilane (APTES, 98%, Alfa Aesar, UK), *N*-[3-(trimethoxysilyl)propyl]ethylenediamine (TMSPD, 97%, Sigma Aldrich, USA), N^{I}-(3-trimethoxysilylpropyl)ethylenetriamine (TMSPT, 97%, Sigma Aldrich, USA), Tetraethyl orthosilicate (TEOS, 98%, Sigma Aldrich, China), Cetyltrimethylammonium bromide (CTABr, 99%, Himedia, India), 1,4-Dioxane (Fisher Scientific, India) Dimethyl sulfoxide (DMSO) (Fisher Scientific, India), Sodium sulphate (Fisher Scientific, India), Sodium hydroxide (Fisher Scientific, India), Potassium carbonate (Fisher Scientific, India), Tetrahydrofuran (THF) (Fisher Scientific, India), Dichloromethane (DCM) (Fisher Scientific, India), Methanol (Rankem, India) and Hydrochloric acid (35%, Rankem, India) were of analytical grade. Pyrrole was distilled and THF was dried by passing over anhydrous Na_2SO_4 prior to use.

2.2.2. Synthesis methods

2.2.2.1. Non-siliceous hybrid nanoporous materials

The non-siliceous inorganic-organic hybrid nanoporous materials were made by incorporating cyclophosphazene moieties into the porous frameworks. The reaction of PNC with MHB and PHB followed by condensation with (i) melamine *via* Schiff base condensation and (ii) pyrrole *via* nucleophilic condensation resulted in the formation of two different categories of products. All the above experiments have been carried out without using any catalyst under nitrogen environment. The detailed procedures for the synthesis of the precursors as well as the condensation products of these two categories of reactions are given below.

2.2.2.1.1. Synthesis of precursors: compound-P and compound-M

The precursors, *compound-P* and *compound-M*, were synthesized by the nucleophilic condensation of the phenolic group of PHB and MHB to the phosphorous of the PNC molecule. The experiments were carried out in presence of a proton abstractor such as K_2CO_3 following the report of Kagit *et al.* with some modifications.[1] Typically for the synthesis of *compound-P*, 39.75 g (121 mmol) of K_2CO_3 was dispersed in a solution of 7.46 g (61.00 mmol) of PHB dissolved in 100 ml dry THF followed by a dropwise addition of a solution of 3.48 g (10.00 mmol) of PNC in 50 ml dry THF. The whole process was carried out under N_2 atmosphere and the reaction mixture was continuously stirred for 48 h at RT. The insoluble salt was separated by filtration and the product soluble in THF was collected by removing THF under reduced pressure using rotary evaporator. The obtained product was re-dissolved in DCM and further combined phase of DCM was extracted with water and brine solution (50 ml each). The extraction was repeated for three times to remove the salts if any. The organic phase was dried by passing it through anhydrous Na_2SO_4. The final product was obtained by removing the DCM under reduced pressure which gives white crystal on recrystallization with ethylacetate.

Similarly, for the synthesis of the precursor *compound-M*, above mentioned methodology adopted for the synthesis of *compound-P* was followed except that MHB was used instead of PHB. Similar white crystals were obtained after recrystallization of the final products. Both the reactions proceeded similarly without any observable change during the course of the reaction.

2.2.2.1.2. Synthesis of aminal linked inorganic-organic hybrid nanoporous materials (HNMs) via Schiff base condensation

The HNMs have been synthesized by the Schiff base condensation of *compound-P* and *compound-M* with melamine as shown in ***Scheme 2.1***. Typically, 1.5 mmol (1.293 g) of *compound-P* dissolved in 5 ml of DMSO was added drop-wise to a solution of 4.5 mmol (0.567 g) of melamine in 25 ml of DMSO with continuous stirring. The experiment was carried out under N_2 atmosphere. After a thorough mixing of both the solutions, the temperature of the reaction mixture was raised to 453 K. The experiment was continued for 48 h with continuous stirring. The product formed as off-white precipitate was filtered out and washed alternatively with acetone and methanol for three times. The trapped DMSO if any in the product was exchanged using the soxhlet extraction with diethyl ether for 8 h. The product was dried under vacuum at 373 K for 18 h and designated as HNM-1P. Two more specimens HNM-2P and HNM-3P were synthesized at the temperature of 423 and 393 K, respectively, keeping all other reaction conditions same.

Similarly, following the aforementioned synthesis protocol for HNM-1P, HNM-2P and HNM-3P, *compound-M* was condensed with melamine to synthesize HNM-1M, HMN-2M and HNM-3M, respectively.

2.2.2.1.3. Synthesis of cyclophosphazene-based hybrid nanoporous materials (CHNMs)

The CHNMs have been synthesized solvothermally, by condensing pyrrole with compound-P at 453 K for 48 h using a Teflon lined autoclave as shown in ***Scheme 2.1***. Prior to the solvothermal treatment, 3.0 mmol of freshly distilled pyrrole and 0.5 mmol of *compound-P* dissolved in 5 ml of dry 1,4-dioxane were stirred at 343 K for 1 h in N_2 atmosphere. After the completion of reaction, the autoclave was cooled naturally to RT. A brownish-black monolith was obtained. It was washed with THF followed by methanol for at least three times. The obtained product was dried in vacuum oven at 353 K for 12 h and designated as CHNM-1P. Two more specimens, CHNM-2P and CHNM-3P, were synthesized by increasing the solvent amount from 5 ml in CHNM-1P to 10 and 15 ml, respectively, keeping all other reaction conditions identical.

Similarly, by following the aforementioned synthesis methodology, *compound-M* was condensed with pyrrole by varying the solvent amount to synthesize CHNM-1M, CHNM-2M and CHNM-3M, respectively.

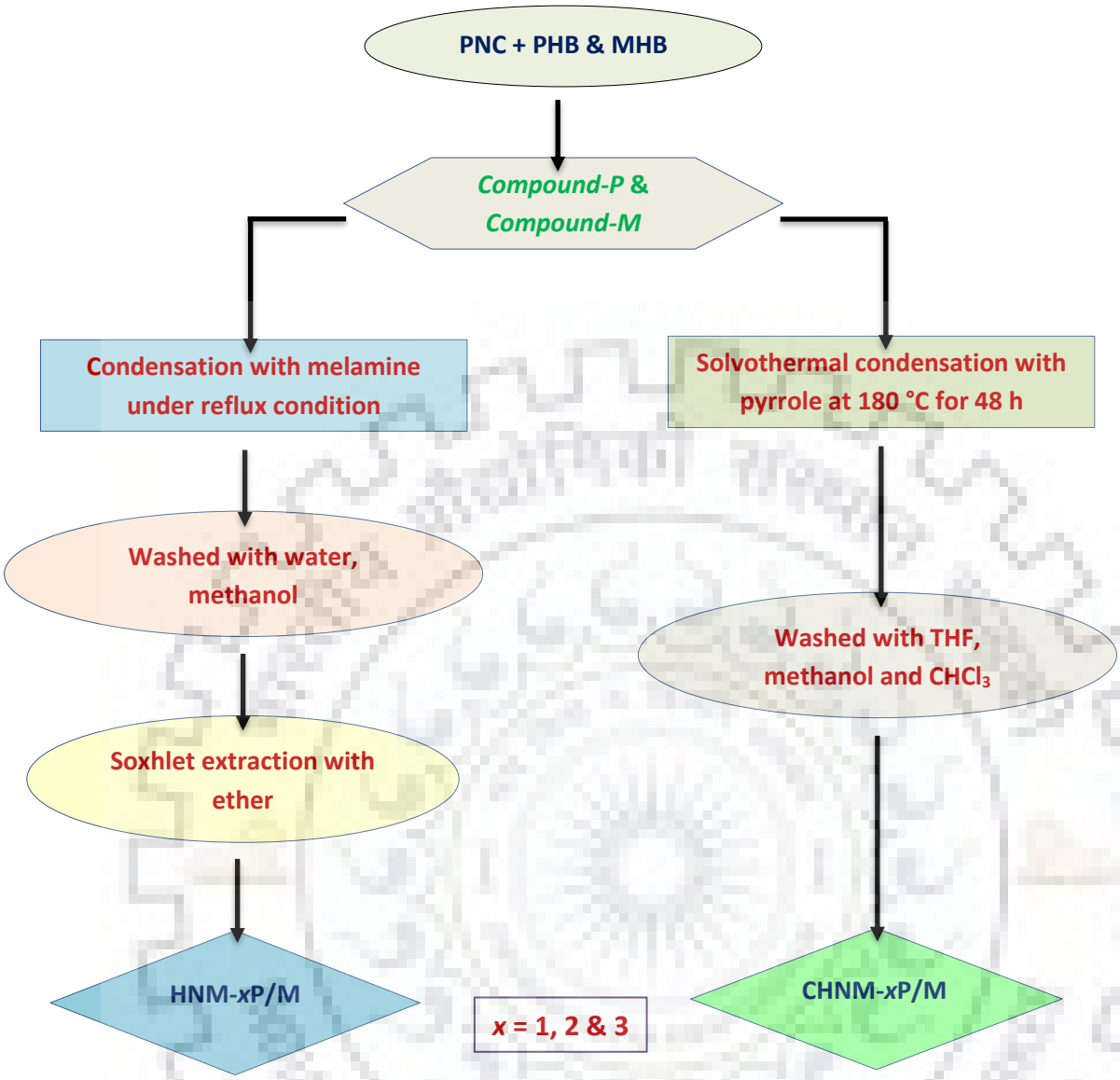

Scheme 2.1: Reaction scheme for the synthesis of non-siliceous inorganic-organic hybrid nanoporous materials via Schiff base condensation with melamine and nucleophilic condensation with pyrrole.

2.2.2.2. Siliceous hybrid materials

The siliceous inorganic-organic hybrid nanoporous materials were synthesized by incorporating nitrogen enriched triazine moieties into the porous siliceous frameworks. The reaction of CC and organosilane precursors with amine functionality followed by hydrolysis and polycondensation in presence of template resulted in the formation of amine functionalized nitrogen rich mesoporous organosilicas. To improve the textural properties of the mesoporous organosilica, on some occasion co-condensation of the organosilane precursor with the TEOS was performed. The detailed synthetic procedure as shown in ***Scheme 2.2***, is given below.

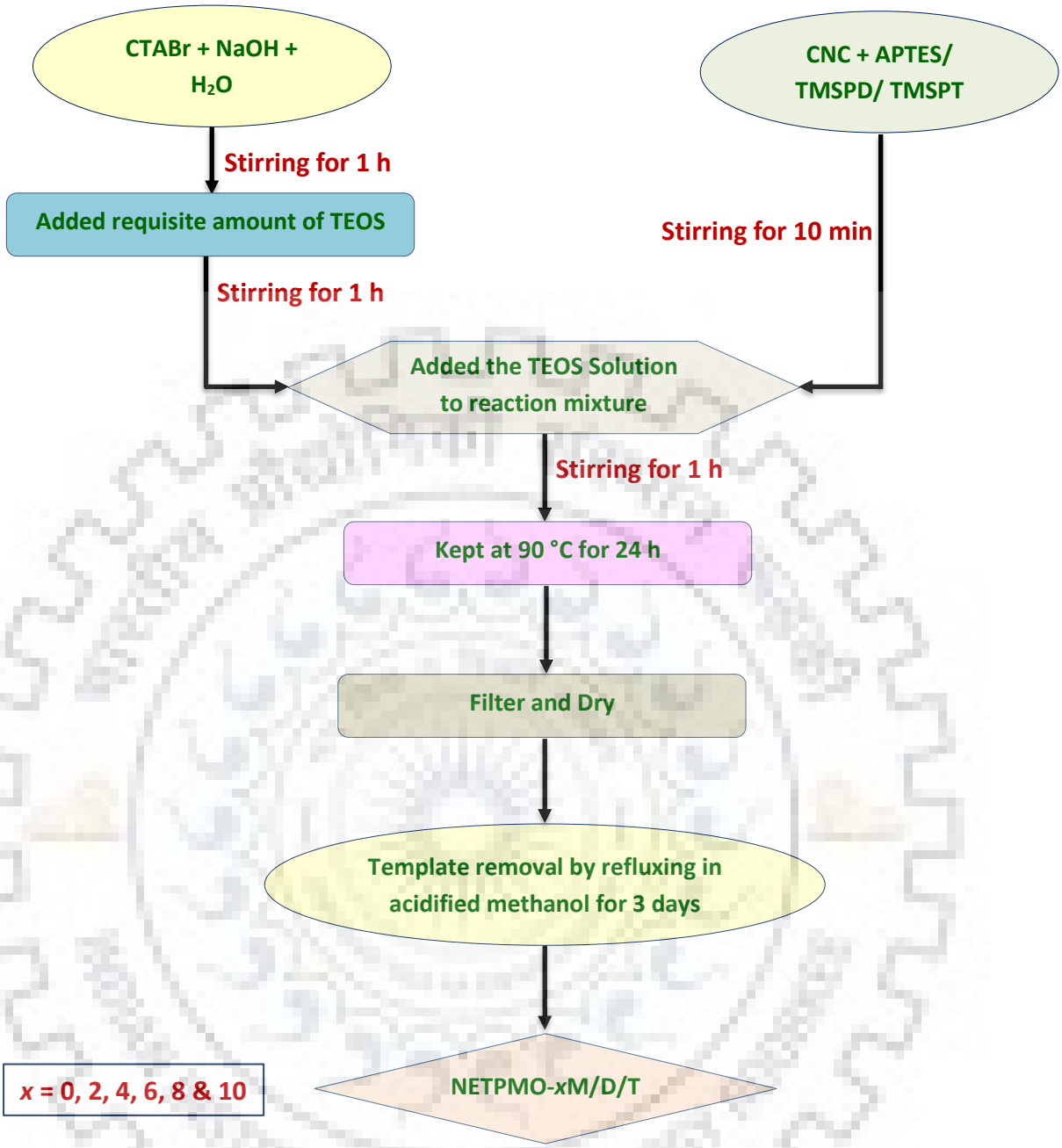

Scheme 2.2: Reaction scheme for synthesis of NETPMOs by condensation of CNC and amine functionalized silica precursors followed by co-condensation with varying quantity of TEOS.

2.2.2.2.1. Synthesis of nitrogen enriched triazine bridged mesoporous organosilicas (NETPMOs)

The synthesis of NETPMOs was carried out by the condensation of CNC with APTES/TMSPD/TMSPT in dioxane in the presence of CTABr as structure directing agent. The synthesis was further extended to synthesize organosilicas by co-condensation of CNC and APTES/TMSPD/TMSPT with a variable amount of TEOS. In a typical synthesis, 1 g of

CTABr was dissolved in 100 ml of 0.125 M NaOH in 250 ml polypropylene bottle. To it, the requisite amount of TEOS was added and the solution was stirred for 1 h. CNC (1 mmol) and APTES/TMSPD/TMSPT (3 mmol) were condensed separately in 5 ml dioxane. The resulting condensed solution was added drop-wise to the solution containing TEOS and CTABr followed by stirring for 1 h. The resulting mixture in the polypropylene bottle was placed in an oven at 90 °C for 24 h (***Scheme 2.2***). The white precipitate formed during this hydrothermal treatment was filtered and dried. The molar composition of reactants in reaction mixture was kept at CNC:APTES/TMSPD/TMSPT:TEOS:CTABr:NaOH:H_2O = 0.33:1:*x*:0.913:4.16:1851.85, where *x* (*x* = 0, 2, 4, 6, 8, 10) is the amount of TEOS in mole. CTABr was extracted by refluxing the as-synthesized sample in a mixture of 100 ml methanol and 10 ml 2 M HCl for 72 h. The specimens synthesised using APTES, TMSPD and TMSPT were designated as NETPMO-*x*M, NETPMO-*x*D and NETPMO-*x*T, where *x* = 0, 2, 4, 6, 8, 10 and M, D and T stand for monoamine in APTES, diamine in TMSPD and triamine in TMSPT, respectively.

2.3. CHARACTERIZATION

2.3.1. Fourier transform infrared (FTIR) spectroscopy

Fourier transform infrared (FTIR) spectroscopy has been the workhorse for investigating the functional group present in a material, which in turn could solve the problems related to the structure elucidation. It is one of the most common characterization facilities that is extensively used in research laboratories as well as industrial R&D and for quality control. FTIR spectroscopy can be used to analyze solid, liquid and gaseous samples.[2,3] It measures the characteristic frequencies of the functional groups present in inorganic, organic and bio-molecules on the irradiation of IR, and is being used for identification of functional groups, structure elucidation, quantitative/qualitative estimation and determination of stereochemistry as well.[2-9] It has also been very popular to elucidate the interaction such as hydrogen bonding, electrostatic interaction between nanoparticle and support materials in polymer composite, molecular orientation in polymeric film, investigate the reaction mechanism and kinetic study. IR analysis takes time of about 1–10 min depending upon the required resolution. For analysis of solid sample, KBr has been preferably used as a matrix while for liquid samples, CCl_4 has been the solvent of choice. The IR analysis doesn't provide elemental composition. In the present research, the synthesis of the precursors and the formation of various condensation products have been analyzed using *PerkinElmer Spectrum 2 FTIR* spectrophotometer. For analysis, the specimens were mixed with oven dried KBr powder in the ratio of 1:100 and grounded into the form of fine powder using mortar and pestle. These mixed

fine powders were pressed to transparent films of 13 mm diameter and about 1 to 1.5 mm thick using hydraulic press and were employed for the analysis in the wavenumber range of 450 – 4000 cm^{-1}.

2.3.2. Nuclear magnetic resonance spectroscopy (NMR)

The NMR, since its discovery has evolved as one of the key spectroscopic techniques for identification, chemical structure proofing, and studying the chemical equilibrium, molecular dynamics, spatial orientation of molecules/nuclei, intermolecular interactions and quantitative estimation of samples present in mixture.[3,10-15] It utilizes the magnetic properties of magnetically active nuclei such as ^{1}H, ^{5}B, ^{9}F, ^{13}C, ^{15}N, ^{31}P, and ^{29}Si etc. to generate the information about the spatial arrangement and chemical environment of nuclei. The NMR has been widely used by chemist, biologist and physicist as well, and now a day, it is extensively used in analysis of biopolymers such as protein and magnetic resonance imaging scanning.[15] This is a non-destructive technique and can be employed for quantitative and qualitative estimation of liquid as well as solid samples.[11-14] Monomers and dimers having magnetically equivalent nuclei cannot be distinguished by this technique. In the present research, *JEOL resonance JNM-ECX-400II* and *JEOL ECZR-600* NMR spectrometers with spectrometer frequency of 400 and 600 MHz, respectively have been utilized to elucidate the chemical environment and chemical structure of liquid as well as solid samples. The liquid state NMR spectra were recorded by dissolving the solid sample in $CDCl_3$. The ^{13}C, ^{29}Si and ^{31}P cross polarization magic angle spinning (CPMAS) solids NMR spectra were recorded at 100, 79.42 and 161.83 MHz, respectively by rotating the samples at 54.74° (magic angle) with sample spinning frequency of 10, 6 and 6 kHz, respectively using rotor of 4 mm diameter. The chemical shifts for ^{13}C, ^{31}P and ^{29}Si nuclei were referenced at 39.47, 0 and 1.445 ppm using adamantane, 85% H_3PO_4 and 3-(trimethylsilyl)propionic acid sodium salt, respectively.

2.3.3. X-ray photo electron spectroscopy (XPS)

The XPS or electron spectroscopy for chemical analysis since its inception in 1951 in the research group of Swedish Professor Kai Siegbahn, has been very popular spectroscopic techniques for surface chemical composition analysis.[3,16,17] It uses the monochromatic low energy X-ray of 1486.6 eV (with Al−K_α radiation source) or 1253.3 eV (with Mg−K_α radiation source) to stimulate the emission of photoelectron from the material surface. The kinetic energy of these emitted photoelectrons is measured using hemispherical analyzer to derive the information about the chemical composition and speciation of various elements present up to

10 nm thickness of the surface of solid samples. Only solid sample can be analyzed using it. The materials susceptible towards X-ray radiation can't be analyzed using XPS. In the present research, *PHI-5000 VersaProbe III, ULVAC-PHI INC"* XPS spectrophotometer equipped with multichannel detector, hemispherical analyzer has been employed to study the chemical composition of materials. The analysis was performed by mounting the sample over carbon tape and keeping it in sample introduction chamber under vacuum for 12 h and then analyzed using monochromatic Al−K_α radiation source (hν = 1486.6 eV) under ultra-high vacuum condition. The binding energy scale for N 1s, O 1s and P 2p were referenced with respect to C 1s at 284.8 eV.[18]

2.3.4. X-ray diffraction (XRD)

The XRD has been widely used as non-destructive analytical tool for materials characterization for over seven decades to analyze materials like powder, sheets and films etc.[2,18-21] It is widely used in academia and industry for myriad of applications such as crystal structure determination, phase identification, sample purity measurement, textural analysis, stress properties and quality control.[18-21] This technique has also been used for the investigation of thermal expansion, phase diagrams and stability under varying temperature and pressure conditions. It only provides information about the crystalline materials and no information could be derived for the amorphous materials. The peak overlapping is one of the bottlenecks of this method that creates problem in phase identification, quantitative and qualitative estimation. The working principle of the XRD is based on Bragg's Law;[18-21]

$$n\lambda = 2d \sin\theta \tag{2.1}$$

The diffraction patterns are observed when incident monochromatic X-rays interact with the sample and produce constructive interference when the condition for Bragg's law are satisfied.[18-22] In the present work, *Ultima IV, Rigaku, Japan,* X-ray diffractometer with Cu-K_α radiation source (λ = 0.15405 nm) has been used to measure the diffraction pattern of specimens. The XRD patterns were recorded with scanning speed of 4°/min in the 2θ range of 10 to 80°. Before the analysis the samples were homogenized by grinding using mortar pestle.

2.3.5. Small angle X-ray scattering (SAXS)

The SAXS has been a very prevalent technique for characterization of materials like molecule, small peptides, powder, thin films etc.[23-25] It provides the vital information about the density, arrangement, sizes and shapes of particles, internal structural ordering of the molecules and much more.[23,24] The measurements are carried out in 2θ range of 0.2 to 5 degree. One

of the major uses of the SAXS in the recent times is the elucidation of mesostructural periodicity.[26] In the present research, the mesoscale ordering of mesoporous organosilica materials was analysed using *Ultima IV, Rigaku, Japan,* X-ray diffractometer equipped with Cu-K_α radiation source (λ = 0.15405 nm) in the 2θ range of 0.2 to 5 degree with scanning speed of 0.25° per min.

2.3.6. Field emission scanning electron microscopy (FESEM)

The FESEM has become an indispensable tool both in science and engineering, and has been widely employed to acquire the microstructural details.[2,27-29] During FESEM analysis, the surface of the sample is bombarded with high energy electrons ejected from electron gun. The secondary electrons are generated from the surface of the sample after interaction with these high energy electrons.[27-29] These secondary electrons ejected at various angle and speed depending upon the nature of the elements present are detected by the secondary electron detector which converts the signals to the microstructure. Similarly, the electrons scattered with an angle close to zero degree with respect to the incident beam, back scattered electrons also provide very vital information about the nature of the microstructure. These electrons are detected by BSE detector and using computer the microstructure is created which provides vital information about the nature of the elements present in the sample surface. Moreover, due to the bombardment of the high energy electrons, X-rays are also produced and these X-rays are characteristics of the elements and hence used to provide information about the elemental composition using the EDAX detectors.[30] Although, the elemental composition is not very much accurate in the order of ppm, but still could provide very close values if the calibration is done precisely. In the present research, *TESCAN MIRA3 FESEM* was used to carry out the microstructural analysis of the samples at an operating voltage of 10 kV. Before the imaging, the specimens were coated with gold using standard sputtering method.

2.3.7. Transmission electron microscopy (TEM)

The TEM like FESEM use high energy electron beam but the difference between FESEM and TEM is that, in case of FESEM the microstructural information is obtained using the secondary and back scattered electrons while in TEM these are obtained using transmitted electrons. The resolution and magnification in TEM is superior compared to FESEM owing to the use of high energetic electron beams.[31,32] During TEM analysis, a high energy electron beam is transmitted through an ultrathin layer of sample deposited over carbon-coated copper grid.[31,32] This beam interacts with sample to provide the information about the

microstructure, chemical composition, crystal structure and defects in the sample.[33,34] In the present research, *TECNAI G*^{2}, *FEI* and *JEOL JEM-3200FS* TEM microscope at an operating voltage of 200 and 300 kV, respectively were used to analyze the microstructure, mesoscale ordering, pore and particle size. Before the analysis, specimens were prepared by dispersing the sample in ethanol by ultra-sonication for 15 min followed by placing a drop of this suspension over carbon coated holy copper grid of 200 mesh size and dried in air.

2.3.8. Thermal analysis

Thermogravimetric analysis (TGA) is combination of techniques and is used to study the glass transition temperature (T_g), melting point, thermal stability and rate of degradation, linear and volumetric expansion, sample purity, effect of additive and blends, rate and level of crystallinity, phase transition temperature and dielectric properties etc.[35-37] It measures the weight loss of the specimen when heated over the range of temperature or held at isothermal condition.[38] It is suitable for solid sample but liquid sample can also be characterized.[39] Change in mass of specimen as a function of time or temperature is recorded. Different atmospheric conditions such as air, N_2, Ar, and CO_2 etc. can be selected. It has also been very popular to study the physisorption and chemisorption phenomenon. In this research, *"EXSTAR TG/DTA6300*" TGA instrument was used to study the thermal stability and thermal decomposition of template or structure directing agent used for the synthesis of porous siliceous hybrid materials. The thermogravimetric analysis experiments were carried out by loading few mg (typically, 5-10 mg) of finely grounded powder sample in alumina sample holder and measured in the temperature range of 298 to 1000 K with a heating rate of 10 K min^{-1} under air. Alumina was also used as a reference material.

2.3.9. CHNS(O) elemental analysis

CHNS(O) elemental analysis, as the name suggest is a technique used for rapid quantification of carbon, nitrogen, hydrogen, sulphur and oxygen contents present in materials.[40-42] It can be used to analyze materials ranging from solid to liquid to volatile and gaseous compounds and is based on burning of sample in the presence of excess oxygen.[40-42] The combustion products of C (CO_2), N (NO_2 and NO), H (H_2O) and S (SO_2) are carried by carrier gas (helium gas) and quantified by thermal conductivity detector.[40] In the present study, *Thermo scientific*, *Flash 2000* and *vario MICRON* CHNS(O) elemental analyzers were used to estimate the quantitative C, N and H composition of porous framework along with C:N ratio of mesoporous organosilica frameworks. In a typical analysis, 2-3 mg of specimen was weighed

and packed in tin capsules followed by loading it in the autosampler. Prior to analysis, instruments were calibrated using analytical reagent grade sulphanilic acid and aspartic acid as reference materials.

2.3.10. Gas sorption

Gas sorption has been one of the well-established techniques for analyzing the textural properties such as specific surface area, pore size, pore volume of the porous solids adsorbents and fine powders.[43-50] For textural analysis, inert gases such as N_2 and Ar have been predominantly used as a probe molecule at their boiling temperature i.e. 77 and 87 K, respectively.[45] The amount of gas adsorbed over the surface of solid has been used to estimate the specific surface area using Brunauer–Emmett–Teller (BET) method. The linear form of BET equation, as shown in ***equation 2.2*** can be written as; [43,44]

$$\frac{1}{v[\left(\frac{p_0}{p}\right)-1]} = c - \frac{1}{v_m c}\left(\frac{p}{p_0}\right) + \frac{1}{v_m c} \tag{2.2}$$

where, v is amount of gas adsorbed, v_m is monolayer adsorbed gas amount, p and p_0 are the equilibrium and saturation pressure of adsorbates at its boiling temperature of adsorption and c is the BET constant. This BET equation can be employed to measure the total surface area (S_{total}) and specific surface area (SA_{BET}) by below given ***equations 2.3 and 2.4***;

$$S_{total} = \frac{(v_m N s)}{V} \tag{2.3}$$

$$SA_{BET} = \frac{S_{total}}{a} \tag{2.4}$$

where, N is Avogadro's number, V is the adsorbate (probe as) molar volume, s is adsorbate cross section and a is adsorbent mass.

In the present research, gas sorption equipment *Autosorb-iQ2, Quantachrome Instruments, USA* was used to measure the N_2 sorption isotherm at 77 K using liquid N_2. Prior to gas adsorption measurements, the samples were degassed at 120 °C for 6 h to remove the unwanted adsorbed gas and moisture on adsorbent surface. The relative pressure range for calculation of SA_{BET} using BET model was obtained using Rouquerol plots.[48] Density functional theory (DFT) with suitable carnel was applied to adsorption or desorption branch of N_2 isotherm to draw the pore size distribution (PSD) profile.[51,52] The total pore volume was estimated from adsorption branch at a relative pressure of 0.90 or 0.99.[53]

Gas sorption instrument has also been used to measure the CO_2, CH_4 and H_2 sorption. The sorption isotherms for CO_2 and CH_4 were measured at 273 and 298 K at 1 bar. The Chiller

circulator containing ethyleneglycol and water (1:1 volumetric ratio) was used to maintain the bath temperature. H_2 uptake was estimated at 77 K and 1 bar. The isosteric heat of adsorption (Q_{st}) for CO_2 and CH_4 was measured by fitting the CO_2 and CH_4 adsorption data into Clausius Clapeyron equation given below e***quation 2.5***.[54,55]

$$ln\frac{p_1}{p_2} = \frac{\Delta H}{R}\left(\frac{1}{T_2} - \frac{1}{T_1}\right) \tag{2.5}$$

where, p_1 and p_2 are pressures (bar) at absolute temperature T_1 (K) and T_2 (K). R and ΔH are gas constant (8.3145 J mol^{-1} K^{-1}) and isosteric heat of adsorption (kJ mol^{-1}), respectively.

References

1. R. Kagit, M. Yildirim, O. Ozay, S. Yesilot and H. Ozay, Phosphazene based multicentered naked-eye fluorescent sensor with high selectivity for Fe^{3+} ions, *Inorg. Chem.*, 2014, **53**, 2144−2151.
2. F. A. Settle, *Handbook of instrumental techniques for analytic chemistry*, Prentice Hall, New Jersey, USA, 1997.
3. B. Stuart, *Infrared spectroscopy: Fundamentals and applications*, John Wiley and Sons, Chichester, UK, 2004.
4. B. C. Smith, *Fundamentals of Fourier transform infrared spectroscopy*, CRC Press, Taylor and Francis Group, London, UK, 2011.
5. M. Tasumi and A. Sakamoto, *Introduction to experimental infrared spectroscopy*, John Wiley and Sons, Chichester, UK, 2015.
6. R. A. Shaw and H. H. Mantsch, *Infrared spectroscopy in clinical and diagnostic analysis*, John Wiley & Sons Ltd, Chichester, UK, 2000.
7. V. P. Tolostoy, I. V. Chernyshova and V. A. Skryshevsky, *Handbook of infrared spectroscopy of ultrathin films*, John Wiley & Sons Ltd, Hoboken, New Jersey, USA, 2003.
8. M. L. McKelvy, T. R. Britt, B. L. Davis, J. K. Gillie, F. B. Graves and L. A. Lentz, Infrared spectroscopy, *Anal. Chem*., 1998, **70**, 119–177.
9. E. A. Carter, C. P. Marshall, M. H. M. Ali, R. Ganendren, T. C. Sorrell, L. Wright, Y.-C. Lee, C.-I. Chen and P. A. Lay, *New approaches in biomedical spectroscopy, Infrared spectroscopy of microorganisms: characterization, identification, and differentiation*, ACS Symposium Series, 963, American Chemical Society, 2007.
10. J. Keeler, *Understanding NMR spectroscopy*, John Wiley & Sons Ltd, Chichester, UK, 2002.
11. F. A. Bovey, L. Jelinski and P. A. Mirau, *Nuclear magnetic resonance spectroscopy*, Academic Press, Inc., San Diego, USA, 1988.
12. N. E. Jacobsen, *NMR spectroscopy explained*, John Wiley & Sons, Inc., Hoboken, New Jersey, USA, 2007.
13. M. J. Duer, *Solid-state NMR spectroscopy principles and applications*, Blackwell Science Ltd, London, UK, 2002.
14. H. N. Cheng and A. D. English, *NMR spectroscopy of polymers in solution and in the solid state*, ACS Symposium Series, American Chemical Society, Washington, DC, USA, 2002.
15. G. S. Rule and T. K. Hitchens, *Fundamentals of protein NMR spectroscopy*, Springer, Dordrecht, Netherlands, 2006.
16. S. Suga and A. Sekiyama, *Photoelectron spectroscopy: Bulk and surface electronic structures*, Springer, Berlin, Germany, 2014
17. C. D. Wagner, W. M. Riggs, L. E. Davis, J. E. Moulder and G. E. Mulenberg, *Handbook of x-ray photoelectron spectroscopy*, Perkin Elmer Corp., Minnesota, USA, 1979.
18. E. Korin, N. Froumin and S. Cohen, Surface analysis of nanocomplexes by X-ray photoelectron spectroscopy (XPS), *ACS Biomater. Sci. Eng.*, 2017, **3**, 882−889.

19. K. Tsuji, J. Injuk and R. V. Grieken, *X-ray Spectrometry: Recent technological advances*, John Wiley and Sons, Chichester, UK, 2004.
20. E. P. Bertin, *Introduction to x-ray spectrometric analysis*, Springer, Berlin, Germany, 1978.
21. J. D. Hanawalt, H. W. Rinn and L. K. Frevel, Chemical analysis by X-ray diffraction, *Ind. Eng. Chem. Anal. Ed.*, 1938, **10**, 457–512.
22. G. A. Jeffrey and M. Sax, X-Ray diffraction, crystal structure analysis, and the high-speed computer, *Anal. Chem.*, 1962, **34**, 339–343.
23. N. K. Mcguire, *Small-angle X-ray scattering was eyeing micron level structures before they were "nano*", Today's Chemist at Work, American Chemical Society, 2003.
24. A. C. Toma and T. Pfohl, *Small-angle X-ray scattering (SAXS) and wide-angle x-ray scattering (WAXS) of supramolecular assemblies supramolecular chemistry: From molecules to nanomaterials*, John Wiley and Sons, Chichester, UK, 2012.
25. B. Qiao, G. Ferru, M. O. de la Cruz and R. J. Ellis, Molecular origins of mesoscale ordering in a metalloamphiphile phase, *ACS Cent. Sci.*, 2015, **1**, 493–503.
26. B. Chu and B. S. Hsiao, Small-angle X-ray scattering of polymers, *Chem. Rev.*, 2001, **101**, 1727−1761.
27. O. C. Wells, *Scanning electron microscopy*, McGraw-Hill, New York, USA, 1974.
28. S. Wischnitzer, *Introduction to electron microscopy*, Pergamon Press, New York, USA, 1962.
29. M. E. Haine and V. E. Cosslett, *The electron microscope*, Spon, London, UK, 1961.
30. A. Laskin and J. P. Cowin, Automated single-particle SEM/EDX analysis of submicrometer particles down to 0.1 μm, *Anal. Chem.*, 2001, **73**, 1023–1029.
31. M. D. Graef, *Introduction to conventional transmission electron microscope*, Cambridge University Press, Cambridge, UK, 2003.
32. D. B. Williams and C. B. Carter, *Transmission electron microscopy: A textbook for materials science*, Springer, 2009.
33. J. C. Yang, M. W. Small, R. V. Grieshaber and R. G. Nuzzo, Recent developments and applications of electron microscopy to heterogeneous catalysis, *Chem. Soc. Rev.*, 2012, **41**, 8179–8194.
34. P. Goodhew, J. Humphreys and R. Beanland, *Electron Microscopy and Analysis*, Taylor & Francis, London, 2001.
35. M. E. Brown, *Introduction to thermal analysis techniques and applications*, Kluwer Academic Publishers, New York, USA, 2001.
36. C. B. Murphy, Differential thermal analysis, *Anal. Chem.*, 1958, **30**, 867–872.
37. P. Gabbott, *Principles and applications of thermal analysis*, Blackwell Publishing Ltd, Oxford, UK, 2008.
38. B. E. Erickson, Product review: The many faces of thermal analysis, *Anal. Chemi.*, 1999, **71**, 689–692.
39. I. G. Anisimov, M. G. Mitrofanov, O. I. Soletskii, Z. V. Fedorova and A. V. Melikhova, Study of solid hydrocarbons by differential thermal analysis, *Chem Technol Fuels Oils*, 1969, **5**, 451–457.
40. B. V. L'vov, *Thermal decomposition of solids and melts*: *New thermochemical approach to the mechanism, kinetics and methodology*, St. Petersburg, USA, 2007.
41. M. E. Brown and P. K. Gallagher, *Handbook of thermal analysis and calorimetry: Recent advances, techniques and applications*, Elsevier, Amsterdam, Netherlands, 2011.
42. T. S. Ma and M. Gutterson, Organic elemental analysis, *Anal. Chem.*, 1970, **42**, 105–114.
43. W. J. Kirsten, *Organic elemental analysis: Ultramicro, micro, and trace methods*, Academic Press, New York, USA, 1983.
44. M. Thompson, *CHNS elemental analysers*, Royal Society of Chemistry, London, UK, 2008.
45. F. Rouquerol, J. Rouquerol and K. Sing, *Adsorption by powders and porous solids: Principle, methodology and applications*, Academic press, London, UK, 1999.
46. S. J. Gregg and K. S. W. Sing, *Adsorption, Surface Area and Porosity*, Academic press, London, UK, 1982.
47. M. Thommes, K. Kaneko, A. V. Neimark, J. P. Olivier, F. R. Reinoso, J. Rouquerol and K. S.W. Sing, Physisorption of gases, with special reference to the evaluation of surface area and

pore size distribution (IUPAC technical report), *Pure Appl. Chem.*, 2015, DOI 10.1515/pac-2014–1117.
48. K. A. Cychosz, R. Guillet-Nicolas, J. Gracia-Martinez and M. Thommes, Recent advances in the textural characterization of hierarchically structure nanoporous materials, *Chem. Soc. Rev.*, 2017, **46**, 189–414.
49. J. U. Keller and R. Staudt, *Gas adsorption equilibria: Experimental methods and adsorptive isotherms*, Springer Science & Business Media, Inc., Boston, USA, 2005.
50. W. Rudziński, W.A. Steele and G. Zgrablich, *Equilibria and dynamics of gas adsorption on heterogeneous solid surfaces*, Academic Press, Amsterdam, Netherlands, 1997.
51. P. I. Ravikovitcha, G. L. Hallera and A. V. Neimarkab, Density functional theory model for calculating pore size distributions: pore structure of nanoporous catalysts, *Adv. Colloid Interface Sci.*, 1998, **76-77**, 203–226.
52. J. P. Olivier, W. B. Conklin and M. V. Szombathely, Determination of pore size distribution from density functional theory: A comparison of nitrogen and argon results, *Studies in Surface Science and Catalysis*, 1994, **87**, 81–89.
53. E. P. Barrett, L. G. Joyner and P. P. Halenda, The determination of pore volume and area distributions in porous substances. Computations from nitrogen isotherms, *J. Am. Chem. Soc.*, 1951, **73**, 373–380.
54. H. Pan, J. A. Ritter and P. B. Balbuena, Examination of the approximations used in determining the isosteric heat of adsorption from the Clausius-Clapeyron equation, *Langmuir*, 1998, **14**, 6323–6327.
55. D. Ramirez, S. Qi and M. J. Rood, Equilibrium and heat of adsorption for organic vapors and activated carbons, *Environ. Sci. Technol.*, 2005, **39**, 5864-5871.

CHAPTER-III

AMINAL LINKED INORGANIC–ORGANIC HYBRID NANOPOROUS MATERIALS (HNMs)

3.1. INTRODUCTION

The comprehensive study of hybrid nanoporous materials (HNMs) synthesized using Schiff base condensation has been included in this chapter. The synthesis has been carried out in two steps. The first step involved the nucleophilic attack of the phenolic group of PHB to the phosphorus of the PNC molecule forming the precursor (*compound-P).* This was carried out in presence of a proton abstractor (K_2CO_3) following the report of Kagit *et al.* with some modifications.[1] The second step involved the reaction of the *compound-P* with melamine via Schiff base condensation to form the final product, HNMs. The comprehensive structural, microstructural and physicochemical investigations of the HNMs were performed by various analytical techniques such as FTIR, CPMAS-NMR, XPS, XRD, TGA/DTG, FESEM, TEM, and N_2 sorption. Furthermore, the HNMs have been employed for gas sorption applications. The synthesis has further been extended to produce a series of HNMs by reacting MHB with the PNC molecule forming the precursor (*compound-M)* followed by condensation with melamine. These HNMs were similarly investigated for the above-mentioned applications. The detailed experimental conditions for the synthesis and characterization of precursors and HNMs have already been conferred in ***Chapter-II***.

3.2. AMINAL LINKED HYBRID NANOPOROUS MATERIALS SYNTHESIZED USING *COMPOUND-P* (HNM-*x*P, *x* = 1, 2 & 3)

3.2.1. Synthesis and characterization of *compound-P*

For the synthesis of HNMs, precursor, *compound-P*, was synthesized by the reaction between PHB and PNC. The detailed synthesis of the *compound-P* has been discussed in ***Chapter-II*** and shown schematically in ***Scheme 3.1***. The proposed structure of *compound-P* was confirmed by NMR and FTIR spectroscopies. The ^{1}H, ^{13}C and ^{31}P NMR spectra of *compound-P* are given in ***Figure 3.1***. The ^{1}H NMR spectrum in ***Figure 3.1a*** shows characteristic resonance signal at chemical shift, δ, of 9.95 ppm (singlet) for the aldehydic proton. Two additional doublets are observed at δ of 7.8 and 7.2 ppm. The doublet at 7.8 ppm is ascribed to the less shielded magnetically equivalent protons attached to carbon no. 2 adjacent to aldehyde group, while the other doublet at 7.2 ppm is attributed to the more shielded magnetically equivalent protons attached to carbon no. 3 near phenolic oxygen. The detailed assignment of the protons is shown in the inset of ***Figure 3.1a***. The ^{13}C NMR spectrum in ***Figure 3.1b*** shows the characteristic resonance signal for aldehydic carbon at δ of 190 ppm. The resonance signal for carbon no 1 adjacent to the aldehyde group is observed at δ of 134 ppm. The carbon no. 2 and 3 are observed at δ of 132 and 122 ppm, respectively. The resonance signal for least shielded carbon

no. 4 adjacent to the phenolic carbon is observed at 155 ppm. The observation of single resonance signal at δ of 7.1 ppm in ^{31}P NMR spectrum shown in ***Figure 3.1c*** further confirms the incorporation of the cyclophosphazene moiety in the synthesized precursor "*compound-P*" and all the P atoms are magnetically equivalent. The absence of any resonance signal around 20 ppm (P of PNC) further excludes the possibility of any unreacted PNC in the *compound-P* and hence, a complete condensation of PHB with PNC as shown in ***Scheme 3.1*** is realized.

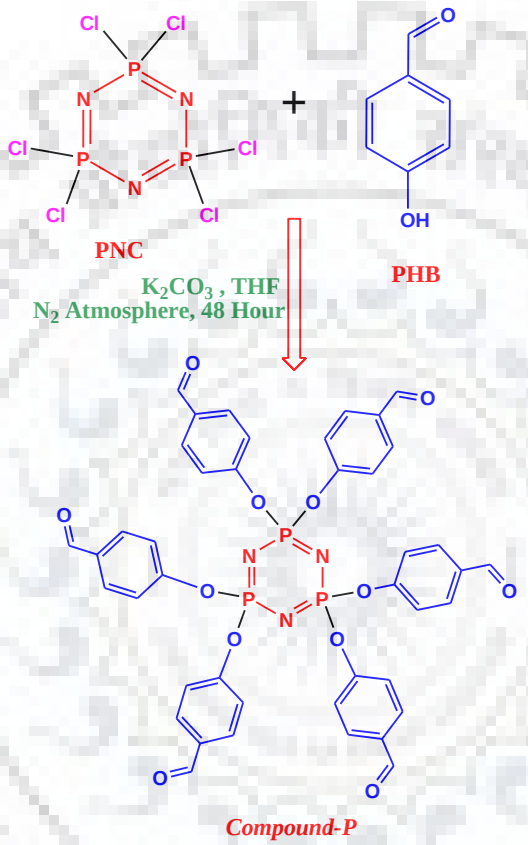

Scheme 3.1: Reaction scheme for the synthesis of *compound-P* via nucleophilic condensation of PNC with PHB in presence of proton abstractor (K_2CO_3).

Further, to confirm the product formation as shown in ***Scheme 3.1*** and corroborate the observation of NMR, the *compound-P* was subjected to FTIR analysis. The typical FTIR spectrum of *compound-P* is given in ***Figure 3.2***. The detailed FTIR band assignment of the *compound-P* is given in ***Table 3.1.*** The characteristic band for aldehyde group is observed at 1705 cm^{-1}. The aromatic –C=C– stretching vibrations are observed at 1600 cm^{-1}. The –C–H stretching of the –CHO group was observed at 2840 cm^{-1}. The characteristic bands for –P=N– and P=N–P originating from the cyclophosphazene moiety are observed in the range of 1210 and 1160 and 510 cm^{-1}, respectively. The band associated with P–O–C is observed at 960 cm^{-1}. The comparison of the FTIR spectra of the *compound-P* with the reactants further confirms the

formation of the desired product as proposed in ***Scheme 3.1***. All the observed bands matches well with the values reported in the literature.[1]

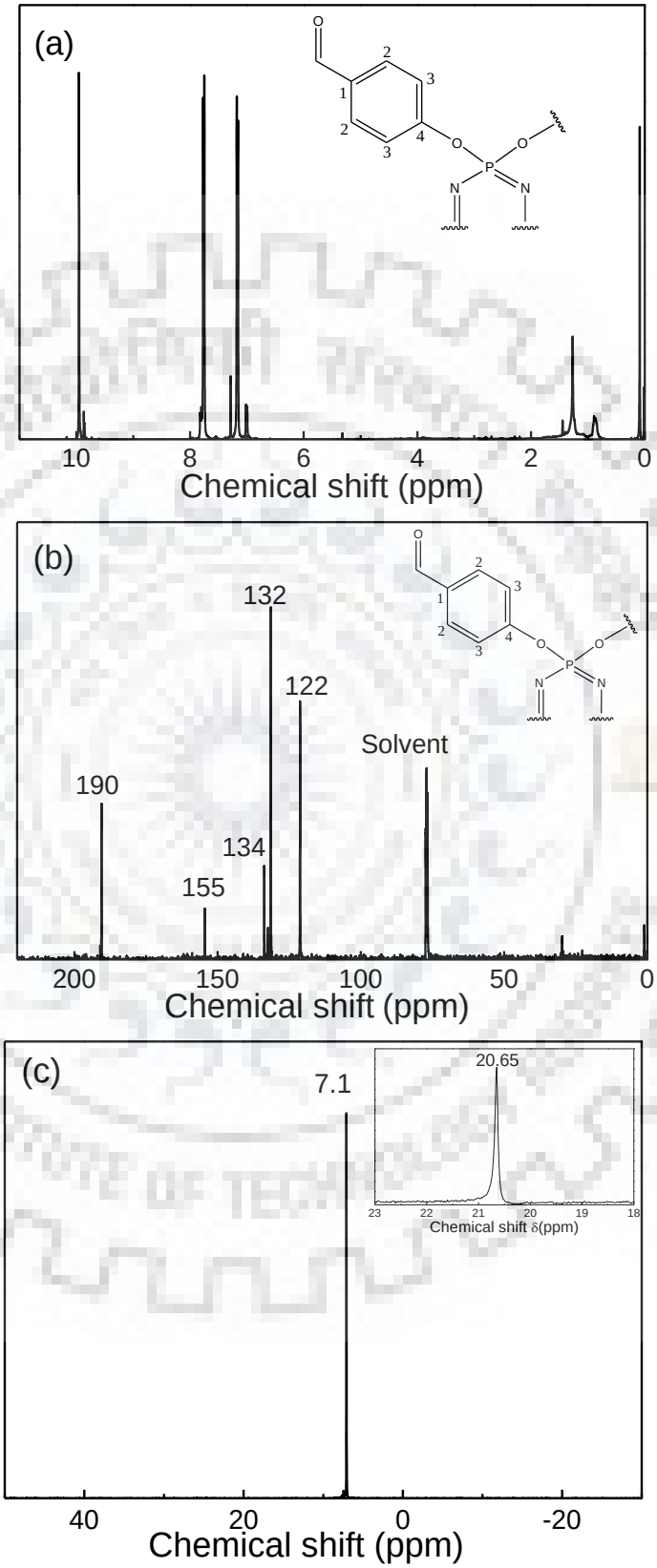

Figure 3.1: (a) ^{1}H NMR, (b) ^{13}C NMR and (c) ^{31}P NMR spectra of *compound-P* analyzed in $CDCl_3$ at 298 K. The ^{31}P NMR spectrum of PNC is given in the inset of (c).

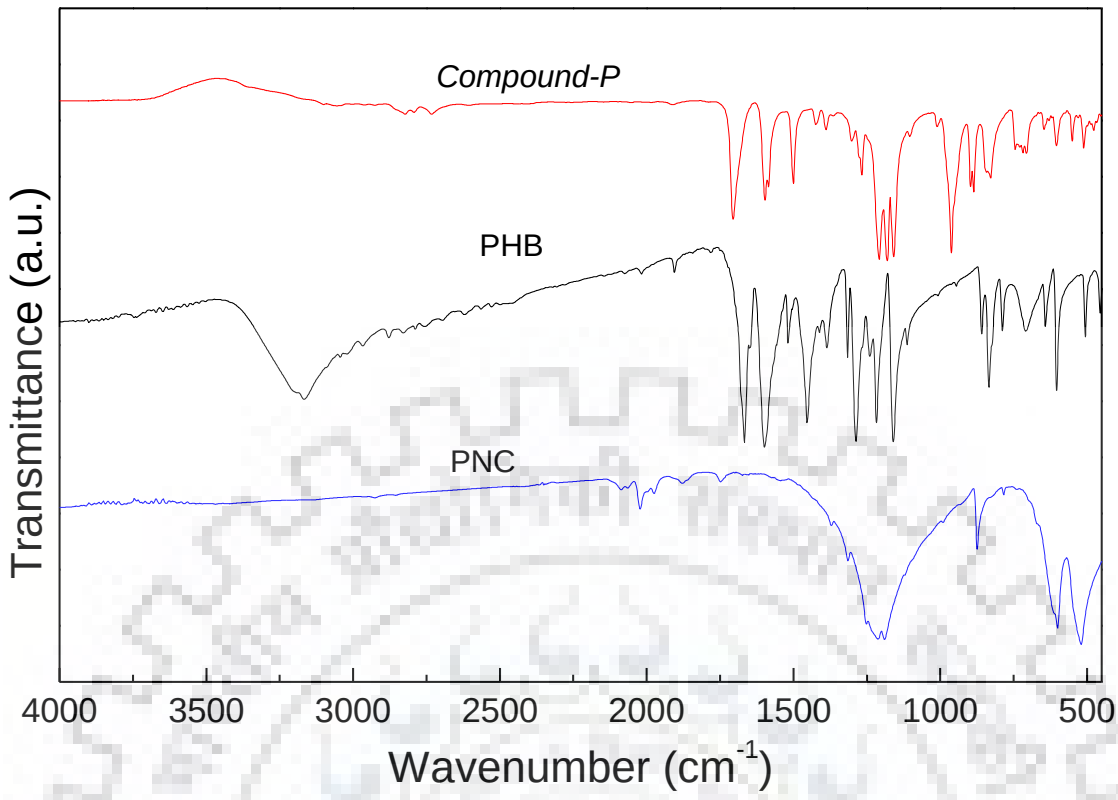

Figure 3.2: FTIR spectra of *compound-P*, PNC and PHB analyzed using KBr film.

Table 3.1: FTIR bands assignments for *compound-P*, PNC and PHB.

Bands assignment	**Bands (cm^{-1})**		
	PNC	**PHB**	***Compound-P***
–O–H stretching	-	3200	-
Aldehydic C–H stretching	-	2876	2840
–CHO stretching band	-	1666	1705
C=C aromatic ring stretching	-	1600	1600
Aromatic C–H bending	-	1503	1503
(C-H) in plane bending vibration		1265-	1270
ν_{as}(P=N–P)	1230	-	1210
ν_{as}(P=N–P)	1190	-	1190
ν_{as}(P=N–P)	1135	-	1160
ν_{as}(P–O–C) vibration	-	-	960
P–Cl	875	-	-
–C–H out of plane wagging		840	845
C-CO out of plane deformation	-	640	640
δ(P=N–P) vibration	520	-	510

3.2.2. Synthesis and characterization of HNM-*x*P

The classical Schiff base condensation discovered by Hugo Schiff [2] in 1864 has traditionally been used for the generation of imine and aminal linkages by condensing aldehydes with different amines.[3,4] In general, the imine double bond is formed, however, more basic primary amines may subsequently attack the imine bond resulting exclusively aminal linkages.[5] The formation of the imine and aminal linkages have been exploited to prepare various types of organic polymeric materials.[6,7] Moreover, recently this reaction has been utilized towards the synthesis of nanoporous organic polymers with high surface area having imine and aminal linkages.[8-15] In this chapter, a discussion on synthesis of the aminal linked inorganic-organic hybrid nanoporous materials has been carried out using condensation of *compound-P* with melamine via Schiff base condensation as shown in ***Scheme 3.2***. Melamine was chosen in this research to facilitate the condensation reaction and most importantly, the synthesized material is expected to have larger nitrogen content of 40% or more, which has not been achieved so far for any types of inorganic-organic hybrid materials. The best reported nitrogen content for any nanoporous material was 53.17% for CNHC (an organic porous polymer).[16] The larger nitrogen content in the material will be very much beneficial for the gas sorption applications, as the lone pair of electrons in the nitrogen acts as Lewis base and potentially could interact with Lewis acidic gases such as CO_2.

The condensation of *compound-P* with the melamine was carried out in DMSO. Detailed experimental condition is given in ***Chapter-II***. The specimen synthesised at reflux condition was designated as HNM-1P. Further, to study the effect of reaction condition on the synthesis of HNMs, two more specimens have been synthesised at reaction temperature of 423 and 393 K, keeping other reaction condition identical to HNM-1P, and these specimens are designated as HNM-2P and HNM-3P, respectively.

In order to confirm the structure and study the chemical environment of synthesized HNM frameworks as proposed in ***Scheme 3.2***, the specimens were investigated initially by FTIR. The broad bands at 3405 and 1650 cm^{-1} in the FT-IR spectra of the HNMs as shown in ***Figure 3.3*** and ***Table 3.2*** due to the (-N-H) stretching and bending vibration, respectively, indicate the formation of the aminal linkage.[10-12] The formation of the aminal linkage was supported by the absence of the characteristic imine band around 1620 cm^{-1} due to the C=N stretching vibration.[10,11] The band at 2930 cm^{-1} was assigned to -C-H stretching of tertiary carbon due to the methine linkage.[10-12] The band at 1600 cm^{-1} is observed due to aromatic -C=C- ring stretching.[11,12] The band at 1548 and 1477 cm^{-1} were attributed to triazine moiety

of melamine.[10,11,16] The absence of C=O stretching vibration around 1705 cm^{-1} confirms the complete condensation of *compound-P* with melamine.[10-12] The observation of bands in the range of 1210 to 1160, 986 and 584 cm^{-1} assigned to ν_{as}(P=N–P), ν_{as}(P–O–C) and δ(P=N–P) vibrations, respectively, confirm the inclusion of the cyclophosphazene moieties in the HNMs frameworks.[1,17-21]

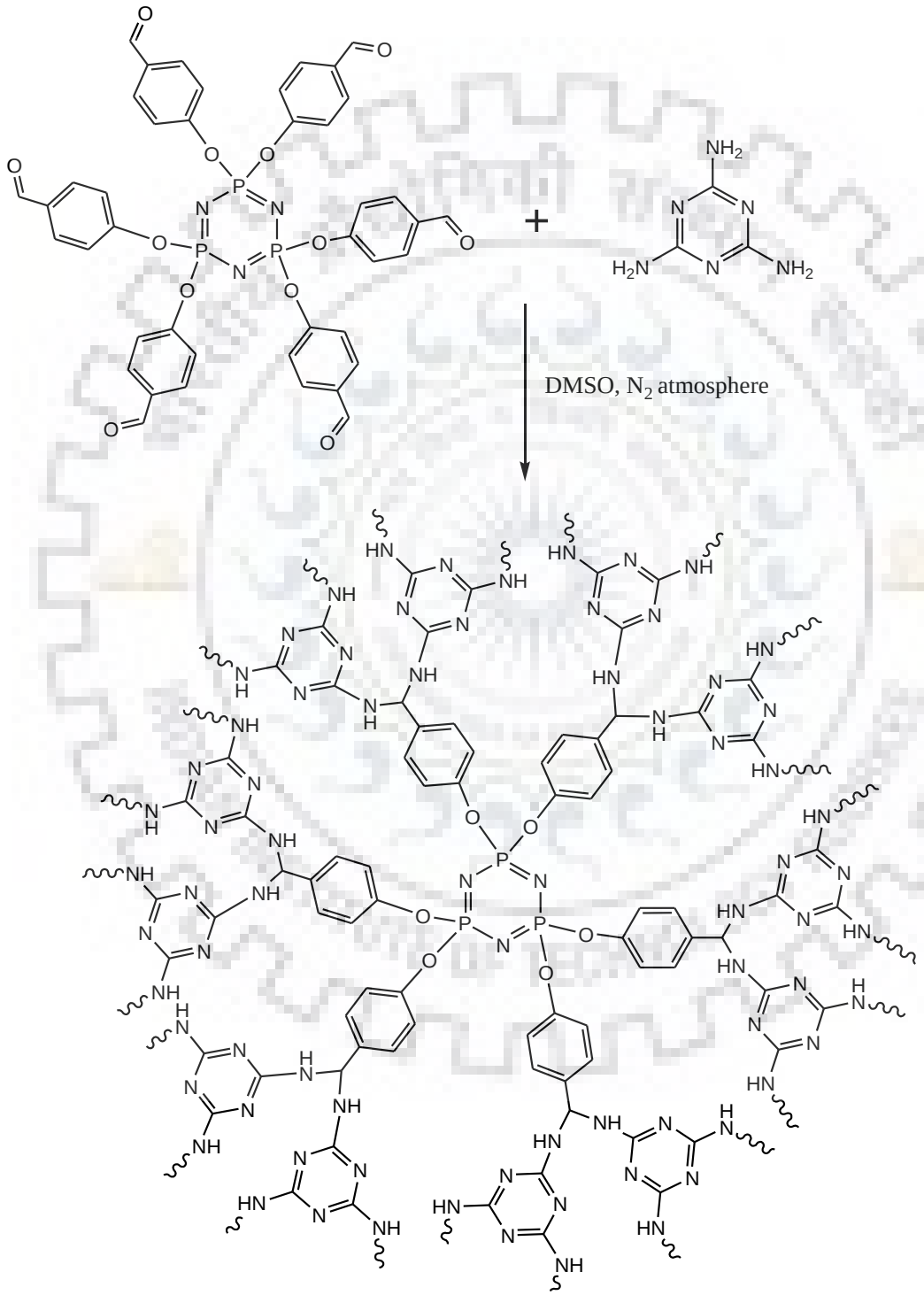

Scheme 3.2: Reaction scheme for the synthesis of HNM-*x*P, showing the condensation of *compound-P* with melamine in DMSO under N_2 atmosphere through Schiff base condensation.

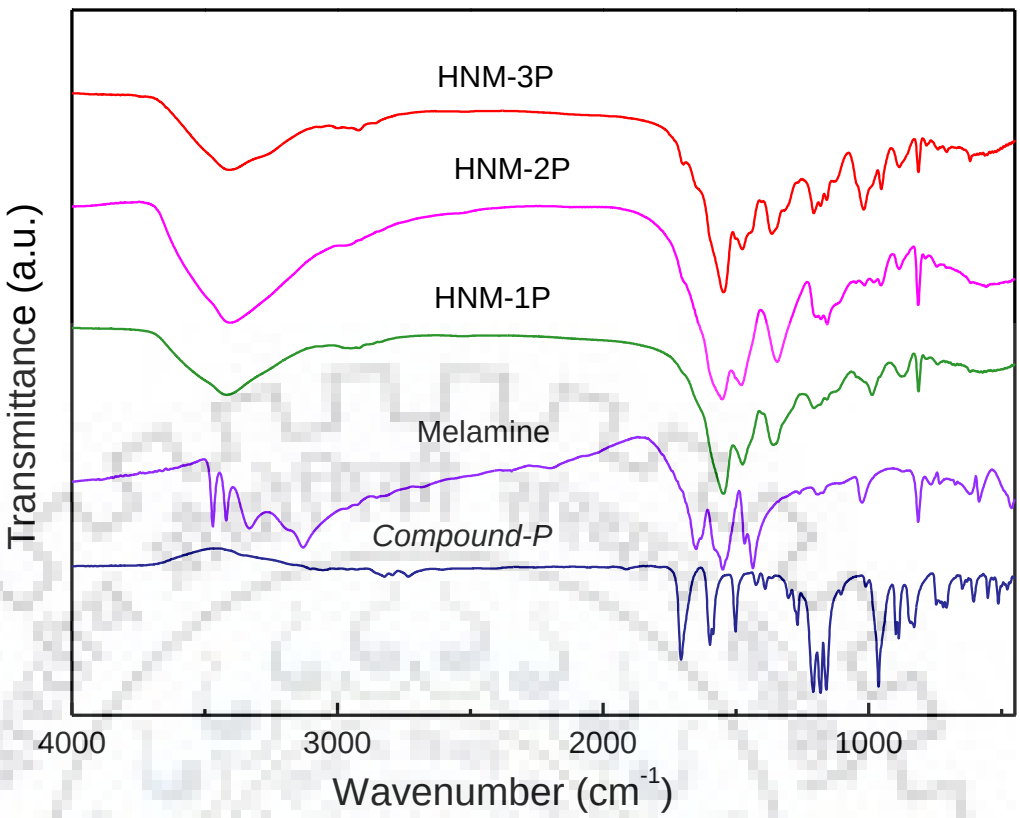

Figure 3.3: FTIR spectra of HNMs: FTIR-spectra of *compound-P*, melamine, and HNM-*x*P synthesized via Schiff base condensation using DMSO under N_2 atmosphere.

Table 3.2: FT-IR bands assignment of HNM-*x*P synthesised by Schiff base condensation.

Functionality	Bands position (cm^{-1})
Aminal N–H stretching	3405
Aliphatic C–H stretching	2930
NH_2 deformation band	1650
C=C aromatic ring stretching	1600
Quadrant stretching of s-triazine ring	1548
Semicircle stretching of s-triazine ring	1477
Ring and side chain CN stretching	1360
ν_{as}(P=N–P)	1210-1160
ν_{as}(P–O–C) vibration	986
–C–H out of plane wagging	850
Ring breathing ring def (out of plane)	814
δ(P=N–P) vibration	584

In order to further confirm the structure as proposed in ***Scheme 3.2***, the ^{13}C and ^{31}P CPMAS NMR spectra of a representative sample, HNM-1P, were analyzed. The ^{13}C CPMAS NMR spectrum for HNM-1P has been given in ***Figure 3.4a***. It shows the resonance signals at 166, 155, 135, 128, 122 and 57 ppm corresponding to carbon no. 1, 2, 3, 4, 5 and 6, respectively as assigned in inset of ***Figure 3.4a***.[1,10-12]

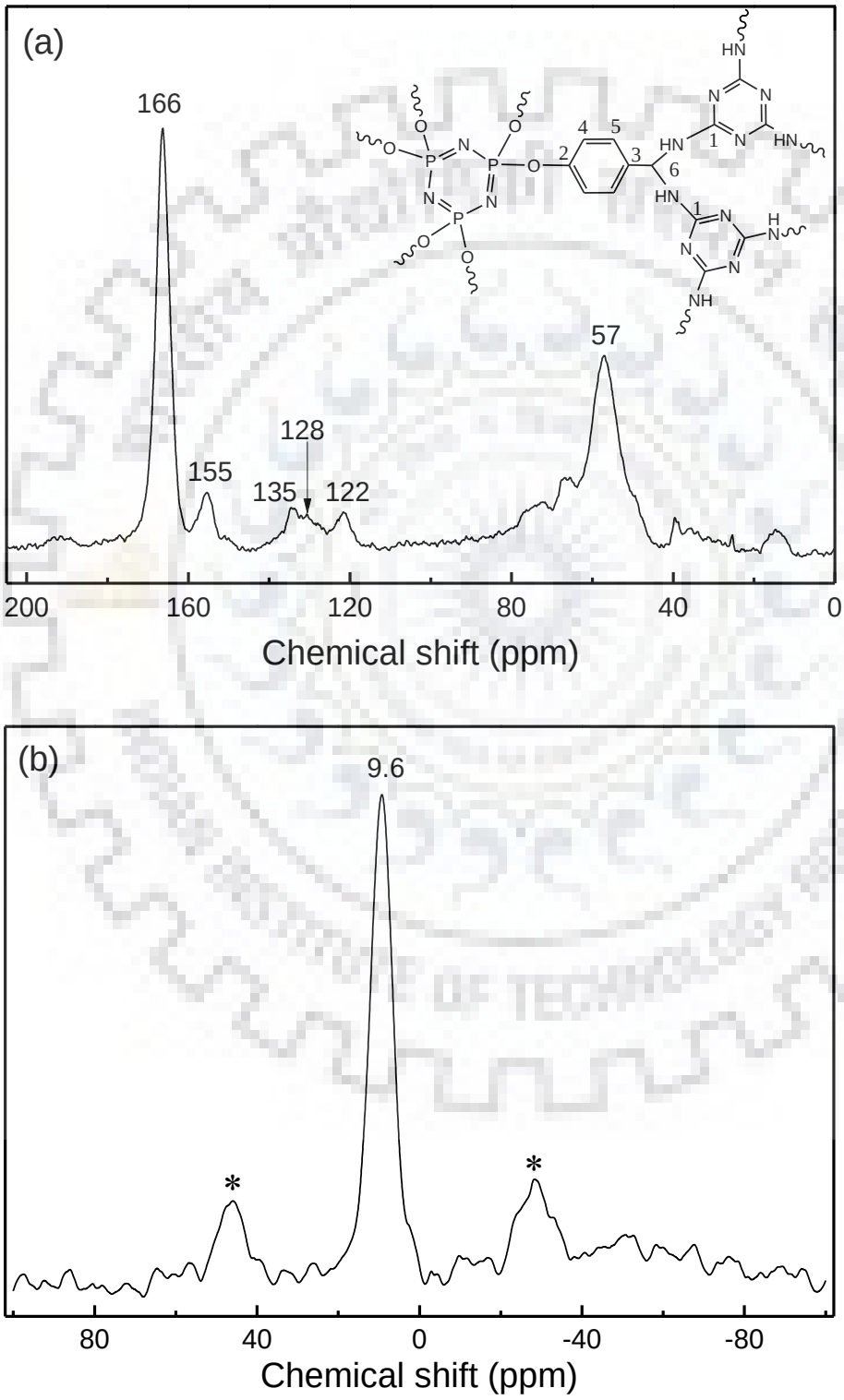

Figure 3.4: (a) ^{13}C and (b) ^{31}P CPMAS NMR spectra of HNM-1P.

The absence of signal at 160 ppm (due to imine linkage) and the observation of the signal at 57 ppm (due to the tertiary carbon) confirm the formation of the aminal linkages in the HNM-1P.[10-12] The observation of a single resonance signal at 9.6 ppm in the ^{31}P CPMAS spectrum of HNM-1P as shown in ***Figure 3.4b*** further confirms the incorporation of the cyclophosphazene moieties in the frameworks.[17-21]

Furthermore, the chemical environment of the HNMs was investigated by the XPS. A typical survey scan shown in the ***Figure 3.5*** confirms the presence of P, C, N, and O in HNMs frameworks. The high-resolution spectra for P 2p, C 1s, O 1s and N 1s as shown in ***Figure 3.6*** revealed the electronic environment of these elements.

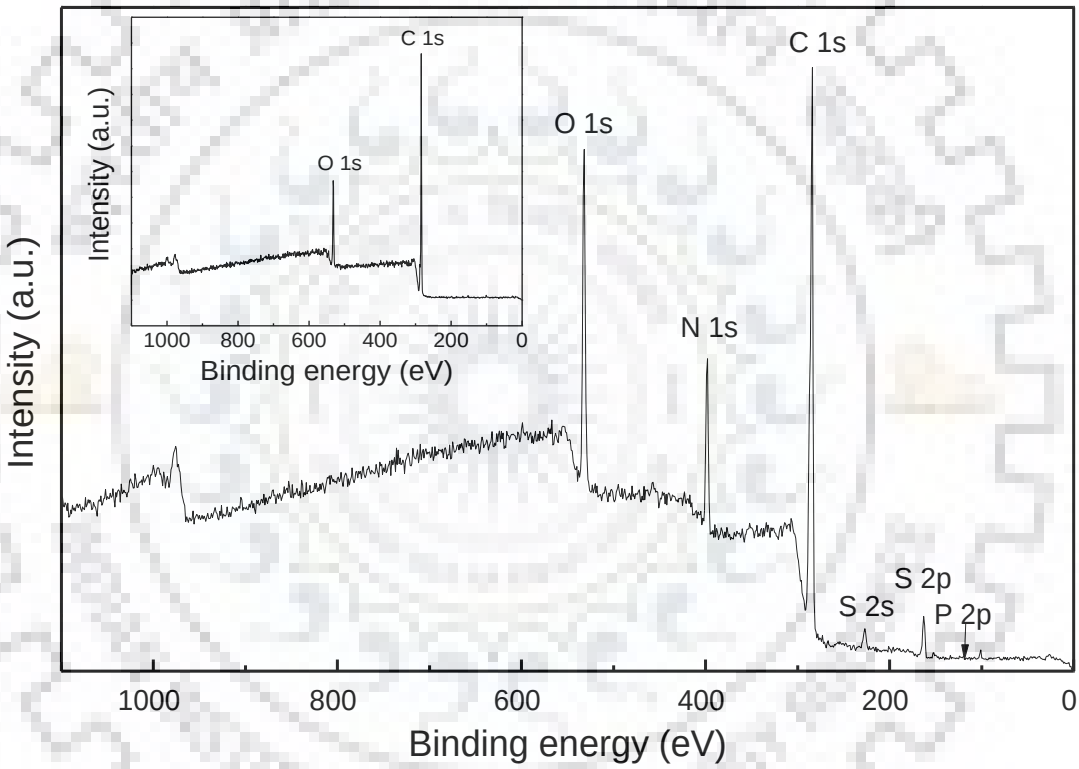

Figure 3.5: XPS survey scan for HNM-1P. The XPS survey scan of carbon tape (used in analysis) is shown in inset

The high-resolution C 1s scan, as shown in ***Figure 3.6a***, display three peaks at 284.8, 285.9 and 287.8 eV. The peak at 284.8 eV originated due to aliphatic carbon. The peaks at 285.9 and 287.8 eV could be ascribed to the carbon of aromatic ring and triazine ring, respectively.[16,23-27] The observation of only one peak at 134.3 in the high-resolution P 2p scan, as shown in ***Figure 3.6b*** confirms the presence of the only phosphorus environment associated to the cyclophosphazene moieties.[22,23] Similarly, the high resolution N 1s scan, as shown in ***Figure 3.6c,*** has shown two peaks at 398.6 and 399.8 eV. The peak at 398.6 eV is

ascribed to the nitrogen of cyclophosphazene moiety while the peak at 399.8 eV is observed due to triazine ring nitrogen.[16,22,23,26] The high resolution O 1s scan is given in ***Figure 3.6d***. The major peak at 532.9 eV could be ascribed to O of -P-O-C linkage in HNM-1P, while the small peaks at lower binding energy could be ascribed to O of carbon tape (inset of ***Figure 3.5***) used in analysis or O of trapped DMSO in the pores of framework.[24, 28,29]

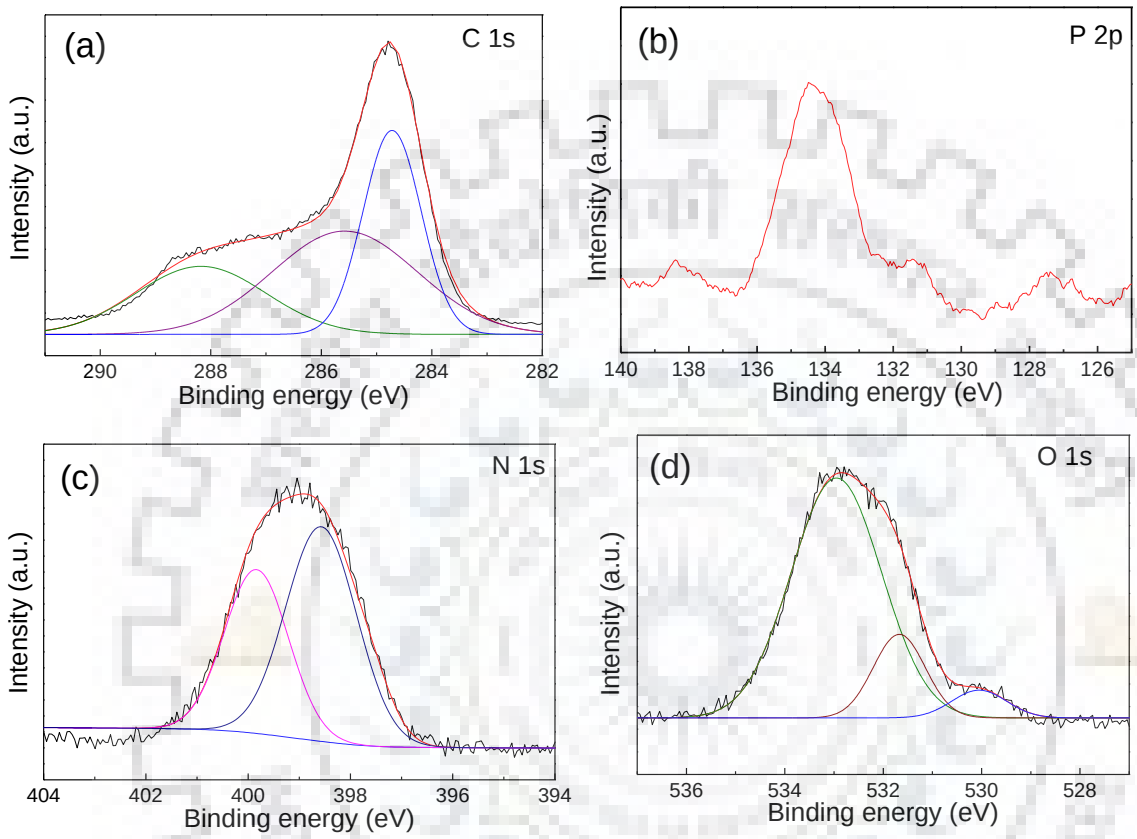

Figure 3.6: XPS high resolution scans; (a) C 1s, (b) P 2p, (c) N 1s and (d) O 1s high resolution XPS scans for HNM-1P.

The aminal linkage in the HNMs was further supported by the elemental analysis given in ***Table 3.3***. Assuming a fully condensed form having aminal linkage as shown in ***Scheme 3.2***, the theoretical composition of the HNMs would be $C_{78}H_{66}N_{75}O_3P_3$. Thus, it will have 41.77, 46.84 and 2.97% of C, N and H, respectively. The observed elemental composition for HNMs given in ***Table 3.3*** is fairly matching with the theoretical composition. The greater mismatch in HNM-3P may be ascribed due to inefficient condensation at lower temperature. The excess H observed was mainly due to the terminal functionality and trapped moisture in the nanopores. Further, assuming the imine linkage in HNMs, the theoretical composition would be $C_{60}H_{30}N_{39}O_6P_3$ with 48.49, 36.76 and 2.03% of C, N and H, respectively, which is not matching with the experimental composition given in ***Table 3.3***.

Table 3.3: Elemental analysis for HNM-*x*P (Theoretical Composition: $C_{78}H_{66}N_{75}O_3P_3$).

Specimens	Observed elemental compositions		
	N	C	H
Theoretical	46.84	41.77	2.97
HNM-1P	42.16	40.18	4.46
HNM-2P	41.14	40.28	5.69
HNM-3P	36.13	31.78	6.20

The HNMs have shown the thermal stability up to a temperature of 623 K in air as evaluated by TGA/DTG analysis shown in ***Figure 3.7***. The TGA thermograms are showing the mass loss in four steps which can also be seen from DTG. The first mass loss observed below 373 K is due to the removal of adsorbed moisture and gases if any in the pores of frameworks. This phenomenon is commonly observed in high surface area materials.[9,12] Second mass loss around 470 K can be ascribed to the removal of trapped DMSO in pores of HNMs, despite being washed several times by acetone, methanol followed by soxhlet extraction using diethyl ether for 8 h to exchange the DMSO from the pores of the framework. Third mass loss at the temperature of 623 K could be due to framework condensation. Final mass loss beyond 800 K could be attributed to the oxidation of carbon and decomposition of P-N frameworks.[17,20]

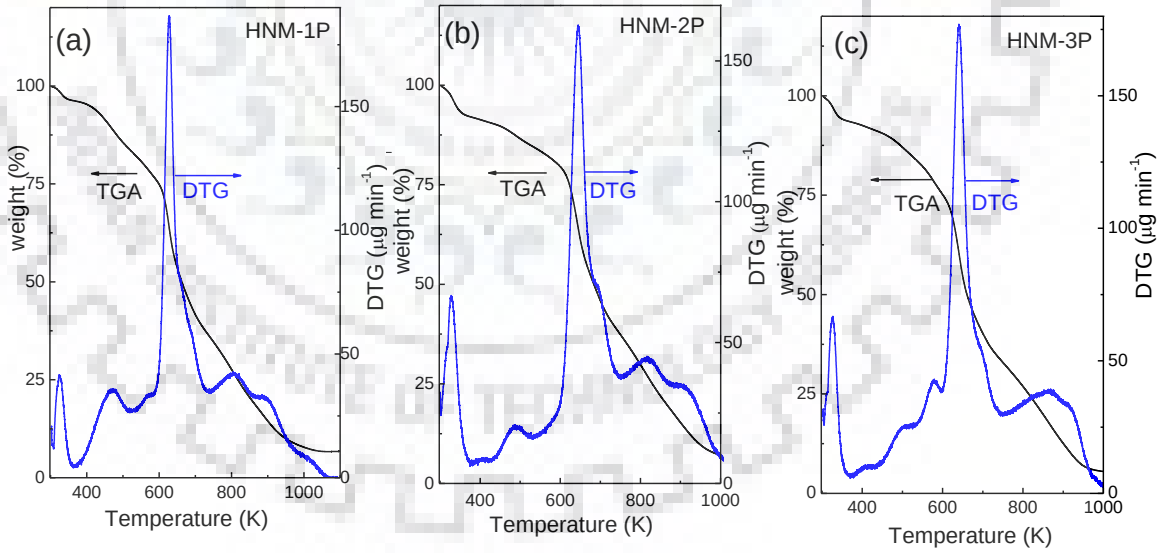

Figure 3.7: TGA and DTG thermograms of HNM-*x*P recorded in air with heating rate of 5 K min^{-1} using alumina sample holder.

The XRD patterns given in ***Figure 3.8*** show broad halo which confirmed the amorphous nature of HNMs. The microstructural analysis given in ***Figure 3.9*** was carried out using FESEM, and it have shown that HNMs consist of particles of size 20 to 60 nm forming the network like structure. The inter-particulate void could also be seen in FESEM images. Further, the microstructural characterization was carried out using TEM, as shown in ***Figure 3.9d***. The

TEM image shows that the HNMs contain the pores in nanoporous regime. The broad diffused ring in SAED patterns, as shown in inset of ***Figure 3.9d*** further corroborate the amorphous nature of the HNMs observed in XRD pattern.

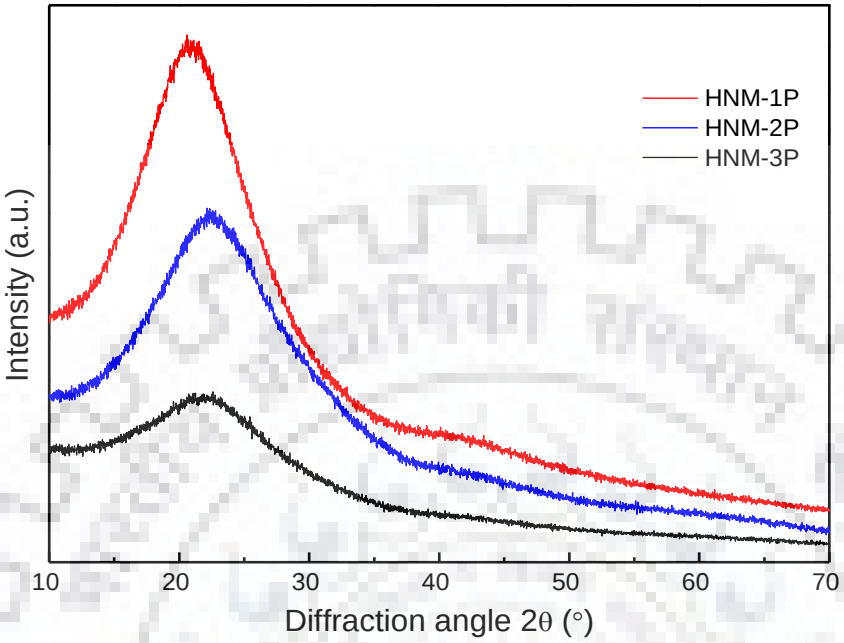

Figure 3.8: X-ray diffraction patterns of HNM-*x*P.

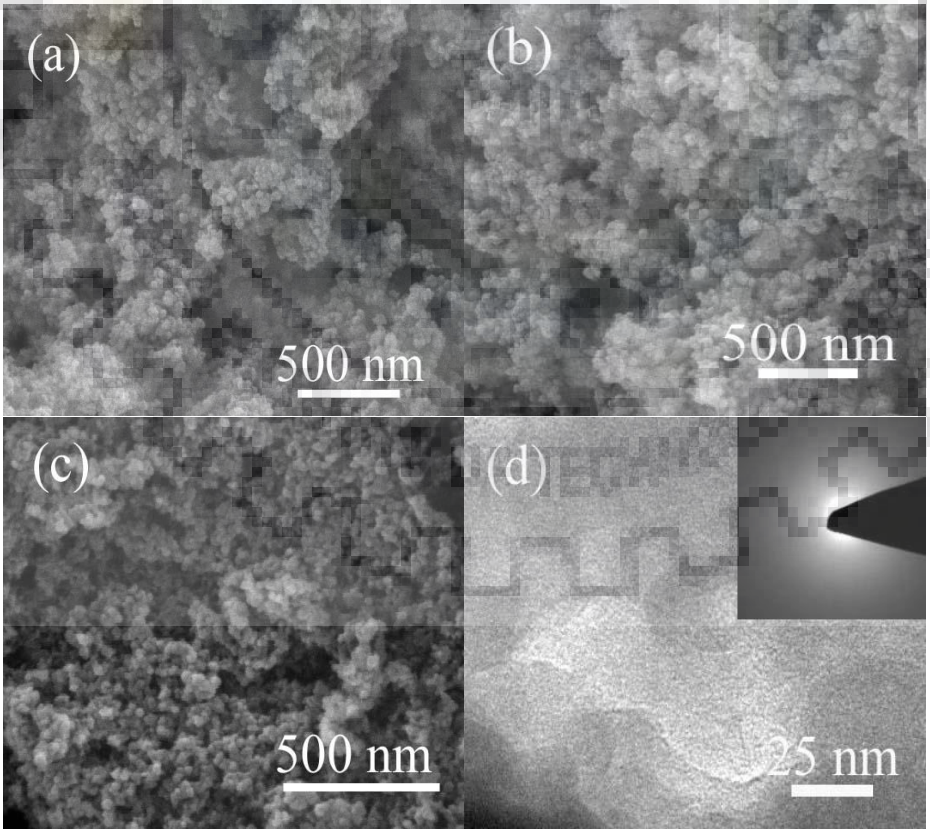

Figure 3.9: Microstructural analysis: FESEM images of (a) HNM-1P, (b) HNM-2P and (c) HNM-3P. (d) TEM images of HNM-1P and its SAED pattern is shown in inset.

3.2.3. Textural analysis of HNM-*x*P

The formation of the aminal linked frameworks as proposed in the ***Scheme 3.2*** and the observation of the nanoporous structure in the TEM images has encouraged us to study the textural properties of the synthesised specimens. The typical N_2 sorption isotherms measured at 77 K are given in ***Figure 3.10***. A type-I isotherm with steep N_2 uptake at low pressure (below P/P_o = 0.01) and significant multilayer adsorption in intermediate section with narrow hysteresis in the higher-pressure range could be seen. The hysteresis at higher pressure could be the combination of significant N_2 adsorption at the voids formed in the small particles of size in the 20-50 nm range and the adsorption at the external surface in the inter-particulate voids. The steep N_2 uptake at low pressure indicates the presence of ultra-micropores in the specimen with minor mesopores and macropores. The PSD estimated by DFT model given in ***Figure 3.11*** shows the average pore diameter of 0.65 nm and majority of the pores were <2 nm in diameters, with some distribution in the higher diameter range.

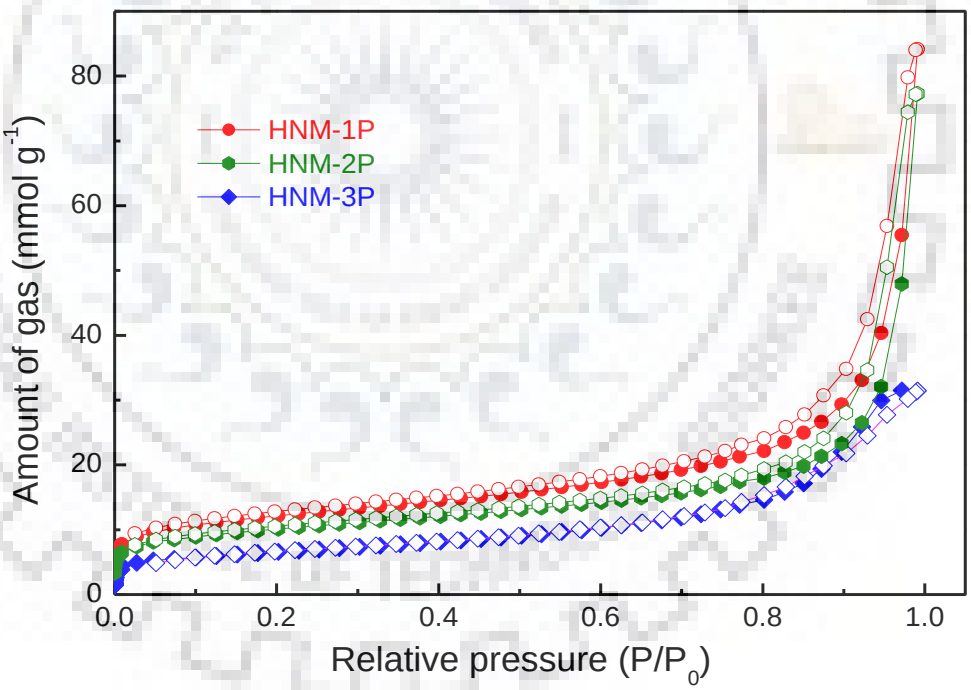

Figure 3.10: N_2 sorption isotherms of HNM-*x*P measured at 77 K.

The maximum specific surface area (SA_{BET}) calculated by using BET model for HNM-1P was found to be to 976 m^2 g^{-1}. This value is comparable with the cumulative surface area (967 m^2 g^{-1}) calculated by DFT & Monte-Carlo analysis. Pore volume calculated at relative pressure (P/P_0) 0.90 from the adsorption branch of the isotherm, was found to be 1.07 cm^3 g^{-1}. The high SA_{BET} and pore volume of HNM-1P could be

attributed to the unique peddle wheel structure of the cyclophosphazene moieties present in the framework, which has been reported earlier.[17-21] It was further observed that with the decrease in the reaction temperature, there was decrease in the SA_{BET} to 807 and 513 m^2 g^{-1}, in HNM-2P and HNM-3P, respectively. The pore size distribution calculated by DFT model for HNM-2P and HNM-3P has profile similar to HNM-1P, and it was found to be centred at about 0.64 nm for both the samples. The lower SA_{BET} in HNM-3P could be attributed to the weaker framework condensation at lower temperature. High temperature led to opening of micropore that led to increase in surface area of HNM-1P as compared to HNM-2P and HNM-3P. However, there was no substantial difference in the particle size and shape (***Figure 3.9)*** although, the experiments were carried out at three different temperatures. The detailed textural properties of HNM-*x*P are given in ***Table 3.4***.

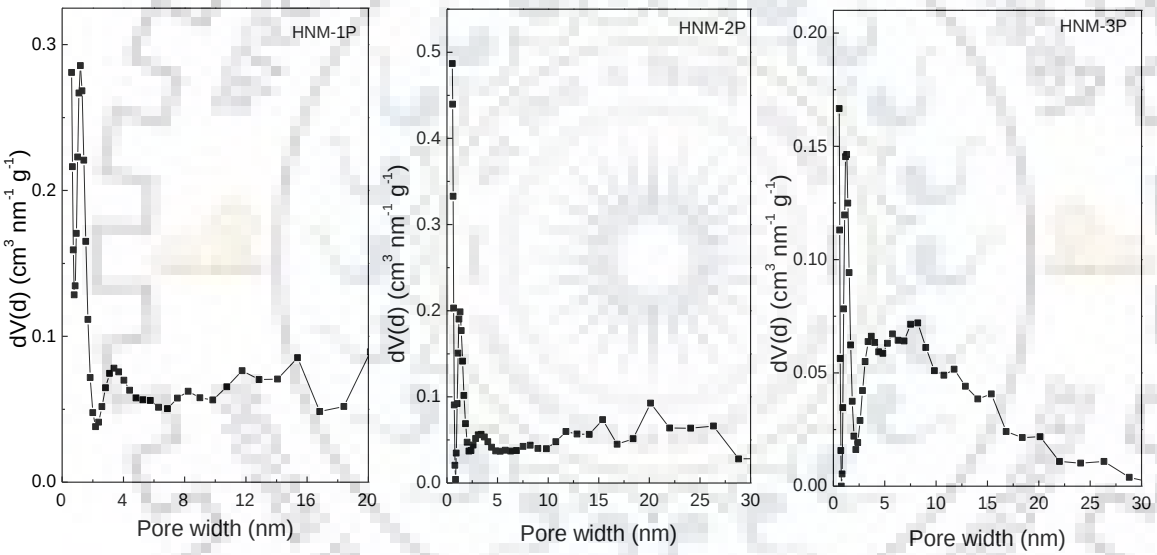

Figure 3.11: Pore size distribution of HNM-*x*P calculated from the N_2 sorption isotherm measured at 77 K using the DFT method.

Table 3.4: Summary of textural properties for HNM-*x*P.

Sample	SA_{BET} (m^2 g^{-1})	DFT and Monte-Carlo Cumulative		Pore size (nm)	Total pore volume (cm^3 g^{-1})
		Surface area (m^2 g^{-1})	Pore volume (cm^3 g^{-1})		
HNM-1P	976	967	2.11	0.65	1.07
HNM-2P	807	861	1.83	0.64	0.86
HNM-3P	513	517	1.03	0.64	0.67

3.2.4. Gas sorption studies of HNM-*x*P

The presence of the ultra-micropores with high SA_{BET} and pore volume coupled with the high nitrogen content (>42%) encouraged us to study the CO_2 sorption properties. ***Figure 3.12a*** and ***3.12b*** shows the CO_2 sorption isotherms of HNM-*x*P measured at 273 and 298 K. Almost complete reversibility was observed with minor hysteresis. The highest CO_2 uptake for HNM-1P was found to be 18.9 and 12.3 wt% at 273 and 298 K, respectively. The HNM-2P and HNM-3P also show noteworthy CO_2 uptake of 13.2 and 9.5 wt%, respectively at 273 K and 1 bar. It is, however, important to note that the high nitrogen content is not the only factor that can tune the CO_2 capture capacity. There could be multiple factors that affect the CO_2 capture capacity such as pore size, pore geometries, surface functionalities and kinetics.[20] The role of high nitrogen content is to enhance the Lewis basic nature of framework which helps in the adsorption of Lewis acidic gas like CO_2. The higher CO_2 uptake of HNM-1P in comparison to HNM-2P and HNM-3P could be due to higher surface area and pore volume. The isosteric heat of adsorption (Q_{st}) of HNM-*x*P was further calculated using Clausius-Clapeyron equation (***Figure 3.12c***). At the onset, the Q_{st} values are 34.7, 35.9 and 32.8 kJ mol^{-1} for HNM-1P, HNM-2P and HNM-3P, respectively. The estimated Q_{st} values below 50 kJ mol^{-1} (for chemisorption) and much above 5 to 10 kJ mol^{-1} (for physisorption) indicate that the interaction between the adsorbent and adsorbate is neither purely physisorption nor purely chemisorption in nature and is at the cusp of these two.[20]

Furthermore, HNM-*x*P were tested for the H_2 and CH_4 storage applications. The H_2 sorption isotherms as shown in ***Figure 3.12d*** were completely reversible without hysteresis and the uptake at maximum pressure range for the HNM-1P was 1.65 wt% at 77 K and 1 bar. It is further worth mentioning that the sorption isotherm was not saturated in the measured pressure range indicating a higher uptake could be achieved at higher pressure.[30] The HNM-2P and HNM-3P also show noteworthy H_2 uptake of 1.35 and 0.92 wt%, respectively at 77 K and 1 bar. The CH_4 uptake for HNM-1P, HNM-2P and HNM-3P was found to be 1.79, 1.48 and 1.10, respectively at 273 and 1 bar. To understand the feasible application of the synthesized materials for the purpose of post combustion CO_2 capture in coal fired power plants, the selective uptake of CO_2 over CH_4 and N_2 is one of the main criteria. The selectivity of CO_2 with respect to CH_4 and N_2 was estimated by using the Henry's law constant.[20] The selectivity of CO_2 over N_2 and CO_2 over CH_4 for HNM-1P were found to be 62 and 14, respectively, at 273 K.

(***Figure 3.13***). The moderate selectivity shown by HNM-*x*P despite having very high nitrogen content could be attributed to the fact that CO_2 might not be interacting with all the nitrogen of the framework and it is interacting with only nitrogen present on the surface. The detailed gas sorption properties are given in ***Table 3.5***.

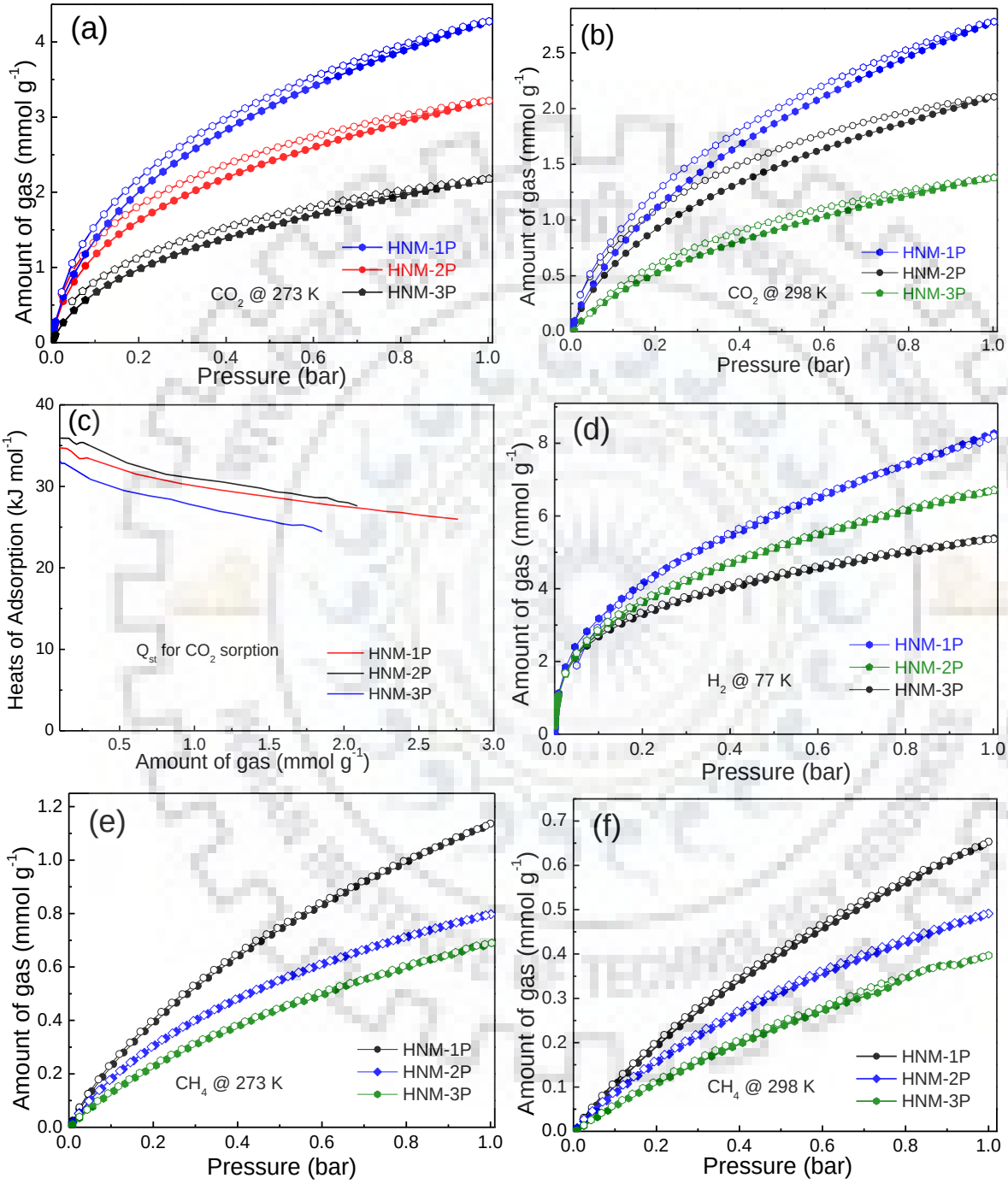

Figure 3.12: Gas sorption isotherms; (a) and (b) are CO_2 sorption isotherms measured at 273 and 298 K, respectively. (c) isosteric heat of adsorption (Q_{st}) for CO_2 sorption. (d) H_2 sorption isotherms measured at 77 K. (e) and (f) CH_4 sorption isotherms measured at 273 and (b) 298 K, respectively.

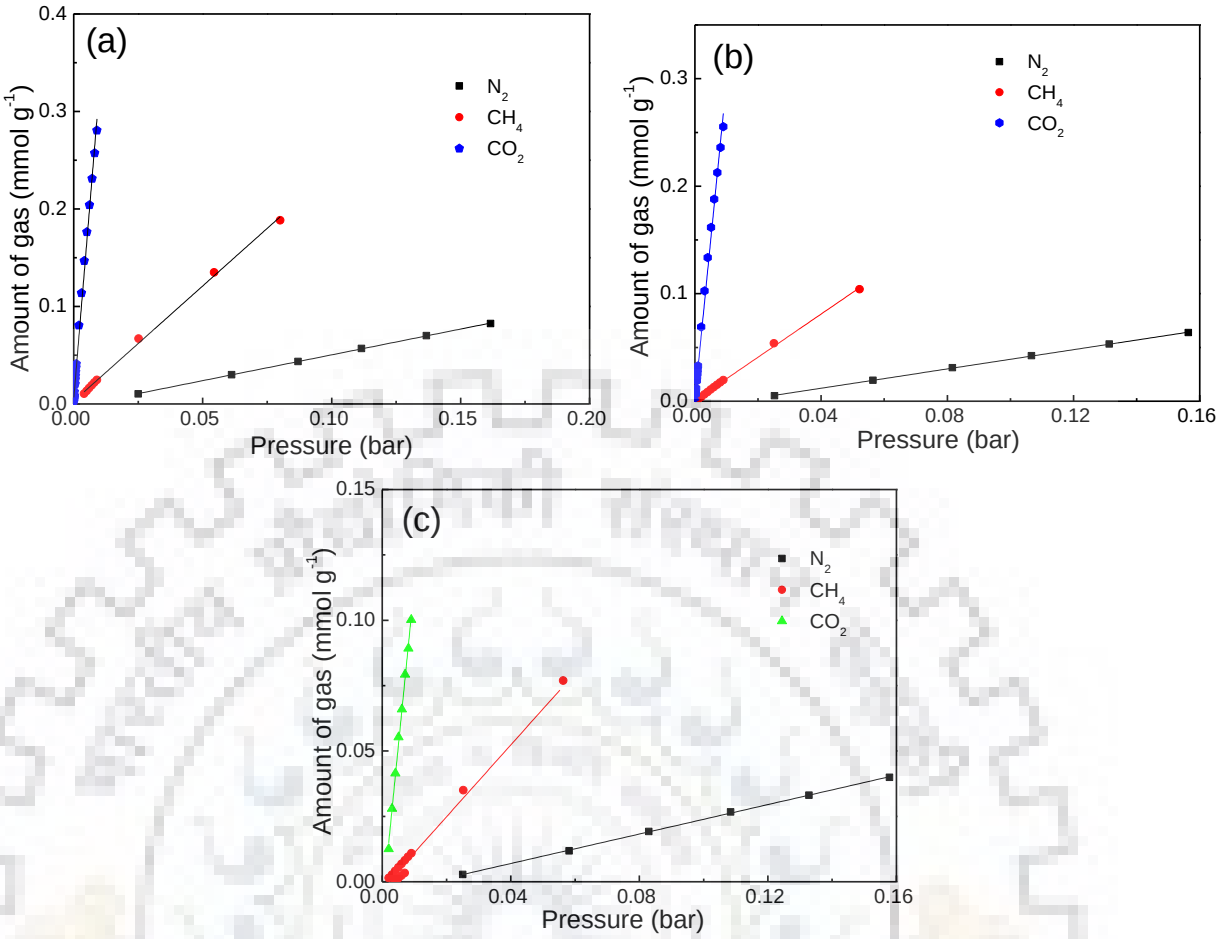

Figure 3.13: Gas selectivity; CO_2 vs N_2 and CO_2 vs CH_4 selective uptake for (a) HNM-1P, (b) HNM-2P and (c) HNM-3P, respectively, calculated by initial slope method at 273 K.

Table 3.5: Summary of gas adsorption properties of HNM-*x*P at low pressure.

Sample ID	CO_2 uptake (wt%)		CH_4 uptake (wt%)		Q_{st} (kJ mol^{-1})		Gas selectivity (273 K)		H_2 uptake wt%
	273 K	298 K	273 K	298 K	CO_2	CH_4	CO_2 vs N_2	CO_2 vs CH_4	77 K
HNM-1P	18.9	12.3	1.79	0.88	34.7	25.7	62	14	1.65
HNM-2P	13.2	8.16	1.48	0.79	35.9	23.0	67	17	1.35
HNM-3P	9.5	6.08	1.10	0.63	32.8	25.2	44	9	0.92

3.3. AMINAL LINKED HYBRID NANOPOROUS MATERIALS SYNTHESIZED USING *COMPOUND-M* (HNM-*x*M, *x* = 1, 2 & 3)

3.3.1. Synthesis and characterization of *compound-M*

As discussed above, the synthesis of HNM-*x*P by the condensation of *compound-P* with melamine resulted in the formation of high surface area nanoporous materials with hierarchical pore structure followed by their application in gas sorption and storage has encouraged us to investigate if a structural change in the precursor could yield any substantial change in the overall properties and applications of the resulting materials. For this purpose, MHB (instead of PHB) was condensed with PNC to produce the precursor, *compound-M*, in presence of K_2CO_3 as shown in ***Scheme 3.3***.

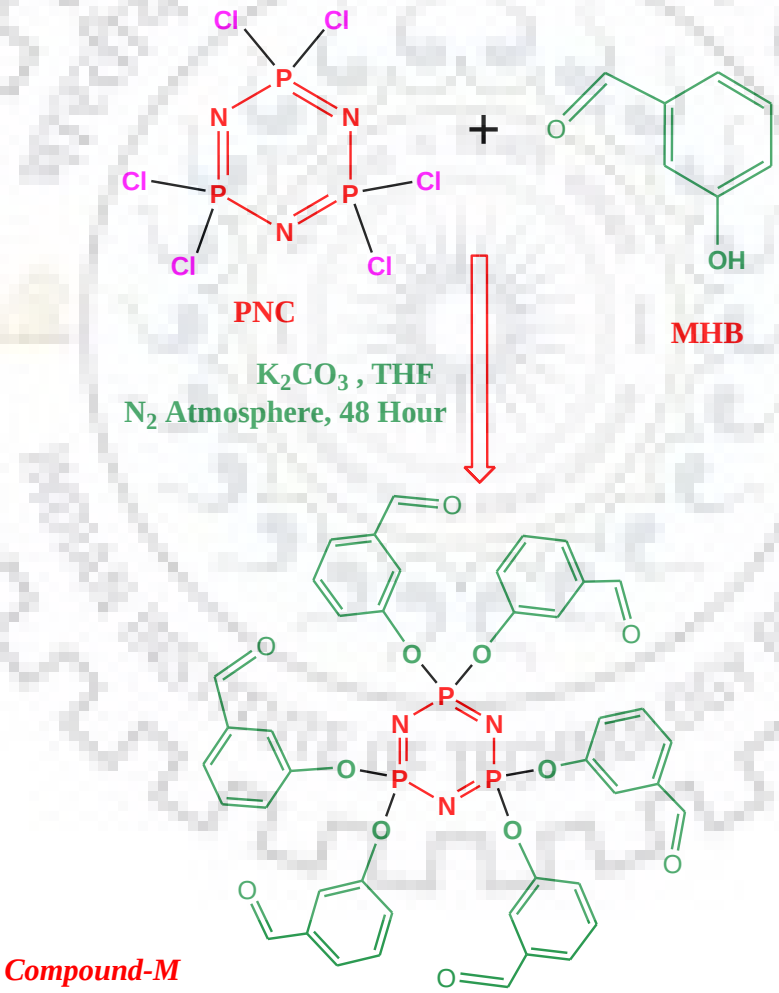

Scheme 3.3: Reaction scheme for the synthesis of *compound-M* via condensation of MHB with PNC in presence of proton abstractor (K_2CO_3).

The structure of *compound-M* was confirmed using ^{1}H, ^{13}C and ^{31}P NMR, and FTIR spectroscopic investigation similar to the characterization of the *compound-P*. The major

difference between the MHB and PHB lies in the position of the hydroxyl and aldehyde functionality in the aromatic ring. Unlike PHB, where there is symmetry in the structure after its condensation with PNC (***Scheme 3.1***), the MHB has an unsymmetrical structure (***Scheme 3.3***). This asymmetry in the structure can be reflected in the spectroscopic investigations of *compound-M*. For example, the ^{1}H NMR spectrum in ***Figure 3.14a*** has four signals at 7.6(*d*), 7.5(*s*), 7.35(*t*) and 7.25(*d*) as compared to only two ^{1}H NMR signals at 7.8(*d*) and 7.2(*d*) ppm in *compound-P* (***Figure 3.1a***). Similarly, the ^{13}C NMR spectrum of *compound-M* has six resonance signals at δ of 151, 138, 130, 127, 126.5 and 121 ppm originated from six different aromatic carbons (***Figure 3.14b***) as compared to only four signals at 155, 134, 132 and 122 ppm in *compound-P* (***Figure 3.1b***). However, only ^{31}P NMR signal is observed both for *compound-P* and *compound-M* at as shown in ***Figure 3.1c*** and ***Figure 3.14c***, respectively. The assignment of individual signals is given in the insets of the respective figures. The detailed comparison of the NMR spectral data of *compound-P* and *compound-M* is summarized in ***Table 3.6***.

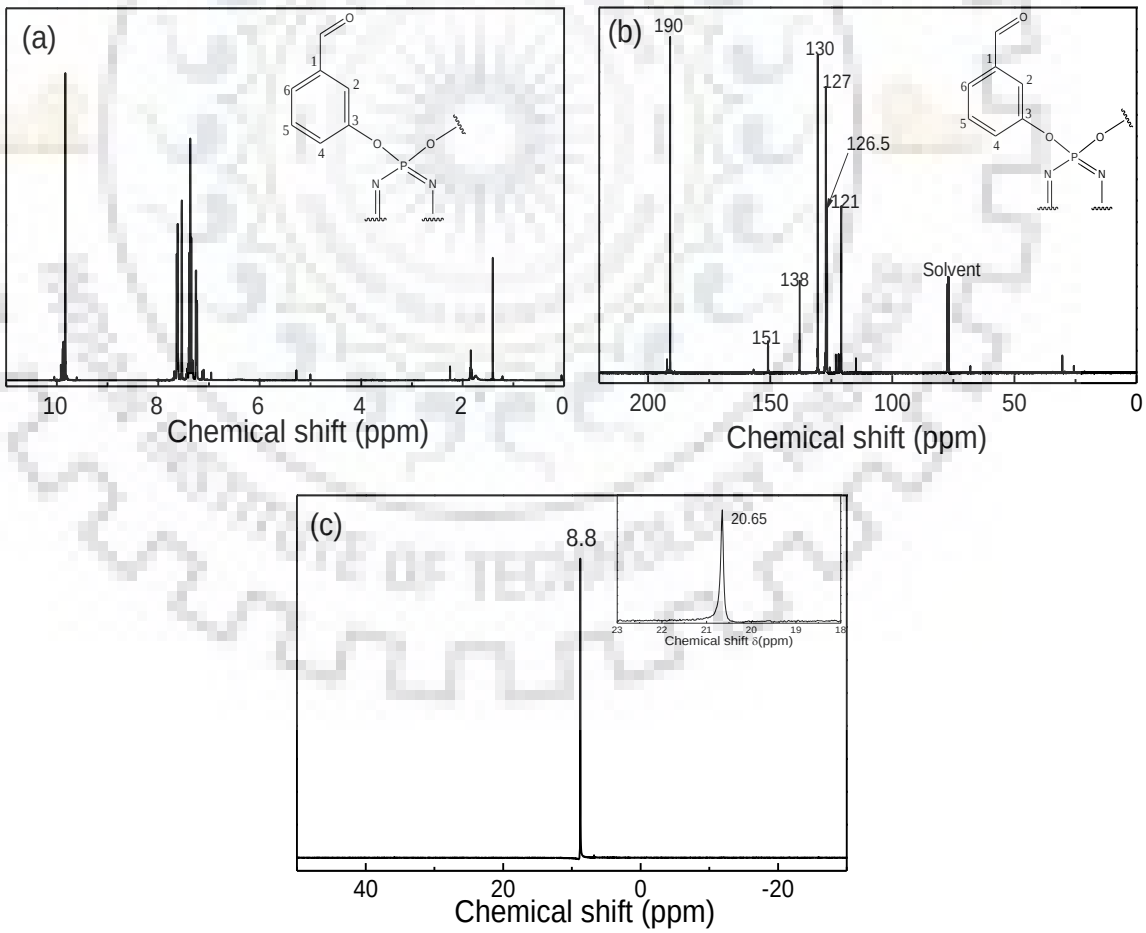

Figure 3.14: (a) ^{1}H NMR, (b) ^{13}C NMR and (c) ^{31}P NMR spectra of *compound-M* analyzed in $CDCl_3$ at 298 K. The ^{31}P NMR spectrum of PNC is given in the inset of (c).

Table 3.6: Comparison of the NMR spectral data of *compound-P* and *compound-M*.

Spectral analysis	***Compound-P***	***Compound-M***
	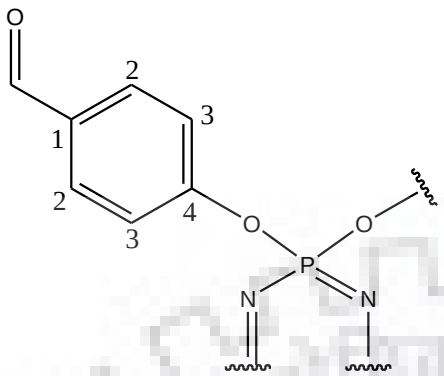	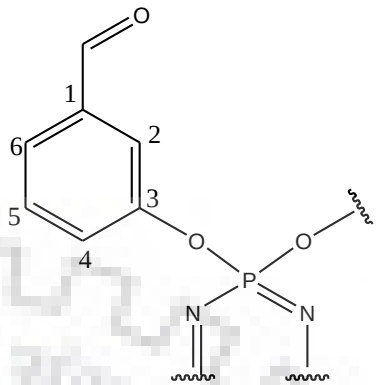
^{1}H NMR	Aldehydic proton; 9.95(*s*) ppm	Aldehydic proton; 9.83(*s*) ppm
	C2 proton; 7.8(*d*) ppm	C2 proton; 7.5(*s*) ppm
	C3 proton; 7.2(*d*) ppm	C4 proton; 7.25 (*d*) ppm
	-	C5 proton; 7.35(*t*) ppm
	-	C6 proton; 7.6(*d*) ppm
^{13}C NMR	aldehydic carbon; 190 ppm	aldehydic carbon; 190 ppm
	C1 carbon; 134 ppm	C1 carbon; 138 ppm
	C2 carbon; 132 ppm	C2 carbon; 127 ppm
	C3 carbon; 122 ppm	C3 carbon; 151 ppm
	C4 carbon; 155 ppm	C4 carbon; 121 ppm
	-	C5 carbon; 126.5 ppm
	-	C6 carbon; 130 ppm
^{31}P NMR	7.1 ppm	8.8 ppm

The FTIR spectroscopic investigation of *compound-M* in ***Figure 3.15*** further corroborates the results obtained from the NMR investigation. An important observation is the aromatic ring bending vibration that can be noticed in the FTIR spectra due to difference in symmetry between the *compound-P* and *compound-M*. This band is observed at 680 cm^{-1} (in *compound-M* only) for the unsymmetrically substituted aromatic ring.[31] Another difference can be seen in the out of plane C–H bending vibration. For *compound-P* and *compound-M*, it is observed at 845 and 793 cm^{-1}, respectively. Most of the other bands are observed at similar wavenumbers with minor deviation. These are assigned to their respective functionalities. The detailed comparison of the FTIR bands of *compound-M* and *compound-P* is given in ***Table 3.7***. Moreover, the FTIR spectra and detailed bands assignment of *compound-M* along with the precursors used for the synthesis is given in ***Figure 3.16*** and ***Table 3.8***.

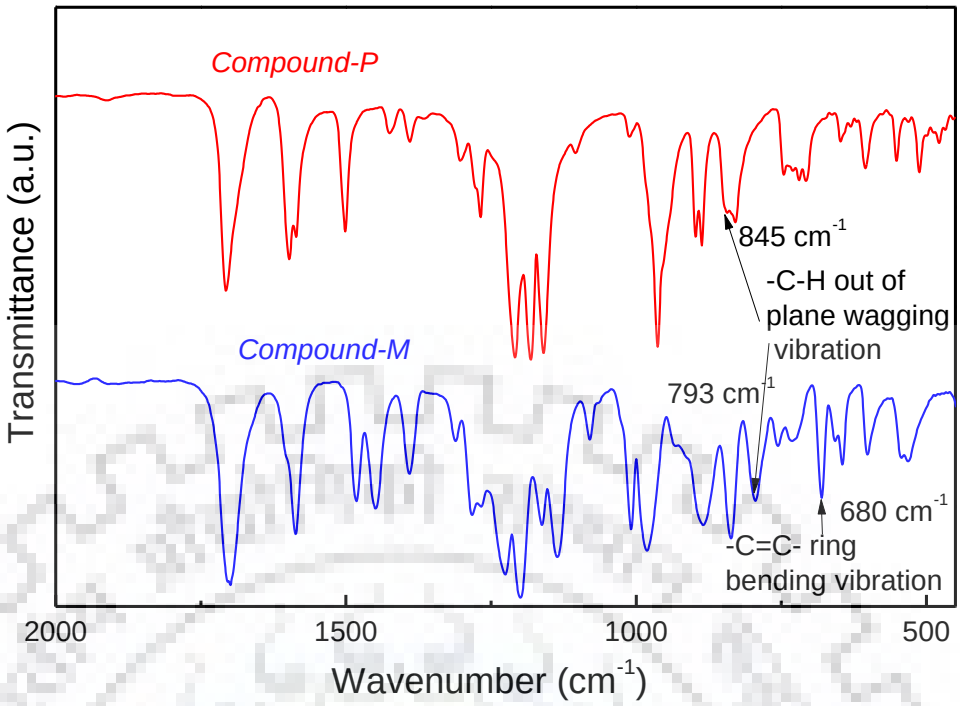

Figure 3.15: FTIR spectra of *compound-P* and *compound-M* analyzed using KBr film.

Table 3.7: FTIR bands comparison for *compound-P* and *compound-M*.

Bands assignment	**Bands (cm^{-1})**	
	Compound-P	*Compound-M*
Aldehydic C-H stretching	2840	2840
–CHO stretching band	1705	1700
C=C aromatic ring stretching	1600	1585
Aromatic C-H bending	1503	1480
Aliphatic –C–H bending	1425	1450
–C–H rocking	1390	1390
(C-H) in plane bending vibration	1270	1285
ν_{as}(P=N–P)	1210	1210
ν_{as}(P=N–P)	1190	1160
ν_{as}(P=N–P)	1160	1130
Aromatic in plane C–H bending	1010	1010
ν_{as}(P–O–C) vibration	960	980
–C–H out of plane wagging	845	793
C=C aromatic ring bending	-	680
δ(P=N–P) vibration	510	525

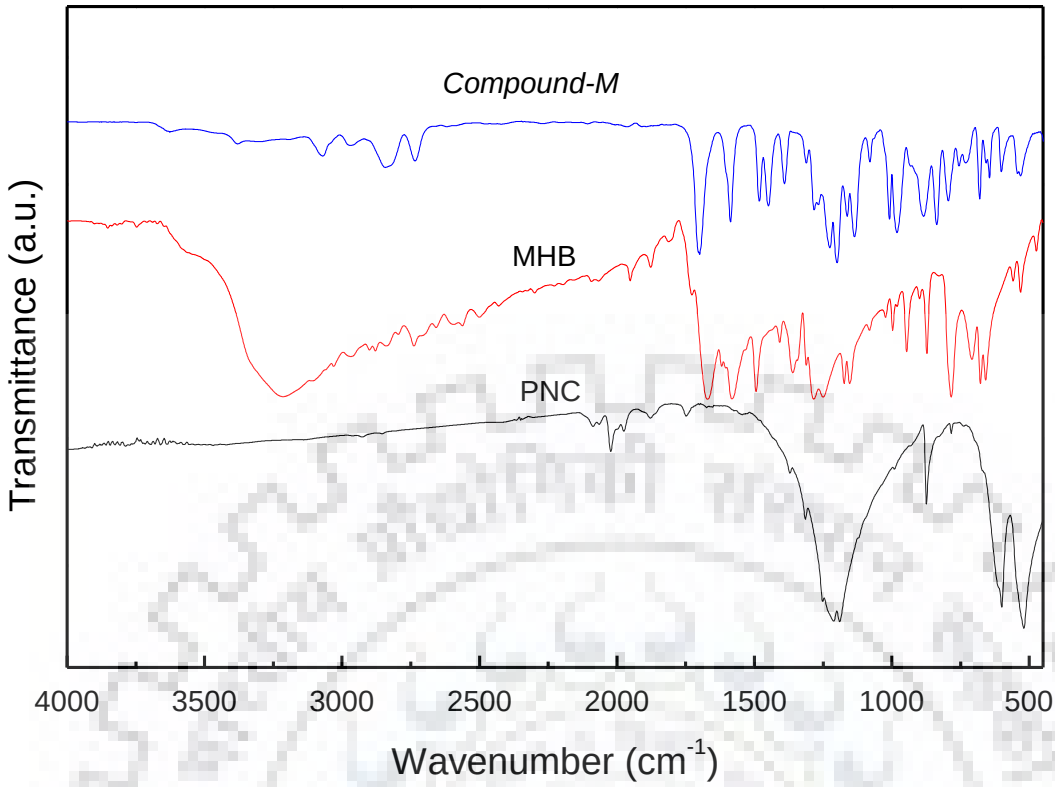

Figure 3.16: FTIR spectra of *compound-M*, PNC and MHB analyzed using KBr film.

Table 3.8: FTIR bands assignments for *compound-M*, PNC and MHB.

Bands assignment	**Bands (cm^{-1})**		
	PNC	MHB	*Compound-M*
–O–H stretching	-	3210	-
Aldehydic C–H stretching	-	2840	2840
–CHO stretching band	-	1690	1700
C=C aromatic ring stretching	-	1580	1585
Aromatic C–H bending	-	1485	1480
(C-H) in plane bending vibration	-	1285	1285
ν_{as}(P=N–P)	1230	-	1210
ν_{as}(P=N–P)	1190	-	1160
ν_{as}(P=N–P)	1135	-	1130
ν_{as}(P–O–C) vibration	-	-	980
P–Cl	875	-	-
–C–H out of plane wagging	-	785	793
C=C aromatic ring bending	-	675	680
δ(P=N–P) vibration	520	-	525

3.3.2. Synthesis and characterization of HNM-*x*M

The condensation of *compound-M* with melamine, similar to the synthesis of HNM-*x*P, was utilized to produce HNM-*x*M as shown in ***Scheme 3.4***. The specimens designated as HNM-1M, HNM-2M and HNM-3M are made at the reaction temperatures of 453, 423 and 393 K, respectively, similar to the synthesis of different HNM-*x*P.

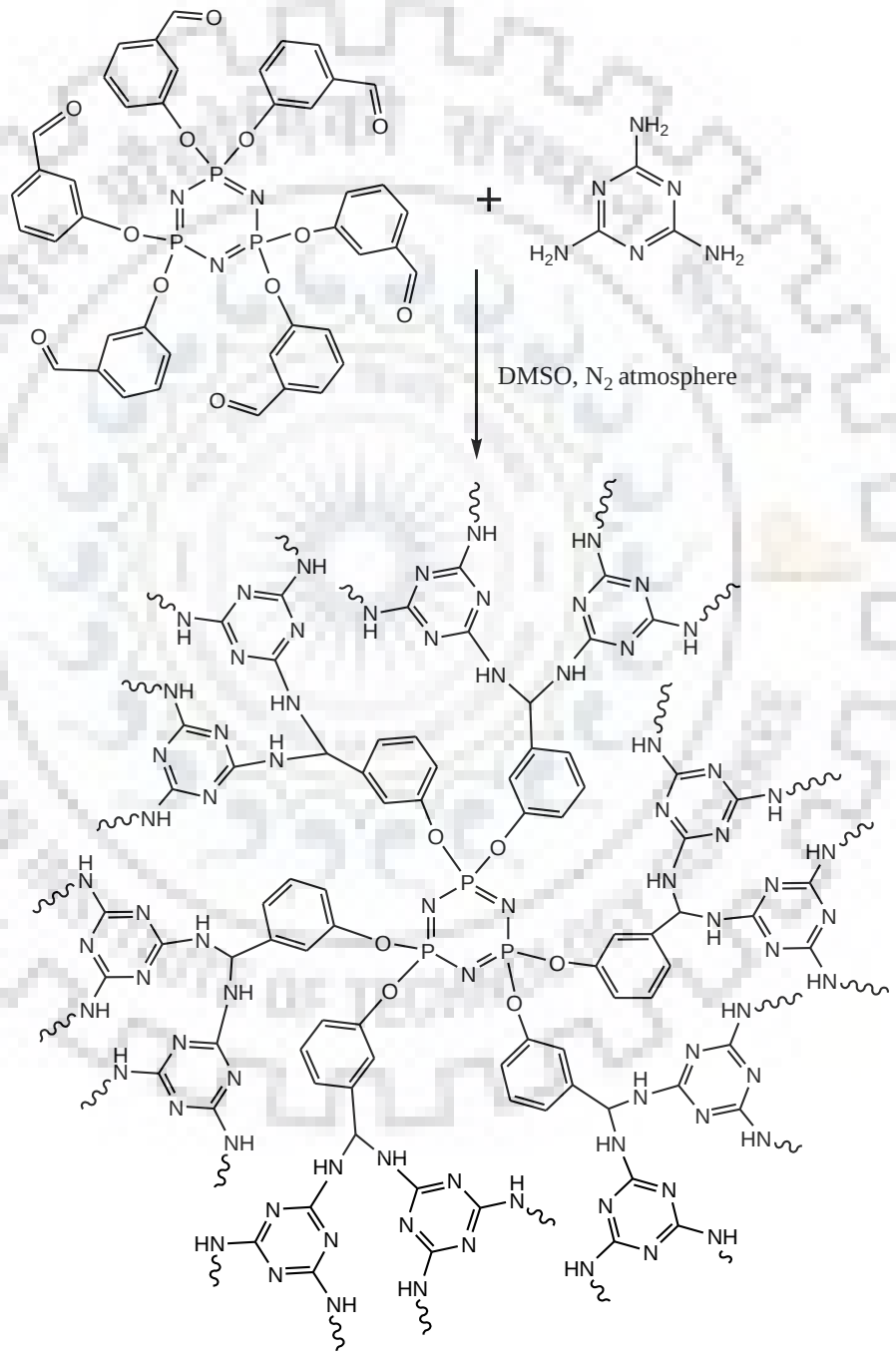

Scheme 3.4: Reaction scheme for the synthesis of HNM-*x*M, showing the condensation of *compound-M* with melamine in DMSO under N_2 atmosphere through Schiff base condensation.

The proposed structure of HNM-*x*M, shown in ***Scheme 3.4***, was confirmed by FTIR and ^{31}P, ^{13}C CPMAS NMR spectroscopies similar to HNM-*x*P. The typical FTIR spectra of HNM-*x*M are given in ***Figure 3.17***. The band observed at 2920 cm^{-1} attributed to the formation of aminal linkage confirms the condensation as proposed. The presence of bands at 3430 and 1635 cm^{-1} due to –N–H stretching and bending vibrations, respectively, and the bands at 1545 and 1470 cm^{-1} due to triazine semi-circle ring stretching and bending vibration confirm the inclusion of melamine moiety in HNM-*x*M.[10-12,16] The band at 1590 cm^{-1} is observed due to aromatic –C=C– ring stretching.[11,12]. The absence of a band around 1700 cm^{-1} due to the –CHO stretching vibration confirms the complete condensation of *compound-M* with melamine.[10-12] The bands in the range of 1200 to 1090, 985 and 536 cm^{-1} observed due to ν_{as}(P=N–P), ν_{as}(P–O–C) and δ(P=N–P) vibrations of the cyclophosphazene skeleton, respectively, confirm the inclusion of the cyclophosphazene moieties.[1,17-21] Further, the ^{13}C CPMAS NMR spectrum of a representative specimen, HNM-1M, is given in ***Figure 3.18a***. The resonance signals at 164.5, 149.7, 142.4, 136.7, 128.8, 119.7 and 52.7 ppm are assigned to carbon no. 1, 2, 3, 4, 5, 6, 7 and 8, respectively (inset of ***Figure 3.18a***).[1,10-12] The observation of signal at 52.7 ppm due to methine linkage further corroborates the aminal linkage. Moreover, the absence of any signal ~160 ppm excludes the possibilty of iminal linkage.[10,11]. The signal at 9.5 ppm in the ^{31}P CPMAS NMR spectrum shown in ***Figure 3.18b*** confirms the incorporation of cyclophosphazene moieties in the framework.[17-21]

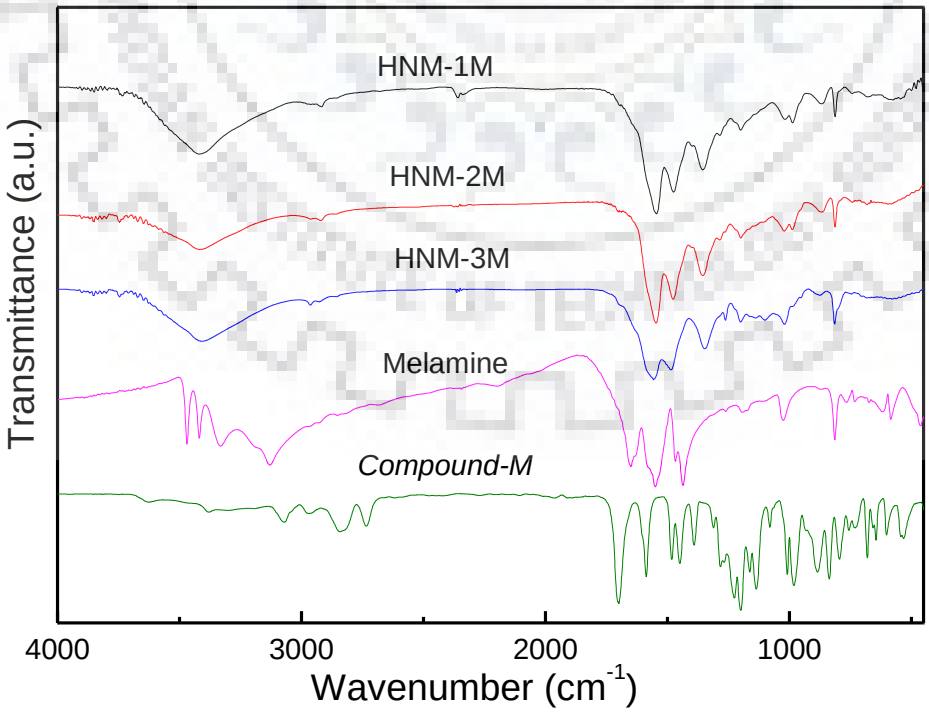

Figure 3.17: The FTIR spectra of *compound-M*, melamine and HNM-*x*M.

Table 3.9: FTIR bands assignment of HNM-*x*M synthesised by Schiff base condensation

Functionality	**Band position (cm^{-1})**
Aminal N–H stretching	3430
Aliphatic C–H stretching	2920
NH_2 deformation band	1635
C=C aromatic ring stretching	1590
Quadrant stretching of s-triazine ring	1545
Semicircle stretching of s-triazine ring	1470
Ring and side chain CN stretching	1350
ν_{as}(P=N–P)	1200-1090
ν_{as}(P–O–C) vibration	985
Ring breathing ring def (out of plane)	816
–C–H out of plane wagging	790
C=C aromatic ring bending	685
δ(P=N–P) vibration	536

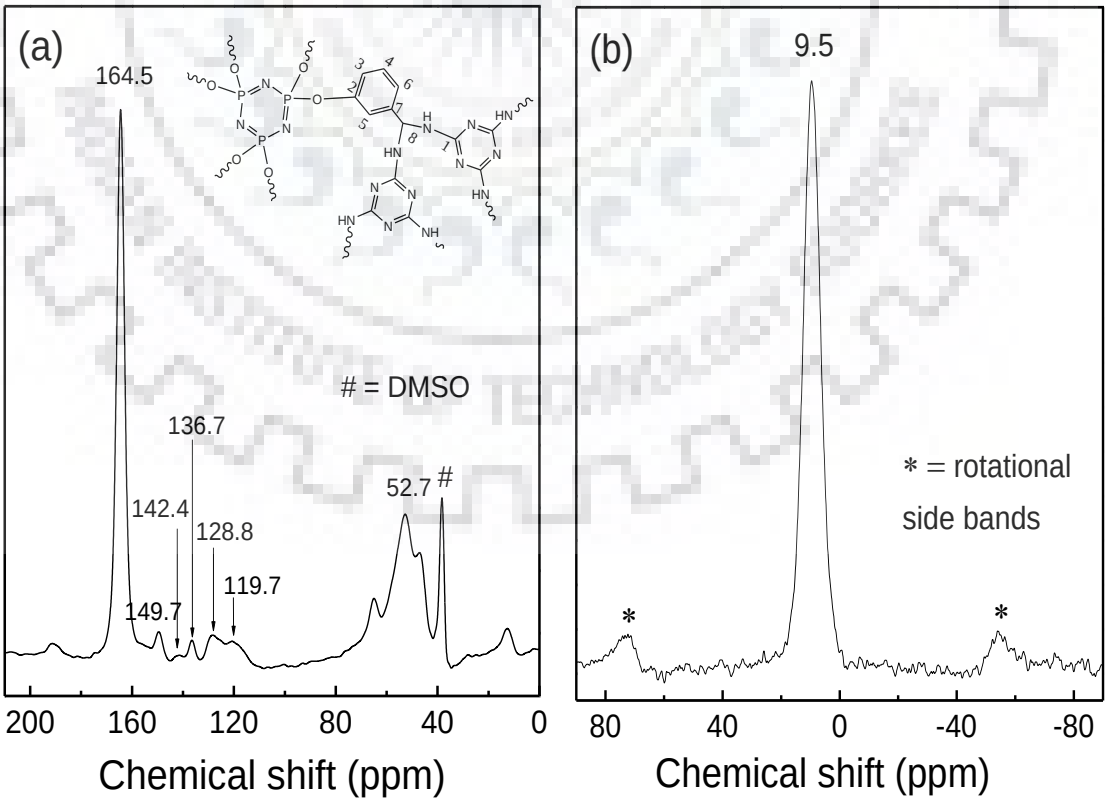

Figure 3.18: (a) ^{13}C and (b) ^{31}P CPMAS NMR spectra of HNM-1M.

Further, similar to HNM-*x*P, the electronic environment of HNM-*x*M was studied by the XPS. The survey scan given in ***Figure 3.19*** revealed the peaks for P, C, N, and O in HNM-1M. The high resolution C 1s XPS scan in ***Figure 3.20a***, displays three peaks at 284.8, 286 and 287.8 eV for aliphatic carbon, aromatic carbon and triazine carbon, respectively.[16,23-27] The P 2p high-resolution scan given in ***Figure 3.20b*** reveals the only peak at 133.4 eV associated to the P of cyclophosphazene moieties.[22,23] Similarly, two peaks in the high resolution N 1s scan shown in ***Figure 3.20c*** at 398.7 and 400.0 eV are ascribed to the nitrogen of cyclophosphazene and triazine moieties, respectively.[16,22,23,26] The high resolution O 1s scan, given in ***Figure 3.20d***, shows two peaks. The peak at 532.2 eV is observed due to O of -P-O-C linkage in HNM-1M, while the peak at 530.8 eV could be ascribed to O of carbon tape or O of trapped DMSO in the pores of framework.[24,28,29]

The formation of aminal linkage in the HNM-*x*M similar to HNM-*x*P was further confirmed by the elemental analysis as given in ***Table 3.10***. The observed elemental composition for HNM-*x*M is fairly matching with the theoretical composition and also excludes the possibility of imine formation as discussed above for the HNM-*x*P.

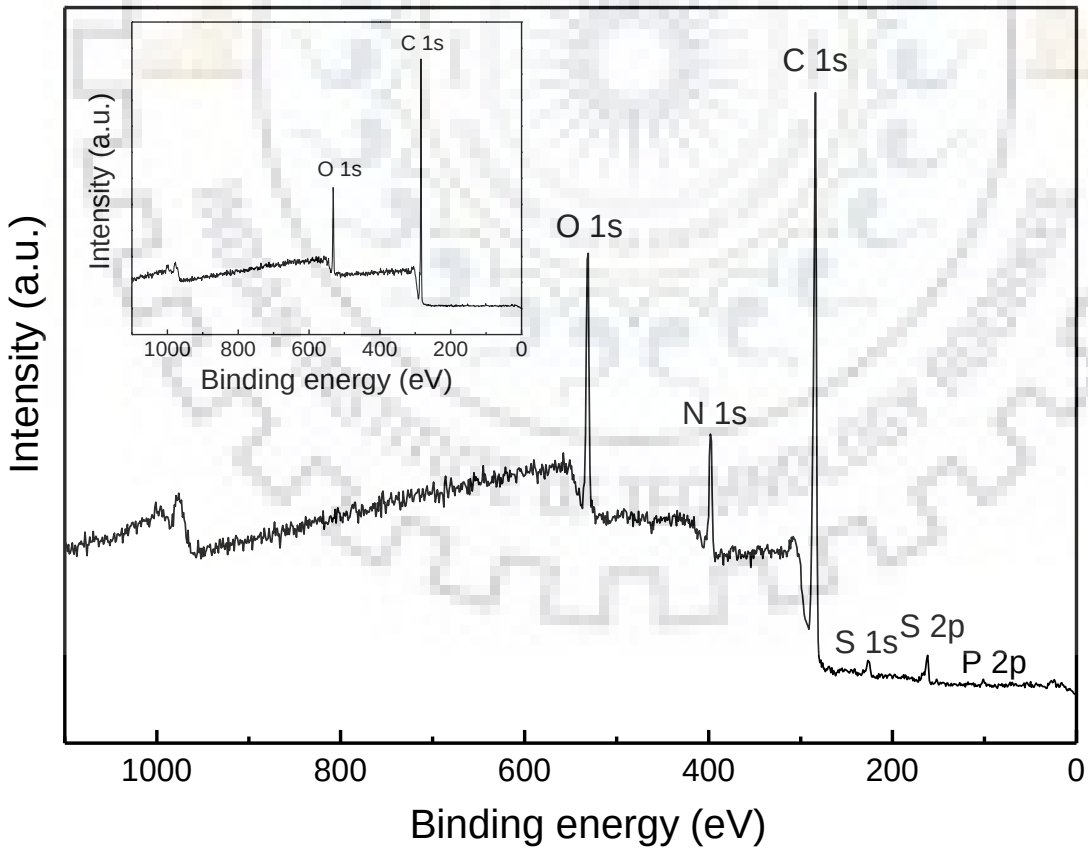

Figure 3.19: XPS survey scan for HNM-1M. The XPS survey scan of carbon tape (used in analysis) is shown in inset.

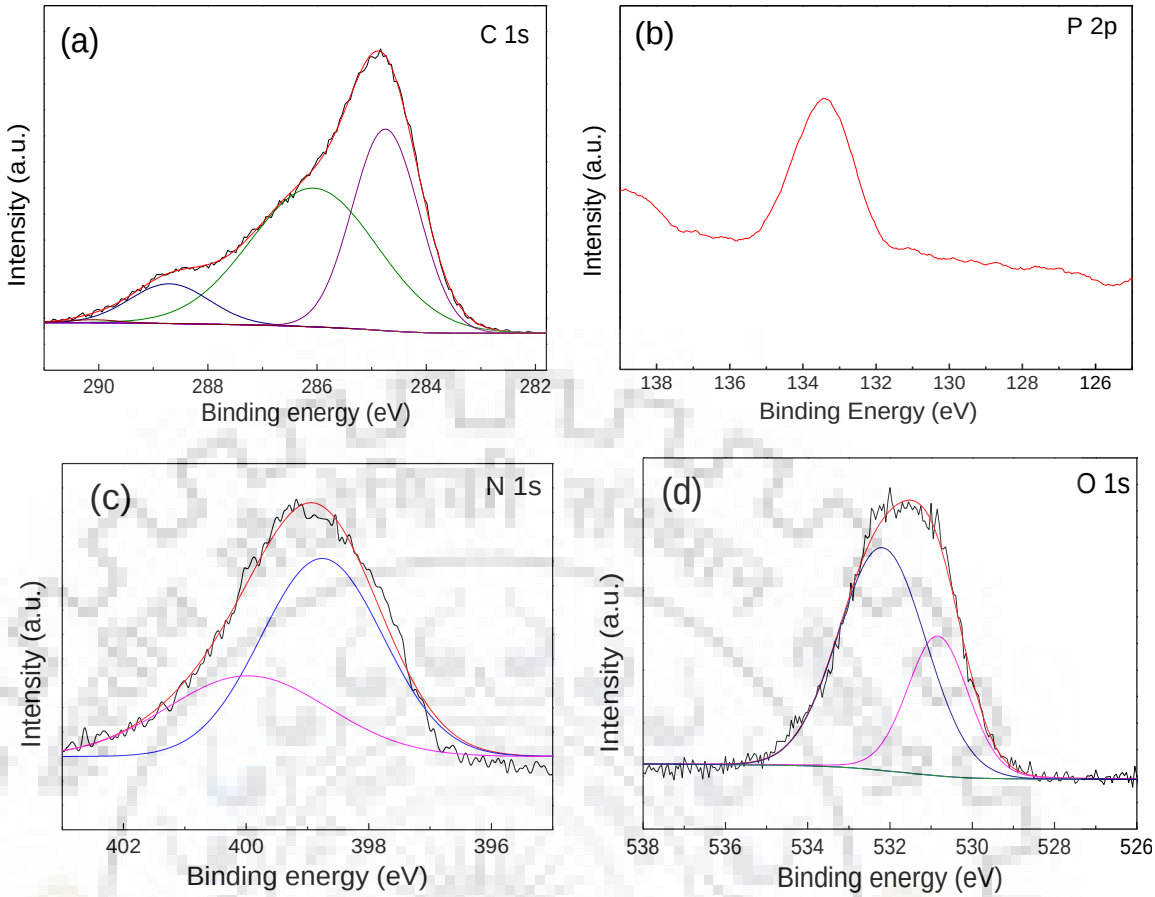

Figure 3.20: XPS high resolution scans; (a) C 1s, (b) P 2p, (c) N 1s and (d) O 1s high resolution XPS scans for HNM-1M.

Table 3.10: Elemental Analysis for HNM-*x*M (Theoretical Composition: $C_{78}H_{66}N_{75}O_3P_3$).

Specimens	Observed elemental compositions		
	N	C	H
Theoretical	46.84	41.77	2.97
HNM-1M	40.23	38.54	5.13
HNM-2M	39.21	38.18	5.72
HNM-3M	37.15	32.52	5.89

The TGA/DTG isotherms for HNM-*x*M given in ***Figure 3.21*** have shown that these specimens are thermally stable up to a temperature of 600 K in air. The mass loss pattern is similar to HNM-*x*P as shown in ***Figure 3.7***. The thermal stability of HNM-*x*M is very much similar to HNM-*x*P. As expected, the XRD patterns of HNM-*x*M shown in ***Figure 3.22*** are similar to HNM-*x*P and confirm the amorphous nature of these specimens. The microstructural analysis given in ***Figure 3.23*** reveals the small particle of 40 to 100 nm size range forming an interconnected network structure similar to the

HNM-*x*P. The TEM images given in ***Figure 3.23d*** shows that the HNM-1M contains the pores in nanoporous regime. The observation of broad diffused ring in SAED pattern (inset of ***Figure 3.23d***) indicates the amorphous nature of the specimen and support the observation of XRD.

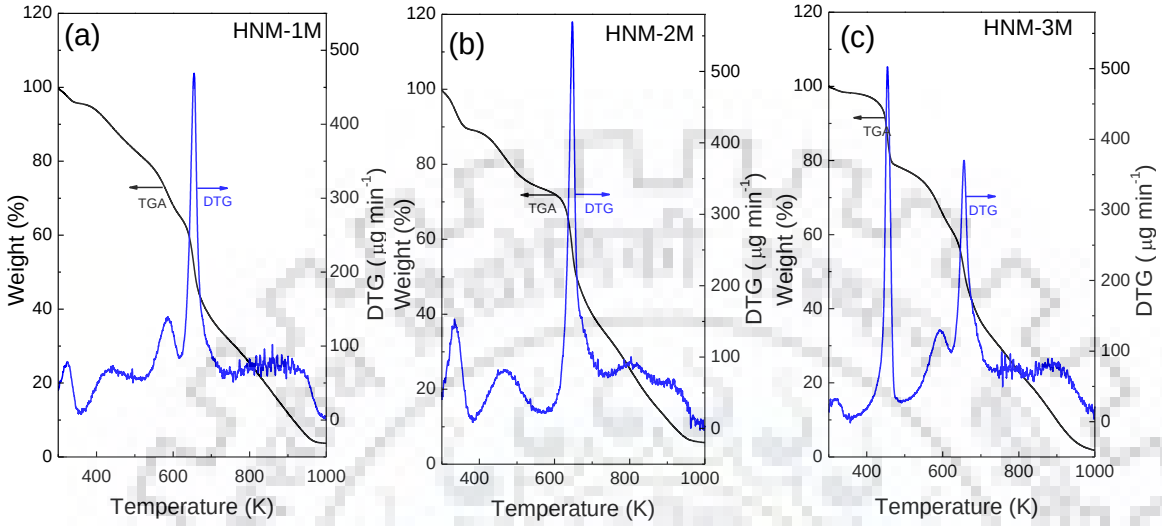

Figure 3.21: TGA and DTG thermograms of HNM-*x*M recorded in air with heating rate of 5 K min^{-1} using alumina sample holder.

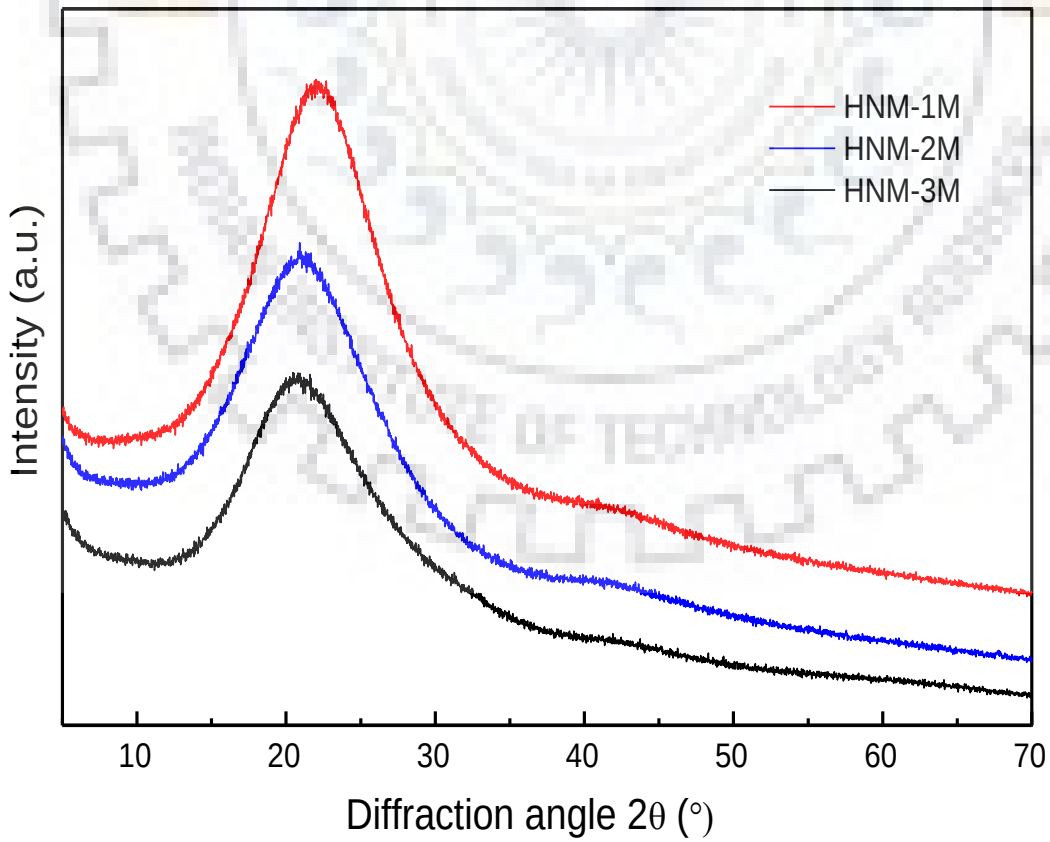

Figure 3.22: X-ray diffraction patterns of HNM-*x*M.

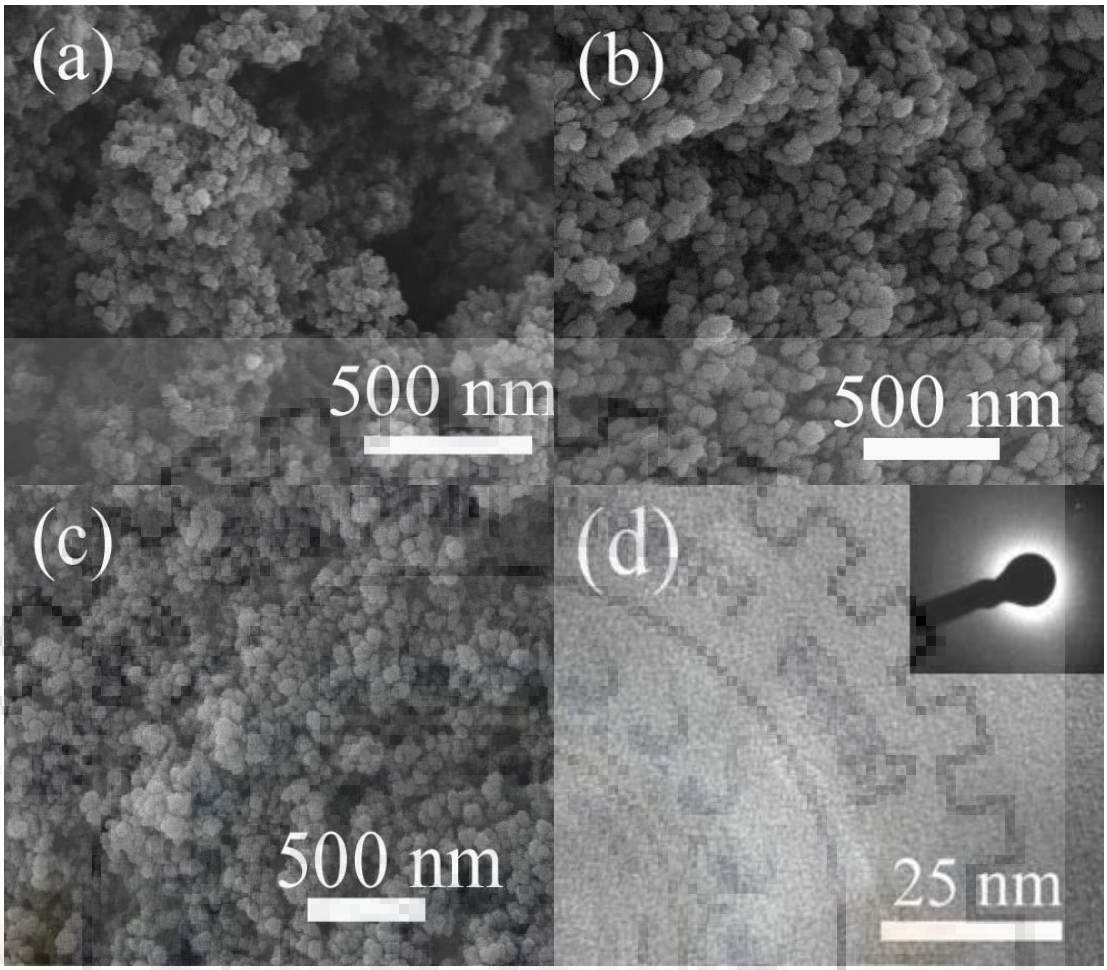

Figure 3.23: FESEM images of (a) HNM-1M, (b) HNM-2M, and (c) HNM-3M, and TEM image of (d) HNM-1M. The SAED pattern of HNM-1M is shown in the inset of figure 3.23(d).

3.3.3. Textural analysis of HNM-*x*M

The textural analysis of HNM-*x*M was conducted by N_2 sorption analysis at 77 K as shown in ***Figure 3.24***. A type-I isotherm with multilayer adsorption in the pressure range of 0.1 to 0.8 and high uptake in pressure region of 0.99 was observed. The significant adsorption in intermediate range is due to adsorption on rough surface of the specimens while the sharp rise at higher pressure range is due to filling of inter-particulate voids.[32] The rise in N_2 uptake at pressure $<0.01(P/P_0)$ revealed the presence of micropores. This was further confirmed by PSD analysis as shown in ***Figure 3.25***. The majority of the pores are found to be centred at 1.15, 1.40 and 1.30 nm with some distribution in the higher diameter range for HNM-1M, HNM-2M and HNM-3M, respectively. The maximum SA_{BET} of 563 m^2 g^{-1} was estimated for the specimen HNM-1M using BET model while it was 429 and 397 m^2 g^{-1} for HNM-2M and HNM-3M, respectively. These values are comparable with the cumulative surface

area calculated by DFT & Monte-Carlo analysis, (***Table 3.11***). The total pore volume estimated at relative pressure (P/P_0) 0.90 from the adsorption branch of the N_2 sorption isotherms, was found to be 0.66, 0.62 and 0.57 cm^3 g^{-1} for HNM-1M, HNM-2M and HNM-3M, respectively.

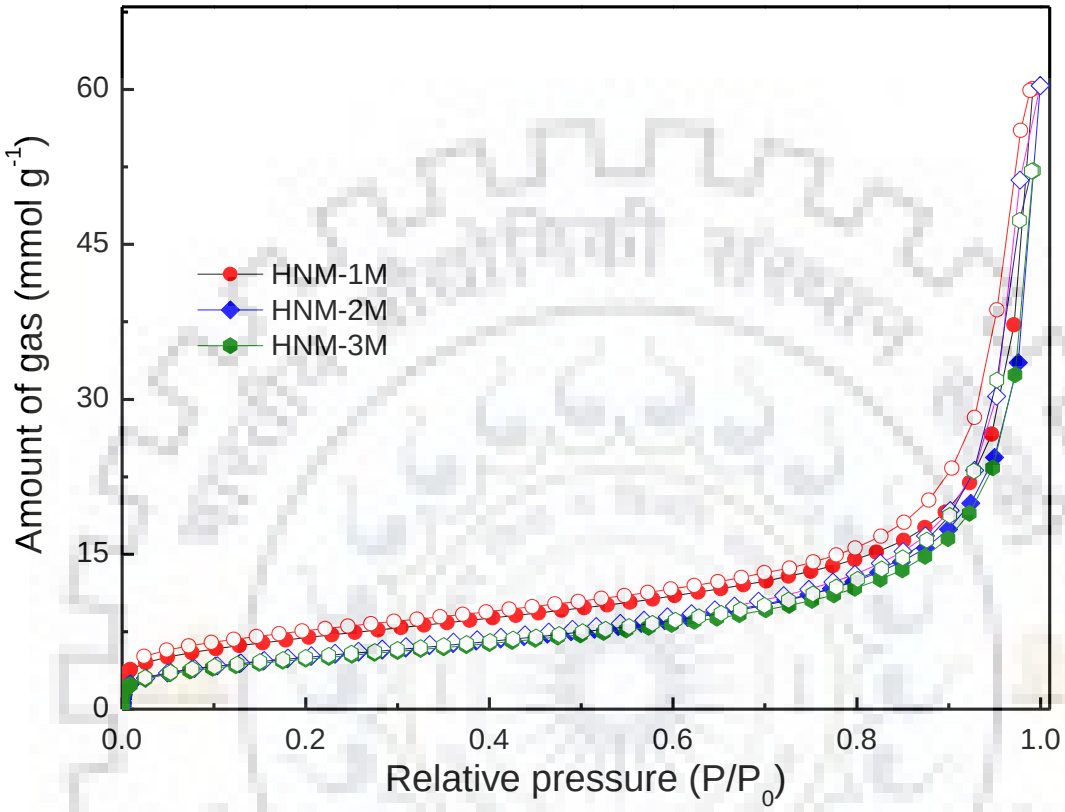

Figure 3.24: N_2 sorption isotherms for HNM-*x*M measured at 77 K.

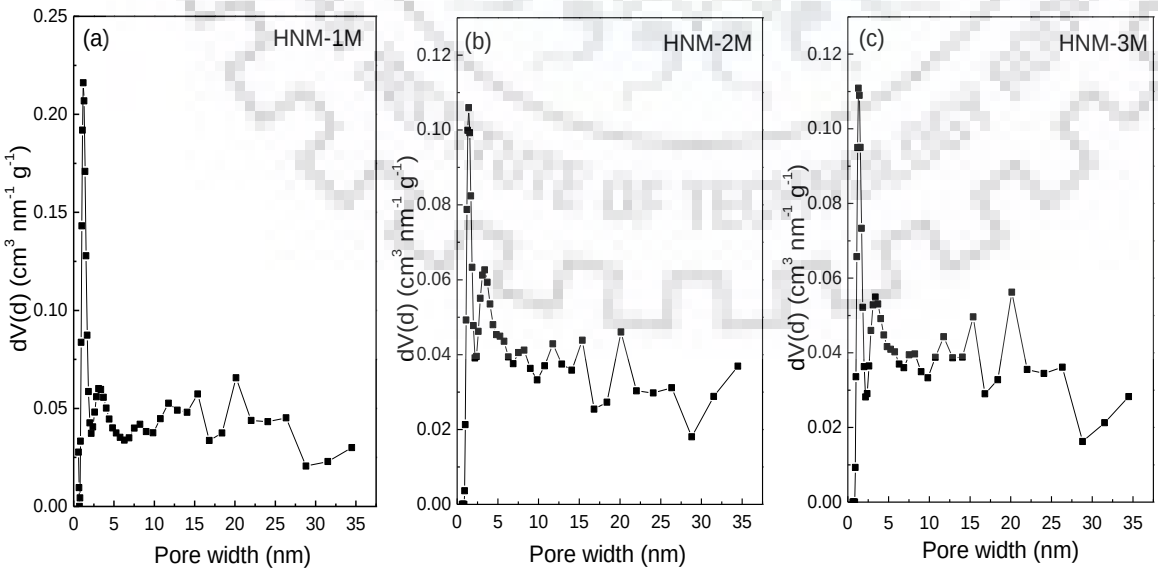

Figure 3.25: PSD of HNM-*x*M calculated from the N_2 sorption isotherm measured at 77 K using the DFT model.

The maximum estimated SA_{BET} of HNM-*x*M as compared to HNM-*x*P is low. This difference in SA_{BET} may be attributed to difference in symmetry in the structure of the precursors used for the synthesis of these materials. Due to absence of symmetry in *compound-M,* steric hindrance is created around the aldehyde functionality and this makes the aldehyde group less accessible for Schiff base condensation. This leads to comparatively sluggish condensation and resulting in lower SA_{BET} of HNM-*x*M.

Table 3.11: Summary of textural properties for HNM-*x*M.

Sample	**Surface Area from N_2 Sorption at 77 K (m^2 g^{-1})**	**DFT and Monte-Carlo Cumulative**		**Pore size (nm)**	**Total pore volume (cm^3 g^{-1})**
		Surface Area (m^2 g^{-1})	Pore volume (cm^3 g^{-1})		
	SA_{BET}	N_2 at 77K	N_2 at 77K		N_2 at 77K
HNM-1M	563	501	1.46	1.15	0.66
HNM-2M	429	336	1.25	1.40	0.62
HNM-3M	397	322	1.22	1.30	0.57

3.3.4. Gas sorption studies of HNM-1M

As the surface area have been the dominating factor towards the gas sorption capacity of HNMs, the specimen HNM-1M with the maximum estimated SA_{BET} among HNM-*x*M was subjected to CO_2, H_2 and CH_4 sorption analyses. The CO_2 sorption isotherms measured at 273 and 298 K at 1 bar are given in ***Figure 3.26a***. The HNM-1M has shown CO_2 uptakes of 9.9 and 5.9 wt% at 273 and 298 K, respectively. The Q_{st} estimated using Clausius-Clapeyron equation, as shown in ***Figure 3.26b*** was found to be 40.2 kJ mol^{-1}, on the onset. Further, the HNM-1M has also been tested for H_2 and CH_4 sorption application. The HNM-1M has demonstrated the H_2 uptake of 0.85 wt% at 77 K with complete reversibility as shown in ***Figure 3.26c***. The CH_4 uptakes shown in ***Figure 3.26d*** for HNM-1M were estimated to be 1.3 and 0.5 wt% at 273 and 298 K at 1 bar, respectively. Further, the selectivity of CO_2 with respect to CH_4 and N_2 was estimated by using the Henry's law constant.[20] The selectivity of CO_2 over N_2 and CO_2 over CH_4 for HNM-1M was found to be 17 and 8, respectively, at 273 K. (***Figure 3.26e***). The moderate selectivity shown by HNM-1M despite the large nitrogen content could be ascribed to lower surface area and only surface contribution towards gas sorption and pores are not accessible for gas sorption. As expected, the gas sorption

capacity of HNM-1M is inferior to the HNM-1P. Moreover, the adsorption capacities of HNMs are compared with some of the recent reports (please see ***Table 3.12*** and ***Table 3.13***).

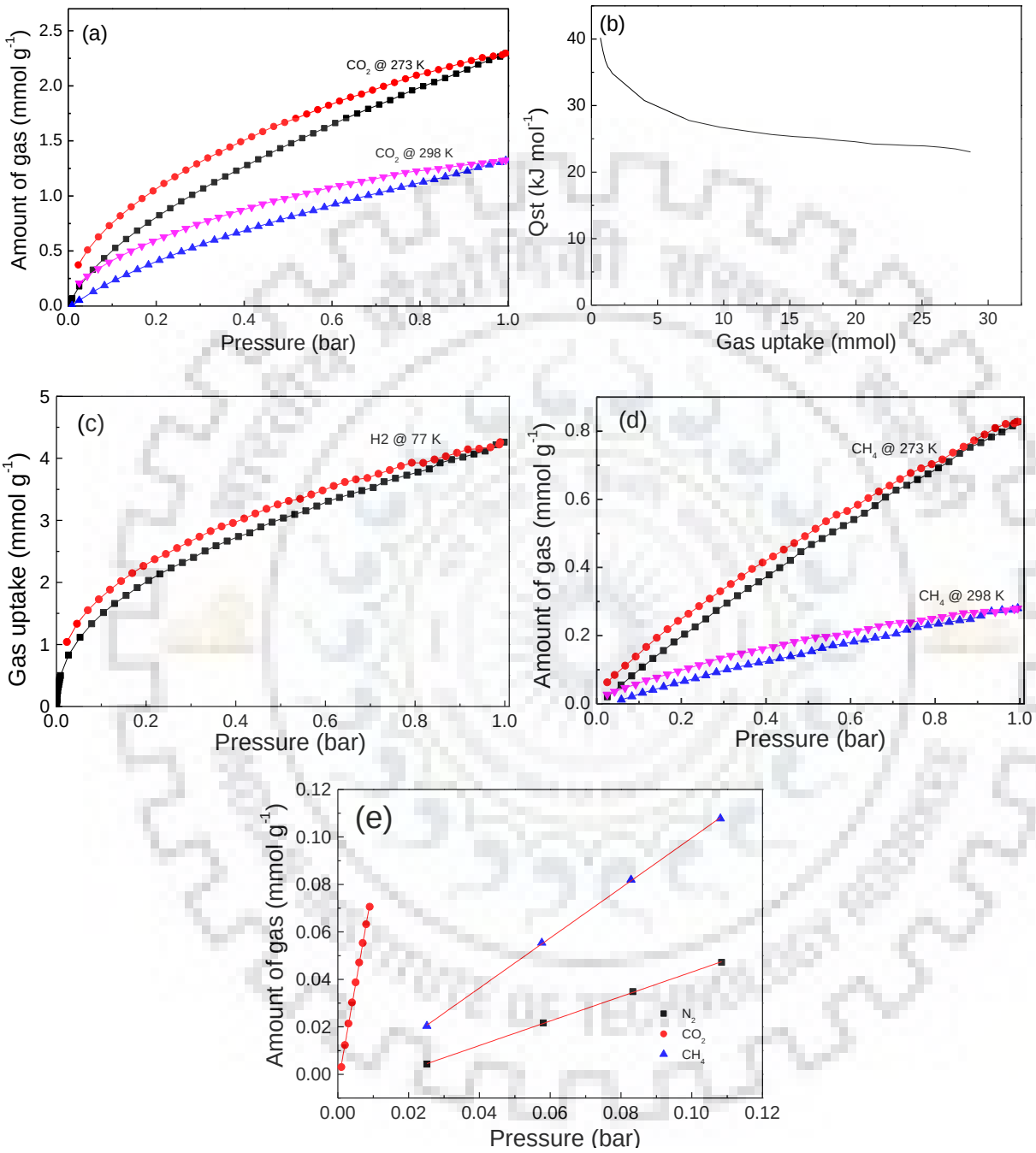

Figure 3.26: Gas sorption for HNM-1M; (a) CO_2 sorption isotherms measured at 273 and 298 K, (b) isosteric heat of adsorption (Q_{st}) for CO_2 sorption, (c) H_2 uptake at 77 K, (d) CH_4 sorption isotherms measured at 273 and 298 K, and (e) CO_2 vs N_2 and CO_2 vs CH_4 selective uptake for HNM-1M at 273 K, calculated by initial slope method (Henry's law constant).

Table 3.12: CO_2 sorption properties of selected adsorbents materials at low pressure.

Sample ID	SA_{BET} (m^2 g^{-1})	CO_2 uptake @273 K (wt%)	Selectivity @273 K CO_2 *vs* N_2	Reference
PAN-1	925	14.8	61	32
TBILP-1	330	11.7	63	33
TBILP-2	1080	22.8	40	33
APOP-3	1402	19.9	27.5	11
PHM	453	8.05	-	17
PAF-3	2932	15.3	87	34
BLP-1(H)	1360	7.4	-	35
BLP-(12)H	2244	12.8	-	35
PECONF-3	851	15.35	77	20
BILP-4	1135	23.5	79	36
fl-CTF350	1235	18.8	27	37
C-NP	946	13.6	29	38
MPC-700	1643	21.5	52	39
ALP-1	1235	23.6	35	40
HCMP-1	308	7.5	-	41
CZ@PON	592	18.96	42	42
IBFNP-1	1040	23.2	33.8	43

Table 3.13: Summary of H_2 storage properties of porous adsorbents at low pressure.

Sample ID	SA_{BET} (m^2 g^{-1})	H_2 uptake @ 77 K (wt%)	Reference
PAF-3	2932	2.07	34
PPF-4	726	1.47	13
BILP-4	1135	2.3	36
ALP-1	1235	2.19	40
ALP-2	1065	1.74	40
PAF-47	956	1.13	44

3.4. SUMMARY

In summary, Schiff base condensation has been employed for the first time to synthesize inorganic-organic hybrid nanoporous materials. Two types of precursors one with symmetrical geometry (*compound-P*) and other with asymmetrical geometry (*compound-M*) were chosen to

synthesize HNMs. HNM-1P synthesized using *compound-P* in DMSO under reflux condition shows a maximum SA_{BET} of 976 m^2 g^{-1} while HNM-1M synthesized using *compound-M* under identical reaction condition shows a maximum SA_{BET} of 563 m^2 g^{-1}. The steric hindrance around the aldehyde group in *compound-M* makes it less accessible which led to sluggish condensation of framework resulting in lowering of SA_{BET}. Further, when the products were synthesized at lower temperatures of 423 or 393 K, ineffective condensation led to the decrease in SA_{BET}. The HNMs can capture a maximum of 18.9 wt% of CO_2 at 273 K and 1.65 wt% of H_2 at 77 K at 1 bar. One of the major achievement in this work is achieving the highest nitrogen content (>42%) among the metal-free nanoporous hybrid materials, which is beneficial for exploiting the Lewis basic character needed for several applications.

References

1. R. Kagit, M. Yildirim, O. Ozay, S. Yesilot and H. Ozay, Phosphazene based multicentered naked-eye fluorescent sensor with high selectivity for Fe^{3+} ions, *Inorg. Chem.*, 2014, **53**, 2144−2151.
2. H. Schiff, Mittheilungen aus dem universitätslaboratorium in Pisa: Eine neue reihe organischer basen, *Justus Liebigs Ann. Chem.*, 1864, **131**, 118–119.
3. N. E. Borisova, M. D. Reshetova and Y. A. Ustynyuk, Metal-free methods in the synthesis of macrocyclic Schiff bases, *Chem. Rev.*, 2007, **107**, 46–79.
4. L. S. M. Forlani and P. E. Todesco, Condensation reactions between aromatic aldehydes and some heterocyclic aromatic amines, *Gazz. Chim. Ital.*, 1986, **116**, 229–232.
5. S. J. Rowan and J. F. Stoddart, Thermodynamic synthesis of rotaxanes by imine, exchange, *Org. Lett.*, 1999, **1**, 1913–1916.
6. M. Y. Khuhawar, M. A. Mughal and A. H. Channar, Synthesis and characterization of some new Schiff base polymers, *Eur. Polym. J.*, 2004, **40**, 805–809.
7. Y. Xin and J. Yuan, Schiff's base as a stimuli-responsive linker in polymer chemistry, *Polym. Chem.*, 2012, **3**, 3045–3055.
8. F. J. U. Romo, J. R. Hunt, H. Furukawa, C. Klock, M. O'Keeffe and O. M. Yaghi, A crystalline imine-linked 3-D porous covalent organic framework, *J. Am. Chem. Soc.*, 2009, **131**, 4570–4571.
9. P. Pandey, A. P. Katsoulidis, I. Eryazici, Y. Wu, M. G. Kanatzidis and S. T. Nguyen, Imine-linked microporous polymer organic frameworks, *Chem. Mater.*, 2010, **22**, 4974–4979.
10. M. G. Schwab, B. Fassbender, H. W. Spiess, A. Thomas, X. Feng and K. Mullen, Catalyst-free preparation of melamine-based microporous polymer networks through Schiff base chemistry, *J. Am. Chem. Soc.*, 2009, **131**, 7216–7217.
11. W. C. Song, X. K. Xu, Q. Chen, Z. Z. Zhuang and X. H. Bu, Nitrogen-rich diaminotriazine-based porous organic polymers for small gas storage and selective uptake, *Polym. Chem.*, 2013, **4**, 4690–4696.
12. A. Laybourn, R. Dawson, R. Clowes, J. A. Iggo, A. I. Cooper, Y. Z. Khimyak and D. J. Adams, Branching out with aminals: Microporous organic polymers from difunctional monomers, *Polym. Chem.*, 2012, **3**, 533–537.
13. Y. Zhu, H. Long and W. Zhang, Imine-linked porous polymer frameworks with high small gas (H_2, CO_2, CH_4, C_2H_2) uptake and CO_2/N_2 selectivity, *Chem. Mater.*, 2013, **25**, 1630–1635.
14. R. Gomes, P. Bhanja and A. Bhaumik, A triazine-based covalent organic polymer for efficient CO_2 adsorption, *Chem. Commun.*, 2015, **51**, 10050–10053.

15. J. L. Segura, M. J. Mancheño and F. Zamora, Covalent organic frameworks based on Schiff-base chemistry: Synthesis, properties and potential applications, *Chem. Soc. Rev.*, 2016, **45**, 5635–5671.
16. J. Zhang, Z. Wang, L. Li, J. Zhao, J. Zheng, H. Cui and Z. Zhu, Self-assembly of CNH nanocages with remarkable catalytic performance, *J. Mater. Chem. A*, 2014, **2**, 8179–8183.
17. P. Rekha, U. Sahoo and P. Mohanty, Click-based porous inorganic–organic hybrid material (PHM) containing cyclophosphazene unit and their application in carbon dioxide capture, *RSC Adv*., 2014, **4**, 34860–34863.
18. P. Rekha, R. Muhammad and P. Mohanty, Sonochemical synthesis of cyclophosphazene bridged mesoporous organosilicas and their application in methyl orange, congo red and Cr(VI) removal, *RSC Adv*., 2015, **5**, 67690–67699.
19. P. Rekha, V. Sharma and P. Mohanty, Synthesis of cyclophosphazene bridged mesoporous organosilicas for CO_2 capture and Cr(VI) removal, *Micropor. Mesopor. Mater.*, 2016, **219**, 93–102.
20. P. Mohanty, L. D. Kull and K. Landskron, Porous covalent electron-rich organonitridic frameworks as highly selective sorbents for methane and carbon dioxide, *Nat. Commun.*, 2011, **2**, 401–406.
21. P. Mohanty and K. Landskron, Simple systematic synthesis of size-tunable covalent organophosphonitridic framework nano-and microspheres, *New J. Chem*, 2010, **34**, 215–220.
22. P. Vassileva, V. Krastev, L. Lakov and O. Peshev, XPS determination of the binding energies of phosphorus and nitrogen in phosphazenes, *J. Mater. Sci.*, 2004, **39**, 3201–3202.
23. H. Ozay and O. Ozay, Synthesis and characterization of drug microspheres containing phosphazene for biomedical applications, *Colloid Surf. A-Physicochem. Eng. Asp*, 2014, **450**, 99–105.
24. X. Li, J. Zhang, L. Shen, Y. Ma, W. Lei, Q. Cui and G. Zou, Preparation and characterization of graphitic carbon nitride through pyrolysis of melamine, *Appl Phys A*, 2009, **94**, 387–392.
25. X. Zhu, C. Tian, S. M. Mahurin, S. H. Chai, C. Wang, S. Brown, G. M. Veith, H. Luo, H. Liu and S. Dai, A superacid-catalyzed synthesis of porous membranes based on triazine frameworks for CO_2 separation, *J. Am. Chem. Soc.*, 2012, **134**, 10478−10484.
26. D. Y. Osadchii, A. I. Olivos-Suarez, A. V. Bavykina and J. Gascon, Revisiting nitrogen species in covalent triazene frameworks, *Langmuir*, 2017, **33**, 14278–14285.
27. K. Heister, M. Zharnikov and M. Grunze, Characterization of X-ray induced damage in alkanethiolate monolayers by high-resolution photoelectron spectroscopy, *Langmuir*, 2001, **17**, 8–11.
28. S. Bhunia, S. K. Das, R. Jana, S. C. Peter, S. Bhattacharya, M. Addicoat, A. Bhaumik and A. Pradhan, Electrochemical stimuli-driven facile metal-free hydrogen evolution from pyrene-porphyrin-based crystalline covalent organic framework, *ACS Appl. Mater. Interfaces*, 2017, **9**, 23843−23851.
29. B. C. Patraa, S. Khilari, R. N. Manna, S. Mondal, D. Pradhan, A. Pradhan and A. Bhaumik, A metal-free covalent organic polymer for electrocatalytic hydrogen evolution, *ACS Catal.*, 2017, **7**, 6120−6127.
30. G. Li, B. Zhang, J. Yan and Z. Wang, Tetraphenyladamantane-based polyaminals for highly efficient captures of CO_2 and organic vapors, *Macromolecules*, 2014, **47**, 6664–6670.
31. B.C. Smith, Distinguishing structural isomers: Mono- and disubstituted benzene rings, *Spectroscopy*, 2015, **30**,16–23.
32. Q. Li, S. Jin and B. Tan, Template-mediated synthesis of hollow microporous organic nanorods with tunable aspect ratio, *Sci. Rep*., 2016, **6**, 31359–31367.
33. A. K. Sekizkardes, S. Altarawneh, Z. Kahveci, T. İslamoğlu and H. M. El-Kaderi, Highly selective CO_2 capture by triazine-based benzimidazole-linked polymers, *Macromolecules*, 2014, **47**, 8328–8334.
34. T. Ben, C. Pei, D. Zhang, J. Xu, F. Deng, X. Jinga and S. Qiu, Gas storge properties in PAFs, *Energy Environ. Sci.*, 2011, **4**, 3991–3999.

35. K. T. Jackson, M. G. Rabbani, T. E. Reich and H. M. El-Kaderi, Synthesis of highly porous borazine-linked polymers and their application to H_2, CO_2, and CH_4 storage, *Polym. Chem.*, 2011, **2**, 2775–2777.
36. M. G. Rabbani and H. M. El-Kaderi, Synthesis and characterization of porous benzimidazole-linked polymers and their performance in small gas storage and selective uptake, *Chem. Mater.*, 2012, **24**, 1511–1517.
37. S. Hug, M. B. Mesch, H. Oh, N. Popp, M. Hirscher, J. Senker and B. V. Lotsch, A fluorene based covalent triazine framework with high CO_2 and H_2 capture and storage capacities, *J. Mater. Chem. A*, 2014, **2**, 5928–5936.
38. M. Saleh and K. S. Kim, Highly selective CO_2 adsorption performance of carbazole based microporous polymers, *RSC Adv.*, 2015, **5**, 41745–41750.
39. J. Wang and Q. Liu, An efficient one-step condensation and activation strategy to synthesize porous carbons with optimal micropore sizes for highly selective CO_2 adsorption, *Nanoscale*, 2014, **6**, 4148–4156.
40. P. Arab, M. G. Rabbani, A. K. Sekizkardes, T. Islamoglu and H. M. El-Kaderi, Copper (I)-catalyzed synthesis of nanoporous azo-linked polymers: Impact of textural properties on gas storage and selective carbon dioxide capture, *Chem. Mater.*, 2014, **26**, 1385–1392.
41. Y. Liao, J. Weber, B. M. Mills, Z. Ren and C. F. J. Faul, Highly efficient and reversible iodine capture in hexaphenylbenzene-based conjugated microporous polymers, *Macromolecules*, 2016, **49**, 6322−6333.
42. S. Mondal, S. K. Kundu and A. Bhaumik, A facile approach for the synthesis of hydroxyl-rich microporous organic networks for efficient CO_2 capture and H_2 storage, *Chem. Commun.*, 2017, **53**, 2752–2755.
43. R. Muhammad, P. Rekha and P. Mohanty, Facile synthesis of a thermally stable imine and benzimidazole functionalized nanoporous polymer (IBFNP) for CO_2 capture application, *Greenhouse Gases: Sci. Technol.*, 2016, **6**, 150–157.
44. L. Li, K. Cai, P. Wang, H. Ren and G. Zhu, Construction of sole benzene ring porous aromatic frameworks and their high adsorption properties, *ACS Appl. Mater. Interfaces*, 2015, **7**, 201–208.

CHAPTER-IV

CYCLOPHOSPHAZENE-BASED INORGANIC-ORGANIC HYBRID NANOPOROUS MATERIALS (CHNMs)

4.1. INTRODUCTION

The condensation products of *compound-P* and *compound-M* with melamine as discussed in the previous chapter have produced HNMs with superior textural properties and these HNMs have been used as efficient adsorbents for gas sorption applications. This has encouraged us to explore if *compound-P* and *compound-M* could be utilized to produce similar inorganic-organic hybrid nanoporous materials. In this regard, pyrrole was chosen, as it reacts with carbonyl functionality via nucleophilic condensation at position 2 and 5 that lead to the formation of condensation products. Thus, cyclophosphazene-based inorganic-organic hybrid nanoporous materials (CHNMs) have been synthesized by condensing pyrrole with *compound-P* and *compound-M*. The structural, microstructural and textural characterization of CHNMs have been conducted using analytical techniques such as, FTIR, CPMAS NMR, XPS, XRD, TGA, FESEM, TEM and N_2 sorption. Furthermore, the gas storage and separation applications of the CHNMs have been investigated.

4.2. CYCLOPHOSPHAZENE-BASED INORGANIC-ORGANIC HYBRID NANOPOROUS MATERIALS SYNTHESIZED USING *COMPOUND-P* (CHNM-*x*P, *x* = 1, 2 or 3)

4.2.1. Synthesis and characterization

The synthesis of CHNM-*x*P was carried out by condensing *compound-P* with pyrrole. The detailed synthesis of *compound-P* has been already discussed in ***Chapter-II*** and the structural characterization in ***Chapter-III***. The synthesis was carried out by a facile solvothermal method in 1,4-dioxane at the temperature of 453 K. At lower temperature as low as 423 K, no product could be obtained. The reaction could not be possible by a simple condensation reaction as utilized in ***Chapter-III*** for the synthesis of HNMs, since the boiling point of pyrrole is 402 K, which is much below the reaction temperature of 453 K. The reaction scheme for the synthesis of CHNM-*x*P is shown in ***Scheme 4.1*** and the detailed synthetic conditions are given in ***Chapter-II***. Three specimens have been made by condensing *compound-P* and pyrrole in 5, 10 and 15 ml of 1,4-dioxane and these specimens are designated as CHNM-1P, CHNM-2P and CHNM-3P, respectively.

The proposed structure in ***Scheme 4.1*** was confirmed by the spectroscopic investigation. Solid-state CPMAS NMR spectra of a representative sample, CHNM-1P are shown in ***Figure 4.1***. The observation of a resonance signal at δ of 43 ppm in ^{13}C CPMAS NMR spectrum (***Figure 4.1a***) originated due to the presence of methine carbon (C5) of the

framework confirms the nucleophilic condensation of pyrrole with aldehyde functionality of *compound-P*.[1] The resonance signal due to pyrrolic carbons (C7) could be seen at the δ of 109 ppm.[2,3] The resonance signal at 150 ppm is observed due to C1 carbon directly attached to the electronegative O atom.[4-7] The resonance signal at 132 ppm is originated due to C3 and C4 aromatic carbons, and C6 carbon of the pyrrole ring. [4-6] The resonance signal for C2 carbon is observed at 121 ppm.[6] All the signals from the ^{13}C CPMAS NMR spectrum could be indexed to different carbons of the proposed structure and it confirms the framework formation. Moreover, the absence of a resonance signal at δ of 170 ppm (due to carbonyl carbon of the *compound-P*) in ^{13}C CPMAS NMR spectrum indicates the completeness of the condensation reaction.[8]

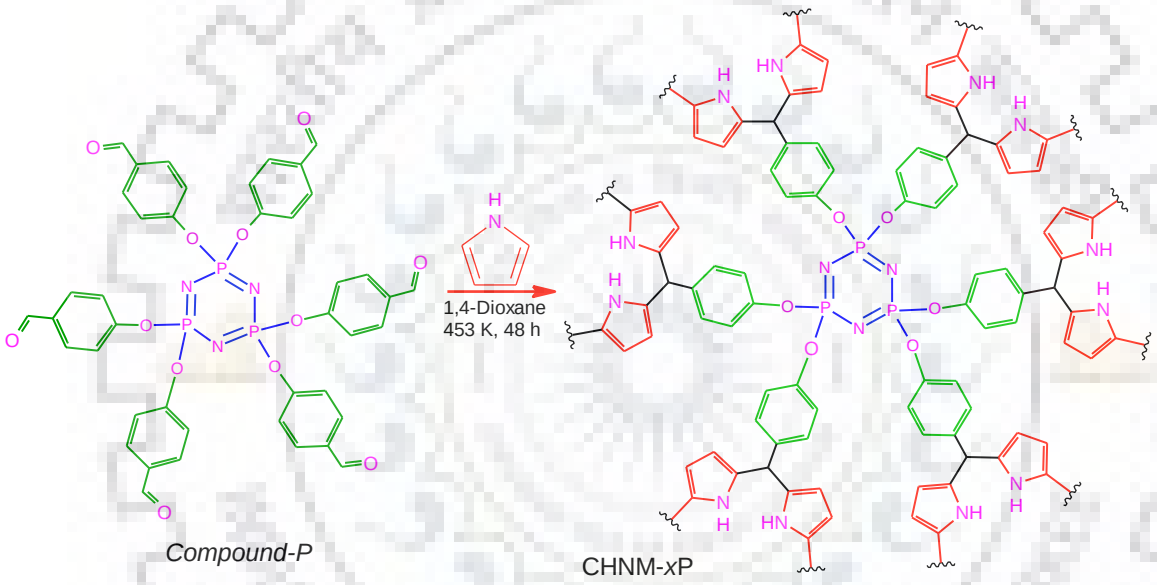

Scheme 4.1: Reaction scheme for the synthesis of CHNM-*x*P.

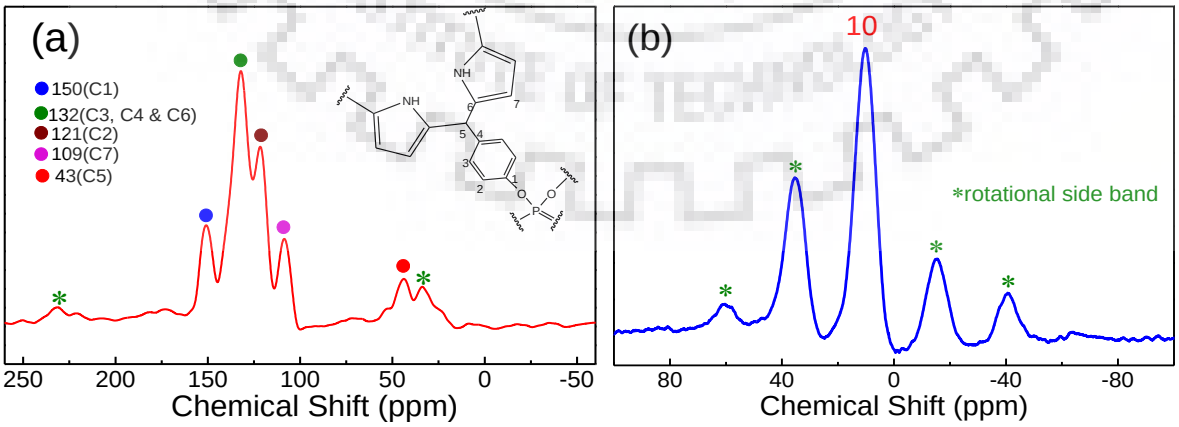

Figure 4.1: (a) ^{13}C and (b) ^{31}P CPMAS NMR spectra of CHNM-1P. The signals marked with the symbol (*) are ascribed to rotational side bands.

Furthermore, the observation of a broad resonance signal at δ of 10 ppm in the ^{31}P CPMAS NMR spectrum, as shown in ***Figure 4.1b***, confirms the inclusion of the cyclophosphazene moieties in the frameworks.[4,5] Moreover, the absence of signals in δ range of ~7 ppm, due to "P" atoms of *compound-P* in ^{31}P CPMAS NMR spectrum further confirm the completeness of condensation reaction.

The FTIR spectra given in ***Figure 4.2*** further corroborated the results obtained from the CPMAS NMR spectra. The disappearance of the band at 1705 cm^{-1} due to the carbonyl group of *compound-P* and observation of band at 2930 cm^{-1} due to methine linkage confirm the condensation.[4] The band at 3430 cm^{-1} in the FTIR spectra is observed due to the –N–H stretching vibrations of pyrrole moieties in the frameworks.[9,10] The band at 1690 cm^{-1} due to C=N stretching present in the pyrrole is also observed in the CHNM-*x*P.[11,12] The presence of bands at 1525 and 1420 cm^{-1} could be ascribed to pyrrole ring stretching and N–H bending, respectively.[6-10] The band at 1600 cm^{-1} is attributed to aromatic ring stretching.[13] The observation of bands in the range of 1210 to 1160 cm^{-1}, 986 cm^{-1} and 510 cm^{-1} assigned to ν_{as}(P=N–P), ν_{as}(P–O–C) and δ(P=N–P) vibrations, respectively, confirm the inclusion of the cyclophosphazene units in the frameworks.[14-18] Detailed FTIR band assignments for CHNM-*x*P, pyrrole and *compound-P* are summarized in ***Table 4.1***.

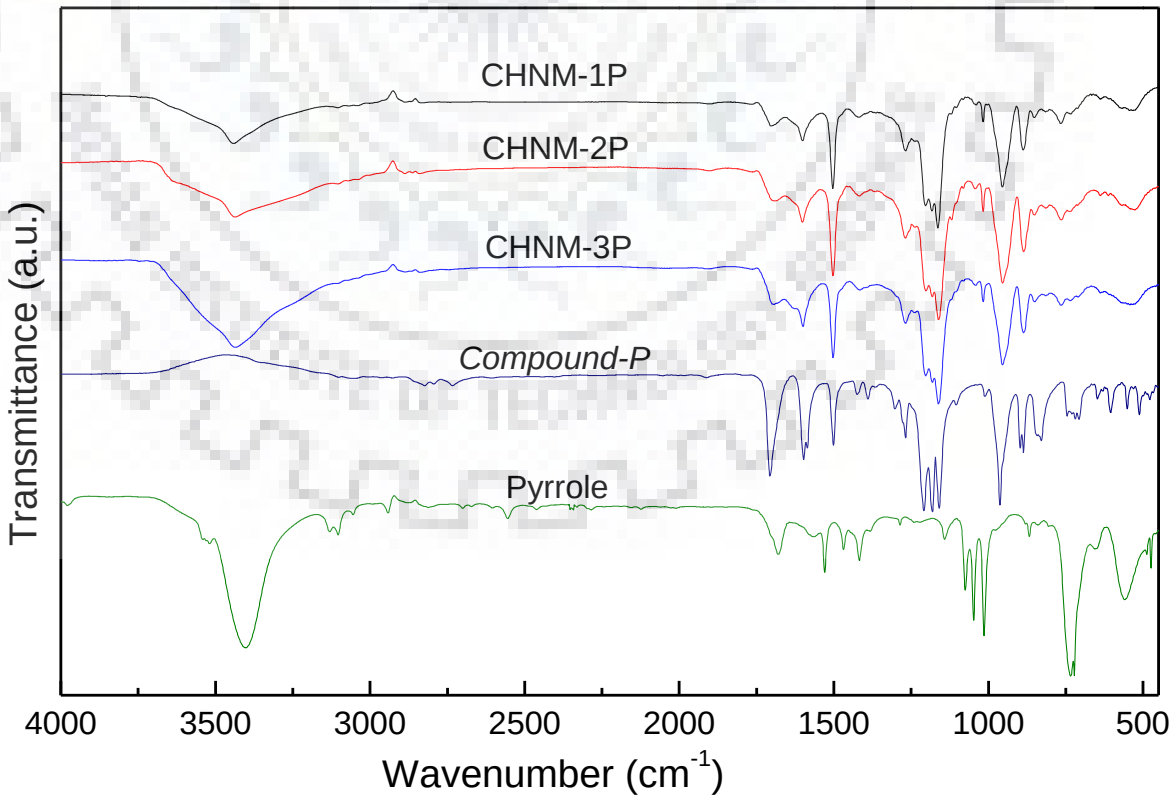

Figure 4.2: FTIR spectra of CHNM-*x*P, pyrrole and *compound-P*.

Table 4.1: Assignment of FT-IR Bands for CHNM-*x*P.

Bands Assignment	**Bands (cm^{-1})**		
	Compound-P	**Pyrrole**	**CHNM-*x*P**
N-H stretching	-	3410	3430
Aromatic –C–H stretch	3100	3105	3105
Aliphatic C–H stretching	-	-	2930
Aldehydic C–H stretching	2840	-	-
–CHO stretching	1705	-	-
Pyrrole -C=N stretching	-	1680	1690
C=C aromatic ring stretching	1600	-	1600
Pyrrole ring stretching	-	1530	1525
N-H bending	-	1420	1420
(C-H) in plane bending vibration	1270	-	1270
ν_{as}(P=N–P),	1210-1160	-	1210-1160
ν_{as}(P-O-C) vibration	960	-	986
ring deformation, (N-H, C2-H)	-	885	895
-C-H out of plane wagging	845	-	845
C-H out of plane bending vibration	750	-	760
C-CO out of plane bending vibration	640	-	640
δ(P=N-P) vibration	510	-	510

The chemical environment of CHNM-*x*P was accessed by the XPS. A typical XPS survey scan of CHNM-1P shown in the ***Figure 4.3*** reveals the peaks for P, C, N, and O. The high-resolution spectra for P 2p, C 1s, O 1s and N 1s as shown in ***Figure 4.4*** further revealed the electronic environment of these elements. The C 1s spectrum given in ***Figure 4.4a,*** shows three peaks at 284.8, 285.3 and 286.8 eV owing to aliphatic methine, aromatic and pyrrolic carbons, respectively.[19-22] The P 2p spectrum shown in ***Figure 4.4b*** shows the only peak at 134.4 eV owing to the phosphorus of cyclophosphazene moieties.[23-25] The N 1s spectrum shown in ***Figure 4.4c*** reveals two peaks at 398.1 and 401.1 eV owing to the nitrogen of cyclophosphazene and pyrrolic nitrogen, respectively.[19-24] The O 1s spectrum has shown two peaks at 533.5 and 531.6 eV associated with the oxygen present in the P-O-C linkage of CHNM-1P and oxygen of carbon tape (***Figure 4.4d***).[25] The XPS survey scan of carbon tape is shown in the inset of ***Figure 4.3***.

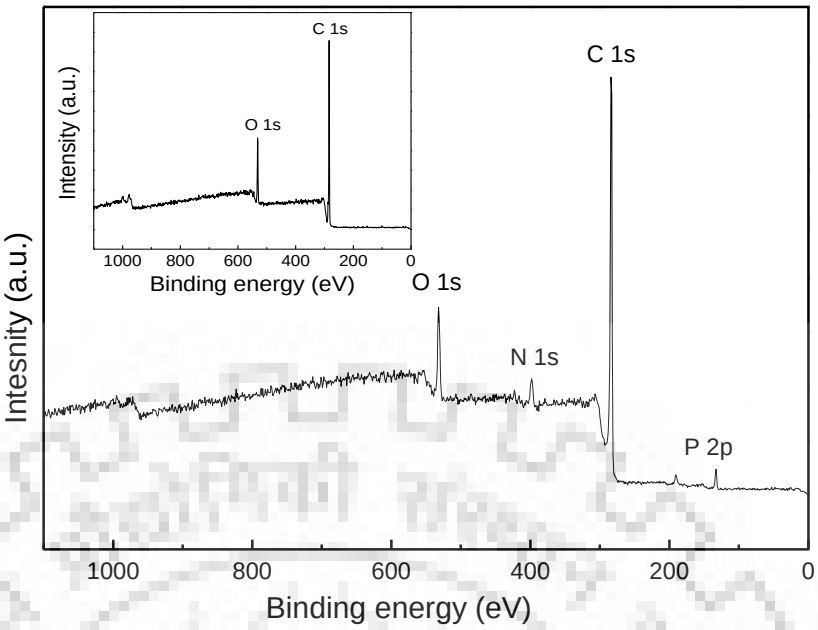

Figure 4.3: XPS survey scan for CHNM-1P. The XPS survey scan of carbon tape is shown in inset.

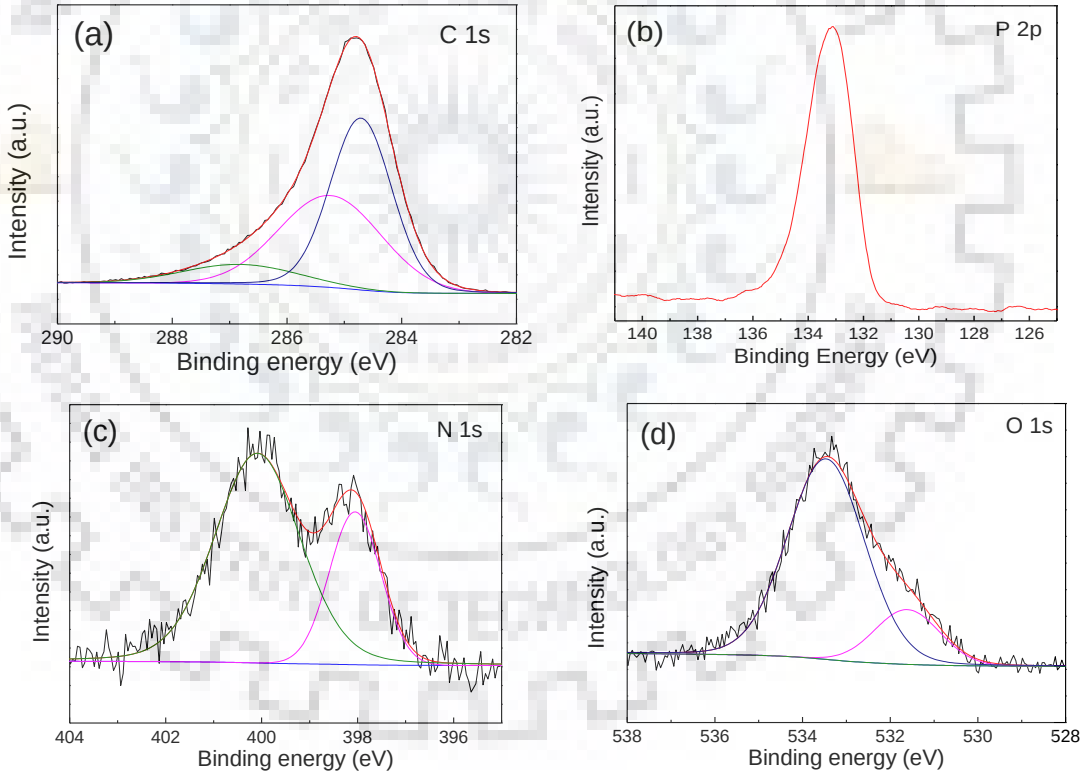

Figure 4.4: XPS high resolution XPS spectra; (a) C 1s, (b) P 2p, (c) N 1s and (d) O 1s high resolution XPS spectra for CHNM-1P.

The CHNM-*x*P were found to be insoluble in most of the common polar and non-polar solvents like tetrahydrofuran, dichloromethane, N, N-dimethylformamide, dimethyl sulfoxide, methanol, ethanol and water etc. The elemental compositions of the CHNM-*x*P estimated from the CHNS elemental analyzer are summarized in ***Table 4.2***. The theoretical and the

experimental estimation of the elemental compositions matched fairly well with marginal deviation owing to the nature of the materials. In general, the experimental elemental compositions of high surface area amorphous frameworks have shown a deviation from their respective theoretical values.[26-28] This could be attributed to several factors such as the presence of end-group functionality, trapping of solvent, moisture and small gas molecules inside the pores.[29,30] This was further observed in TGA/DTG analysis of CHNM-*x*P, as shown in ***Figure 4.5***. The initial mass loss above 373 K could be ascribed to the removal of trapped moisture and atmospheric gases. The second mass loss below 400 K is associated with the loss of solvents used during synthesis. Third mass loss at the temperature of 640 K could be associated with framework condensation. The framework decomposition, carbonization and polymerization of P-N framework could be observed about 770 K.[14,18] The phase analysis of the CHNM-*x*P was carried out by powder XRD. The absence of any sharp diffraction peak and presence of two broad halos centered around 12 and 20.5 degree in the 2θ scale in the XRD patterns shown in ***Figure 4.6*** indicate the amorphous nature of specimens.

Table 4.2: Elemental Analysis for CHNM-*x*P **(**Theoretical Composition: $C_{72}H_{48}N_9O_6P_3$).

Elements / Sample	Carbon (wt%)	Nitrogen (wt%)	Hydrogen (wt%)
Theoretical	70.41	10.27	3.91
CHNM-1P	62.79	8.40	3.49
CHNM-2P	63.37	8.96	3.78
CHNM-3P	62.12	8.74	3.77

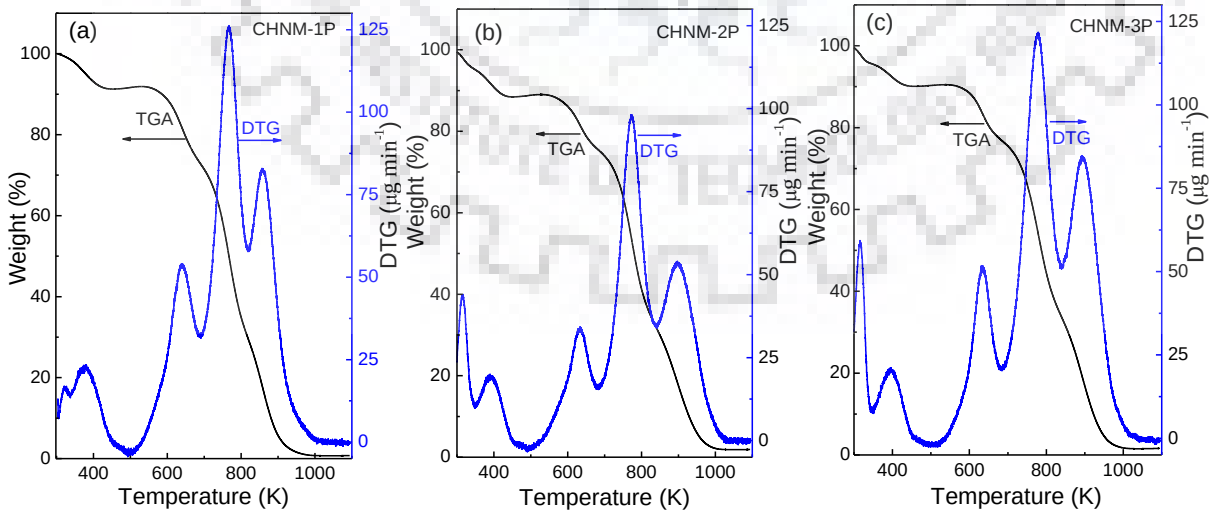

Figure 4.5: TGA and DTG thermograms of CHNM-*x*P recorded in the air with heating rate of 5 K min^{-1} using alumina sample holder.

The microstructure of the specimens has been investigated by FESEM and TEM. The typical FESEM images of the CHNM-1P, CHNM-2P and CHNM-3P are shown in the ***Figure 4.7a, 4.7b*** and ***4.7c***, respectively. The CHNM-1P has a different microstructure as compared to the other two samples. It can be seen from the ***Figure 4.7*** that the CHNM-2P and CHNM-3P have spherical particles of micrometer size connected with each other. The surface of these spherical particles is comparatively smooth. However, small particles with average diameter around 120 nm with irregular shapes can be observed in the FESEM image of CHNM-1P in ***Figure 4.7a***. These small particles are agglomerated with each other forming clusters. Interestingly, the TEM analysis of this sample reveals a porous nature of the specimen as shown in ***Figure 4.7d***. The pores are of different sizes in the nanometer range forming a hierarchical pore structure. The corresponding SAED pattern shown in the inset of ***Figure 4.7d*** has diffused ring further supporting the amorphous nature of the CHNM-1P as observed in the XRD patterns. The observation of different microstructures on changing the concentration of the reactants in these CHNM-*x*P could be attributed to the different kinetics of condensation. At the higher concentration, due to supersaturation condition large numbers of nuclei are formed at the beginning of the reaction and for the growth fewer numbers of materials are left in the reaction solution resulting in the formation of smaller particles with a rough surface. On the other hand, at a higher dilution less number of nuclei formed and these nuclei have got enough materials in the reaction solution for the growth of the particles with larger sizes and comparatively smooth surface.

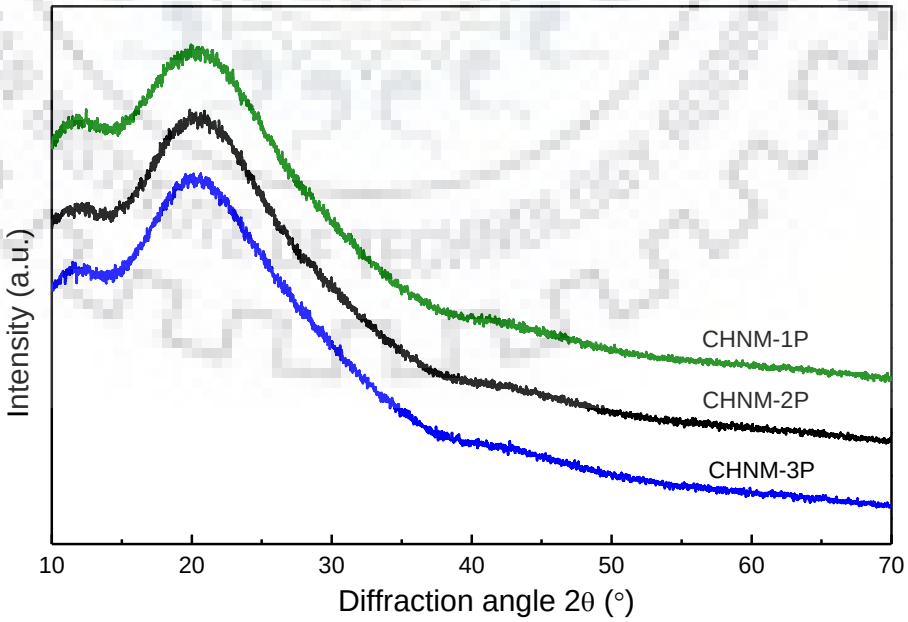

Figure 4.6: X-ray diffraction patterns of CHNM-*x*P.

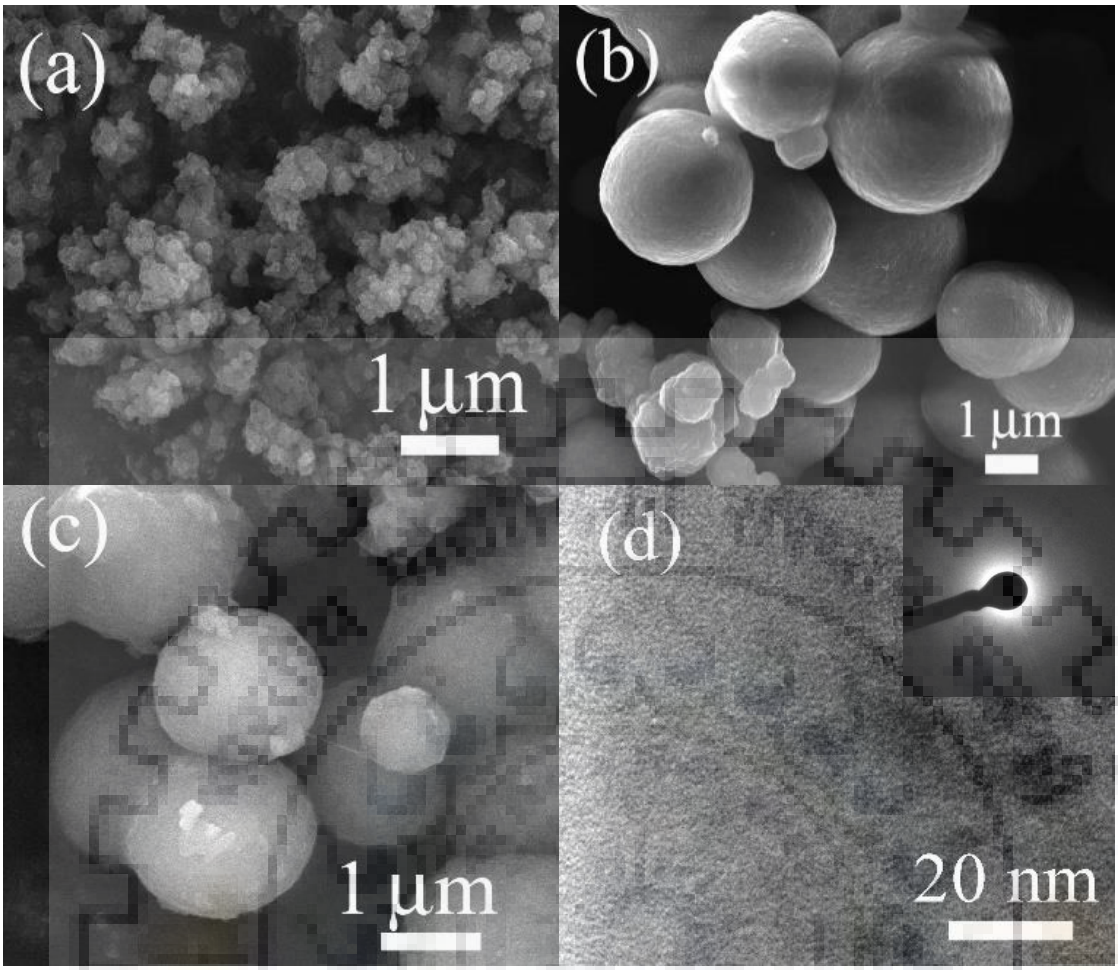

Figure 4.7: Microstructural analysis: FESEM images of (a) CHNM-1P, (b) CHNM-2P and CHNM-3P. (d) TEM images of CHNM-1P and its SAED pattern is shown in the inset.

4.2.2. Textural analysis of CHNM-*x*P

Observation of the nanoporous structure from the TEM image in the ***Figure 4.7d*** has encouraged us to investigate the textural properties of the CHNM-*x*P. The N_2 sorption isotherms of CHNM-*x*P as shown in ***Figure 4.8a*** exhibit a combination of type-I and type-IV isotherm. A sharp uptake at low relative pressure (P/P_0) of <0.01 represents the type-I isotherm owing to the presence of the micropores. Moreover, a hysteresis above 0.45, which extends up to 0.9 indicates the presence of the mesopores in the specimens, thus forming a hierarchical pore structure. This corroborates the TEM observation, which was further confirmed from the PSD analysis that shows the presence of micropores centered around 1.18 nm and mesopores in the region of 2.6 to 3.6 nm (***Figure 4.8b***) forming a hierarchical pore structure.

This is very interesting and important for the materials to be used as adsorbents. The ultra-small pores help in achieving a higher loading due to the enhanced interaction of the pore surface with the adsorbates owing to the shorter distance between these (thermodynamically

favorable processes) in combination with the capillary action, whereas, the larger mesopores help in the kinetics of the adsorbate molecules to have a facile mass transfer.[31,32] Such phenomenon has already been reported by our group and other groups.[18,31,33] There is a gradual increase in the adsorption that extends throughout the pressure range in the CHNM-1P, whereas, in CHNM-2P and CHNM-3P, the adsorption branch of the isotherms is comparatively flat. This may be attributed to the particle size, shape and the roughness of the particle surfaces. As discussed above with the FESEM images, a comparatively rough surface can be seen in the CHNM-1P with smaller particle size. The inter-particulate voids could further increase the adsorption at higher pressure range.[34] It is worth mentioning that the desorption branch of all the specimens has not closed even at low-pressure range. This could be attributed to the swelling effect.[35,36] Such swelling effect is commonly observed in high surface area nanoporous polymeric materials owing to the access of the ultra-micropores by the probe molecules with some restrictions.[35-38]

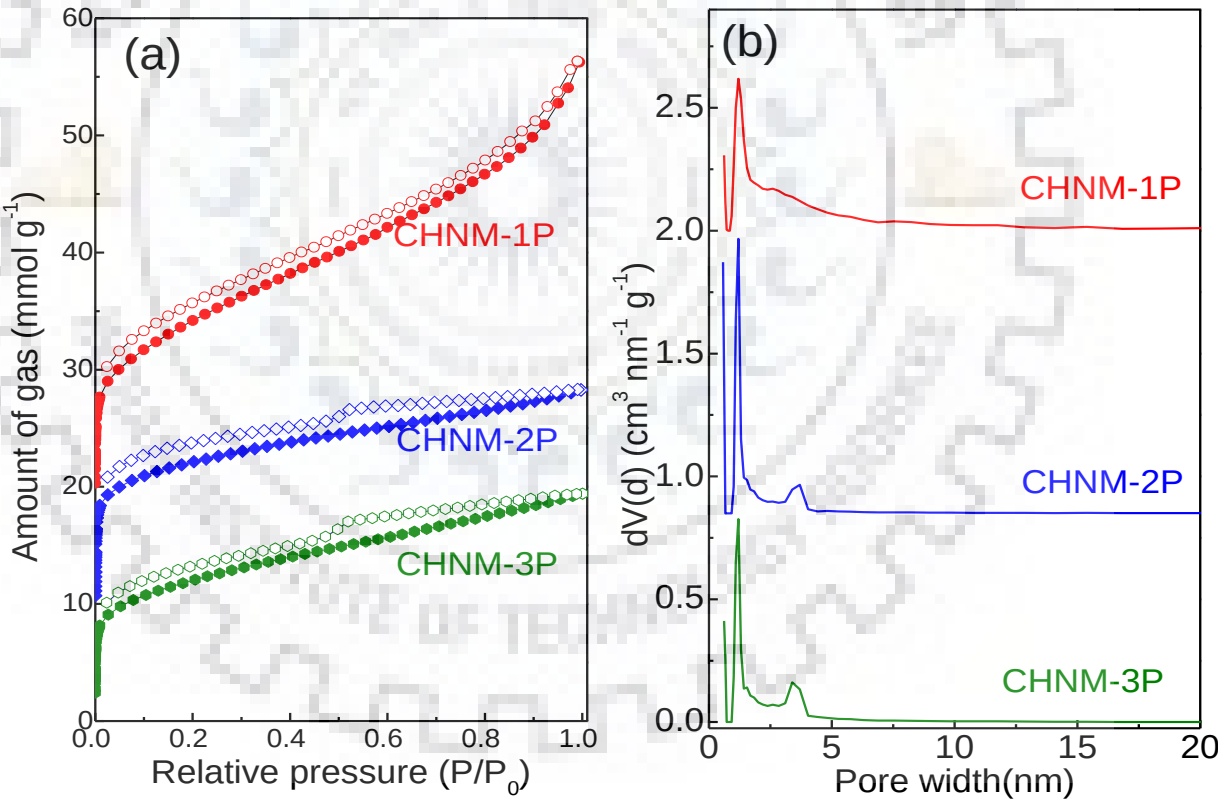

Figure 4.8: (a) N_2 sorption isotherm and (b) pore size distribution analysis of CHNM-*x*P measured at 77 K and 1 bar. N_2 sorption isotherm for CHNM-1P and CHNM-2P, have been upshifted by 20 and 10 mmol g^{-1}, respectively.

It has been observed that there was a gradual decrease in the SA_{BET} with an increase in the dilution. The CHNM-1P has a maximum SA_{BET} of 1328 m^2 g^{-1}. The SA_{BET} of CHNM-2P

and CHNM-3P was estimated to be 1070 and 960 $m^2 g^{-1}$, respectively. As discussed above, the difference in the SA_{BET} could be attributed to the surface roughness as well as particle sizes. This correlates the observation in the microstructure with the textural properties. The CHNM-1P has a large pore volume of 1.30 $cm^3 g^{-1}$ estimated at relative pressure (P/P_0) of 0.99. This could be attributed to the smaller particles having larger inter-particulate voids corroborate the observation in FESEM. The pore volume of CHNM-2P and CHNM-3P are same (0.67 $cm^3 g^{-1}$) at the same relative pressure. Detailed textural properties of all these specimens are summarized in ***Table 4.3***.

Table 4.3: Textural properties of CHNM-*x*P.

Sample	**SA_{BET} ($m^2 g^{-1}$)**	**Pore Size (nm)**	**Pore Vol. ($cm^3 g^{-1}$)**
CHNM-1P	1328	1.18 & 2.6	1.30
CHNM-2P	1070	1.18 & 3.6	0.67
CHNM-3P	960	1.18 & 3.4	0.67

4.2.3. Gas sorption and storage behavior of CHNM-*x*P

The high SA_{BET}, narrow PSD, hierarchical pore structure and the presence of Lewis basic sites in CHNM-*x*P have propelled us to study the CO_2 adsorption. The CO_2 sorption isotherms measured at 273 K and 1 bar, given in ***Figure 4.9a*** show the CO_2 uptake of 22.8, 18.3 and 16.4 wt% for CHNM-1P, CHNM-2P and CHNM-3P, respectively, at 273K and 1 bar. At 298 K, as expected, the CO_2 uptake decreases to 14.1, 10.5 and 8.9 wt% for CHNM-1P, CHNM-2P, and CHNM-3P, respectively (***Figure 4.9b***). It can further be observed that desorption branch of the isotherms does not close even at low pressure. This may be attributed to the enhanced Lewis acid-Lewis base interaction (higher heat of adsorption), smaller pore size and swelling effect.[35]

The isosteric heat of adsorption (Q_{st}) for CO_2 sorption for the CHNM-*x*P was estimated using Clausius-Clayperon equation. At zero coverage, the Q_{st} of CO_2 with CHNM-1P, CHNM-2P, and CHNM-3P was estimated to be 31.76, 37.16 and 34.92 kJ mol^{-1}, respectively (***Figure 4.9c***). The higher Q_{st} for CHNM-2P than CHNM-1P and CHNM-3P could be attributed to the higher nitrogen content as can be seen in ***Table 4.2***. However, as the SA_{BET} of CHNM-2P is only 80.6 % of the CHNM-1P, the total CO_2 capture capacity could not exceed. The high CO_2 capture capacity for CHNM-*x*P is due to the favorable interactions between the Lewis acidic CO_2 molecules and Lewis basic N-functionality in the porous framework. The Q_{st} of CHNM-*x*P

fall on the cusp of physisorption and chemisorption. This is because the materials that have basic sites usually display higher affinity towards CO_2 and hence, higher Q_{st}. But as there is no permanent covalent bond formation, the energy input is low enough compared to the chemisorbed surfaces as in the case of primary alkanol amine MEA that remains one of the great challenges for its use in current CO_2 capture technologies.

The use of molecular H_2 as a fuel has been considered the best alternative to replace the traditional fossil-based energy system for the automotive application.[1] Hence, we have employed CHNM-*x*P for H_2 storage at 77 K and 1 bar, and typical H_2 sorption isotherms are given in ***Figure 4.9d***. CHNM-1P, CHNM-2P and CHNM-3P have shown reversible H_2 uptake of 2.02, 1.82 and 1.70 wt%, respectively. Interestingly, the isotherms are completely reversible in nature and do not show saturation up to the measured pressure range of 1 bar which indicates the physisorption reversibility of CHNM-*x*P. Thus, an elevated pressure could improve the H_2 storage capacity substantially.[36]

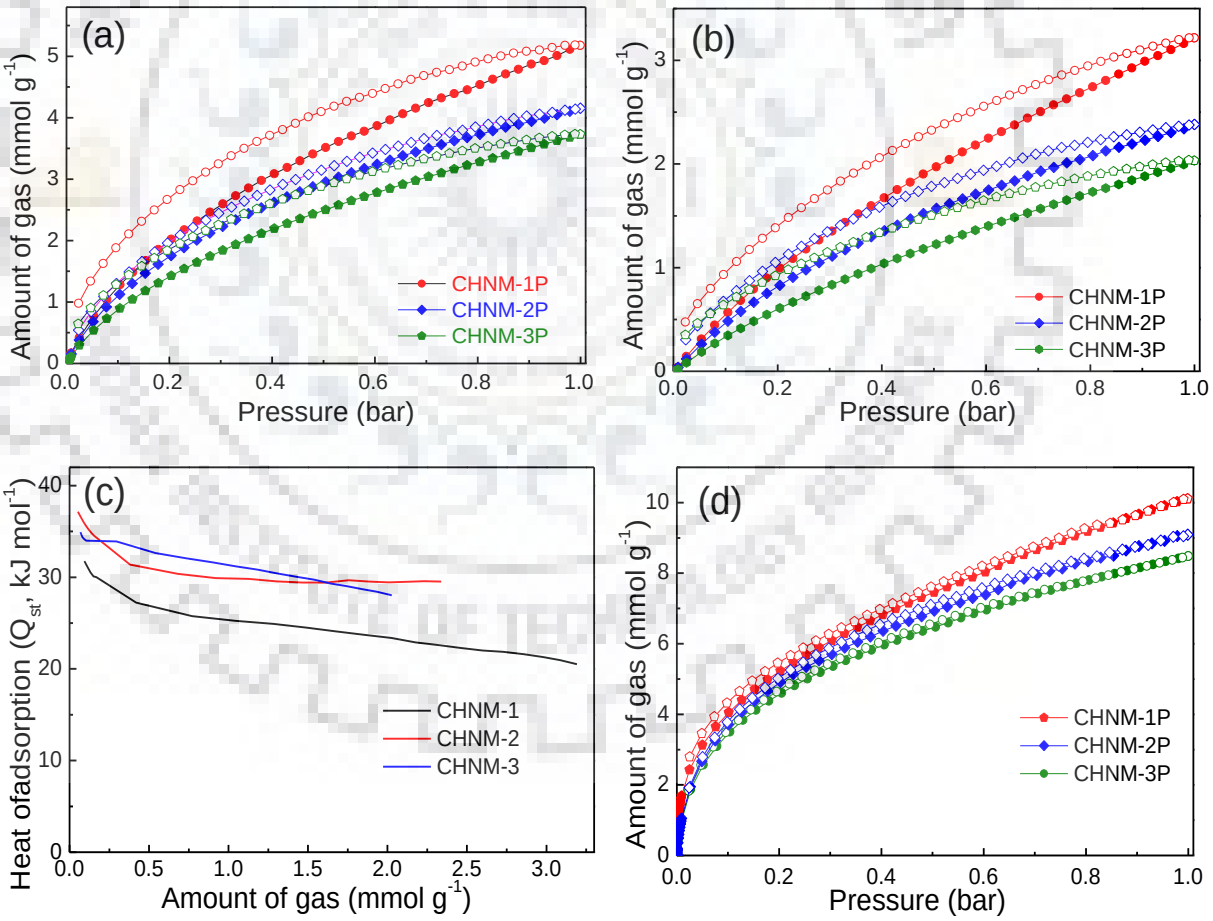

Figure 4.9: Gas sorption study; (a) and (b) are CO_2 sorption isotherms measured at 273 and 298 K, respectively at 1 bar, (c) isosteric heat of adsorption for CO_2 sorption and (d) H_2 sorption isotherms measure at 77 K and 1 bar of CHNM-*x*P.

The efficiency of the adsorbent to be used industrially to capture and separate CO_2 from the flue gas stream depends upon several factors, and gas selectivity is one of them. The selectivity of CO_2 vs N_2 is important particularly as N_2 is the major component amounting about 70 % in the flue gas.[18] Using Henry's law constant, the selectivity of CO_2 over N_2 was estimated at 273 K to be 66, 77, 47, for CHNM-1P, CHNM-2P and CHNM-3P, respectively (***Figure 4.10***). The higher selectivity of the CHNM-2P could be resulted due to the higher Q_{st}, owing to the higher nitrogen content among these samples.

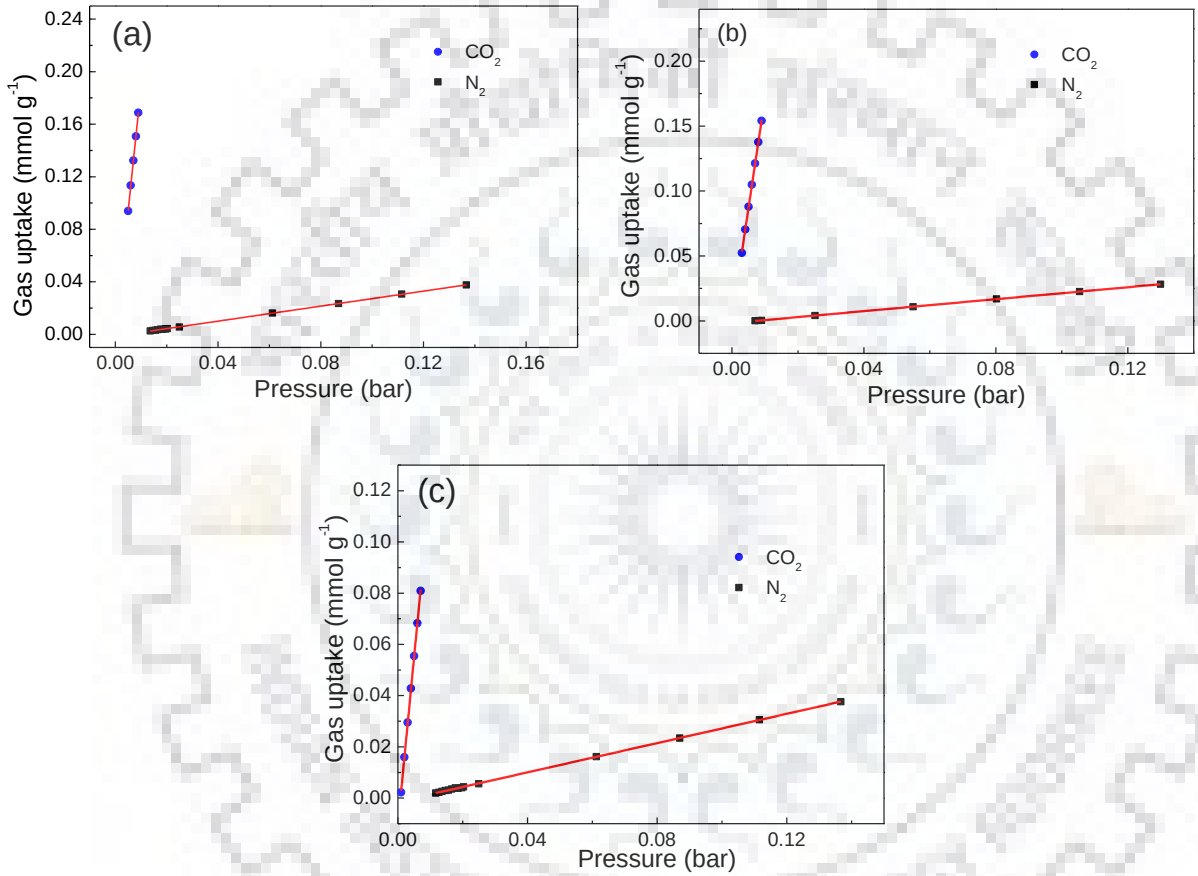

Figure 4.10: CO_2 vs N_2 selective uptake of (a) CHNM-1P, (b) CHNM-2P and (c) CHNM-3P calculated at 273 K using initial slope method (Henry's law constant).

Table 4.4: Gas sorption summary of CHNM-*x*P.

Sample	CO_2 uptake (wt%)		Q_{st} for CO_2 (kJ mol^{-1})	CO_2 vs N_2 selectivity at 273 K	H_2 uptake (wt%) 77 K
	273 K	298 K			
CHNM-1P	22.8	14.1	31.76	66	2.02
CHNM-2P	18.3	10.5	37.16	77	1.82
CHNM-3P	16.4	8.9	34.92	47	1.70

4.3. CYCLOPHOSPHAZENE-BASED INORGANIC-ORGANIC HYBRID NANOPOROUS MATERIALS SYNTHESIZED USING *COMPOUND-M* (CHNM-*x*M, *x* = 1, 2 or 3)

4.3.1. Synthesis and characterization of CHNM-*x*M

As discussed above, the synthesis of CHNM-*x*P by condensation of pyrrole with *compound-P* resulted in the formation of high surface area nanoporous materials with hierarchical pore structure. The large gas uptake observed in these materials has impelled us to investigate the nature of the products obtained by condensing *compound-M* to produce CHNM-*x*M similar to the study performed for HNMs in ***Chapter-III***. For this purpose, the *compound-M* was condensed with pyrrole under identical experimental conditions used for the synthesis of CHNM-*x*P as shown in ***Scheme 4.2***. The specimens designated as CHNM-1M, CHNM-2M and CHNM-3M are made using 5, 10 and 15 ml of 1,4-dioxane, respectively, similar to the synthesis of different CHNM-*x*P.

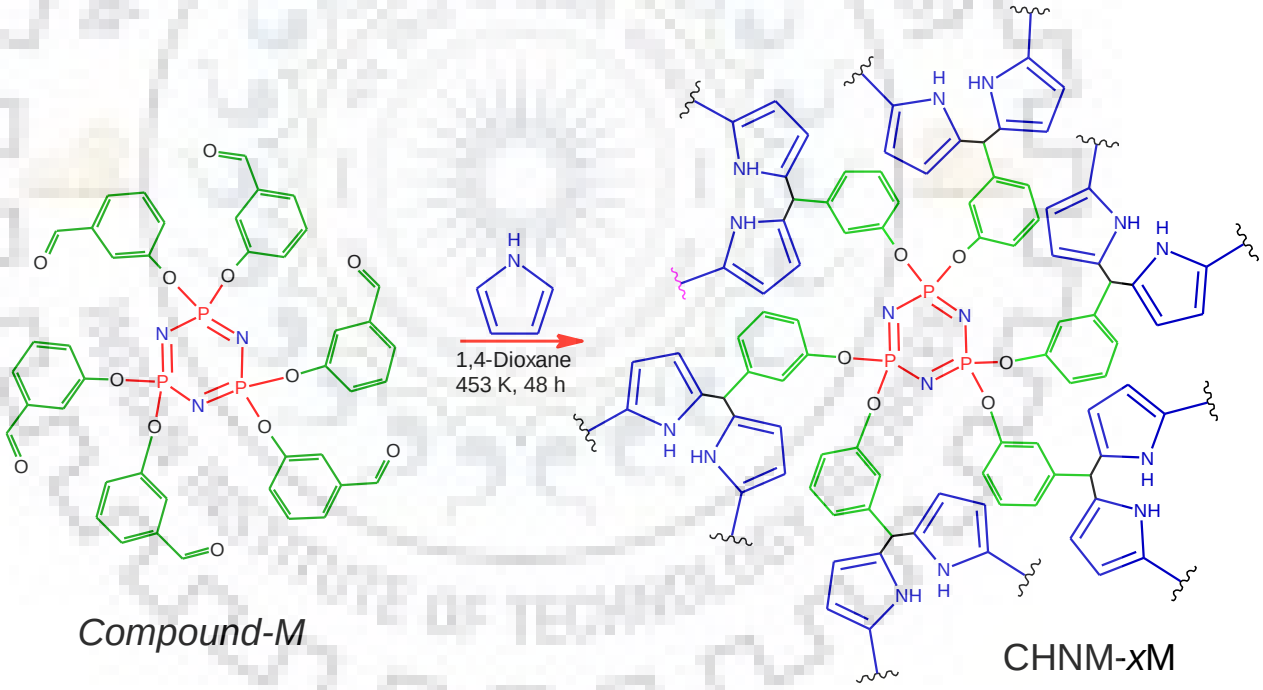

Scheme 4.2: Reaction scheme for the synthesis CHNM-*x*M.

The successful product formation, similar to CHNM-*x*P, was confirmed by characterizing the specimens using CPMAS NMR and FTIR spectroscopy. The observation of a resonance signal at 44 ppm in the ^{13}C CPMAS NMR spectrum given in ***Figure 4.11a*** assigned to the aliphatic methine carbon along with the signals originated from pyrrole moieties and carbons in the precursor confirm the formation of the product as proposed in the ***Scheme 4.2*** [1,39]. Further, a broad resonance signal at 10.7 ppm in the ^{31}P CPMAS NMR spectrum

given in ***Figure 4.11b*** originated from the P of the cyclophosphazene moieties in the synthesized specimen strongly supports the condensation and incorporation of the cyclophosphazene moieties in the polymeric framework as proposed.[39] The assignment of all other ^{13}C CPMAS NMR signals is shown in ***Figure 4.11a*** and are consistent with the structure.[1,2] Moreover, the absence of the characteristic signal of carbonyl carbon at ~170 ppm and P of *compound-M* at ~8 ppm in ^{13}C and ^{31}P CPMAS NMR spectra, respectively, in ***Figure 4.11***, further confirms the complete condensation.[39]

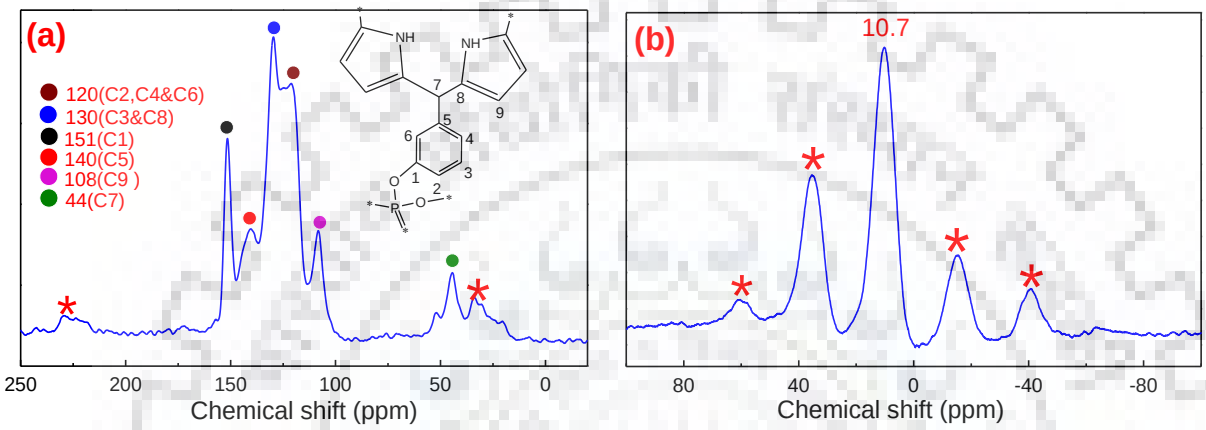

Figure 4.11: (a) ^{13}C and (b) ^{31}P CPMAS NMR spectra of CHNM-1M. The signals marked with the symbol (*) are ascribed to rotational side bands.

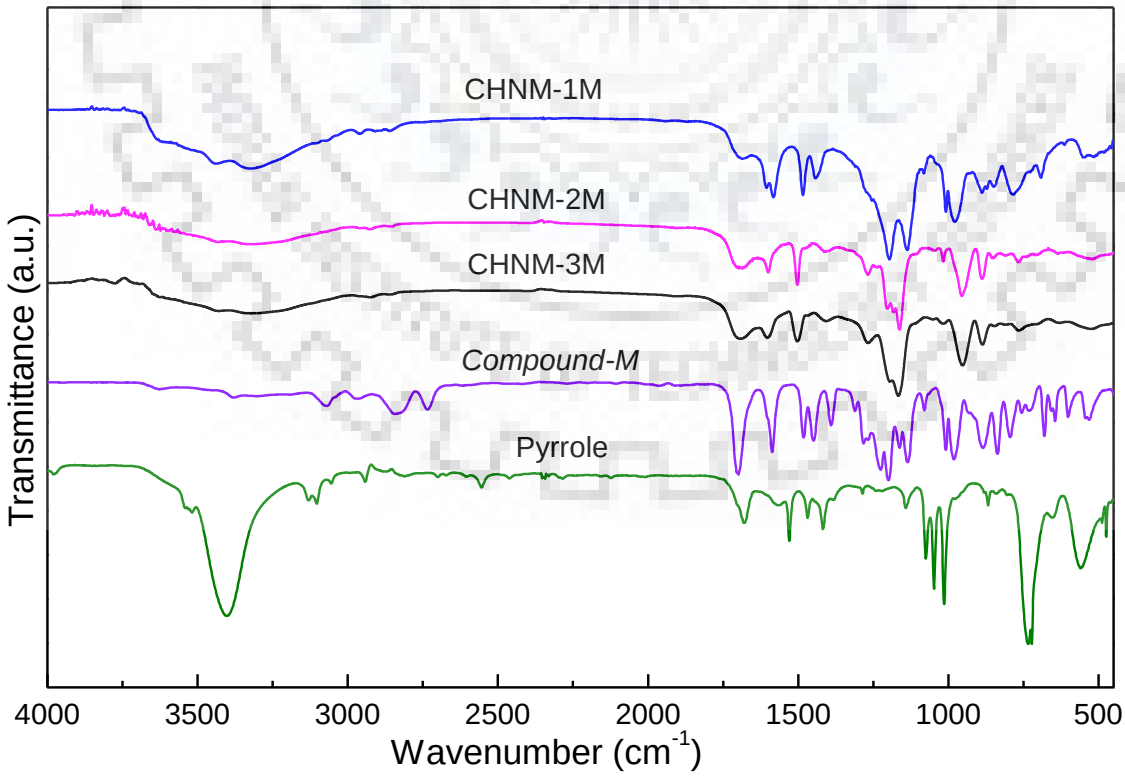

Figure 4.12: FTIR spectra of CHNM-*x*M, pyrrole and *compound-M*.

A similar conclusion was also drawn from the FT-IR investigation shown in ***Figure 4.12***, and observed bands were consistent with the FTIR bands of CHNM-*x*P as shown in ***Figure 4.2*** except the bands for asymmetrically substituted aromatic ring bending and -C-H wagging vibrations. The aromatic ring bending vibration for CHNM-*x*P is not seen due to symmetry in the structure of *compound-P* while due to asymmetry in the structure of *compound-M*, it was observed at 680 cm^{-1} for CHNM-*x*M. Similarly, the -C-H wagging vibrations were observed at 793 cm^{-1} for CHNM-*x*M while for CHNM-*x*P it was observed at 845 cm^{-1}. The trend in the observed FTIR bands are consistent with the results observed in case of the HNMs as discussed in ***Chapter-III***. Detailed assignments of the FTIR bands is given in the ***Table 4.5***.

Table 4.5: Assignment of FT-IR Bands for CHNM-*x*M.

Bands Assignment	**Bands (cm^{-1})**		
	Compound-M	**pyrrole**	**CHNM-*x*M**
N-H stretching	-	3410	3430
Aromatic –C–H stretch	3100	3105	3105
Aliphatic C–H stretching	-		2930
Aldehydic C–H stretching	2840	-	-
–CHO stretching	1700	-	-
Pyrrole -C-N stretching	-	1680	1690
C=C aromatic ring stretching	1585	-	1600
Pyrrole ring stretching	-	1530	1500
N-H bending	-	1420	1400
(C-H) in plane bending vibration	1285	-	1275
ν_{as}(P=N–P),	1210-1130	-	1210-1160
ν_{as}(P-O-C) vibration	980	-	960
ring deformation, (N-H, C2-H)	-	885	895
C-H out of plane wagging	793	-	760
C=C aromatic ring bending	680	-	685
C-CO out of plane bending vibration	560	-	560
δ(P=N-P) vibration	525	-	510

The XPS investigation of the CHNM-1M further provided similar conclusions observed for CHNM-1P as shown in ***Figure 4.13*** and ***4.14***. The peaks in both the survey scans and the high-resolution scans are observed in very much similar binding energy values with very minor deviation. Detailed comparisons of the various peaks are given in ***Table 4.6*** with their respective assignments.

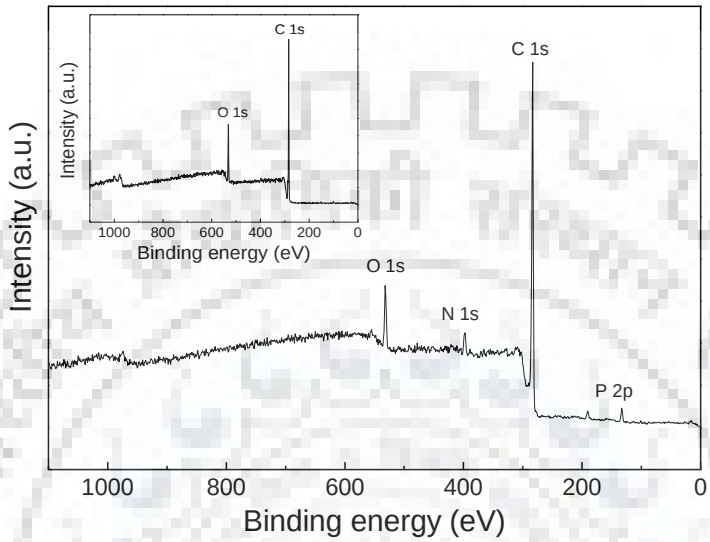

Figure 4.13: XPS survey scan for CHNM-1M. The XPS survey scan of carbon tape is shown in inset.

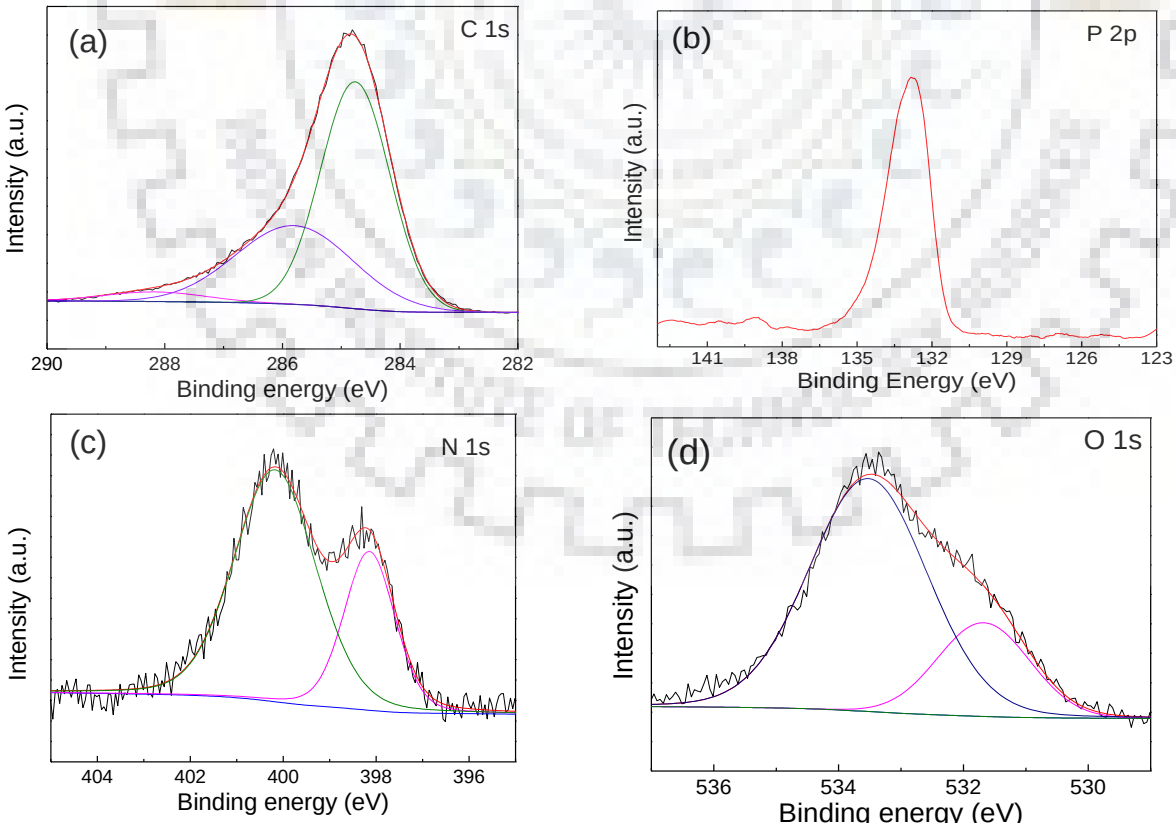

Figure 4.14: XPS high resolution XPS spectra; (a) C 1s, (b) P 2p, (c) N 1s and (d) O 1s high resolution XPS spectra for CHNM-1M.

Table 4.6: Comparison of XPS binding energy of CHNM-1M with CHNM-1P.

Elements	Binding energy (eV)	
	CHNM-1M	CHNM-1P
C 1s	284.8, 285.8, 288.2	284.8, 285.3, 286.8
P 2p	132.8	134.4
N 1s	398.2, 400.2	398.1, 401.1
O 1s	531.6, 533.5	531.6, 533.5

The elemental analysis of CHNM-*x*M given in ***Table 4.7*** is fairly matching with the theoretical elemental analysis with minor deviation. The results were consistent with the results obtained for CHNM-*x*P (***Table 4.2***). The CHNM-*x*M were found to be thermally stable up to a temperature of 500 K in the air (***Figure 4.15***). The thermal stability and mass loss profile of CHNM-*x*M are identical to the thermal stability and mass loss profile of CHNM-*x*P.

Table 4.7: Elemental Analysis for CHNM-*x*M (Theoretical Composition: $C_{72}H_{48}N_9O_6P_3$).

Elements / Sample	Carbon (wt%)	Nitrogen (wt%)	Hydrogen (wt%)
Theoretical	70.41	10.27	3.91
CHNM-1M	64.38	9.79	4.7
CHNM-2M	62.49	9.05	4.00
CHNM-3M	60.61	8.79	3.90

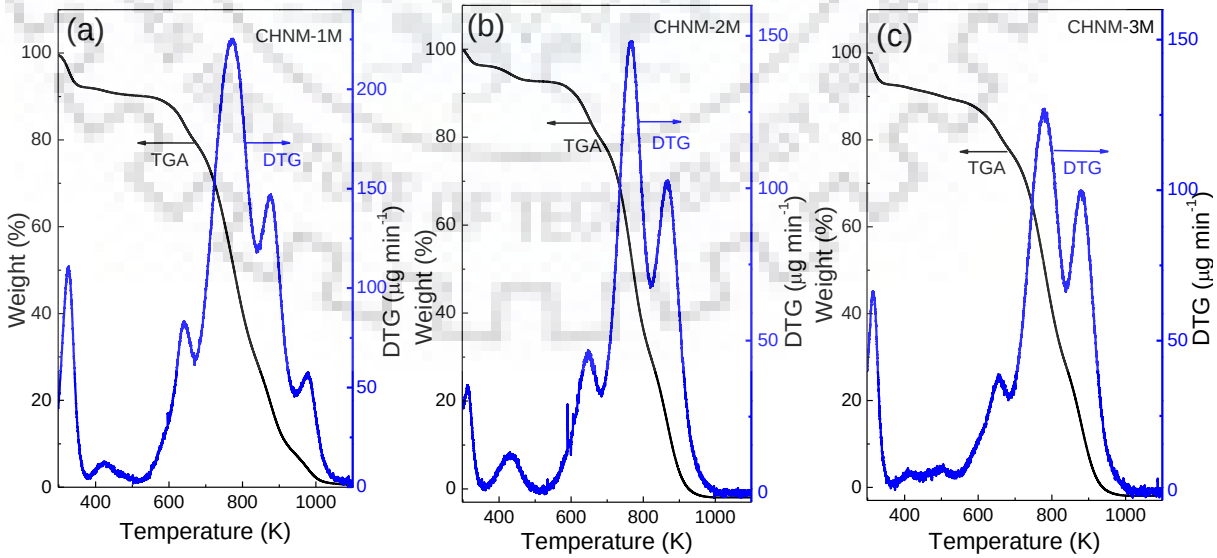

Figure 4.15: TGA and DTG thermograms of CHNM-*x*M recorded in the air with heating rate of 5 K min^{-1} using alumina sample holder.

As expected, the phase analysis using XRD in ***Figure 4.16*** demonstrated the amorphous nature of CHNM-*x*M similar to CHNM-*x*P. The effect of dilution on the microstructure as investigated by FESEM (***Figure 4.17a, 4.17b*** and ***4.17c***) in the CHNM-*x*M is similar to the observation in CHNM-*x*P (***Figure 4.7***). The TEM image given in ***Figure 4.17d*** indicated the presence of nanopores in CHNM-1M. The SAED pattern of CHNM-1M shown in the inset of ***Figure 4.17d*** corroborates the amorphous structure of CHNM-xM observed in XRD analysis.

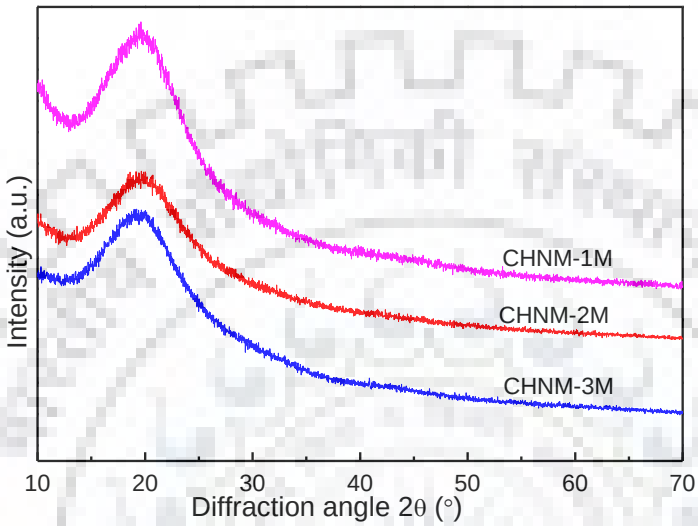

Figure 4.16: X-ray diffraction patterns of CHNM-*x*M.

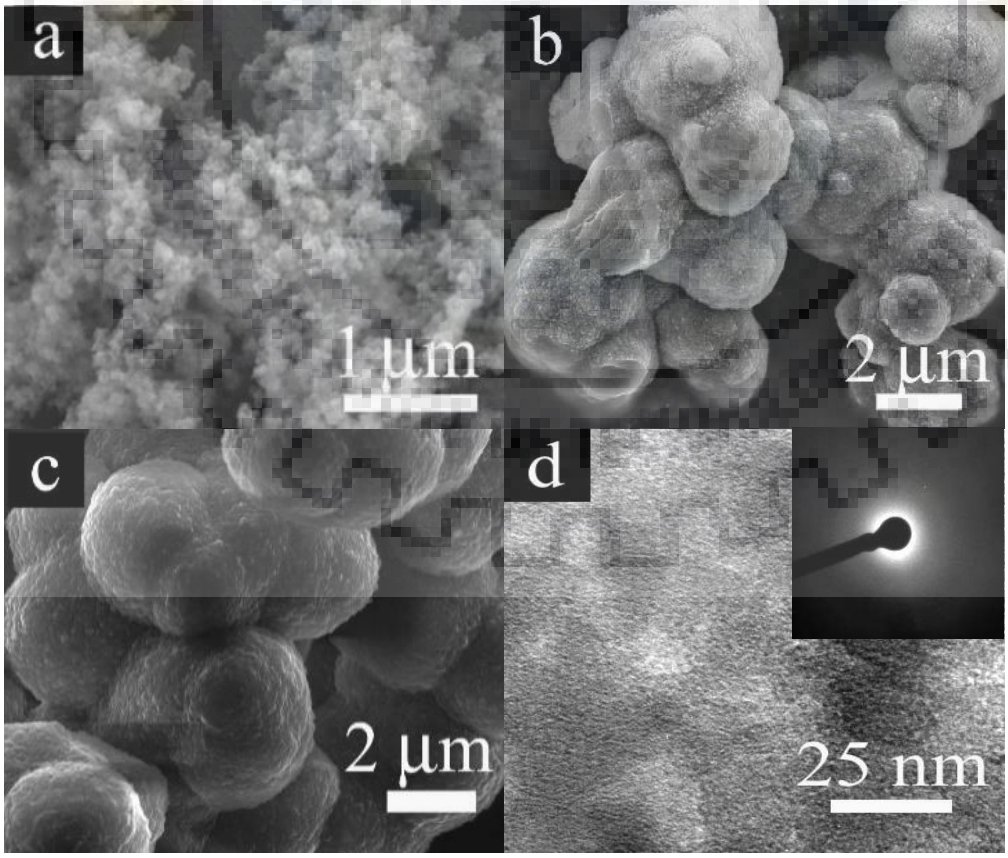

Figure 4.17: FESEM images of (a) CHNM-1M, (b) CHNM-2M and (c) CHNM-3M. (d) TEM image of CHNM-1M. The SAED pattern of the CHNM-1M is given in the inset of (d).

4.3.2. Textural analysis of CHNM-*x*M

The textural properties of these specimens have been investigated by N_2 sorption analysis. The typical N_2 sorption isotherms of CHNM-*x*M as shown in ***Figure 4.18*** exhibit sharp N_2 uptake at low relative pressure (P/P_0) range below 0.01 indicating the presence of micropores. The desorption branch in the N_2 sorption isotherms similar to CHNM-*x*P is not closing at a low relative pressure range (P/P_0) due to the swelling phenomenon and presence of pores not easily accessible with probe molecules (N_2 gas).[35,36,38] The maximum estimated SA_{BET} of 870 m^2 g^{-1} was estimated for CHNM-1M. The SA_{BET} for CHNM-2M and CHNM-3M was estimated to be 639 and 548 m^2 g^{-1}, respectively. Similar to CHNM-*x*P, the SA_{BET} of CHNM-*x*M decreases with dilution. The PSD estimated from the N_2 sorption analysis has shown a multimodal PSD in ***Figure 4.18b*** with the majority of the pores centered below 2 nm (micropore) and a significant number of pores in mesopore region spread in the range of 3.06 to 6.3 nm. The nature of hierarchy observed in the pore structure of CHNM-*x*M is similar to CHNM-*x*P. The pore volume for CHNM-1M, CHNM-2M and CHNM-3M were estimated to be 0.83, 0.52 and 0.50 cm^3 g^{-1}, respectively at relative pressure (P/P_0) of 0.90. The detailed textural properties of these specimens are given in the ***Table 4.8***.

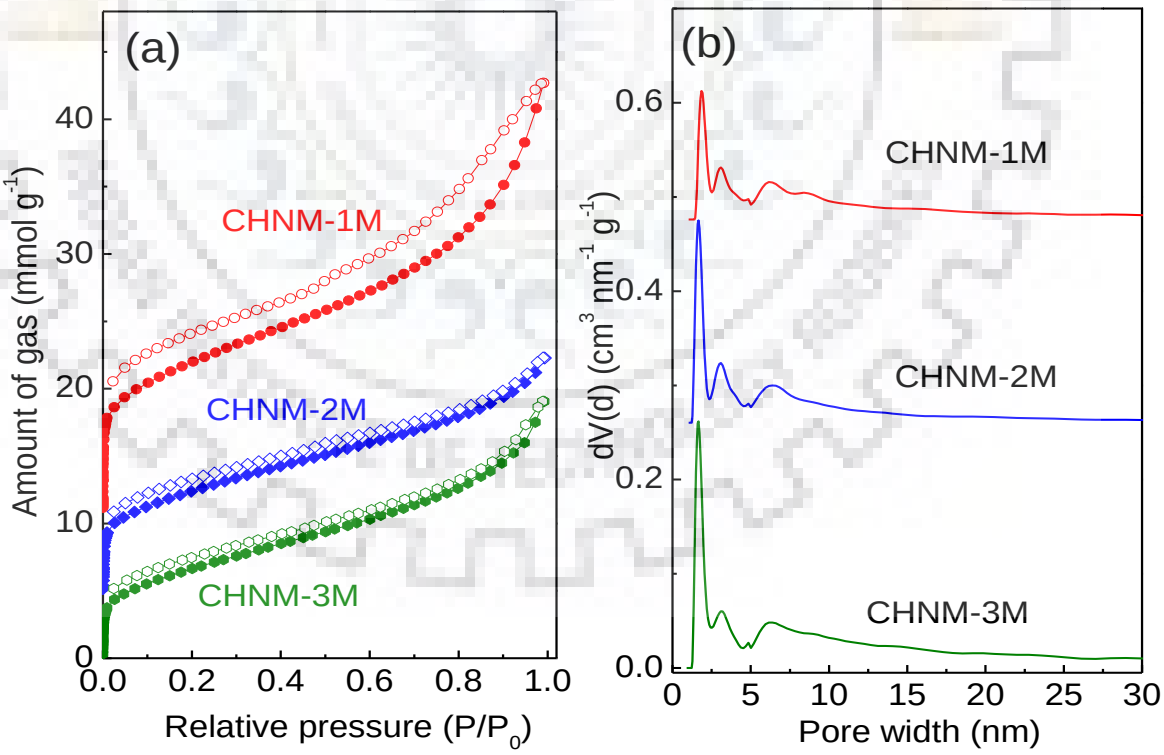

Figure 4.18: (a) N_2 sorption isotherm and (b) PSD analysis of CHNM-*x*M measured at 77 K and 1 bar. N_2 sorption isotherm for CHNM-1M and CHNM-2M, have been upshifted by 10 and 5 mmol g^{-1}, respectively.

Table 4.8: Textural properties of CHNM-*x*M.

Sample	SA_{BET} ($m^2\ g^{-1}$)	Pore size distribution (nm)	Pore volume ($cm^3\ g^{-1}$)
CHNM-1M	870	1.84, 3.06, 6.3	0.83
CHNM-2M	639	1.64, 3.06, 6.3	0.52
CHNM-3M	548	1.64, 3.14, 6.3	0.50

4.3.3. Gas sorption and storage behavior of CHNM-1M

As observed in HNMs as well as in CHNM-*x*P, the SA_{BET} is the dominating factor that determines the gas sorption performance. Hence, CHNM-1M having the highest SA_{BET} among the CHNM-*x*M was used for gas sorption studies. The CO_2 sorption isotherms measured at 273 and 298 K have shown the uptake of 14.8 and 9.9 wt%, respectively, at 1 bar (***Figure 4.19a***). The Q_{st} value at zero coverage was estimated to be 34.82 kJ mol^{-1} (***Figure 4.19b***). The H_2 sorption isotherm given in ***Figure 4.19c*** is completely reversible in nature with the maximum uptake of 1.6 wt% at 77 K and 1 bar. The selectivity of CO_2 vs N_2 estimated using initial slope method (Henry's law constant) at 273 K was found to be 34 (***Figure 4.19d***). The gas sorption comparison of CHNMs with recently reported adsorbents is given in ***Table 4.9*** and ***Table 4.10***.

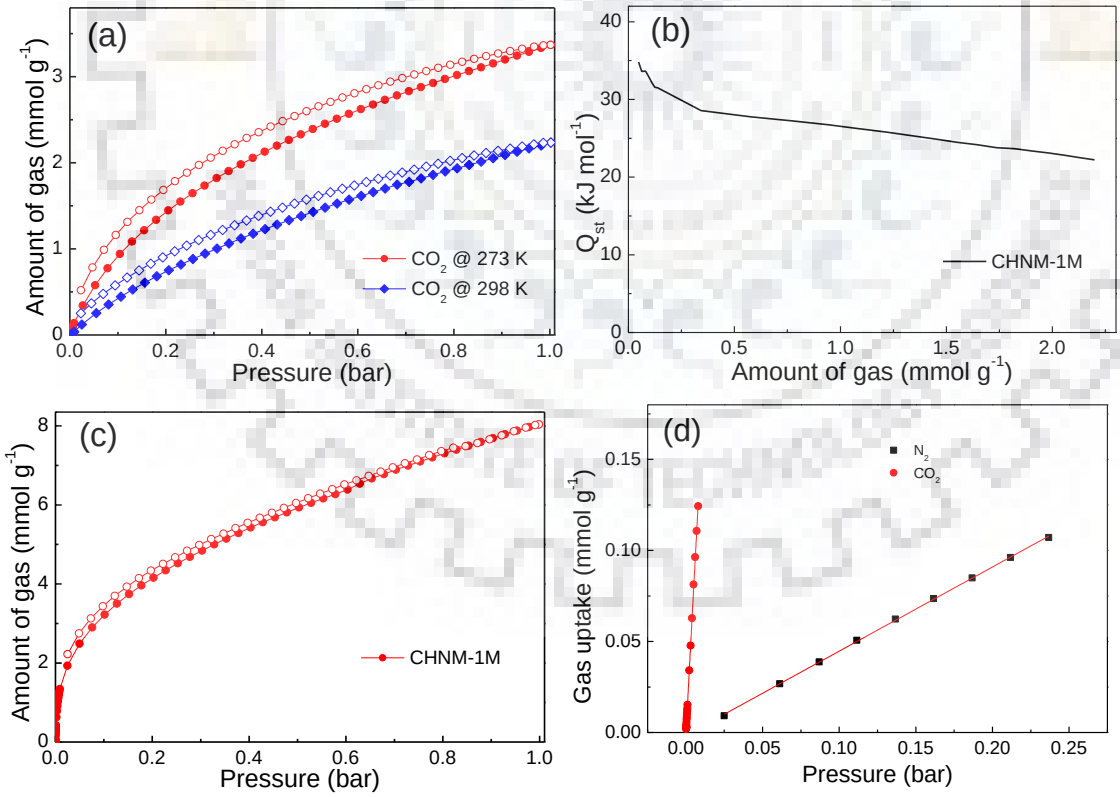

Figure 4.19: (a) CO_2 sorption isotherms measured at 273 and 298 K, (b) Q_{st} for CO_2 sorption, (c) H_2 sorption isotherm measured at 77 K and (d) CO_2 vs N_2 selective uptake at 273 K for CHNM-1M.

Table 4.9: Summary of gas sorption properties of porous adsorbents at low pressure.

Sample ID	SA_{BET} (m^2 g^{-1})	CO_2 @ 273 K			Reference
		uptake (wt%)	Q_{st} (kJ mol^{-1})	selectivity CO_2 vs N_2	
PECONF-3	851	15.35	24.9	77	18
PHM	453	8.05	26	-	14
MPC-700	1643	21.5	28	52 (1 bar)	40
PAF-3	2932	15.3	19.2	87	41
CZ@PON	592	18.96	42	107	37
PPF-1	1740	26.7	25.6	14.5 (1 bar)	13
ALP-1	1235	23.6	29.2	35	42
BILP-4	1135	23.5	28.7	79	28
BILP-6-NH_2	1185	24.48	29.5	-	33
IBFNP-1	1040	23.2	33.8	65	43
APOP-3	1402	19.9	27.5	27.5	44
HCMP-1	308	7.5	-	-	36
TBILP-1	330	11.7	35	63	45
PAN-1	925	14.8	36.5	61	46
fl-CTF350	1235	18.8	32.7	27	47

Table 4.10: Summary of H_2 storage properties of porous adsorbents at low pressure.

Sample ID	SA_{BET} (m^2 g^{-1})	H_2 uptake @ 77 K (wt%)	Reference
PAF-3	2932	2.07	42
PPF-4	726	1.47	13
BILP-4	1135	2.3	28
ALP-1	1235	2.19	43
ALP-2	1065	1.74	43
PAF-47	956	1.13	48

4.4. SUMMARY

In summary, a facile solvothermal method was used to synthesize a series of cyclophosphazene-based inorganic-organic hybrid nanoporous materials (CHNMs) using *compound-P* and *compound-M*. Among these, the sample synthesized using *compound-P* has shown the maximum SA_{BET} of 1328 m^2 g^{-1}. It has further been observed that the incorporation

of cyclophosphazene has a synergic effect in improving the textural properties. With increasing the dilution, the microstructural and textural properties both changed to a great extent in both the series. The structural geometry of precursors has a profound effect on the textural properties of the CHNMs, this further corroborates a similar observation in HNMs. The steric hindrance around the reactive functional group make access of the active functionality difficult, and sluggish condensation rate of building block resulted in the formation of frameworks with lower SA_{BET}. The maximum CO_2 uptake of 22.8 wt% at 273 K was recorded at 1 bar. The maximum H_2 storage of 2.02 wt% at 77 K was realized. The large CO_2 uptake could be attributed to the higher adsorbent-adsorbate affinity due to the presence of Lewis basic functionality on the pore surface. The high H_2 storage was mainly due to the hierarchical pore structure with the presence of a majority of the pores in the micropore regime. The observed physicochemical properties make CHNMs front-runners for the future generation metal-free adsorbents and catalyst for energy and environmental applications.

References

1. A. P. Katsoulidis, S. M. Dyar, R. Carmieli, C. D. Malliakas, M. R. Wasielewski and M. G. Kanatzidis, Copolymerization of terephthalaldehyde with pyrrole, indole and carbazole gives microporous POFs functionalized with unpaired electrons, *J. Mater. Chem. A*, 2013, **1**, 10465–10473.
2. S. Melhi, X. Ding, Z. W. Liu, C. X. Cao and B. H. Han, A new strategy to microporous polypyrrole networks based on condensation of pyrrole and diketone, *Macromol. Chem. Phys.*, 2016, **217**, 1529–1533.
3. R. Yamashita, T. Koizumi, S. Sasaki and T. Yamamoto, Preparation of soluble polypyrrole with -CC-p-C_6H_4-hexyl side chains at the N-position and its self-assembling behavior, *Polymer J.*, 2007, **39**, 1202–1206.
4. A. Modak, M. Pramanik, S. Inagaki and A. Bhaumik, A triazine functionalized porous organic polymer: Excellent CO_2 storage material and support for designing Pd nanocatalyst for C–C cross-coupling reactions, *J. Mater. Chem. A*, 2014, **2**, 11642–11650.
5. D. Lee, C. Y. Zhang, C. Wei, B. L. Ashfeld and H. F. Gao, Hierarchically porous materials via assembly of nitrogen-rich polymer nanoparticles for efficient and selective CO_2 capture, *J. Mater. Chem. A*, 2013, **1**, 14862–14867.
6. A. Modak, M. Nandi, J. Mondal and A. Bhaumik, Porphyrin based porous organic polymers: Novel synthetic strategy and exceptionally high CO_2 adsorption capacity, *Chem. Commun.*, 2012, **48**, 248–250.
7. A. Modak, J. Mondal, M. Sasidharan and A. Bhaumik, Triazine functionalized ordered mesoporous polymer: a novel solid support for Pd-mediated C–C cross-coupling reactions in water, *Green Chem.*, 2011, **13**, 1317–1331.
8. J. Wang, S. Xu, Y. Wang, R. Cai, C. Lv, W. Qiao, D. Long and L. Linga, Controllable synthesis of hierarchical mesoporous/microporous nitrogen-rich polymer networks for CO_2 and Cr(VI) ion adsorption, *RSC Adv.*, 2014, **4**, 16224–16232.
9. S. Y. Lee and B. H. Boo, Molecular structures and vibrational spectra of pyrrole and carbazole by density functional theory and conventional ab initio calculations, *J. Phys. Chem.*, 1996, **100**, 15073–15078.
10. J. Jang and H. Yoon, Facile fabrication of polypyrrole nanotubes using reverse microemulsion polymerization, *Chem. Commun.*, 2003, 720–721.
11. M. A. Chougule, S. G. Pawar, P. R. Godse, R. N. Mulik, S. Sen and V. B. Patil, Synthesis and characterization of polypyrrole (PPy) thin films, *Soft Nanosci. Letter*, 2011, **1**, 6–10.

12. K. Arora, A. Chaubey, R. Singhal, R. P. Singh, M. K. Pandey, S. B. Samanta, B. D. Malhotra and S. Chand, Application of electrochemically prepared polypyrrole–polyvinyl sulphonate films to DNA biosensor, *Biosens. Bioelectron.*, 2006, **21**, 1777–1783.
13. Y. Zhu, H. Long and W. Zhang, Imine-linked porous polymer frameworks with high small gas (H_2, CO_2, CH_4, C_2H_2) uptake and CO_2/N_2 selectivity, *Chem. Mater.*, 2013, **25**, 1630–1635.
14. P. Rekha, U. Sahoo and P. Mohanty, Click-based porous inorganic–organic hybrid material (PHM) containing cyclophosphazene unit and their application in carbon dioxide capture, *RSC Adv.*, 2014, **4**, 34860–34863.
15. P. Rekha, R. Muhammad and P. Mohanty, Sonochemical synthesis of cyclophosphazene bridged mesoporous organosilicas and their application in methyl orange, congo red and Cr(VI) removal, *RSC Adv.*, 2015, **5**, 67690–67699.
16. P. Rekha, R. Muhammad, V. Sharma, M. Ramteke and P. Mohanty, Unprecedented adsorptive removal of $Cr_2O_7^{2-}$ and methyl orange by using a low surface area organosilica, *J. Mater. Chem. A*, 2016, **4**, 17866–17874.
17. P. Rekha, V. Sharma and P. Mohanty, Synthesis of cyclophosphazene bridged mesoporous organosilicas for CO_2 capture and Cr(VI) removal, *Micropor. Mesopor. Mater.*, 2016, **219**, 93–102.
18. P. Mohanty, L. D. Kull and K. Landskron, Porous covalent electron-rich organonitridic frameworks as highly selective sorbents for methane and carbon dioxide, *Nat. Commun.*, 2011, **2**, DOI: 10.1038/ncomms1405.
19. S. Bhunia, S. K. Das, R. Jana, S. C. Peter, S. Bhattacharya, M. Addicoat, A. Bhaumik and A. Pradhan, Electrochemical stimuli-driven facile metal-free hydrogen evolution from pyrene-porphyrin-based crystalline covalent organic framework, *ACS Appl. Mater. Interfaces*, 2017, **9**, 23843−23851.
20. B. C. Patraa, S. Khilari, R. N. Manna, S. Mondal, D. Pradhan, A. Pradhan and A. Bhaumik, A metal-free covalent organic polymer for electrocatalytic hydrogen evolution, *ACS Catal.*, 2017, **7**, 6120−6127.
21. K. Wang, H. Huang, D. Liu, C. Wang, J. Li and C. Zhong, Covalent triazine-based frameworks with ultramicropores and high nitrogen contents for highly selective CO_2 capture, *Environ. Sci. Technol.*, 2016, **50**, 4869−4876.
22. B. S. Liu, L. Jiang, H. Sun and C. T. Au, XPS, XAES, and TG/DTA characterization of deposited carbon in methane dehydroaromatization over Ga–Mo/ZSM-5 catalyst, *Appl. Surf. Science*, 2007, **253**, 5092–5100.
23. P. Vassileva, V. Krastev, L. Lakov and O. Peshev, XPS determination of the binding energies of phosphorus and nitrogen in phosphazenes, *J. Mater. Sci.*, 2004, **39**, 3201–3202.
24. H. Ozay and O. Ozay, Synthesis and characterization of drug microspheres containing phosphazene for biomedical applications, *Colloid Surf. A-Physicochem. Eng. Asp*, 2014, **450**, 99–105.
25. H. R. Allcock, J. S. Rutt and R. J. Fitzpatrick, Surface reaction of poly[bis(trifluoroethoxy)phosphazene] films by basic hydrolysis, *Chem. Mater.*, 1991, **3**, 442–449.
26. J. Zhang, Z. Wang, L. Li, J. Zhao, J. Zheng, H. Cui and Z. Zhu, Self-assembly of CNH nanocages with remarkable catalytic performance, *J. Mater. Chem. A*, 2014, **2**, 8179–8183.
27. P. Puthiaraj, S. S. Kim and W. S. Ahn, Covalent triazine polymers using a cyanuric chloride precursor via Friedel–Crafts reaction for CO_2 adsorption/separation, *Chem. Eng. J.* 2016, **283**, 184–192.
28. M. G. Rabbani and H. M. El-Kaderi, Synthesis and characterization of porous benzimidazole-linked polymers and their performance in small gas storage and selective uptake, *Chem. Mater.*, 2012, **24**, 1511–1517.
29. P. Pandey, A. P. Katsoulidis, I. Eryazici, Y. Wu, M. G. Kanatzidis and S. T. Nguyen, Imine-linked microporous polymer organic frameworks, *Chem. Mater.*, 2010, **22**, 4974–4979.
30. A. Laybourn, R. Dawson, R. Clowes, J. A. Iggo, A. I. Cooper, Y. Z. Khimyak and D. J. Adams, Branching out with aminals: Microporous organic polymers from difunctional monomers, *Polym. Chem.*, 2012, **3**, 533–537.

31. M. Sevilla, J. B. Parra and A. B. Fuertes, Assessment of the role of micropore size and N-doping in CO_2 capture by porous carbons, *ACS Appl. Mater. Interfaces*, 2013, **5**, 6360–6368.
32. G.-Y. Lee, J. Lee, H. T. Vo, S. Kim, H. Lee and T. Park, Amine-functionalized covalent organic framework for efficient SO_2 capture with high reversibility, *Sci. Rep.*, 2017, **7**, 557–557.
33. T. Islamoglu, S. Behera, Z. Kahveci, T. D. Tessema, P. Jena and H. M. El-Kaderi, Enhanced carbon dioxide capture from landfill gas using bifunctionalized benzimidazole-linked polymers, *ACS Appl. Mater. Interfaces*, 2016, **8**, 14648–14655.
34. Q. Li, S. Jin and B. Tan, Template-mediated synthesis of hollow microporous organic nanorods with tunable aspect ratio, *Sci. Rep.*, 2016, **6**, 31359–31367.
35. R. T. Woodward, L. A. Stevens, R. Dawson, M. Vijayaraghavan, T. Hasell, I. P. Silverwood, A. V. Ewing, T. Ratvijitvech, J. D. Exley, S. Y. Chong, F. Blanc, D. J. Adams, S. G. Kazarian, C. E. Snape, T. C. Drage and A. I. Cooper, Swellable, water-and acid-tolerant polymer sponges for chemoselective carbon dioxide capture, *J. Am. Chem. Soc.*, 2014, **136**, 9028–9035.
36. Y. Liao, J. Weber, B. M. Mills, Z. Ren and C. F. J. Faul, Highly efficient and reversible iodine capture in hexaphenylbenzene-based conjugated microporous polymers, *Macromolecules*, 2016, **49**, 6322−6333.
37. S. Mondal, S. K. Kundu and A. Bhaumik, A facile approach for the synthesis of hydroxyl-rich microporous organic networks for efficient CO_2 capture and H_2 storage, *Chem. Commun.*, 2017, **53**, 2752–2755.
38. L. Tan, B. Li, X. Yang, W. Wang and B. Tan, Knitting hypercrosslinked conjugated microporous polymers with external crosslinker, *Polymer*, 2015, **70**, 336–342.
39. R. Muhammad, P. Rekha and P. Mohanty, Aminal linked inorganic–organic hybrid nanoporous materials (HNMs) for CO_2 capture and H_2 storage applications, *RSC Adv.*, 2016, **6**, 17100–17105.
40. J. Wang and Q. Liu, An efficient one-step condensation and activation strategy to synthesize porous carbons with optimal micropore sizes for highly selective CO_2 adsorption, *Nanoscale*, 2014, **6**, 4148–4156.
41. T. Ben, C. Pei, D. Zhang, J. Xu, F. Deng, X. Jinga and S. Qiu, Gas storage in porous aromatic frameworks (PAFs), *Energy Environ. Sci.*, 2011, **4**, 3991–3999.
42. P. Arab, M. G. Rabbani, A. K. Sekizkardes, T. Islamoglu and H. M. El-Kaderi, Copper (I)-catalyzed synthesis of nanoporous azo-linked polymers: Impact of textural properties on gas storage and selective carbon dioxide capture, *Chem. Mater.*, 2014, **26**, 1385–1392.
43. R. Muhammad, P. Rekha and P. Mohanty, Facile synthesis of a thermally stable imine and benzimidazole functionalized nanoporous polymer (IBFNP) for CO_2 capture application, *Greenhouse Gases: Sci. Technol.*, 2016, **6**, 150–157.
44. W. C. Song, X. K. Xu, Q. Chen, Z. Z. Zhuang and X. H. Bu, Nitrogen-rich diaminotriazine-based porous organic polymers for small gas storage and selective uptake, *Polym. Chem.*, 2013, **4**, 4690–4696.
45. A. K. Sekizkardes, S. Altarawneh, Z. Kahveci, T. İslamoğlu and H. M. El-Kaderi, Highly selective CO_2 capture by triazine-based benzimidazole-linked polymers, *Macromolecules*, 2014, **47**, 8328–8334.
46. G. Li, B. Zhang, J. Yan and Z. Wang, Tetraphenyladamantane-based polyaminals for highly efficient captures of CO_2 and organic vapors, *Macromolecules*, 2014, **47**, 6664–6670.
47. S. Hug, M. B. Mesch, H. Oh, N. Popp, M. Hirscher, J. Senker and B. V. Lotsch, A fluorene based covalent triazine framework with high CO_2 and H_2 capture and storage capacities, *J. Mater. Chem. A*, 2014, **2**, 5928–5936.
48. L. Li, K. Cai, P. Wang, H. Ren and G. Zhu, Construction of sole benzene ring porous aromatic frameworks and their high adsorption properties, *ACS Appl. Mater. Interfaces*, 2015, **7**, 201–208.

CHAPTER-V

NITROGEN ENRICHED TRIAZINE BRIDGED MESOPOROUS ORGANOSILICAS (NETPMOs)

5.1. INTRODUCTION

In this chapter, a systematic investigation of nitrogen enrichment in the framework of mesoporous organosilicas is being discussed. Mesoporous organosilica, a class of hybrid nanoporous materials is quite popular after its first report in 1999. In general, these classes of hybrid materials are formed by the combination of siliceous moiety along with various aliphatic and aromatic organic components. The majority of the applications of organosilicas are derived based on the organic functionalities present in the materials. In this regard, although, there are a large number of articles published incorporating different organic functionalities, but a systematic investigation on nitrogen enrichment in the organosilica frameworks is a research area yet to be explored well. One of the major application of nitrogen enrichment due to its Lewis basic nature lies in the capture of Lewis acidic gas such as CO_2. For this purpose, organosilica precursors such as (3-aminopropyl)triethoxysilane (APTES), *N*-[3-(trimethoxysilyl)propyl]ethylenediamine (TMSPD) and N^1-(3-trimethoxysilylpropyl)ethylenetriamine (TMSPT) with varying nitrogen content are chosen. To further enhance the nitrogen enrichment, these precursors are condensed with cyanuric chloride (CNC), a nitrogen rich molecule, followed by the hydrolysis and polycondensation of the siliceous moieties. The hydrolysis and polycondensation of these precursors are further carried out by adding varying amount of tetraethyl orthosilicate (TEOS), which in general improves the textural properties of several organosilica frameworks. These materials can be classified as nitrogen enriched triazine bridged mesoporous organosilicas (NETPMOs). The structural characterization has been performed using FTIR and NMR spectral analysis. FESEM and TEM were used to investigate the microstructure. The textural analysis was carried out using N_2 sorption. The NETPMOs were employed for the CO_2 sorption applications.

5.2. SYNTHESIS OF NETPMOs

As discussed above, NETPMOs were synthesized using three precursors viz., APTES, TMSPD and TMSPT in a two-step method. The first step involves the condensation of the precursors with CNC followed by their hydrolysis and polycondensation in the second step. All these experiments were carried out in basic condition and cetyltrimethylammonium bromide (CTABr) was used as structure directing agent. Moreover, a co-condensation with TEOS was also carried out for improving the textural properties. The specimens are designated according to the precursors used for the synthesis of NETPMOs as discussed in ***Chapter-II***. The specimens, NETPMO-*x*M, NETPMO-*x*D and NETPMO-*x*T are synthesized when APTES, TMSPD and TMSPT are used, respectively.

5.2.1. NETPMO-*x*M (*x* = 0, 2, 4, 6, 8 and 10)

5.2.1.1. Synthesis and characterization of NETPMO-xM

Incorporation of the triazine moieties into the NETPMO-*x*M framework was carried out by the condensation of CNC with APTES through covalent bonding as shown in ***Scheme 5.1***. The first step for the synthesis of NETPMO-*x*M proceeds through nucleophilic condensation reaction between APTES and CNC. Hydrolysis of ethoxy group attached to the Si followed by the polycondensation resulted in the formation of the siliceous frameworks. The synthesis was carried out in presence of a structure directing agent, CTABr, in basic medium. Detailed synthesis was given in ***Chapter-II***. The synthesis was further extended to synthesize organosilicas by co-condensation with variable amount of TEOS. The amount of TEOS w.r.t. APTES was varied in the ratio of 1:0, 1:2, 1:4, 1:6, 1:8 and 1:10, and accordingly the specimens are designated as NETPMO-*x*M, (*x* = 0, 2, 4, 6, 8, 10) where *x* is the molar ratio of APTES:TEOS.

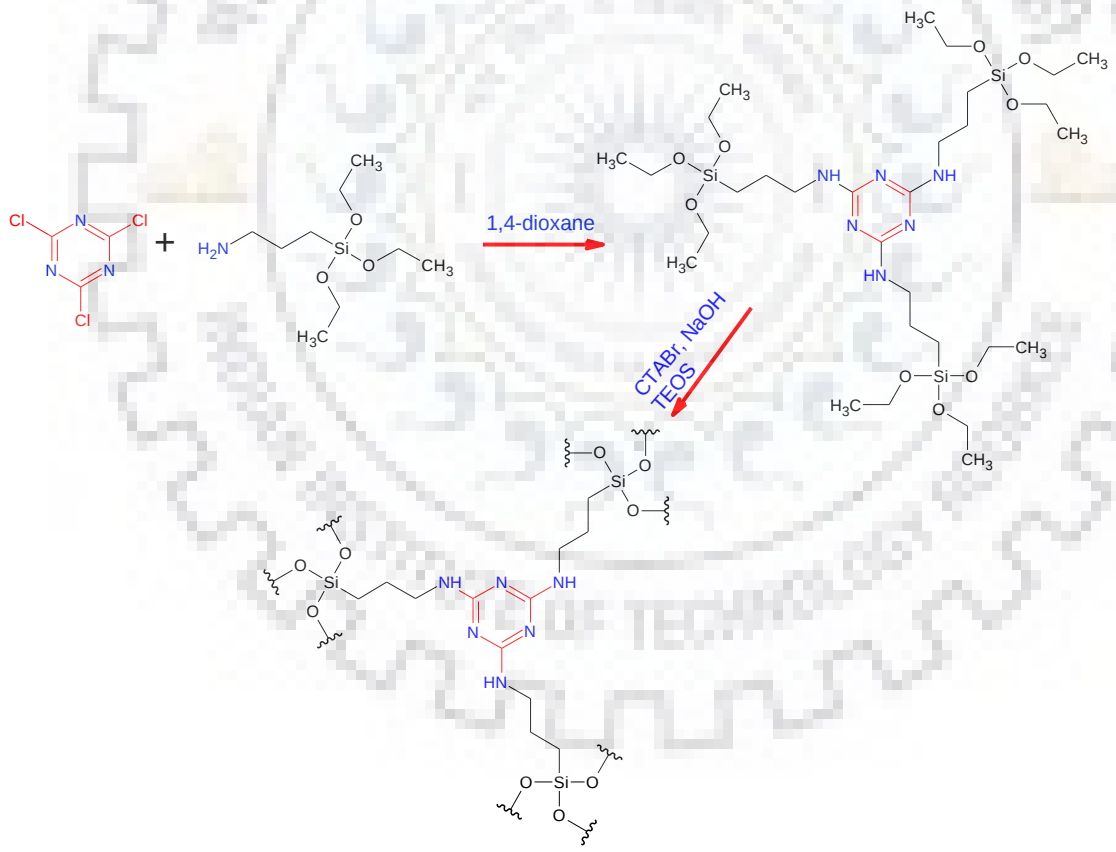

NETPMo-*x*M

Scheme 5.1: Reaction scheme for the synthesis of NETPMO-*x*M using nucleophilic condensation of CNC with APTES followed by co-condensation with TEOS, (where *x* is the molar ratio of APTES with respect to TEOS and its values are *x* = 0, 2, 4, 6, 8 and 10).

In order to understand the successful condensation of NETPMO-*x*M, spectroscopic investigation such as ^{13}C and ^{29}Si CPMAS NMR and FTIR were performed. The incorporation of triazine moiety in NETPMO-0M and NETPMO-8M was confirmed by the observation of resonance signal at δ of 165 ppm in ^{13}C CPMAS NMR spectra as shown in ***Figure 5.1a***.[1-4] Moreover, the additional signals at δ of 44, 23 and 10 ppm could be ascribed to aliphatic carbons of APTES as assigned in the inset of ***Figure 5.1a***.[5,6] The observation of only T sites in the ^{29}Si CPMAS NMR spectrum (***Figure 5.1b***) of NETPMO-0M confirms the absence of any inorganic silica, as no TEOS was used for the condensation.[7,8] This was further supported by the presence of both T and Q sites in ^{29}Si CPMAS NMR spectrum of NETPMO-8M, where APTES was co-condensed with TEOS (***Figure 5.1b***).[7,8] Detailed assignment of individual ^{13}C and ^{29}Si CPMAS NMR signals is given in ***Table 5.1a*** and ***5.1b***.

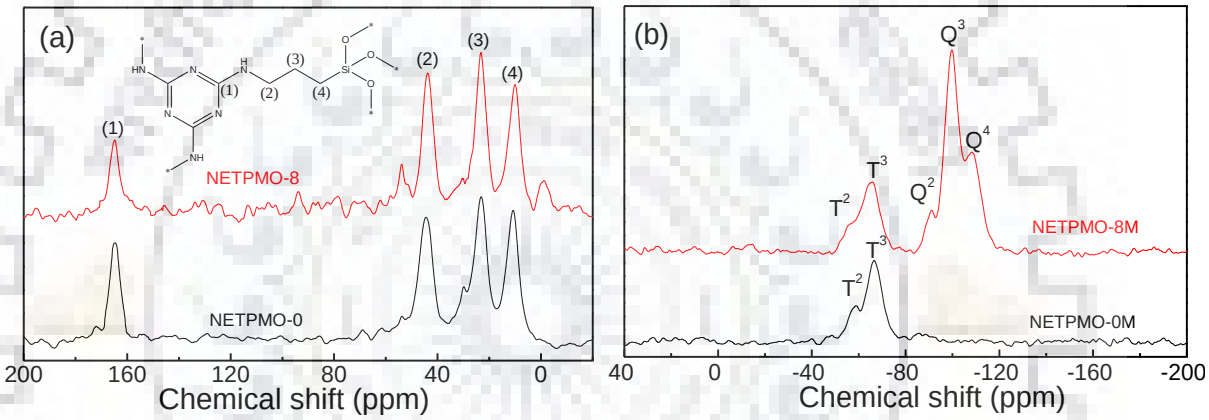

Figure 5.1: (a) ^{13}C and (b) ^{29}Si CPMAS NMR spectra of NETPMO-0M and NETPMO-8M.

Table 5.1a: ^{13}C CPMAS NMR signal description for NETPMO-0M and NETPMO-8M.

Sample ID	δ for Carbons (ppm)			
	(1)	(2)	(3)	(4)
NETPMO-0M	165	44	23	10
NETPMO-8M	165	44	23	10

Table 5.1b: ^{29}Si CPMAS NMR signal description for NETPMO-0M and NETPMO-8M.

Sample ID	δ for *T* sites (ppm)		δ for *Q* sites (ppm)		
	T^2	T^3	Q^2	Q^3	Q^4
NETPMO-0M	-59	-66	-	-	-
NETPMO-8M	-57	-65	-90	-100	-110

The observation of CPMAS NMR analysis was further corroborated by the FTIR investigation shown in ***Figure 5.2***, where bands at 1560 to 1340 cm^{-1} were observed due to -C=N- quadrant stretching and torsional bending, respectively in all the samples.[1,2] The -C=N- stretching and out-of-plane bending of triazine ring vibration bands were observed at 1270 and 740 cm^{-1}, respectively.[1,2] Additionally, the presence of stretching vibrations below 3000 cm^{-1} confirms the presence of $-CH_2-$ aliphatic chain originated from APTES.[5,6] The intensity of this band decreases in accordance with the increasing TEOS content with respect to APTES. Moreover, the absence of band at 850 cm^{-1}, due to -C-Cl stretching further prove the complete condensation of CNC in NETPMO-*x*M.[9] As expected, the -Si-O-Si- bands were observed in the region of 1205-1040 cm^{-1}.[5,6] The as-synthesized (non-extracted) samples display the sharp band at 2878 cm^{-1} due to aliphatic -C-H stretching of CTABr (***Figure 5.2b***).[5-7] This characteristic band in extracted specimen is attenuated while the other weak bands in this region correspond to -C-H stretching of APTES (***Figure 5.2a***). Detailed assignment of individual bands is given in ***Table 5.2***.

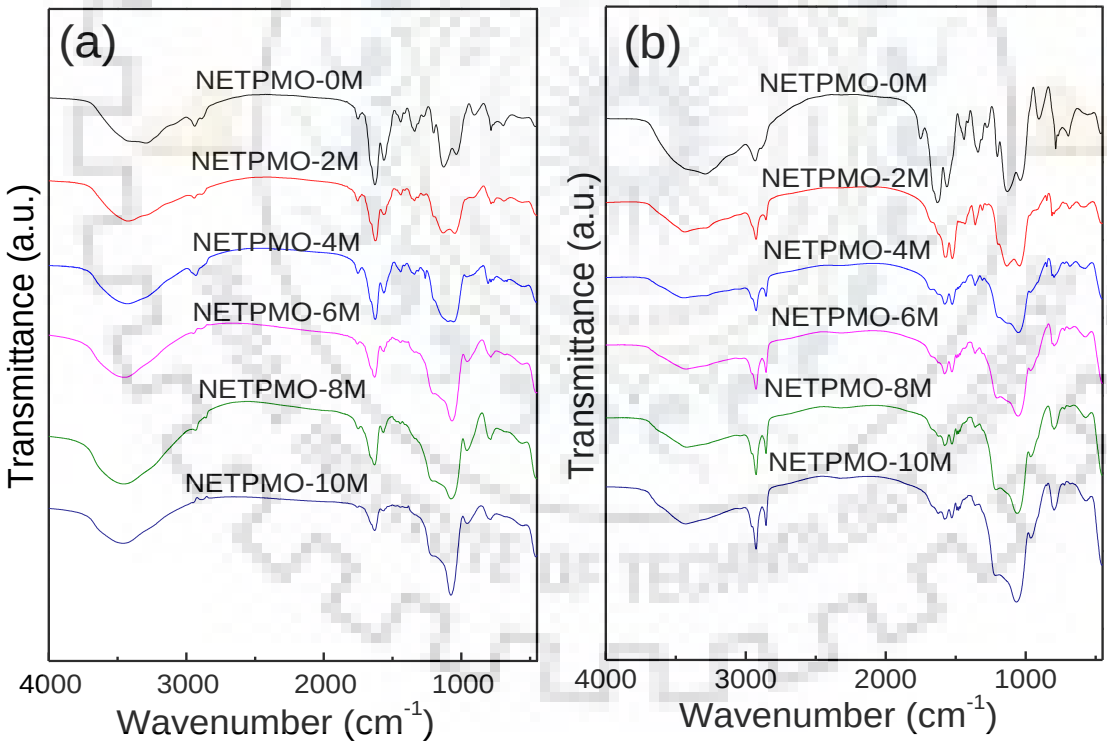

Figure 5.2: FTIR spectra of (a) extracted and (b) as synthesised NETPMO-*x*M specimens.

To further access the chemical environment and nature of elements, two representative samples, one synthesized without TEOS (NETPMO-0M) and the other synthesized with TEOS (NETPMO-8M), were analyzed by XPS as shown in the ***Figure 5.3*** and it revealed the peaks for Si, C, N and O.[10-14].

Table 5.2: FTIR band description for NETPMO-*x*M.

Sample ID / Band Assignments	Band positions in cm^{-1}	
	NETPMO-*x*M	**NETPMO-*x*M as-synthesized**
-O-H Stretching	3435	3435
-N-H stretching	3270	3270
-C-H stretching (APTES)	2930	2930
-C-H stretching (CTABr)	-	2878
O-H bending	1630	1630
-C=N quadrant stretching	1560	1560
-N-H bending	1505	1505
-C-H bending (APTES)	1450	1450
-C=N torsional bending	1340	1345
-C=N- stretching	1270	1270
Si-O-Si	1205	1205
Si-O-Si	1040	1035
Si-OH	905	905
Si-O-Si	785	785
oop triazine ring bending	740	740

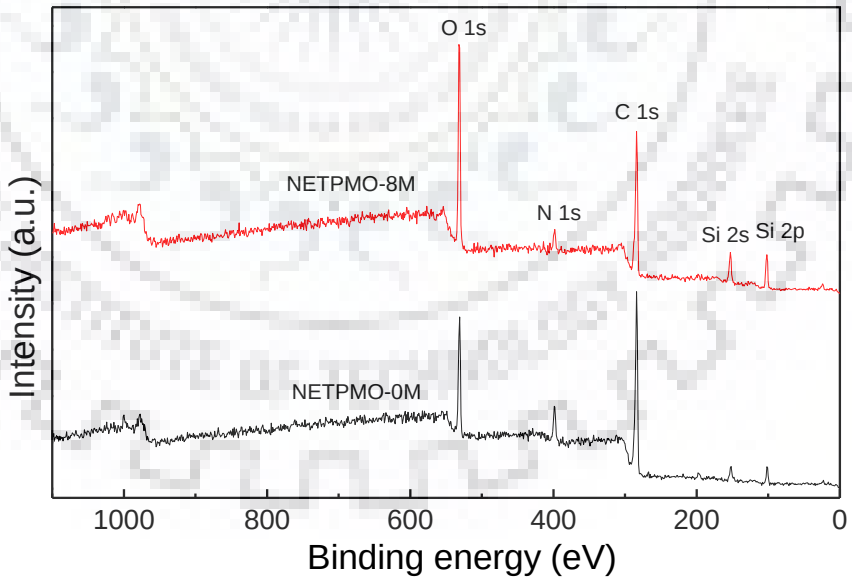

Figure 5.3: XPS survey scan for NETPMO-0M and NETPMO-8M.

The high-resolution C 1s spectrum of NETPMO-0M, as shown in ***Figure 5.4(a)*** has three peaks at 284.8, 285.7 and 288.7 eV corresponding to -C-Si, -C-H and -C-N carbons, respectively.[15,16] The peak at 288.7 eV owing to -C-N further confirms the incorporation of triazine and corroborate the CPMAS NMR analysis. The high-resolution C 1s spectrum of

NETPMO-8M, shows the peaks at similar binding energy for -C-Si, -C-H and triazine ring carbons at 284.8, 285.7 and 288.7 eV, respectively. [15-17] The N 1s high resolution spectra given in ***Figure 5.4b*** have shown the peaks at 398.4 and 399.7 eV due to aminal and triazine nitrogen, respectively.[18-21] The O 1s high resolution spectra shown in ***Figure 5.4c*** have demonstrated the peaks at 532 and 533 eV owing to Si-O-Si and Si-O-H, respectively.[17] The Si 2p high resolution spectrum of NETPMO-0M given in ***Figure 5.4d*** have shown two peaks at 101.4 and 102.5 eV pertaining to organosilica and Si-OH. The Si 2p spectrum of NETPMO-8M have peaks at 102.2, 102.9 and 104.2 eV. The peak at 102.9 eV is observed due to inorganic silica which further confirm the condensation of TEOS while the peaks at 102.2 and 104.2 eV are ascribed to organosilica and Si-OH. The increase in the binding energy in NETPMO-8M, is attributed to the increase of electronegative oxygen as compared to NETPMO-0M.[10,17]

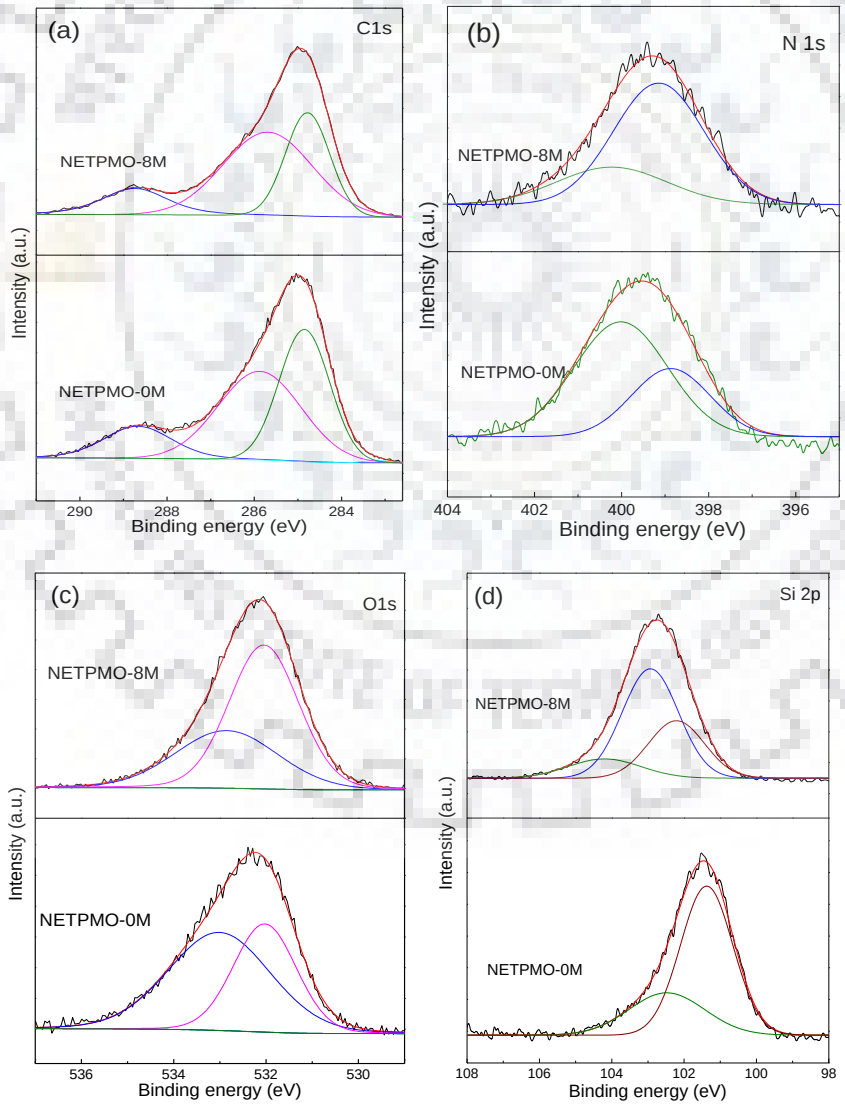

Figure 5.4: (a) C 1s, (b) N 1s, (c) O 1s and (d) Si 2p high resolution spectra of NETPMO-0M and NETPMO-8M.

Thermogravimetric analysis (TGA) performed in air revealed that NETPMO-*x*M are stable up to 620 K as shown in ***Figure 5.5***. The mass loss below 373 K could be ascribed to release of adsorbed water, atmospheric gases and organic solvents. The second mass loss beyond 620 K and up to 700 K is due to decomposition of incorporated organic moiety -CH_2- and triazine in the framework.[22] When the as-synthesized samples were employed for the TGA (***Figure 5.5b, Figure 5.5d and Figure 5.5f***), all the above-mentioned mass loss steps are observed in these samples. Additionally, mass loss between 420 to 520 K was observed and this mass loss step is not seen in the extracted specimens. This mass loss is due to the decomposition of the CTABr template.[23] This further indicates that the procedure adopted in this study to remove the template is effective. As expected, the mass loss of the NETPMO-*x*M is a function of TEOS content. With increase in the TEOS content, there was a regular decrease in the mass loss that further supports the incorporation of organic moiety in framework.

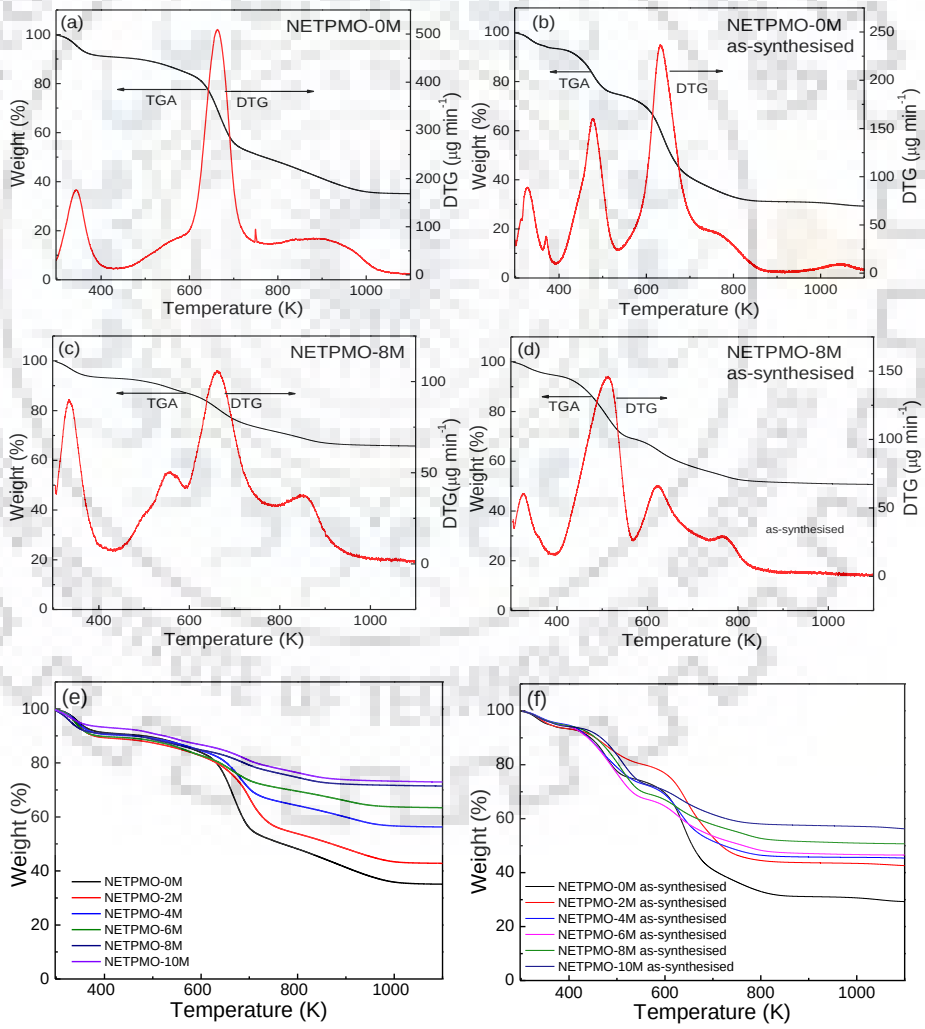

Figure 5.5: TGA/DTG thermograms of (a) extracted NETPMO-0M, (b) as-synthesised NETPMO-0M, (c) extracted NETPMO-8M, (d) as-synthesised NETPMO-8M, (e) extracted NETPMO-*x*M and (f) as-synthesised NETPMO-*x*M measured in air.

The elemental composition (C, N and H %) of NETPMO-*x*M estimated using CHNS/O analyser has been summarized in ***Table 5.3***. The wt% of C and N keeps on decreasing with increasing TEOS but their C/N ratio remains about 1.75 similar to their theoretical C/N ratio with minor deviation. This deviation could be ascribed to unhydrolyzed ethoxy group which is well documented.[5-7,24] With increasing TEOS, the wt% of N and C decreases because Si content is increasing. In order to introduce the long-range mesoscale periodicity, NETPMO-*x*M were synthesized using CTABr as structure directing agent. The SAXS patterns of NETPMO-*x*M are shown in ***Figure 5.6***. The SAXS patterns didn't reveal any sharp peak which indicates that NETPMO-*x*M lack long range mesoscale periodicity.

Table 5.3: C, H and N elemental analyses of NETPMO-*x*M.

Element / Sample ID	N wt%	C wt%	H wt%	C/N ratio
NETPMO-0M	16.57	29.08	6.22	1.75
NETPMO-2M	11.13	19.07	5.66	1.71
NETPMO-4M	7.34	13.14	6.16	1.79
NETPMO-6M	6.14	11.60	5.82	1.88
NETPMO-8M	4.95	9.48	5.57	1.91
NETPMO-10M	4.48	8.48	4.72	1.89

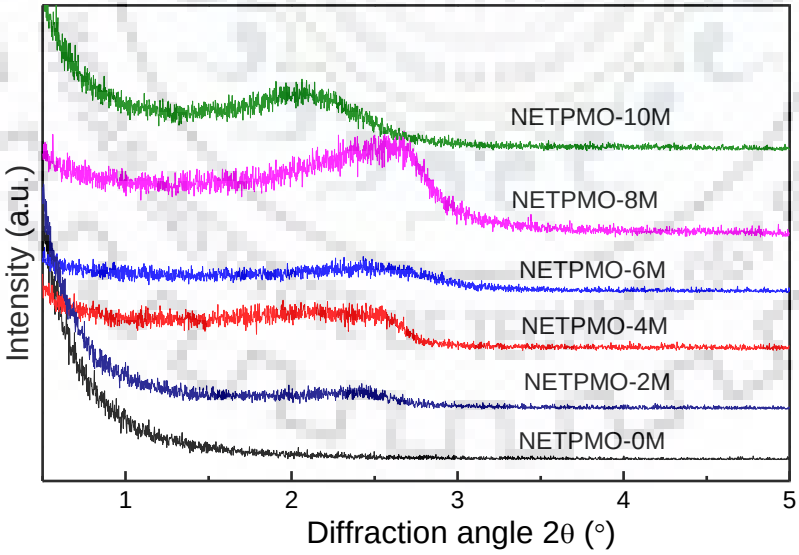

Figure 5.6: SAXS patterns of NETPMO-*x*M.

The microstructural analysis of NETPMO-*x*M was carried out by FESEM and TEM. The FESEM images given in ***Figure 5.7*** have revealed that NETPMO-*x*M consists of agglomerated particles of nearly spherical shape with variable sizes in the range of 500 nm to 1 μm. Further, TEM analysis of representative sample i.e. NETPMO-8M revealed ultra-small

pores with diameters of 2-3 nm in ***Figure 5.8a***. The SAED pattern given in ***Figure 5.8b*** has broad diffused ring which indicate that the NETPMO-8M is amorphous in nature.

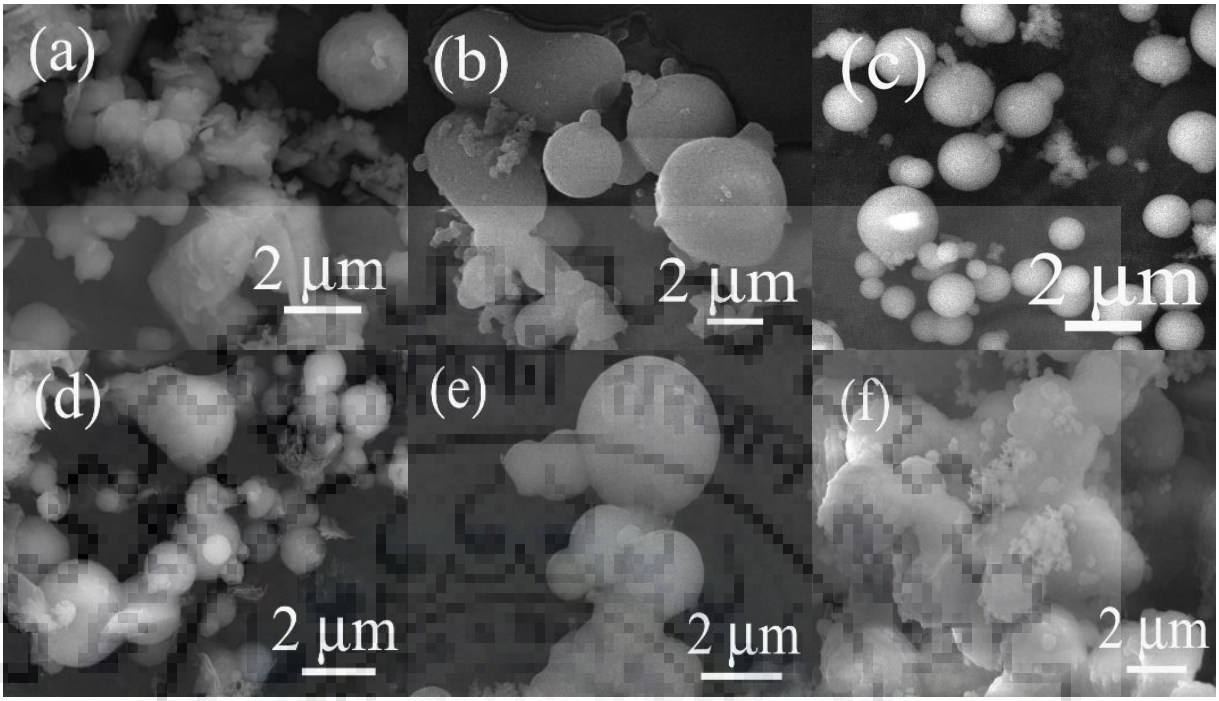

Figure 5.7: FESEM images of (a) NETPMO-0M, (b) NETPMO-2M, (c) NETPMO-4M, (d) NETPMO-6M, (e) NETPMO-8M and (f) NETPMO-10M.

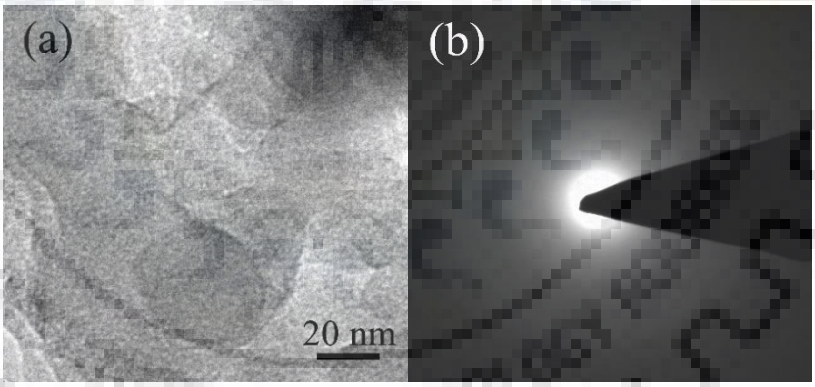

Figure 5.8: (a) TEM image and (b) SAED pattern of NETPMO-8M.

5.2.1.2. Textural analysis of NETPMO-xM

The textural property carried out using N_2 sorption analysis at 77 K as shown in ***Figure 5.9*** confirms the porous nature of NETPMO-*x*M. N_2 sorption isotherms are completely reversible in nature. Among all the specimens synthesized in this work, the NETPMO-8M has the maximum SA_{BET} of 1304 m^2 g^{-1}. The isotherm is type-IV with small hysteresis that extends from low pressure range to higher pressure range. This indicates that the material has hierarchical pore structure which is mainly due to the combination of the mesopores originated from the structure directing agent along with the inter-particulate pores, which can be seen in

the TEM image also. The PSD shown in ***Figure 5.10*** was performed by DFT model. The majority of the pores in these specimens were found to be centred in the range of 2.5 to 3.7 nm with minority of these have distributions centred at 8.1 and 9.4 nm. The observed reduction in pore width with increasing TEOS content could be ascribed to thickening of pore wall.[25] Similarly, all other specimens synthesized in this work have similar isotherm characteristics, with observation of additional microporosity in sample NETPMO-4M. Detailed textural properties of all these specimens have been summarized in ***Table 5.4***. It can be seen that the SA_{BET} of NETPMO-*x*M increased from 232 to 1304 m^2 g^{-1} on increasing the APTES to TEOS ratio up to 1:8, however, on further increasing the ratio to 1:10, there was a decrease in the SA_{BET} (***Table 5.4***). This phenomenon is commonly observed in the organosilica frameworks synthesized by a similar co-condensation of organosilica precursors with TEOS.[5,7] In such cases, SA_{BET} reduces owing to increase in pore wall thickness [47]. Further, in order to understand the effect of triazine moiety on textural properties of silica framework, a sample AP-TEOS-8 was synthesised by co-condensing APTES with TEOS at the ratio of 1:8 without using CNC. In this sample, the estimated SA_{BET} was only 454 m^2 g^{-1} (***Figure 5.9b***) as against 1304 m^2 g^{-1} in NETPMO-8M. This indicates that the presence of triazine moiety is tuning the textural properties of the synthesized organosilicas by providing a synergy effect. Similar synergy effect in the textural properties of organosilicas have earlier been observed.[5,7]

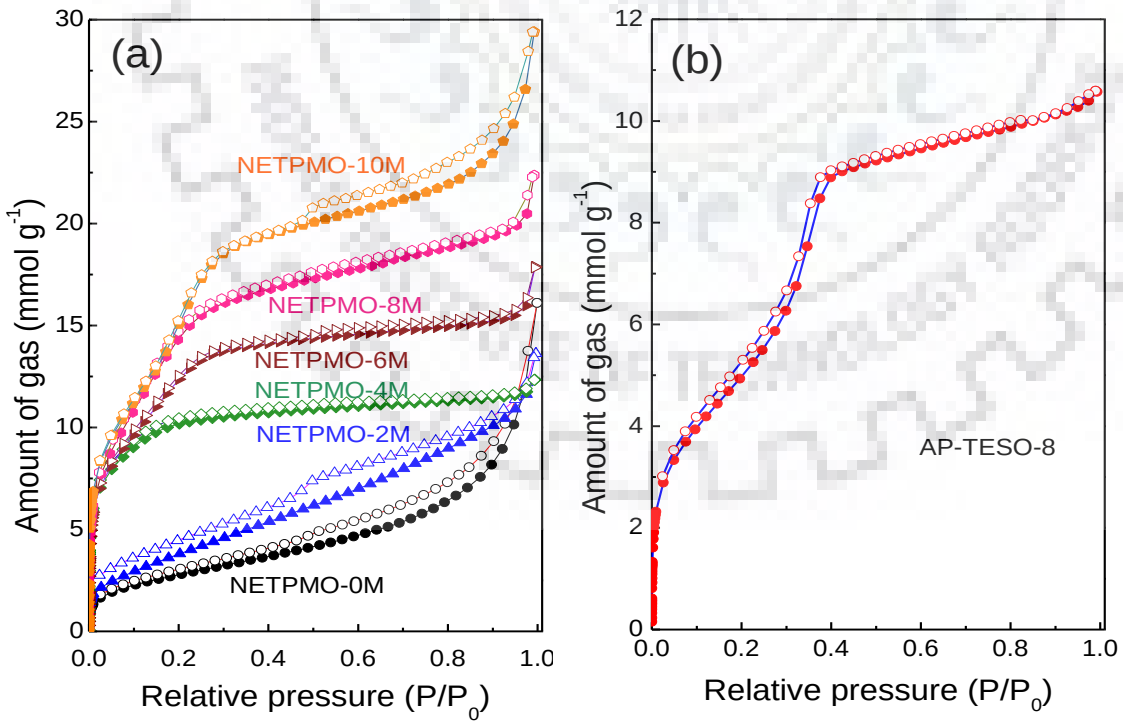

Figure 5.9: N_2 adsorption (filled symbols) and desorption (empty symbols) isotherms for (a) NETPMO-*x*M and (b) AP-TEOS-8 measured at 77 K.

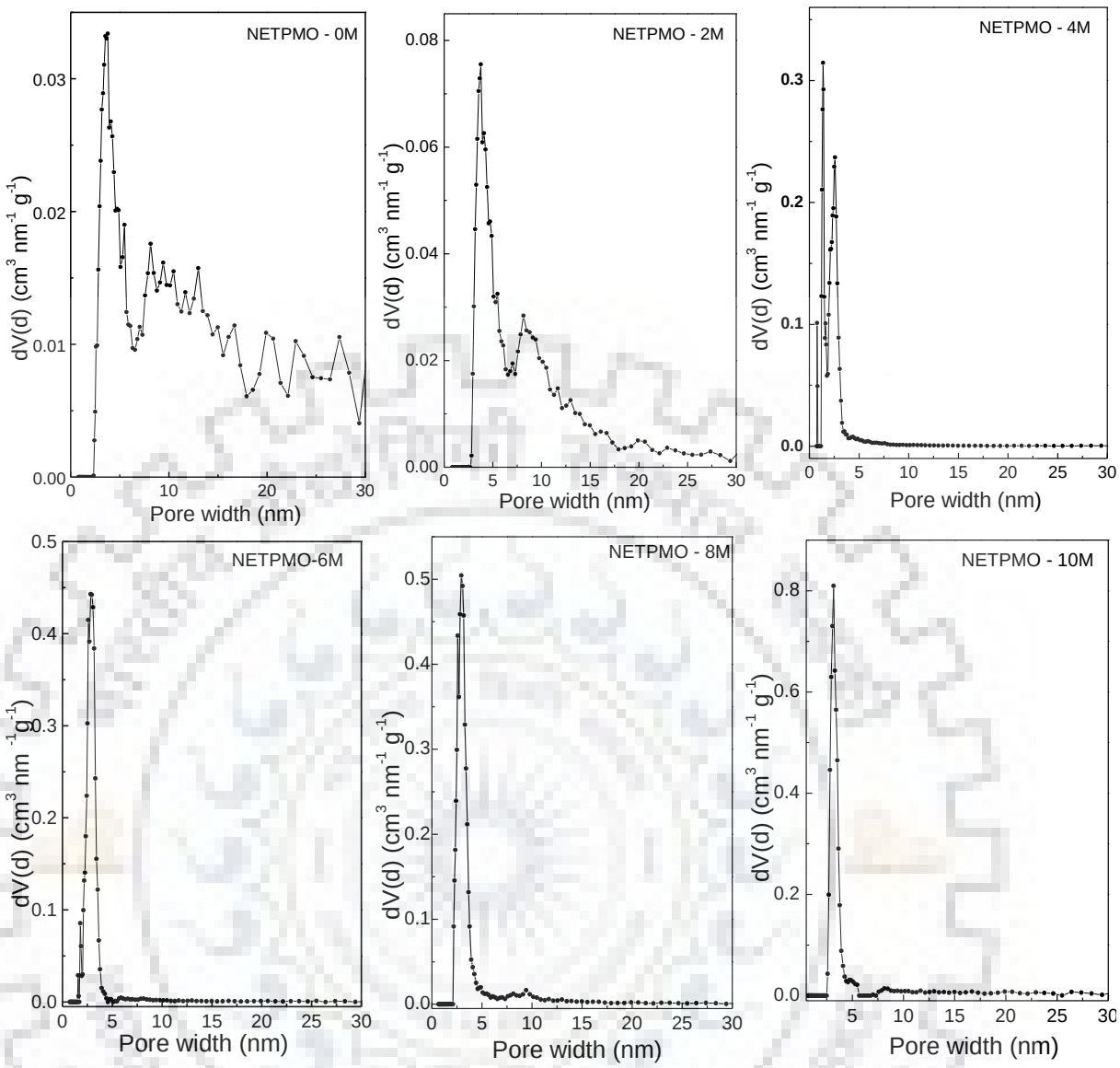

Figure 5.10: PSD plots for NETPMO-*x*M calculated using DFT model.

5.2.1.3. CO_2 sorption study of NETPMO-xM

The presence of amine groups attached to the nitrogen rich triazine ring of the NETPMO-*x*M framework with substantially high SA_{BET} has encouraged us to investigate the CO_2 capture behaviour of these specimens. The CO_2 sorption of the adsorbents has been studied at 273 K and up to 1 bar pressure. The CO_2 sorption isotherms of NETPMO-*x*M have been given in ***Figure 5.11***. It is important to note that all the isotherms measured at 273 K are reversible in nature with a maximum CO_2 uptake of 11.6 wt% observed in NETPMO-8M. It is important to note that the CO_2 adsorption on the surface is a complex phenomenon and depends upon several factors. Some of the important parameters that decide the overall CO_2 capture capacity are; (i) SA_{BET}, (ii) PSD, (iii) pore volume, and (iv) surface functionality. The higher the surface area higher will be the adsorption capacity keeping all other parameters identical. The PSD has

a complex role in tuning the CO_2 capture capacity. In general, a small PSD especially in the micropore region enhances the CO_2 capture capacity owing to enhanced capillary action and superior van der Waals interaction. However, this is not always true as the kinetic factor limits the accessibility of the active site on many occasions. A higher pore volume holds larger amount of CO_2. The increase in the electron density in the framework by introducing various functionalities, in general, could improve the CO_2 capture capacity due to the Lewis base-Lewis acid interaction. Thus, as discussed above there is always a trade-off between the kinetics and thermodynamics that ultimately determines the overall CO_2 capture capacity of any adsorbent material.

In the present research, the CO_2 uptake of 11.6 wt% by NETPMO-8M could be attributed to the highest SA_{BET} among all these specimens. The CO_2 uptake of 10.2 wt% in NETPMO-0M is marginally lower compared to NETPMO-8M, although, the SA_{BET} of NETPMO-0M (232 m^2 g^{-1}) is 5.6 times lower than NETPMO-8M (1304 m^2 g^{-1}). This indicates that the higher content of electron rich nitrogen has significant role in CO_2 uptake for NETPMO-0M. This was further supported by the fact that all other samples with higher SA_{BET} have lower CO_2 capture capacity as compared to NETPMO-0M (***Table 5.4***). However, the CO_2 uptake for NETPMO-4M and NETPMO-6M is lower than NETPMO-8M despite having higher nitrogen content. The presence of micro-porosity in NETPMO-4M evident from N_2 sorption isotherm is not reflecting its effect on CO_2 uptake, which could be due to the pore blockage. Thus, as discussed above, there is a trade-off between surface functionality, SA_{BET} and PSD that dictates the CO_2 capture capacity. The presence of triazine ring and high amine functionality in framework is the additional advantage which is helpful in enhancing the Lewis basic nature of framework.

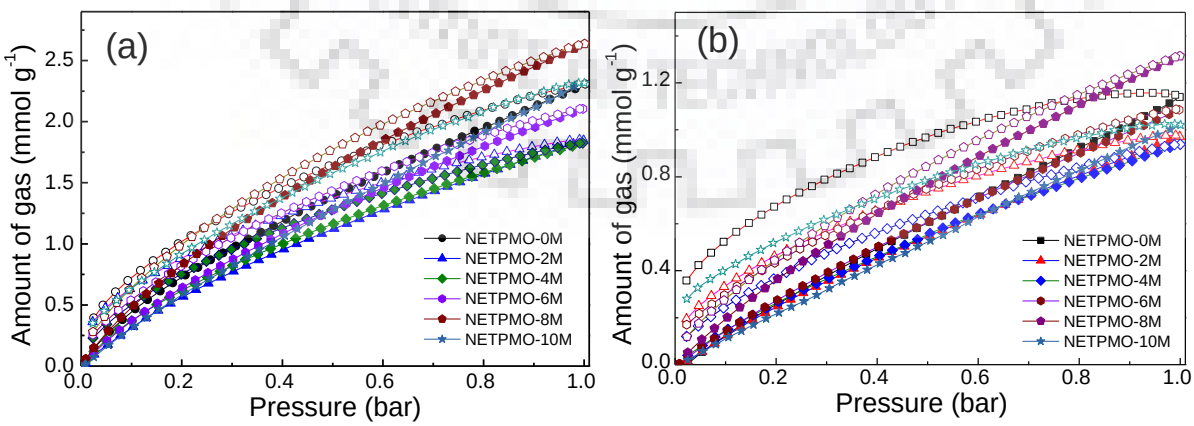

Figure 5.11: (a) and (b) are CO_2 adsorption (filled symbols) and desorption (empty symbols) isotherms of NETPMO-*x*M measured at 273 and 298 K, respectively at 1 bar.

The CO_2 capture capacities of the NETPMO-*x*M have been further investigated at 298 K to study the capture capacity at higher temperature and also to understand the thermodynamics properties. The isotherms measured at 298 K are shown in ***Figure 5.11b***. The CO_2 capture capacity of 5.8 wt% was estimated for the NETPMO-8M. The CO_2 capture capacities of all the samples are given in ***Table 5.4***. Further, to access the interaction of CO_2 with NETPMO-*x*M, the Q_{st} was calculated using Clausius–Clapeyron equation (***Figure 5.12***). The Q_{st} value of 48.6 kJ mol^{-1} for NETPMO-0M, was highest among all NETPMO-*x*M which further indicates the presence of significantly higher nitrogen content in NETPMO-0M than all other samples (***Table 5.4***). The Q_{st} values for NETPMO-*x*M lies in the range of 24.4 to 48.6 kJ mol^{-1}, which indicates that the interaction of CO_2 with NETPMO-*x*M is physisorption in nature.

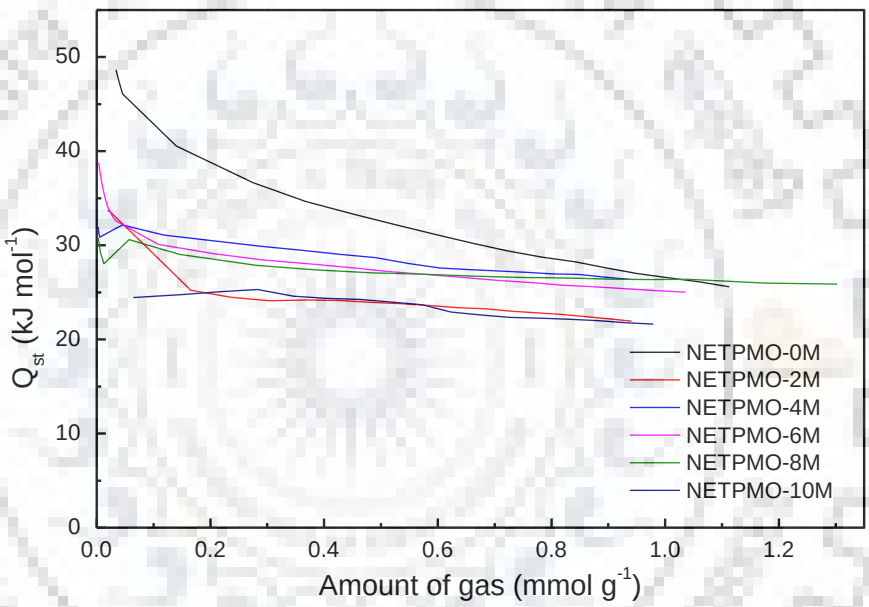

Figure 5.12: Q_{st} for CO_2 adsorption on NETPMO-*x*M.

Table 5.4: Textural properties and CO_2 adsorption for NETPMO-*x*M.

Sample	SA_{BET} (m^2 g^{-1})	Pore size (nm)	Pore Vol. (cm^3 g^{-1})	CO_2 uptake (wt%)		Q_{st} (kJ mol^{-1})
				273 K	298 K	
NETPMO-0M	232	3.6	0.55	10.2	5.0	48.6
NETPMO-2M	339	3.7	0.47	8.1	4.3	33.7
NETPMO-4M	625	2.5	0.31	8.0	4.1	31.8
NETPMO-6M	1085	2.9	0.62	9.3	4.7	38.7
NETPMO-8M	1304	2.9	0.78	11.6	5.8	30.7
NETPMO-10M	1131	3.2	1.02	10.1	4.5	24.4

5.2.2. NETPMO-*x*D (*x* = 0, 2, 4, 6, 8 and 10)

5.2.2.1. Synthesis and characterization of NETPMO-xD

As discussed above, the condensation of APTES with CNC followed by co-condensation with TEOS resulted in the formation high surface area NETPMO-*x*M with impressive CO_2 capture capacity. As proposed, the enrichment of frameworks by the electron rich heteroatoms has profound effect on the CO_2 capture capacity. To further increase the nitrogen content in the materials, a diamine precursor (TMSPD) was condensed with CNC as shown in ***Scheme 5.2***, followed by polycondensation to synthesize NETPMO-*x*D. The NETPMO-*x*D were analyzed by the similar techniques used for NETPMO-*x*M, and further used for CO_2 sorption application.

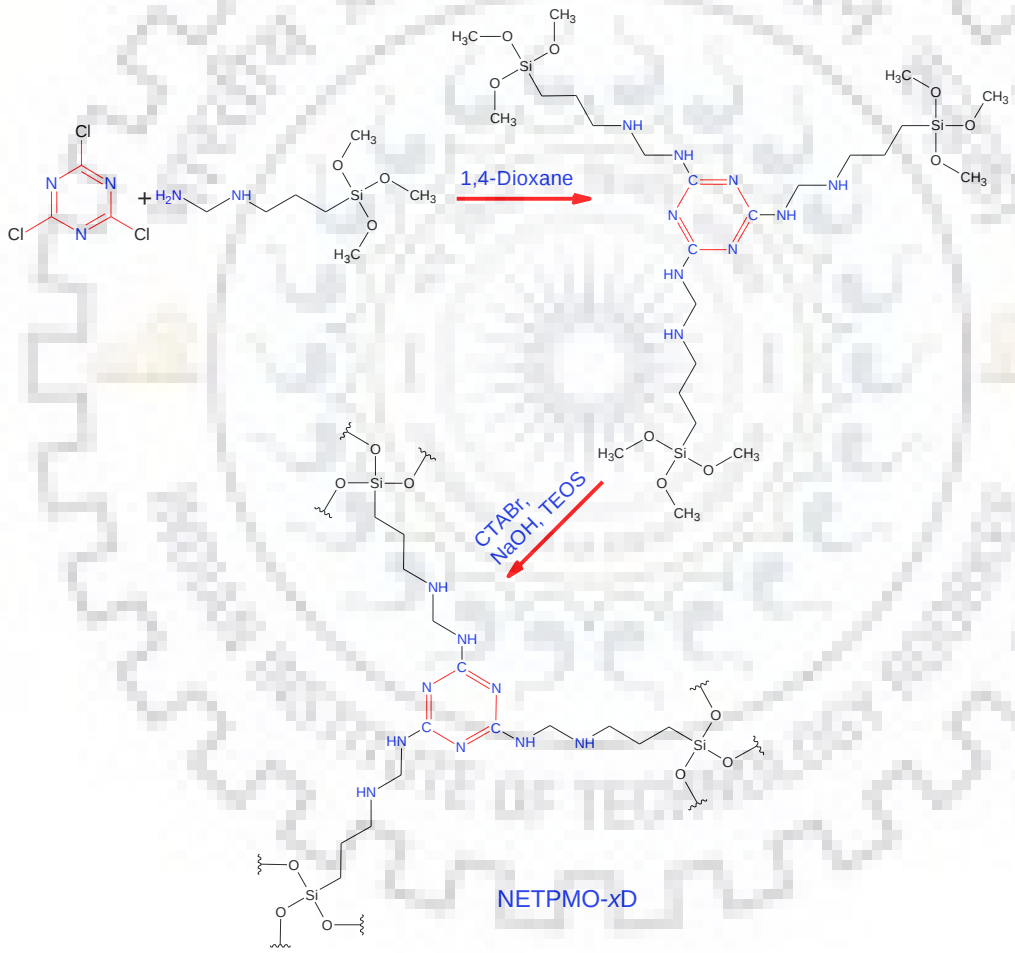

Scheme 5.2: Reaction scheme for the synthesis of NETPMO-*x*D using nucleophilic condensation of CNC with TMSPD followed by co-condensation with TEOS, (where *x* is the molar ratio of TMSPD with respect to TEOS and its values are *x* = 0, 2, 4, 6, 8 and 10).

The ^{13}C and ^{29}Si CPMAS NMR, and FTIR spectroscopic investigation confirmed the proposed structure. Observation of a signal at ~165 ppm in ^{13}C CPMAS NMR spectra as shown in ***Figure 5.13a*** confirms the incorporation of triazine moiety in the NETPMO-0D and

NETPMO-6D.[1-4] The signal at 153 ppm could be ascribed to end group functionality. The signals in the δ range of 51 to 08 ppm are observed due to aliphatic carbons of TMSPD. The ^{13}C CPMAS NMR signals shown in ***Figure 5.13a*** have been assigned to various carbon as per their chemical environment and are well aligned with the proposed structure. The ^{29}Si CPMAS NMR spectrum of NETPMO-0D possess the signal for *T sites* only while and NETPMO-6D possess the signals for *T sites* as well as *Q sites* (***Figure 5.13b***), and NMR spectral patterns are similar to NETPMO-0M and NETPMO-8M. The detailed assignment of individual ^{13}C and ^{29}Si CPMAS NMR signals is given in ***Table 5.5a*** and ***5.5b***, respectively.

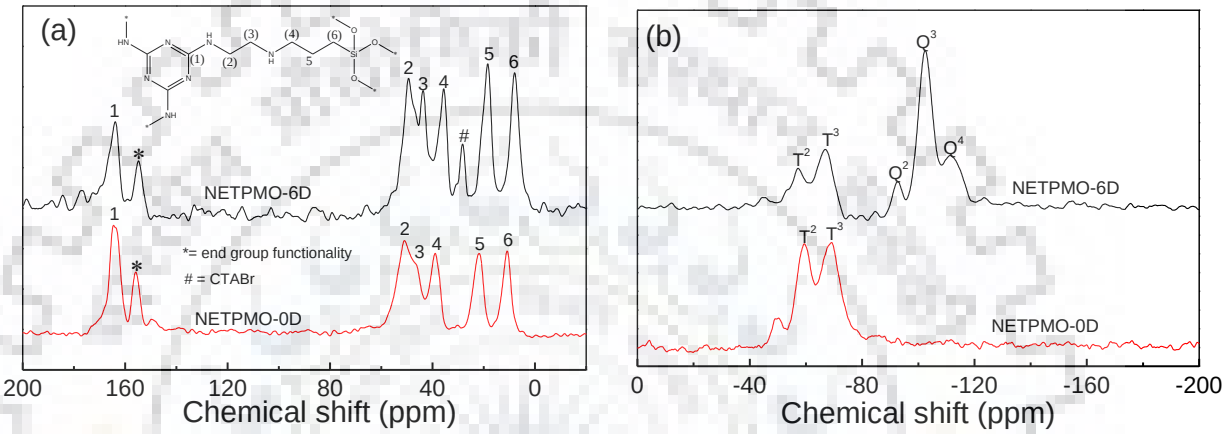

Figure 5.13.: (a) ^{13}C and (b) ^{29}Si CPMAS NMR spectra of NETPMO-0D and NETPMO-6D.

Table 5.5a: ^{13}C CPMAS NMR signal description for NETPMO-0D and NETPMO-6D.

Sample ID	δ for Carbons (ppm)					
	(1)	(2)	(3)	(4)	(5)	(6)
NETPMO-0D	165	51	46	39	21	10
NETPMO-6D	164	50	44	36	19	08

Table 5.5b: ^{29}Si CPMAS NMR signal description for NETPMO-0D and NETPMO-6D.

Sample ID	δ for *T* sites (ppm)		δ for *Q* sites (ppm)		
	T^2	T^3	Q^2	Q^3	Q^4
NETPMO-0D	-59	-69	-	-	-
NETPMO-6D	-57	-67	-93	-102	-112

As expected, the FTIR spectra in ***Figure 5.14*** further corroborated the CPMAS NMR analysis. The FTIR band patterns of extracted and as-synthesised NETPMO-*x*D specimens are consistent with the FTIR band patterns of NETPMO-*x*M. The observation of bands due to -C=N quadrant stretching and -C=N torsional bending at 1545 and 1345 cm^{-1} confirm the incorporation of triazine ring in NETPMO-*x*D.[1-4] The absence of band at 2878 cm^{-1} due to -

C-H stretching of CTABr confirms the removal of template.[5-7] The bands for rest of the functionality are summarised in ***Table 5.6***.

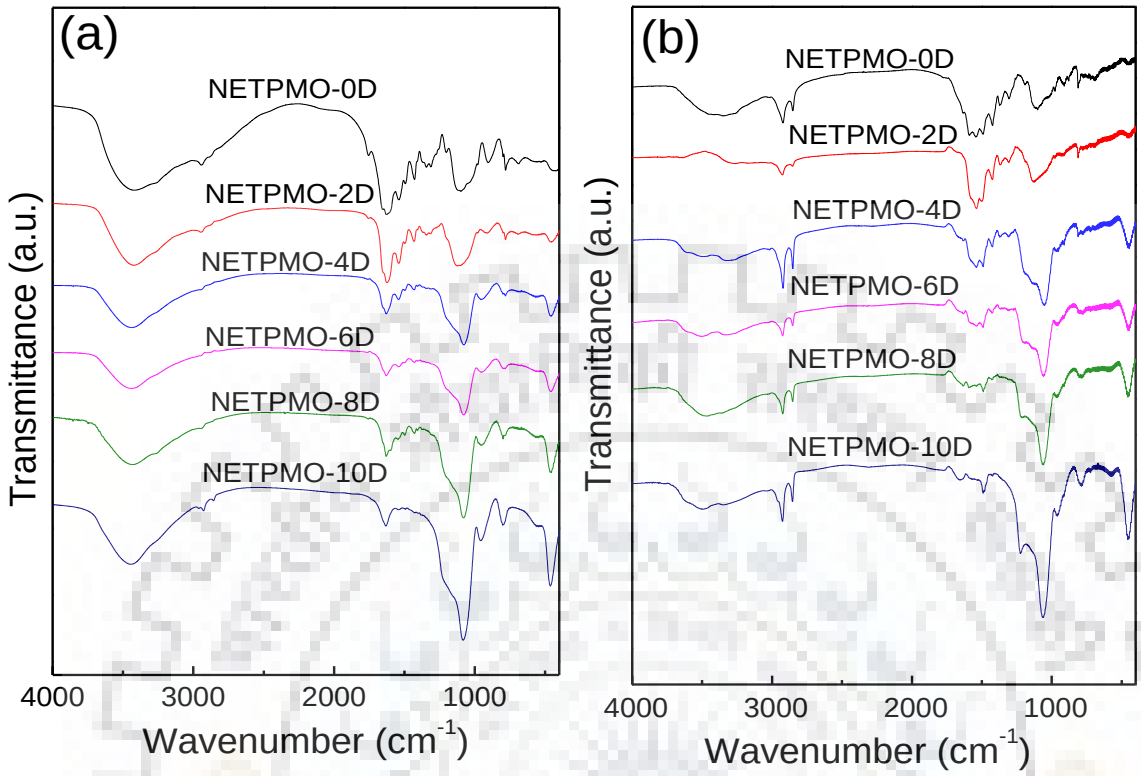

Figure 5.14: FTIR spectra of (a) extracted and (b) as-synthesised NETPMO-*x*D.

Table 5.6: FTIR band description for NETPMO-*x*D.

Bands assignments	**Band positions (cm^{-1})**
-O-H stretching	3451
-N-H stretching	3256
-C-H stretching	2946
O-H bending	1660
-C=N quadrant stretching	1545
-N-H bending	1495
-C-H bending (APTES)	1435
-C=N torsional bending	1345
Si-O-Si	1202
Si-O-Si	1032
Si-OH	907
Si-O-Si	780
Out-of-plane ring bending of triazine	715

The TGA as shown in ***Figure 5.15***, demonstrated that the NETPMO-*x*D are thermally stable up to a temperature of 500 K in air. The mass loss profile is similar to the NETPMO-*x*M. The elemental composition (C, N and H) of NETPMO-*x*D has been summarized in ***Table 5.7***. The N content of NETPMO-*x*D is higher than NETPMO-*x*M. The wt% of C and N keeps on decreasing with increasing TEOS but their C/N ratio remains about 1.75 similar to their theoretical C/N ratio with minor deviation, a pattern similar to NETPMO-*x*M.[5-7] The absence of peaks in SAXS pattern shown in ***Figure 5.16*** confirms the disordered nature of the samples. The FESEM images given in ***Figure 5.17*** have revealed that NETPMO-*x*D consists of agglomerated particles of variable sizes in the range of 100 nm to 2 µm. TEM image of representative sample, NETPMO-6D, revealed that the pores of 2-3 nm diameters could be seen in ***Figure 5.18a***. The SAED pattern given in ***Figure 5.18b*** consists of broad diffused ring which confirms the amorphous nature of the sample.

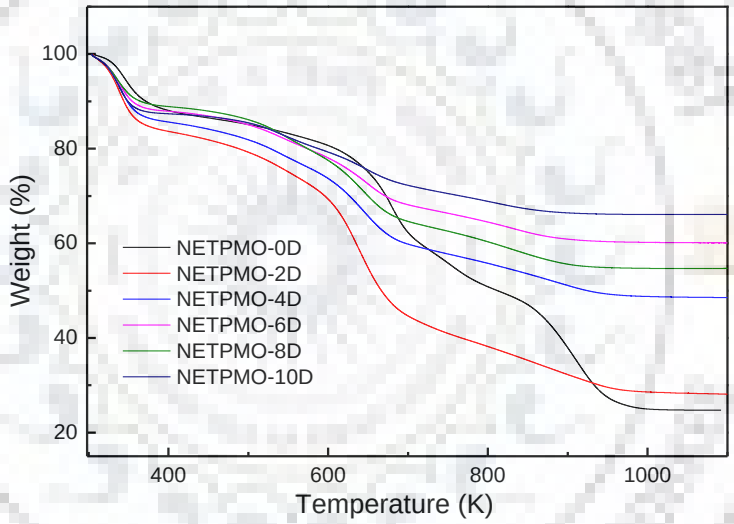

Figure 5.15: TGA thermograms of NETPMO-*x*D.

Table 5.7: C, H and N elemental analyses of NETPMO-*x*D.

Element / Sample	N wt%	C wt%	H wt%	C/N ratio
NETPMO-0D	17.66	31.88	5.76	1.81
NETPMO-2D	14.59	25.48	5.03	1.75
NETPMO-4D	8.26	15.20	4.16	1.84
NETPMO-6D	6.52	11.59	3.44	1.78
NETPMO-8D	5.36	10.02	3.35	1.86
NETPMO-10D	4.96	8.92	2.93	1.80

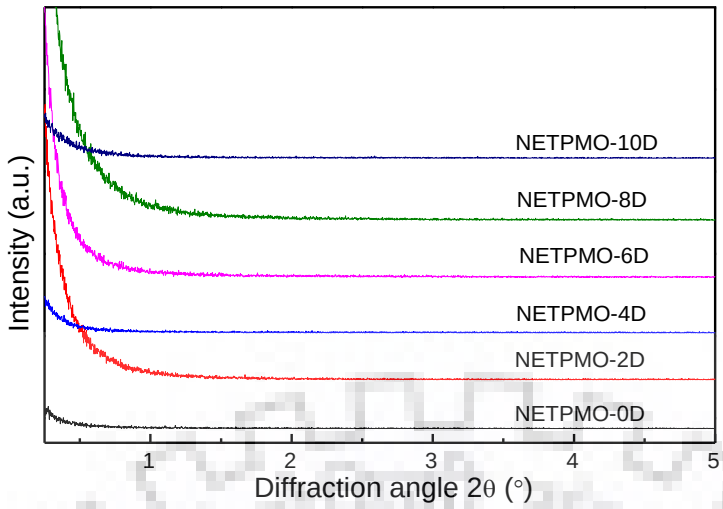

Figure 5.16: SAXS patterns of NETPMO-*x*D.

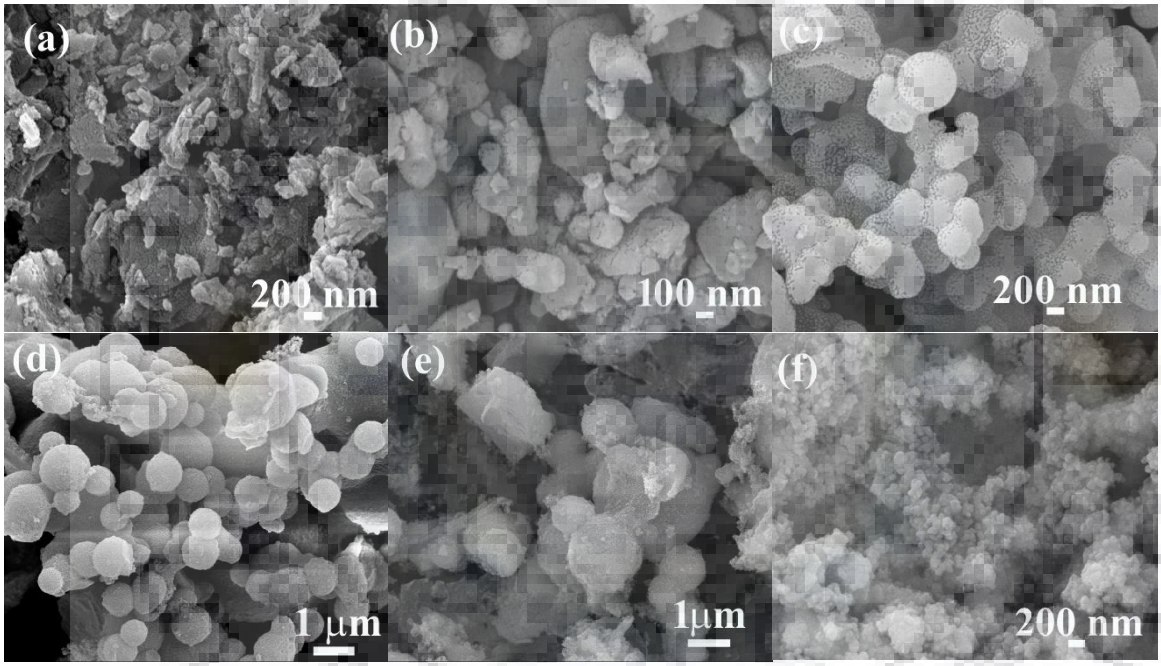

Figure 5.17: FESEM images of (a) NETPMO-0D, (b) NETPMO-2D, (c) NETPMO-4D, (d) NETPMO-6D, (e) NETPMO-8D and (f) NETPMO-10D.

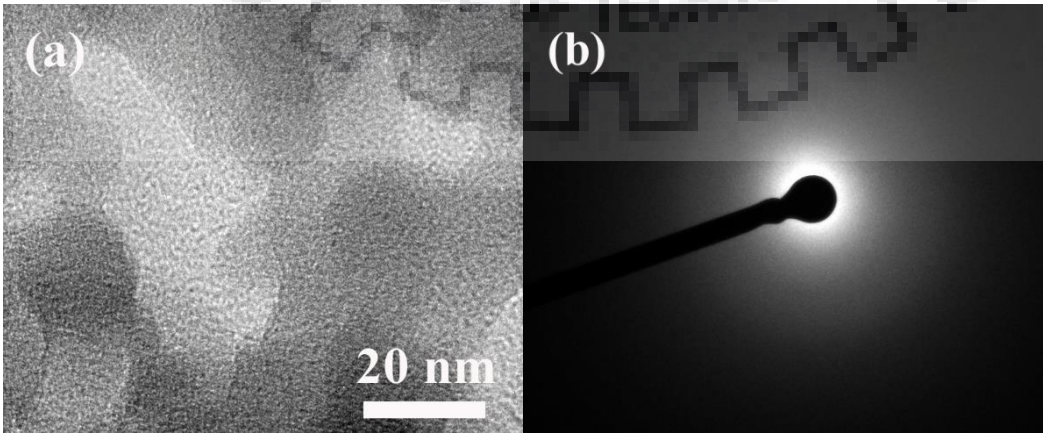

Figure 5.18: (a) TEM images and (b) SAED pattern of NETPMO-6D.

5.2.2.2. Textural analysis of NETPMO-xD

The textural analysis of NETPMO-*x*D was performed using N_2 sorption analysis at 77 K. The typical N_2 sorption isotherms of all the specimens are shown in ***Figure 5.19***. The SA_{BET} of NETPMO-*x*D varies in the range of 29 to 484 m^2 g^{-1} with increasing the ratio of TMSPD to TEOS up to 1:6 and beyond this, the increased ratio of TMSPD to TEOS was not effective in increasing the SA_{BET}. A similar phenomenon was also observed for NETPMO-*x*M and well reported for the organo-silica materials synthesized by co-condensation with TEOS.[5-7] The N_2 sorption isotherms show hysteresis in higher pressure range indicating the presence of mesopores. This was further supported by the PSD study. The majority of the pores of NETPMO-*x*D were found to be centered in mesopore region with pore diameter in the range of 2.8 to 4.8 nm (***Figure 5.20).*** The detailed textural properties have been given in ***Table 5.8***.

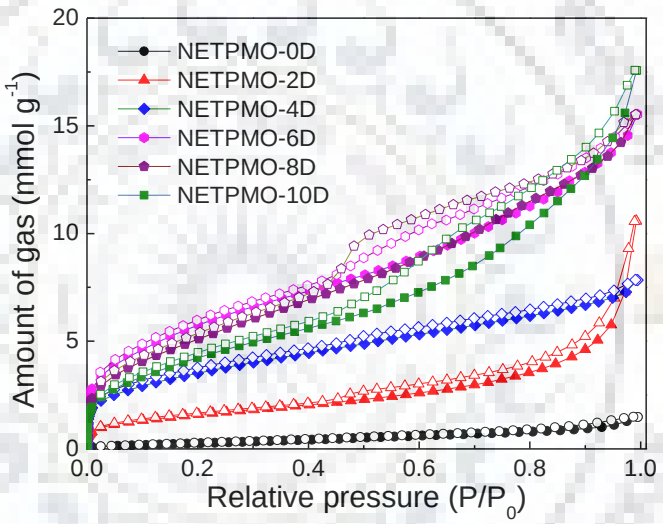

Figure 5.19: N_2 adsorption (filled symbols) and desorption (empty symbols) isotherms for NETPMO-*x*D measured at 77 K.

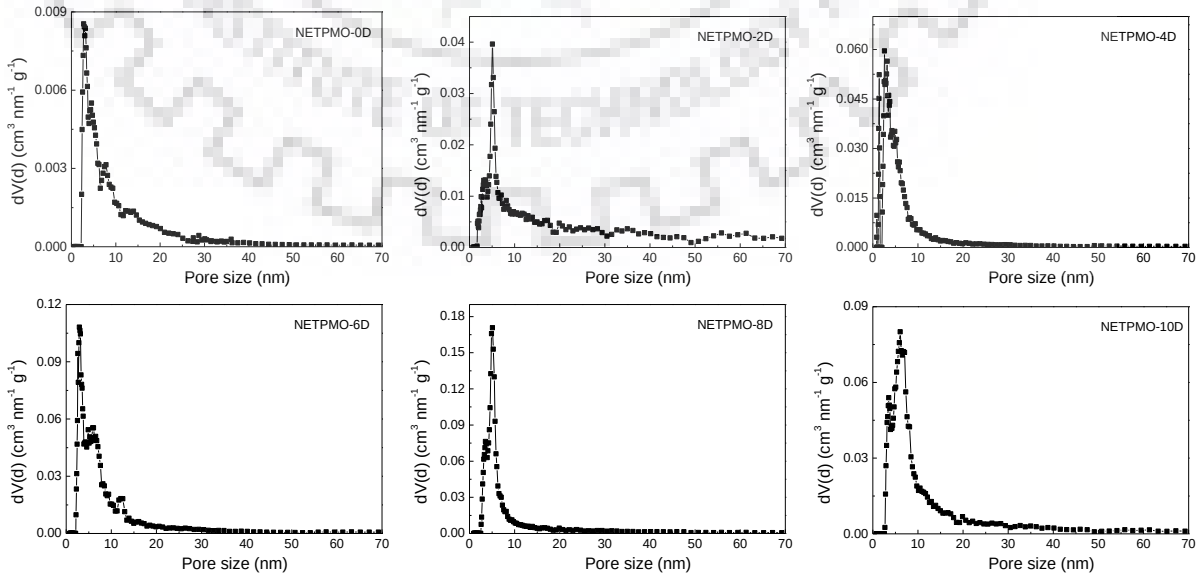

Figure 5.20: PSD plots for NETPMO-*x*D calculated using DFT model.

Table 5.8: Textural properties of NETPMO-*x*D.

Sample	TMSPD:TEOS	SA_{BET} ($m^2\ g^{-1}$)	Pore size (nm)	Pore Vol. ($cm^3\ g^{-1}$)
NETPMO-0D	1:0	29	4.8	0.05
NETPMO-2D	1:2	131	3.6	0.30
NETPMO-4D	1:4	287	2.8	0.27
NETPMO-6D	1:6	484	2.9	0.54
NETPMO-8D	1:8	440	3.5	0.54
NETPMO-10D	1:10	362	3.6	0.61

5.2.2.3. CO_2 sorption study of NETPM-6D

As, the SA_{BET} of NETPMO-6D was highest among NETPMO-*x*D, so this was further used for CO_2 sorption application at 273 and 298 K. The typical CO_2 sorption isotherms given in ***Figure 5.21a*** show hysteresis and are not reversible in nature. The hysteresis could be observed due to strong interaction between amine group (Lewis basic binding sites) and CO_2 (Lewis acidic gas). The effect of strong interaction is also reflected in its Q_{st} value (***Figure 5.23b***). NETPMO-6D could capture a maximum of 8.6 wt% CO_2 at 273 K which decreases to 3.7 wt% at 298 K. The Q_{st} value was estimated to be 39.2 kJ mol^{-1} at zero coverage.

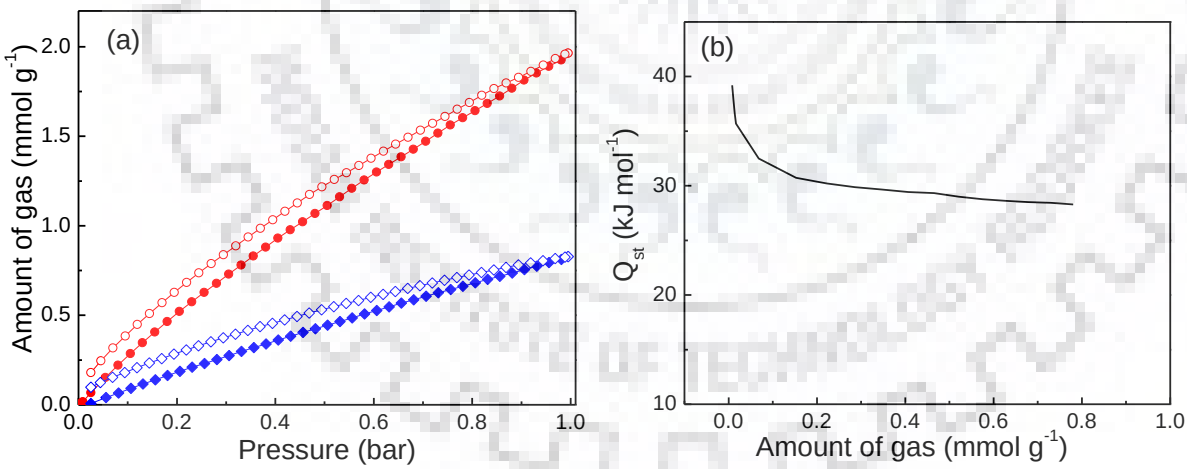

Figure 5.21: (a) CO_2 adsorption (filled symbols) and desorption (empty symbols) isotherms measured at 273 and 298 K at1 bar and (b) Q_{st} for CO_2 sorption of NETPMO-6D.

5.2.3. NETPMO-*x*T (*x* = 0, 2, 4, 6, 8 and 10)

5.2.3.1. Synthesis and characterization of NETPMO-xT

The condensation of APTES and TMSPD with CNC followed by polycondensation led to the formation of high surface area NETPMOs with appreciable CO_2 capture capacity. In the same

line, the synthesis of NETPMOs was further extended in the direction of enhancing the nitrogen content in the hybrid siliceous framework. To achieve this, condensation of CNC with triamine precursor (TMSPT) followed by polycondensation led to the formation of NETPMO-*x*T, as shown in ***Scheme 5.3***. The synthesised specimens were characterized by the techniques used above for characterization of NETPMO-*x*M and NETPMO-*x*D. The NETPMO-*x*T were further utilized for CO_2 capture application.

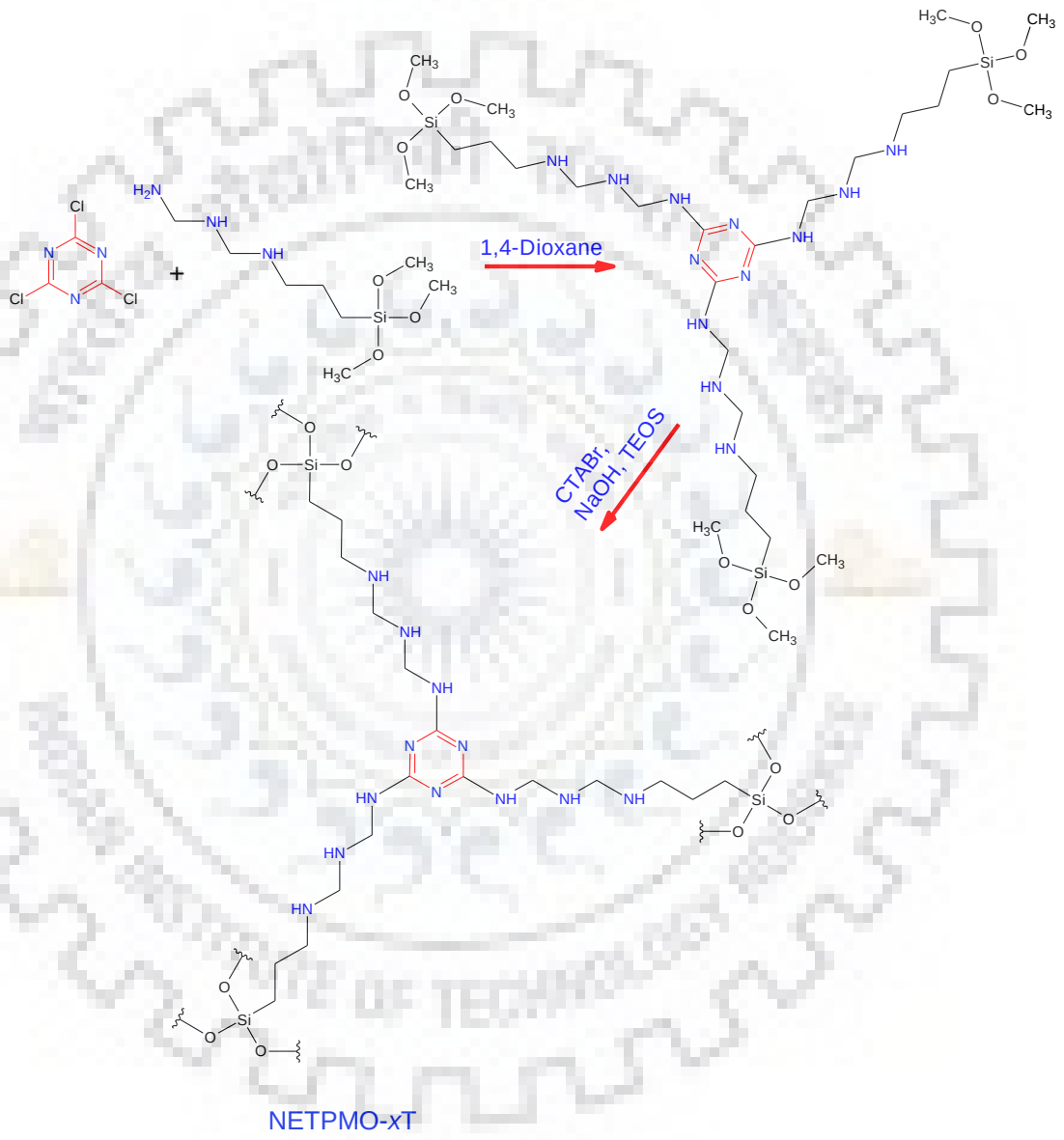

Scheme 5.3: Reaction scheme for the synthesis of NETPMO-*x*T using nucleophilic condensation of CNC with TMSPT followed by co-condensation with TEOS, (where *x* is the molar ratio of TMSPT with respect to TEOS and its values are *x* = 0, 2, 4, 6, 8 and 10).

The proposed structure of NETPMO-*x*T was confirmed using ^{13}C and ^{29}Si CPMAS NMR, and FTIR spectroscopy. The observation of signals at ~164 ppm and in the range of 53 to 08 ppm confirm the condensation of TMSPT with CNC and incorporation of triazine ring in

NETPMO-0T and NETPMO-6T.[1-7] The assignment of all the ^{13}C CPMAS NMR signals is shown in ***Figure 5.22a*** and is consistent with the proposed structure. The detailed assignment is also summarised in the ***Table 5.9a***. The ^{29}Si CPMAS NMR spectrum of NETPMO-0T shown in the ***Figure 5.22b*** possess the signals for organosilica (*T sites*) while of NETPMO-6T has the signal for organosilica (*T sites*) as well as inorganic silica (*Q sites).* The observation of signals due to *Q sites* confirm the condensation of TEOS in the NETPMO-6T.[5-7] The detailed description of the bands assignment is given in the ***Table 5.9b***. The FTIR spectra shown in ***Figure 5.23***, further support the findings of CPMAS NMR analysis and confirm the incorporation of triazine moiety. The detailed analysis of the individual FTIR bands are summarised in ***Table 5.10***.

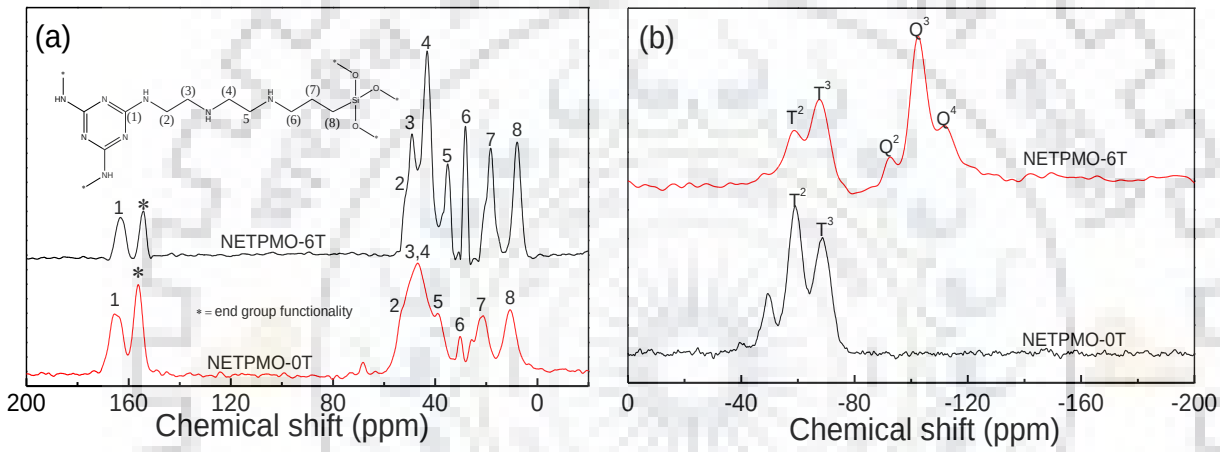

Figure 5.22: (a) ^{13}C and (b) ^{29}Si CPMAS NMR spectra of NETPMO-0T and NETPMO-6T.

Table 5.9a: ^{13}C CPMAS NMR signal description for NETPMO-0T and NETPMO-6T.

Sample ID	δ for Carbons (ppm)							
	(1)	(2)	(3)	(4)	(5)	(6)	(7)	(8)
NETPMO-0T	165	53	49	46	39	30	21	10
NETPMO-6T	164	51	49	43	35	28	18	08

Table 5.9b: ^{29}Si CPMAS NMR signal description for NETPMO-0T and NETPMO-6T.

Sample ID	δ for *T* sites (ppm)		δ for *Q* sites (ppm)		
	T^2	T^3	Q^2	Q^3	Q^4
NETPMO-0T	-59	-69	-	-	-
NETPMO-6T	-57	-67	-92	-102	-112

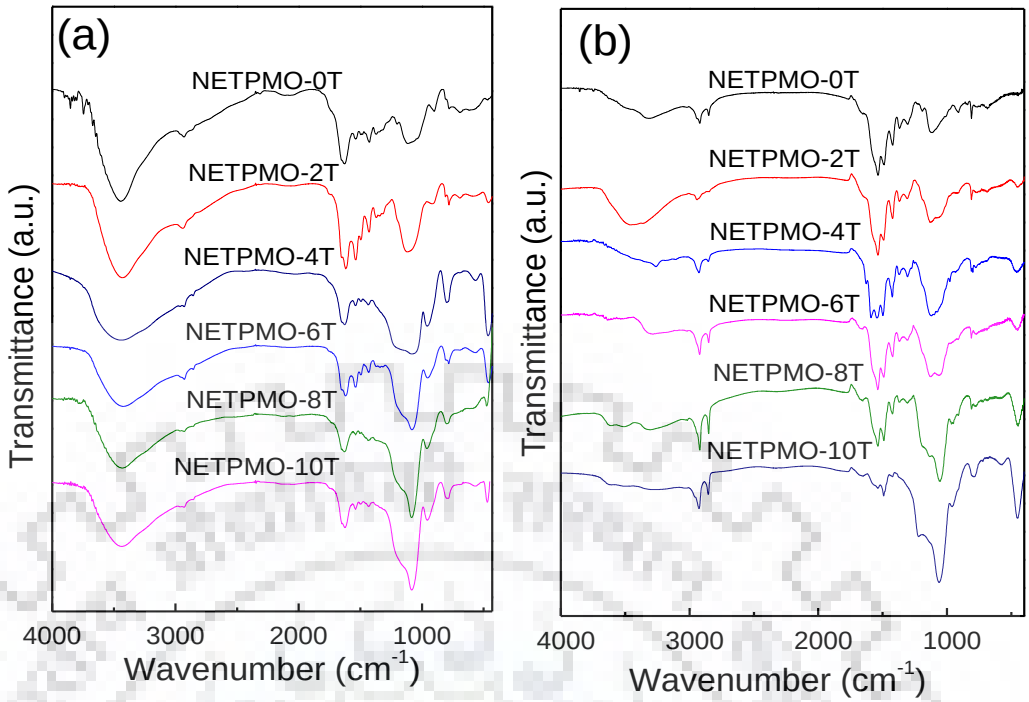

Figure 5.23: FTIR spectra of (a) extracted and (b) as-synthesised NETPMO-*x*T.

Table 5.10: FTIR band description for NETPMO-*x*T.

Band Assignments	**Band positions (cm^{-1})**
-O-H stretching	3455
-N-H stretching	3245
-C-H stretching	2930
-O-H bending	1660
-C=N quadrant stretching	1535
-N-H bending	1500
-C-H bending (APTES)	1430
-C=N torsional bending	1360
-C=N- stretching	1280
Si-O-Si	1206
Si-O-Si	1035
Si-OH	905
Si-O-Si	782
Out-of-plane ring bending of triazine	705

The NETPMO-*x*T are thermally stable up to a temperature of 500 K in air (***Figure 5.24***) with mass loss profile matching to the NETPMO-*x*M and NETPMO-*x*D. The elemental composition of NETPMO-*x*T has been summarized in ***Table 5.11***. As expected, the N content of NETPMO-*x*T is higher than NETPMO-*x*D and NETPMO-*x*M. However, the C/N ratio remains same at ~1.75 similar to NETPMO-*x*D and NETPMO-*x*M.[5-7] The SAXS pattern of

NETPMO-*x*T didn't show any sharp peak, which confirms the absence of long range mesoscale ordering (***Figure 5.25***).

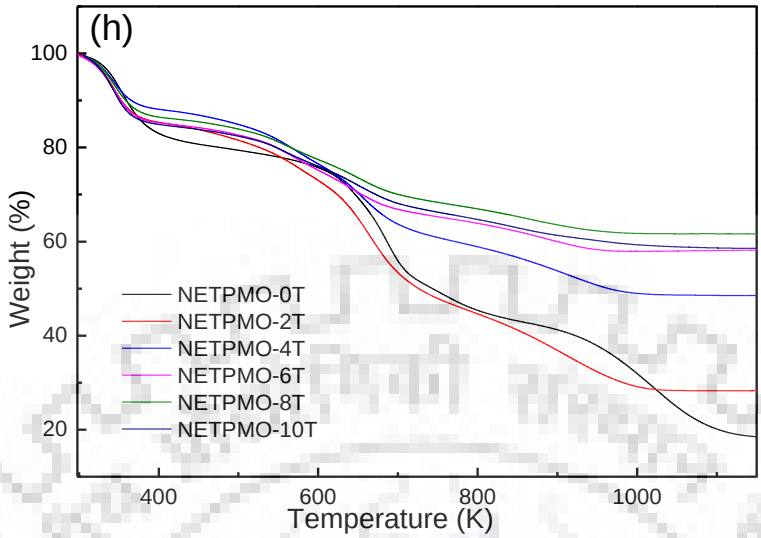

Figure 5.24: TGA thermograms of NETPMO-*x*T.

Table 5.11: C, H and N elemental analyses of NETPMO-*x*T.

Element / Sample	N (wt%)	C (wt%)	H (wt%)	C/N ratio
NETPMO-0T	19.15	32.56	5.96	1.70
NETPMO-2T	15.66	27.70	5.46	1.76
NETPMO-4T	9.15	17.14	4.39	1.86
NETPMO-6T	6.37	12.03	3.76	1.88
NETPMO-8T	5.75	10.83	3.73	1.88
NETPMO-10T	5.26	9.78	3.71	1.86

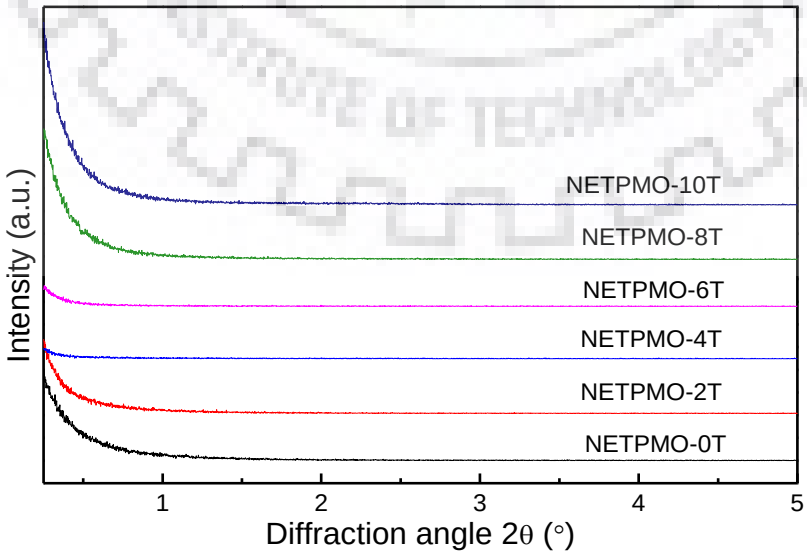

Figure 5.25: SAXS patterns of NETPMO-*x*T.

The FESEM images have shown that NETPMO-*x*T don't have any well-defined microstructure and consist of particles with different shape and sizes in the range of 0.1 to 1 μm (***Figure 5.26***). Further, TEM image of representative sample, NETPMO-6T, indicates the presence of small pores of 2-3 nm size (***Figure 5.27a).*** The observation of broad diffused ring in SAED pattern (***Figure 5.27b***) confirms the amorphous nature of sample.

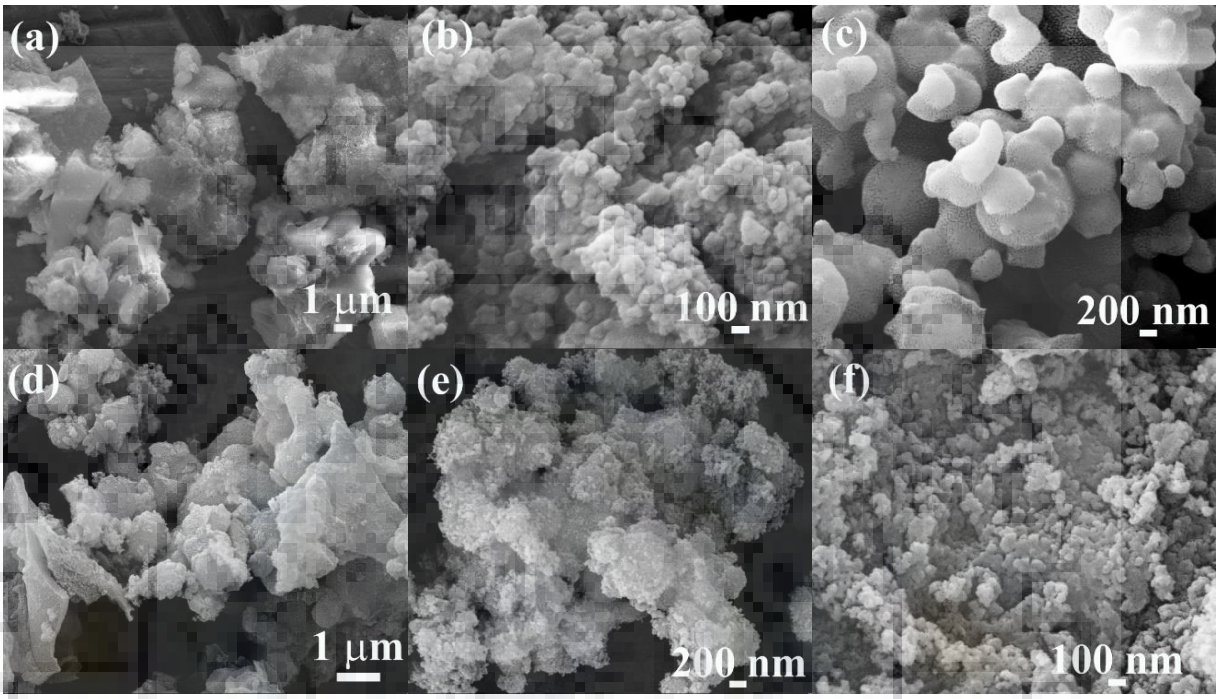

Figure 5.26: FESEM images of (a) NETPMO-0T, (b) NETPMO-2T, (c) NETPMO-4T, (d) NETPMO-6T, (e) NETPMO-8T and (f) NETPMO-10T.

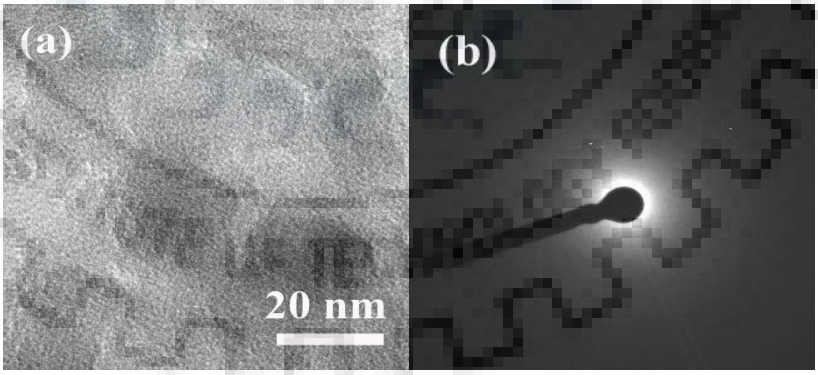

Figure 5.27: (a) TEM images and (b) SAED pattern of NETPMO-6T.

5.2.3.2. Textural analysis of NETPMO-xT

The N_2 sorption of all the specimens except NETPMO-0T has shown type-IV isotherms (***Figure 5.28***). The SA_{BET} of NETPMO-*x*T varies in the range of 30 to 343 $m^2\ g^{-1}$ on increasing the TMSPT to TEOS ratio up to 1:6 and decreased on further increasing the ratio to 1:8 or 1:10. The PSD analysis has shown that the majority of the pores for NETPMO-*x*T are centered in

mesopore region in the range of 2.7 to 4.8 nm (***Figure 5.29***). Detailed textural properties of all these specimens have been summarized in ***Table 5.12***.

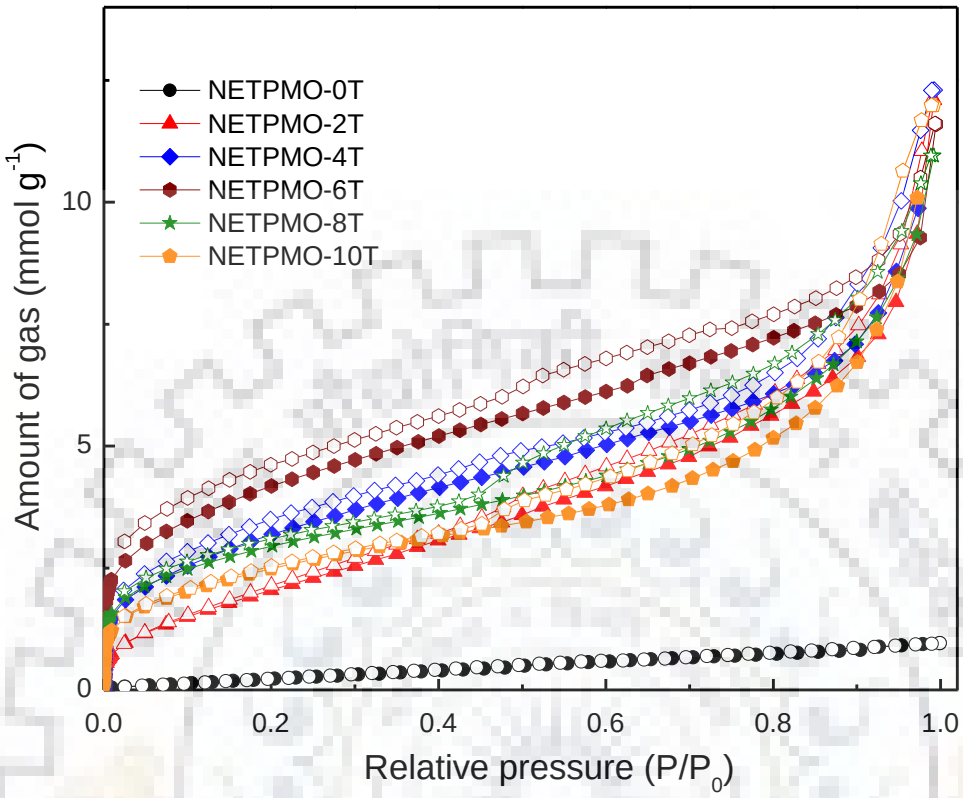

Figure 5.28: N_2 adsorption (filled symbols) and desorption (empty symbols) isotherms for NETPMO-*x*T measured at 77 K.

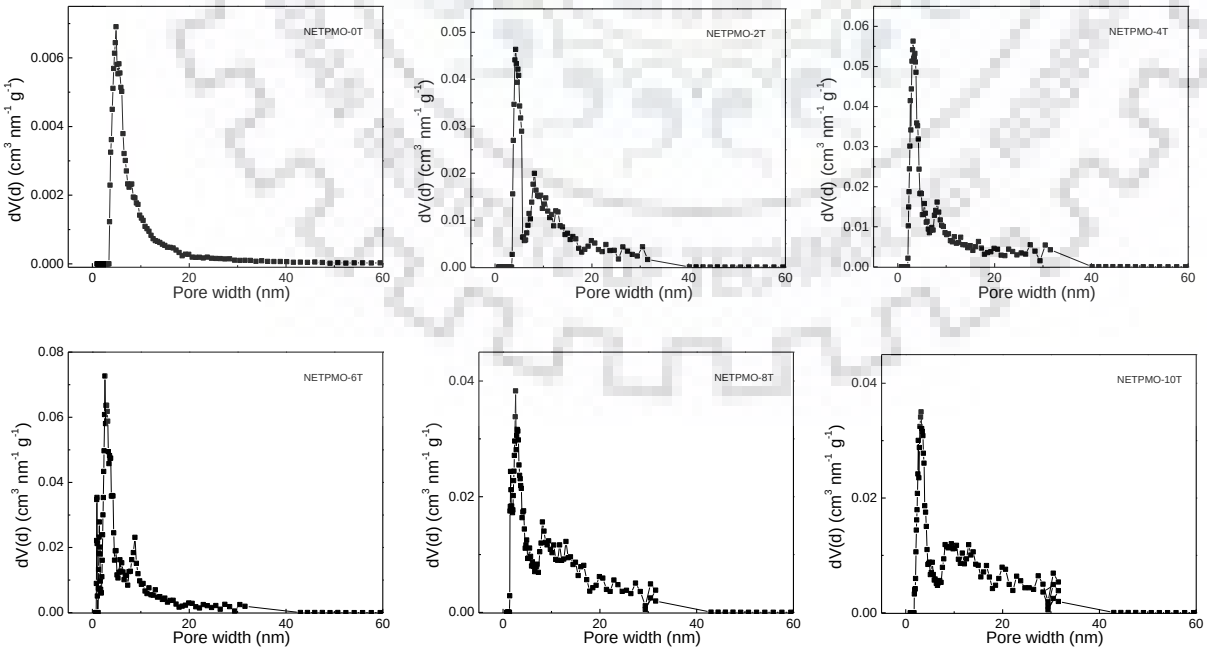

Figure 5.29: PSD plots for NETPMO-*x*T calculated using DFT model.

Table 5.12: Textural properties of NETPMO-*x*T.

Sample	TMSPT:TEOS	SA_{BET} (m^2 g^{-1})	Pore size (nm)	Pore Vol. (cm^3 g^{-1})
NETPMO-0T	1:0	30	4.8	0.03
NETPMO-2T	1:2	198	4.3	0.42
NETPMO-4T	1:4	270	3.4	0.43
NETPMO-6T	1:6	343	2.8	0.41
NETPMO-8T	1:8	240	2.7	0.38
NETPMO-10T	1:10	203	3.2	0.42

5.2.3.3. CO_2 sorption study of NETPMO-6T

The NETPMO-6T with maximum SA_{BET} was chosen for CO_2 capture application. The maximum uptake of 7.3 and 3.9 wt% were estimated at 273 and 298 K, respectively (***Figure 5.30a***). The estimated Q_{st} value of 39.6 kJ mol^{-1} for CO_2 sorption further support this (***Figure 5.30b***). The CO_2 uptake of NETPMOs is compared with reported solid adsorbents (***Table 5.13***).

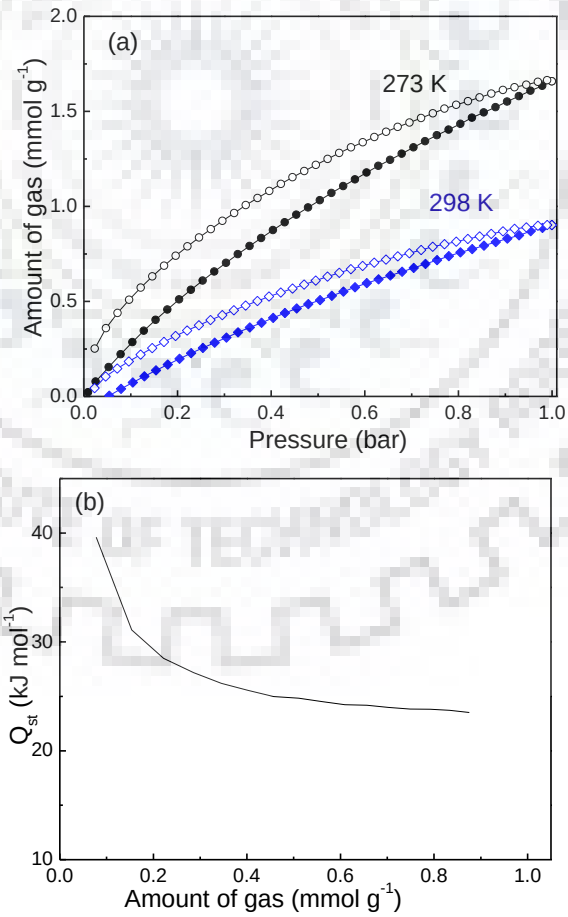

Figure 5.30: (a) CO_2 adsorption (filled symbols) and desorption (empty symbols) isotherms measured at 273 and 298 K at1 bar, and (b) Q_{st} for CO_2 sorption of NETPMO-6T.

Table 5.13: Comparison of CO_2 capture capacity of NETPMOs with reported adsorbents.

S. N.	Adsorbent	CO_2 uptake (wt%), 273 K	CO_2 uptake (wt%), 298 K	*Reference*
1	CPMO-8SR	5.72	-	5
2	GD0	10.12	-	23
3	flourinated Zn^{II} HFMOF	4.66	4.27	26
4	TDCOF-5	9.24	-	27
5	TBILP-1	11.70	-	28
6	Fepc–TiO_2	9.24	-	29
7	CP-40 AO*	-	5.37	30
8	PAF-54	14.10	8.36	31
9	CL-NP	9.50	5.50	32
10	PCz–C5–Cz	12.14	9.64	33
11	HCP-9-DMM	9.30	-	34
12	STPI-3	11.10	6.90	35
13	TPA@PON	16.94	5.85	36
14	SB-TRZ-TPA	16.00	-	37
15	IBFNP-1	23.2	14.8	38
16	PECONF-1	8.18	5.90	39

5.3. SUMMARY

The nitrogen enriched triazine bridged mesoporous organosilicas (NETPMOs) were synthesized by condensing CNC and APTES/TMSPD/TMSPT followed by co-condensation with TEOS. The maximum SA_{BET} of 1304 m^2 g^{-1} was estimated for NETPMO-8M. In order to increase the nitrogen content, the precursors TMSPD and TMSPT were selected but the increased chain lengths in these precursors have a negative effect on the overall textural properties. The SA_{BET} decreased regularly with the increased chain length due to an increased flexibility of the chains. The maximum SA_{BET} of 484 and 343 m^2 g^{-1} were estimated for NETPMO-6M and NETPMO-6T, respectively. The APTES/TMSPD/TMSPT to TEOS ratios plays an important role in tuning the textural properties of the NETPMOs. The SA_{BET} increases linearly with the increase in the APTES/TMSPD/TMSPT to TEOS ratios. It is interesting to note that the incorporation of triazine ring in the siliceous framework has substantially improved the SA_{BET} from 454 m^2 g^{-1} (without triazine moiety) to 1304 m^2 g^{-1} (with triazine moieties). NETPMO-8M have shown the CO_2 uptake of 11.6 wt% but NETPMO-0M has SA_{BET} of 232 m^2 g^{-1} and has shown good CO_2 capture capacity of 10.2 wt% due to higher

nitrogen content. Although the nitrogen content of NETPMO-6D and NETPMO-6T is higher but due to lower SA_{BET} their CO_2 uptake in comparison to NETPMO-8M is inferior. However, the effect of nitrogen enrichments in NETPMO-6D and NETPMO-6T is reflected in their estimated Q_{st} values.

References

1. M. G. Schwab, B. Fassbender, H. W. Spiess, A. Thomas, X. Feng and K. Mullen, Catalyst-free preparation of melamine-based microporous polymer networks through Schiff base chemistry, *J. Am. Chem. Soc.*, 2009, **131**, 7216–7217.
2. G. Li, B. Zhang, J. Yan and Z. Wang, Tetraphenyladamantane-based polyaminals for highly efficient captures of CO_2 and organic vapours, *Macromolecules*, 2014, **47**, 6664–6670.
3. M. K. Bhunia, S. K. Das, P. Pachfule, R. Banerjee and A. Bhaumik, Nitrogen-rich porous covalent imine network (CIN) material as an efficient catalytic support for C–C coupling reactions, *Dalton Trans.*, 2012, **41**, 1304–1311.
4. Y. Liao, J. Weber and C. F. J. Faul, Fluorescent microporous polyimides based on perylene and triazine for highly CO_2-selective carbon materials, *Macromolecules*, 2015, **48**, 2064−2073.
5. P. Rekha, R. Muhammad and P. Mohanty, Sonochemical synthesis of cyclophosphazene bridged mesoporous organosilicas and their application in methyl orange, congo red and Cr (VI) removal, *RSC Adv.*, 2015, **5**, 67690–67699.
6. P. Rekha, V. Sharma and P. Mohanty, Synthesis of cyclophosphazene bridged mesoporous organosilicas for CO_2 capture and Cr (VI) removal, *Micropor. Mesopor. Mater.*, 2016, **219**, 93–102.
7. P. Rekha, R. Muhammad, V. Sharma, M. Ramteke and P. Mohanty, Unprecedented adsorptive removal of $Cr_2O7_2^-$ and methyl orange by using a low surface area organosilica, *J. Mater. Chem. A*, 2016, **4**, 17866–17874.
8. B. G. Trewyn, I. I. Slowing, S. Giri, H. T. Chen and V. S. Y. Lin, Synthesis and functionalization of a mesoporous silica nanoparticle based on the sol–gel process and applications in controlled release, *Acc. Chem. Res.*, 2007, **40**, 846–853.
9. H. A. Patel, F. Karadas, A. Canlier, J. Park, E. Deniz, Y. Jung, M. Atilhan and C. T. Yavuz, High capacity carbon dioxide adsorption by inexpensive covalent organic polymers, *J. Mater. Chem.*, 2012, **22**, 8431–8437.
10. T. Asefa, M. Kruk, N. Coombs, H. Grondey, M. J. Maclachlan, M. Jaroniec and G. A. Ozin, Novel route to periodic mesoporous aminosilicas, PMAs: Ammonolysis of periodic mesoporous organosilicas, *J. Am. Chem. Soc.*, 2003, **125**, 11662–11673.
11. M. A. Markowitz, J. Klaehn, R. A. Hendel, S. B. Qadriq, S. L. Golledge, D. G. Castner and B. A. Gaber, Direct synthesis of metal-chelating mesoporous silica: Effects of added organosilanes on silicate formation and adsorption properties, *J. Phys. Chem. B*, 2000, **104**, 10820–10826.
12. J. F. Moulder, W. F. Stickle, P. E. Sobol and K. D. Bomben, *Handbook of X-ray Photoelectron Spectroscopy*, Physical Electronics, Inc. USA, October 1995.
13. P. K. Brow and C. G. Pantano, Thermochemical nitridation of microporous silica films in ammonia, *J. Am. Ceram. Soc.*, 1987, **70**, 9–14.
14. M. A. Wahab, I. Kim and C. S. Ha, Bridged amine-functionalized mesoporous organosilica materials from 1,2-bis(triethoxysilyl)ethane and bis[(3-trimethoxysilyl)propyl]amine, *J. Solid State Chem.*, 2004, **177**, 3439–3447.
15. A. S. M. Chong and X. S. Zhao, Functionalization of SBA-15 with APTES and characterization of functionalized materials, *J. Phys. Chem. B*, 2003, **107**, 12650–12657.
16. A. Deryło-Marczewska, J. Goworek, S. Pikus and E. Kobylas, Characterization of melamine-formaldehyde resins by XPS, SAXS, and sorption techniques, *Langmuir*, 2002, **18**, 7538–7543.
17. M. A. Wahab and C.-S. Ha, Ruthenium-functionalised hybrid periodic mesoporous organosilicas: Synthesis and structural characterization, *J. Mater. Chem.*, 2005, **15**, 508–516.
18. J. Zhang, Z. Wang, L. Li, J. Zhao, J. Zheng, H. Cui and Z. Zhu, Self-assembly of CNH nanocages with remarkable catalytic performance, *J. Mater. Chem. A*, 2014, **2**, 8179–8183.

19. P. Vassileva, V. Krastev, L. Lakov and O. Peshev, XPS determination of the binding energies of phosphorus and nitrogen in phosphazenes, *J. Mater. Sci.*, 2004, **39**, 3201–3202.
20. H. Ozay and O. Ozay, Synthesis and characterization of drug microspheres containing phosphazene for biomedical applications, *Colloid Surf. A-Physicochem. Eng. Asp*, 2014, **450**, 99–105.
21. D. Y. Osadchii, A. I. Olivos-Suarez, A. V. Bavykina and J. Gascon, Revisiting nitrogen species in covalent triazene frameworks, *Langmuir*, 2017, **33**, 14278–14285.
22. X. Qiu, S. Han, Y. Hu, M. Gao and H. Wang, Periodic mesoporous organosilicas for ultra-high selective copper (II) detection and sensing mechanism, *J. Mater. Chem. A*, 2014, **2**, 1493–1501.
23. Y. Tang and K. Landskron, CO_2-sorption properties of organosilicas with bridging amine functionalities inside the framework, *J. Phys. Chem. C*, 2010, **114**, 2494–2498.
24. K. M. Parida and D. Rath, Amine functionalized MCM-41: An active and reusable catalyst for Knoevenagel condensation reaction, *J. Mol. Catal. A: Chem.*, 2009, **310**, 93–100.
25. X. Zhang, A. Hsu, H. Wang, Y. Song, J. Kong, M. S. Dresselhaus and T. Palacios, Impact of chlorine functionalization on high-mobility chemical vapor deposition grown graphene, *ACS Nano*, 2013, **7**, 7262–7270.
26. S. S. Dhankhar, M. Kaur and C. M. Nagaraja, Green synthesis of a microporous, partially fluorinated Zn^{II} paddlewheel metal–organic framework: H_2/CO_2 adsorption behavior and solid-state conversion to a ZnO–C nanocomposite**,** *Eur. J. Inorg. Chem.*, 2015, **34**, 5669–5676.
27. Z. Kahveci, T. Islamoglu, G. A. Shar, R. Ding and H. M. El-Kaderi, Targeted synthesis of a mesoporous triptycene-derived covalent organic framework, *CrystEngComm*, 2013, **15**, 1524–1527.
28. A. K. Sekizkardes, S. Altarawneh, Z. Kahveci, T. İslamoğlu and H. M. El-Kaderi, Highly selective CO_2 capture by triazine-based benzimidazole-linked polymers, *Macromolecules*, 2014, **47**, 8328–8334.
29. P.V.R.K. Ramacharyulu, R. Muhammad, J. P. Kumar, G. K. Prasad and P. Mohanty, Iron phthalocyanine modified mesoporous titania nanoparticles for photocatalytic activity and CO_2 capture applications, *Phys. Chem. Chem. Phys.*, 2015, **17**, 26456–26462.
30. C. Gunathilake and M. Jaroniec, Mesoporous organosilica with amidoxime groups for CO_2 sorption, *ACS Appl. Mater. Interfaces*, 2014, **6**, 13069−13078.
31. W. Wang, Y. Yuan, F. X. Sun and G. S. Zhu, Targeted synthesis of novel porous aromatic frameworks with selective separation of CO_2/CH_4 and CO_2/N_2, *Chin. Chem. Lett.*, 2014, **25**, 1407–1410.
32. M. Saleh and K. S. Kim, Highly selective CO_2 adsorption performance of carbazole based microporous polymers, *RSC Adv.*, 2015, **5**, 41745–41750.
33. C. Gu, Y. Bao, W. Huang, D. Liu and R. Yang, Four simple structure carbazole-based conjugated microporous polymers with different soft connected chains, *Macromol. Chem. Phys.*, 2016, **217**, 748−756.
34. D. Zhang, L. Tao, J. Ju, Y. Wang, Q. Wang and T. Wang, Postmodification of linear poly-p-phenylenes to prepare hyper-crosslinked polymers: Tuning the surface areas by the molecular weight, *Polymer*, 2015, **60**, 234−240.
35. C. Zhang, T. L. Zhai, J. J. Wang, Z. Wang, J. M. Liu, B. Tan, X. L. Yang and H. B. Xu, Triptycene-based microporous polyimides: Synthesis and their high selectivity for CO_2 capture, *Polymer*, 2014, **55**, 3642–3647.
36. S. Mondal, S. K. Kundub and A. Bhaumik, A facile approach for the synthesis of hydroxyl-rich microporous organic networks for efficient CO_2 capture and H_2 storage, *Chem. Commun.*, 2017, **53**, 2752–2755.
37. S. Bhunia, P. Bhanja, S. K. Das, T. Sen and A. Bhaumik, Triazine containing N-rich microporous organic polymers for CO_2 capture and unprecedented CO_2/N_2 selectivity, *J. Solid State Chem.*, 2017, **247**, 113–119.
38. R. Muhammad, P. Rekha and P. Mohanty, Facile synthesis of a thermally stable imine and benzimidazole functionalized nanoporous polymer (IBFNP) for CO_2 capture application, *Greenhouse Gas: Sci. Technol.*, 2016, **6**, 150–157.
39. P. Mohanty, L. D. Kull and K. Landskron, Porous covalent electron-rich organonitridic frameworks as highly selective sorbents for methane and carbon dioxide, *Nat. Commun.*, 2011, **2**, doi:10.1038/ncomms1405.

CHAPTER-VI

SUMMARY, CONCLUSIONS AND DIRECTIONS FOR FUTURE RESEARCH

6.1. SUMMARY AND CONCLUSIONS

Inorganic-organic hybrid materials since their first inception during pre-Spanish era 5000 years ago have been one of the fast-growing fields in the material science and engineering discipline.[1-5] Nature inspired artistic creativity has made it possible to look for efficient materials and the find was none other than the hybrid materials and composites.[5] These are obtained by blending inorganic and organic moieties together at the molecular scale, and the beauty of these materials is the retention of the features of parent moieties with some additional novel features such as porosity. Due to ease of synthesis, high specific surface area, tunable pore functionality, high mechanical strength, thermal and hydrothermal stability, and low density, this class of porous materials have captured the imaginations of scientists working in diverse fields.[6-10] With the evolvements of science and technology, a lot of possibilities have risen to play with the chemistry of these materials and mould their properties to enlarge the application fields.[5-7] These materials have been used for several applications including the CO_2 sorption and H_2 storage.[10-13]

The most acceptable reason for the global warming is the increase of the CO_2 content in the atmosphere that reached as high as 408 ppm.[14] Based on the extensive literature studies, it has been concluded that the CO_2 capture using high surface area solid adsorbents from the flue gas stream is a potential solution to decrease this CO_2 content to acceptable level. The use of various high surface area nanoporous materials such as ACs, zeolites, COFs, MOFs, ZIFs and mesoporous silicas for this purpose further cemented the notion.[11,12,15-17] Improving textural properties, tuning pore functionality and enrichment with electron-rich heteroatoms are some of the strategies that improve the materials quality for CO_2 sorption applications.[18-20] Keeping in mind all of the above facts and proofs, the objectives of the present research were formulated to synthesize high surface area hybrid nanoporous adsorbents to efficiently capture CO_2. The choice of the functionalities in these materials is mostly directed towards synthesizing electron rich materials to initiate a Lewis base-Lewis acid interaction with the acidic gas CO_2. Two types of heteroatoms enriched hybrid nanoporous adsorbents such as cyclophosphazene-based non-siliceous hybrid frameworks and triazine bridged siliceous hybrid framework were synthesized.

The choice of both conventional and non-conventional synthetic approaches for the introduction of nanopores in these materials is one of the major achievements. In the non-siliceous hybrid nanoporous materials, simple condensation of appropriate precursors has resulted in the

formation of high surface area adsorbents. The beauty of the synthetic approaches is the introduction of porosity in the materials without using template or surfactant. Moreover, no catalyst was also used for the synthesis. The siliceous materials are made by using CTABr as SDA. Selecting appropriate organosilane precursors that have the potential for nitrogen enrichment is one of the major achievements. Finding the suitable experimental conditions that could provide a decent yield for such precursors was always a big challenge and, in this research, it was achieved with precision. Almost all possible state of the art analytical methods have been utilized for characterizing the specimens.

The HNMs synthesized using Schiff base condensation under catalyst-free condition have shown the SA_{BET} as high as 976 m^2 g^{-1} with ultra-small pore of 0.65 nm size. The estimated nitrogen content of 42% HNMs is highest for any type of porous hybrid frameworks. Owing to high surface area, ultra-small pore and high nitrogen contents, the HNMs have shown the maximum uptake of 18.9 wt% CO_2 at 273 K. The materials have further demonstrated the storage of 1.65 wt% H_2 at 77 K. Further, the nucleophilic condensation of aldehyde with pyrrole yielded CHNMs with maximum estimated SA_{BET} of 1328 m^2 g^{-1} with hierarchical pore structure. The CHNMs have shown the maximum CO_2 and H_2 uptake of 22.8 and 2.02 wt% at 273 and 77 K, respectively. The exploitation of peddle wheel structure of cyclophosphazene for the synthesis of HNMs and CHNMs have shown synergy in achieving the high surface area. Although the SA_{BET} and CO_2 uptake of CHNMs are high in comparison to HNMs, but due to higher nitrogen content HNMs have also shown appreciable CO_2 capture capacity.

The assumption of enhancement of the CO_2 capture capacity by increasing the nitrogen content was proved in the CHNMs and HNMs. In a similar concept, the nitrogen enriched triazine bridged mesoporous organosilicas (NETPMOs) were synthesized using three precursors APTES, TMSPD and TMSPT with varying nitrogen content. The two-step synthetic approach involves the condensation of the precursors with CNC in the first step followed by their hydrolysis and polycondensation in the second step under basic condition in presence of CTABr as SDA. As there was not an impressive SA_{BET} apprehended in these materials, a co-condensation with TEOS was also performed to improve the textural properties. The SA_{BET} of NETPMO-*x*M synthesized using CNC and APTES increased from 232 to 1304 m^2 g^{-1} on introducing TEOS in the synthesis with the ratio of 1:8 (APTES:TEOS). On further increasing the ratio, there was a decline of the SA_{BET}. Interestingly, the triazine moiety of the CNC has a synergy in tuning the textural properties. The

SA_{BET} of 1304 m^2 g^{-1} was recorded in NETPMO-8M having the triazine moiety in comparison to 454 m^2 g^{-1} in a specimen, AP-TEOS-8, synthesized without using CNC. Similar observations were made in case of NETPMO-*x*D and NETPMO-*x*T also synthesized using TMSPD and TMSPT, respectively barring the difference that the effect of TEOS was seen on increasing the TMSPD/TMSPT to TESO ratio up to 1:6 instead of 1:8. The maximum estimated SA_{BET} was 484 and 343 m^2 g^{-1} for NETPMO-6D and NETPMO-6T, respectively.

The presence of amine groups in NETPMOs has shown profound effect on the CO_2 capture capacity. The maximum uptake of 11.6 wt% was observed for NETPMO-8M. It is interesting to note that NETPMO-0M have shown the CO_2 uptake of 10.2 wt% despite having a much lower SA_{BET} of 232 m^2 g^{-1}, which is 5.6 times lower than NETPMO-8M (1304 m^2 g^{-1}). This is due to the higher nitrogen content of 16.57 wt% in NETPMO-0M as compared to 4.95 in NETPMO-8M. The presence of triazine ring and high amine functionality in NETPMOs were instrumental in enhancing the Lewis basic nature of the framework. The effect of nitrogen content was reflected in its Q_{st} values. The Q_{st} for NETPMO-0M was estimated to be 48.6 kJ mol^{-1} as compared to 30.7 kJ mol^{-1} for NETPMO-8M. The SA_{BET} of NETPMO-6D and NETPMO-6T is 0.37 and 0.26 time lower as compared to the SA_{BET} of NETPMO-8M. Due to low SA_{BET}, the CO_2 uptake decreases despite the nitrogen enrichment of frameworks. There is a trade-off between the SA_{BET} and nitrogen content for the CO_2 capture capacity. A moderately high SA_{BET}, with a moderately high Q_{st} could provide the best CO_2 uptake.

6.2. NEW ACHIEVEMENTS

The major achievements of the present research are as follow;

- Synthesis of two families of high surface area nanoporous inorganic-organic hybrid materials i.e., siliceous and non-siliceous frameworks
- The control of textural properties in the non-siliceous frameworks by the inclusion of cyclophosphazene moieties with a peddle wheel structure
- The use of Schiff base condensation for the first time to synthesize metal free hybrid nanoporous materials with the nitrogen enrichment of framework that reaches the nitrogen content of 42 wt%, which is highest for any reported hybrid materials
- A maximum of 22.8 wt% of CO_2 capture capacity was achieved, that is among the best reported metal-free hybrid materials. Moreover, high H_2 storage capacity of 2.02 wt% could be

realized by these non-siliceous metal-free hybrid nanoporous materials

- A systematic investigation of nitrogen enrichment in the mesoporous organosilica was carried out successfully with the maximum nitrogen content of 19.15 wt%, which is the maximum value to the best of our knowledge for the organosilica frameworks
- The inclusion of triazine moiety in the organosilica frameworks along with the co-condensation of TEOS was instrumental in tuning the textural properties
- A CO_2 capture capacity of 11.6 wt% was achieved in the organosilica frameworks, which is comparable to the best-reported organosilica framework materials, although the value is less in comparison to the non-siliceous hybrid materials

6.3. CHALLENGES TO OVERCOME IN THIS RESEARCH WORK

Although, all the objectives that were defined at the beginning of the research were achieved by synthesizing varieties of nitrogen enriched high surface area materials and investigating their applications for CO_2 capture and H_2 storage, yet a significant number of hurdles had to overcome. Some of the major challenges are discussed below;

- **Improving the specific surface area:** The gas sorption by solid adsorbents is a complex process which depends upon several factors including the physical properties and chemical nature of the adsorbents. Among many, the specific surface area has a prominent role. The specific surface area estimated for these synthesized materials reaches as high as 1300 m^2 g^{-1}, which is on the upper side. However, being the metal free systems that comprise of mostly the light elements such as C, N, O, H and P, the specific surface area could go even higher. When compared with their MOF, COF and POPs counterparts, the reported specific surface area is less. Tremendous efforts were put to improve the specific surface area of these materials, and to a greater extent we were successful but still there remains a challenge to further increase the specific surface area.

- **Synthesis of periodic mesoporous organosilica hybrid materials:** The synthesis of siliceous hybrid materials in presence of structure directing agents (SDA) leads to long-range mesoscale ordering. In the present research, although, the SDA was used for the synthesis but it remains a great challenge to achieve a periodic mesoscale ordering. This was mainly due to the use of flexible long aliphatic chain organosilica precursors for the synthesis with a target to enrich the frameworks with sufficient nitrogen so that the

proposed objectives could be achieved. The aliphatic chain length along with the stereochemistry of the precursor molecules play a significant role in controlling the mesoscale periodicity. It was very difficult to produce the mesoscale ordering in the structure of materials synthesized by large and flexible precursors such as the condensation products of CNC and APTES/TMSPD/TMSPT, despite the use of SDA.

- **Improvements in CO_2 capture capacity:** The sky has no limit. Although at the beginning of the present research a target of 20 odd wt% of CO_2 capture capacity was set, which was successfully achieved (22.8 wt%), still there is always a scope for further increase the capture capacity. As discussed above, it can be possible by synthesizing materials with the higher specific surface area and more control on the textural properties and framework functionalities.

6.4. DIRECTIONS FOR THE FUTURE RESEARCH WORK

The major focus of this research was to synthesize hybrid materials with high specific surface area having electron rich heteroatoms distributed uniformly throughout the framework to facilitate the CO_2 sorption applications. The gas sorption properties of the synthesized materials have been carried out extensively, however, there are many other applications that can be explored for these materials. Some of the focused areas are given below;

- **Heterogeneous catalysis**: The electron rich framework materials could be very much useful as a heterogeneous catalyst for several organic transformations, where a Lewis base can activate the process. Further, these materials could be used as support for metal and metal oxide based heterogeneous catalysts.
- **Wastewater treatment**: The high specific surface area and electron rich frameworks could be useful for adsorptive removal of cations and synthetic organic dyes with Lewis acidic character most commonly found in the industrial effluent.
- **Drug delivery and other biomedical applications**: The biocompatible cyclophosphazene moiety along with high specific surface area with a control over the pore size distribution may lead the application of these materials as support for drug in delivery applications.
- **Applications for energy storage**: The materials could be tested as electrode materials for energy storage devices.

- **Theoretical calculations**: The experimental finding of the current research work could be used to hypothesize and start the theoretical/computational simulation studies which will help the rational design of even better materials and systems that can be most ideal for CO_2 adsorption and scrubbing.

References

1. M. M. Unterlass, Green synthesis of inorganic–organic hybrid materials: State of the art and future perspectives, *Eur. J. Inorg. Chem.*, 2016, 1135–1156.
2. M. L. V. Á. Pascual, M. T. D. Carbóa and A. D. Carbó, Characterization of Maya Blue pigment in pre-classic and classic monumental architecture of the ancient pre-Columbian city of Calakmul (Campeche, Mexico), *J. Cultur. Herit.*, 2011, **12**, 140–148.
3. H. V. Olphen, Maya Blue: A clay-organic pigment? *Science*, 1966, **154**, 645-646.
4. M. J. Yacaman, L. Rendon, J. Arenas and M. C. S. Puche, Maya Blue paint: An ancient nanostructured material, *Science*, 1996, **273**, 223–225.
5. P. G. Romero and C. Sanchez, Hybrid materials. Functional properties. From Maya Blue to 21st century materials, *New J. Chem.*, 2005, **29**, 57–58.
6. T. Noisser, G. Reichenauer and N. Husing, In situ modification of the silica backbone leading to highly porous monolithic hybrid organic-inorganic materials via ambient pressure drying, *Appl. Mater. Interfaces*, 2014, **6**, 1025–1029.
7. X. Wang and S. C. Jana, Synergistic hybrid organic-inorganic aerogels, *Appl. Mater. Interfaces*, 2013, **5**, 6423–6429.
8. C. Liu, Z. Wang, C. Shi, E. Z. Liu, C. He and N. Zhao, Nanostructured hybrid layered-spinel cathode material synthesized by hydrothermal method for lithium-ion batteries, *Appl. Mater. Interfaces*, 2014, **6**, 8363–8368.
9. H. Li, M. Eddaoudi, M. O'Keeffe and O. M. Yaghi, Design and synthesis of an exceptionally stable and highly porous metal-organic framework, *Nature*, 1999, **402**, 276–279.
10. S. S. Park, M. S. Moorthy and C. S. Ha, Periodic mesoporous organosilicas for advanced applications, *NPG Asia Materials*, 2014, **6**, 1–21.
11. P. Mohanty, L. D. Kull and K. Landskron, Porous covalent electron-rich organonitridic frameworks as highly selective sorbents for methane and carbon dioxide, *Nat. Commun.*, 2011, **2**, 401–406.
12. D. M. D'Alessandro, B. Smit and J. R. Long, Carbon dioxide capture: Prospects for new materials, *Angew. Chem. Int. Ed.*, 2010, **49**, 6058–6082.
13. T. He, P. Pachfule, H. Wu, Q. Xu and P. Chen, Hydrogen carriers, *Nat. Rev. Mater.*, 2016, **1**, 16059–16075.
14. https://www.co2.earth/
15. Q. Wang, J. Luo, Z. Zhong and A. Borgna, CO_2 capture by solid adsorbents and their applications: Current status and new trends, *Energy Environ. Sci.*, 2011, **4**, 42–55.
16. B. Sreenivasulu and I. Sreedhar, Development trends in porous adsorbents for carbon capture, *Environ. Sci. Technol.*, 2015, **49**, 12641–12661.
17. L. Zou, Y. Sun, S. Che, X. Yang, X. Wang, M. Bosch, Q. Wang, H. Li, M. Smith, S. Yuan, Z. Perry, H.-C. Zhou, Porous organic polymers for post-combustion carbon capture, Adv. Mater. 2017, 29, 1700229–1700263.
18. J. A. A. Gibson, E. Mangano, E. Shiko, A. G. Greenaway, A. V. Gromov, M. M. Lozinska, D. Friedrich, E. E. B. Campbell, P. A. Wright and S. Brandani, Adsorption materials and processes for carbon capture from gas fired power plants: AMPGas, *Ind. Eng. Chem. Res.*, 2016, **55**, 3840−3851.

19. C. A. Trickett, A. Helal, B. A. Al-Maythalony, Z. H. Yamani, K. E. Cordova and O. M. Yaghi, The chemistry of metal–organic frameworks for CO_2 capture, regeneration and conversion, *Nat. Rev. Mater.*, 2017, **2**, 17045-17060.
20. J. Hu, J. Liu, Y. Liu and X. Yang, Improving carbon dioxide storage capacity of metal organic frameworks by lithium alkoxide functionalization: A molecular simulation study, *J. Phys. Chem. C*, 2016, **120**, 10311−10319.

RSC Advances

PAPER

View Article Online
View Journal | View Issue

Cite this: *RSC Adv.*, 2016, **6**, 17100

Aminal linked inorganic–organic hybrid nanoporous materials (HNMs) for CO_2 capture and H_2 storage applications†

Raeesh Muhammad, Pawan Rekha and Paritosh Mohanty*

Received 5th December 2015
Accepted 1st February 2016

DOI: 10.1039/c5ra25933a

www.rsc.org/advances

Nitrogen-rich aminal linked inorganic–organic hybrid nanoporous materials (HNMs) with cyclophosphazene moieties in the frameworks were synthesized by a Schiff base condensation reaction. The ultra-microporous materials have a specific surface area (S_{BET}) upto 976 m^2 g^{-1} and could capture 18.9 wt% CO_2 and 1.6 wt% H_2 at 273 and 77 K, respectively, at 1 bar. The materials have a nitrogen content upto 42% which is the highest among the nanoporous materials category. The high nitrogen content is beneficial for several applications such as CO_2 capture.

1. Introduction

The recent advancement in the synthesis of inorganic–organic hybrid nanoporous materials (HNMs) possessing high surface area, tuneable pore structure, low density, mechanical and hydrothermal stability with tailor-made functionalities have drawn tremendous interest among researchers in the areas of catalysis, drug delivery, environment, gas sorption and separation applications.[1–3] In general, the inorganic moiety provides the thermal stability, mechanical strength, and structural order, whereas, the tuneable functionality, porosity, hydrophobicity, optical and electrical properties of the organic moiety make hybrid materials superior to their both inorganic and organic counter parts.[4] Achieving permanent porosity has always been a challenge, as nature tends to have a compact structure with minimum volume having least energy and surface area.[5] Recently, our group has reported the synthesis of cyclophosphazene based inorganic–organic hybrid porous materials.[6–8] It was observed that the cyclophosphazene units in the framework has the synergic effect in achieving the high surface area in the obtained hybrid materials. This was mainly due to the paddle-wheel structure of the cyclophosphazene derivatives as reported earlier.[6–11]

The classical Schiff base condensation discovered by Hugo Schiff[12] in 1864 has traditionally been used for the generation of imine and aminal linkages by condensing aldehydes with different amines.[13,14] In general, the imine double bond is formed, however, primary amines may subsequently attack resulting exclusively aminal linkages.[15] The mechanism was thoroughly investigated and involves a number of reversible steps. The formation of the imine and aminal linkages have been exploited to prepare various types of organic polymers.[16,17] Moreover, recently the reaction has been used for the synthesis of nanoporous organic polymers with high surface area having imine and aminal linkages.[18–24] To the best of our knowledge, there is no report available for the synthesis of nanoporous inorganic–organic hybrid materials using Schiff base condensation. In this paper, we report the synthesis of aminal linked inorganic–organic hybrid nanoporous materials using Schiff base condensation.

The first step involves the synthesis of aldehyde precursor (compound-**I**) and the second step involves the condensation of the compound-**I** with melamine as shown in Scheme 1. Melamine was chosen in this research to facilitate the condensation and most importantly the synthesized material will have larger nitrogen content of 40% or more, which has not been achieved so far for any types of inorganic–organic hybrid materials. The best reported nitrogen content for any nanoporous material was 40.42% for SNW-3.[20] The larger nitrogen content in the material will be very much beneficial for the gas sorption applications, as the lone pair of electrons in the nitrogen acts as Lewis base and potentially could interact with Lewis acidic gases such as CO_2. The capture and separation of CO_2 from the flue gas stream has been considered to be the potential solution for global warming.[25–27] Moreover, the hybrid materials with ultra-micropores could be exploited for the hydrogen storage applications. Hydrogen is being considered an ideal fuel for future given its abundance and non polluting nature when used with fuel cells, and it has emerged as an ideal substitute for fossil fuels.[28–34] Finding the suitable adsorbents for both CO_2 capture and H_2 storage is a great challenge and leads to the extensive research in the recent times.

Department of Chemistry, Indian Institute of Technology Roorkee, Roorkee, Uttarakhand-247667, India. E-mail: pmfcy@iitr.ac.in; paritosh75@gmail.com

† Electronic supplementary information (ESI) available: Experimental details, XRD, TGA, multi-point BET plot, Langmuir plot, selectivity and isosteric heat of adsorption. See DOI: 10.1039/c5ra25933a

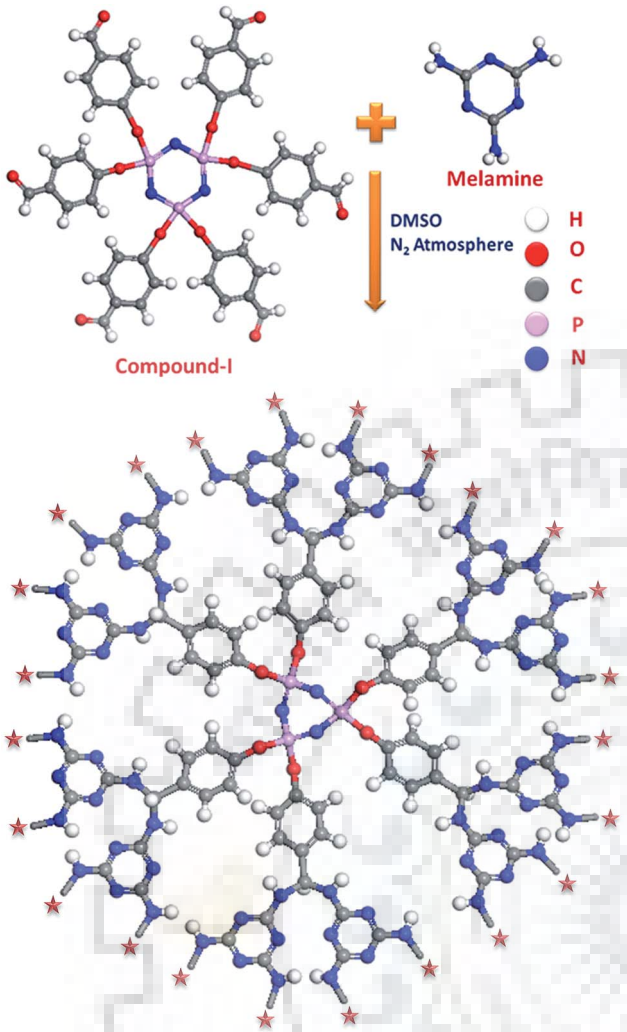

Scheme 1 Reaction scheme for the synthesis of HNMs.

2. Experimental section

2.1 Materials

Phosphonitrilic chloride trimer (PNC) (99%, Sigma Aldrich, India), melamine (99%, Sigma Aldrich, India), *p*-hydroxybenzaldehyde (99%, Sigma Aldrich, India), dimethylsulfoxide (DMSO) (Fisher Scientific, India), Na_2SO_4 (Fisher Scientific, India), K_2CO_3 (Fisher Scientific, India), tetrahydrofuran (THF) and dichloromethane (DCM) (Fisher Scientific, India) were of analytical grade and used as received.

2.2 Synthesis of compound I

The compound-**I** was synthesised by following the work of Kagit *et al.* with some modification as shown in Scheme S1.†[9] Typically, the solution of PNC 3.48 g, (10.00 mmol) in dry THF (50 ml, dried by passing over anhydrous Na_2SO_4) was added to a magnetically stirred solution of *p*-hydroxybenzaldehyde (7.46 g, 61.00 mmol) and K_2CO_3 (39.75 g, 121 mmol) in dry THF (100 ml) under N_2 atmosphere. The reaction mixture was stirred for 48 h at RT. After this insoluble salts were removed by filtration and the soluble product in THF was obtained by removing THF under reduced pressure. It was then re-dissolved in DCM and further combined phase of DCM was extracted with water and brine solution (50 ml each). The extraction was repeated for three times. The organic phase was dried by passing it through anhydrous Na_2SO_4. The final product was obtained by removing the DCM under reduced pressure which gives white crystal on recrystallization with ethylacetate. The detailed characterization of compound-**I** is given in Fig. S1–S4.†

2.3 Synthesis of HNMs

The HNMs have been synthesized, as shown in Schemes 1 and S2 (ESI†), by Schiff base condensation of compound-**I** with melamine. Typically, 1.5 mmol (1.293 g) of compound-**I** dissolved in 5 ml of DMSO was added drop-wise to a solution of 4.5 mmol (0.567 g) of melamine in 25 ml of DMSO under N_2 atmosphere with continuous stirring. The temperature was then raised to 453 K for 48 h under stirring condition. A off-white precipitate was formed which was filtered and washed with acetone, methanol and finally soxhlet extracted with diethyl ether for 8 h to exchange the DMSO from the pores of the framework. The product was dried under vacuum at 373 K for 18 h to give the final product designated as HNM-1.

2.4 Characterization

FT-IR analysis was carried out by using PerkinElmer Spectrum Two. The ^{31}P and ^{13}C cross polarization magic angle spinning (CP-MAS) NMR spectra were recorded on JEOL resonance JNM-ECX-400II at 161.83 MHz (^{31}P), and 100 MHz (^{13}C) with sample spinning frequency of 6 and 10 kHz, respectively. Total number of scans for ^{31}P and ^{13}C were 512 and 9000, respectively. X-ray diffraction patterns were obtained using a Rigaku Ultima IV with Cu-K_α radiation source ($\lambda = 0.15405$ nm) with a scanning speed of 5° per min measured in the range of 10 to 80° in the 2θ scale. The microstructural analysis of the samples was done using the instrument "TESCAN MIRA 3" and the samples were measured at accelerating voltage of 10 kV. Before the analysis, the samples were dispersed in sticky carbon tape attached to a flat aluminium sample holder. Then samples were coated with gold by a standard sputtering technique for 60 s at 1×10^{-4} mbar of pressure in N_2 atmosphere before imaging. TEM images were recorded by using TECNAIG^{2}S-TWIN with field emission gun operating at 200 kV. The samples were prepared by dispersing in ethanol using sonicator and dropping it over carbon coated copper grid. The elemental analysis (C/H/N/S/O) was performed using Thermo Flash 2000. The elemental composition of nitrogen (N), carbon (C), hydrogen (H) and oxygen (O) was determined by thermal conductivity detector (TCD). The amount of sample loaded in the sample vial was 2–3 mg. Thermogravimetric analysis was carried out under air with a heating rate of 5 K min^{-1} at a flow rate of 200 ml min^{-1} with alumina powder as reference using the instrument "EXSTAR TG/DTA6300".

Porosity and gas sorption studies were performed using Autosorb iQ2 volumetric physisorption analyzer

(Quantachrome Instruments, USA) using adsorbate of ultra-high purity (99.999%, Sigma Gases and Services, India). The N_2 sorption was performed at 77 K using liquid nitrogen bath after degassing the specimen at 393 K for 6 h with heating rate of 5 K min^{-1}. The specific surface area was calculated by fitting the gas sorption data to BET and Langmuir model in the relative pressure range of 0.05 to 0.30. Pore size distribution was calculated by fitting the nitrogen sorption isotherm to density functional theory (DFT) model using Kernel: "N_2 at 77 K on carbon (slit pore, QSDFT equilibrium model)". CO_2 and CH_4 adsorption isotherms were measured at 273 and 298 K using chiller/circulator. The temperature of chiller/circulator bath was maintained by using the mixture of ethylene glycol and water in the ratio of 1 : 1 volumetrically. The hydrogen adsorption isotherms were measured at 77 K using liquid nitrogen bath. The isosteric heat of adsorption (Q_{st}) for CO_2 and CH_4 was calculated using the Clausius–Clapeyron equation.

3. Results and discussion

In order to confirm the structure as proposed in Scheme 1, the HNM-1 has been investigated by FT-IR and ^{31}P, ^{13}C CP-MAS NMR spectroscopy. The broad bands at 3405 and 1650 cm^{-1} in the FT-IR spectrum of the HNM-1 as shown in Fig. 1a and Table S1, (ESI†) due to the (–N–H) stretching and bending vibration, respectively, indicate the formation of the aminal linkage.[20,21] The formation of the aminal linkage was supported by the absence of the characteristic imine band around 1620 cm^{-1} due to the C=N stretching vibration.[20,21] The band at 2930 cm^{-1} was assigned to –C–H stretching of tertiary carbon due to the aminal linkage.[20] The band at 1548 and 1477 cm^{-1} were attributed to triazine moiety of melamine.[20] The absence of the C=O stretching vibration around 1700 cm^{-1} confirms the complete condensation of compound-**I** with melamine.[20,21] The observation of bands in the range of 1203 to 1193, 986 and 584 cm^{-1} assigned to ν_{as}(P=N–P), ν_{as}(P–O–P) and δ(P=N–P) vibrations, respectively, confirm the inclusion of the cyclophosphazene units in the frameworks.[6–10]

The detailed analysis about the chemical structure of HNM-1 was performed by ^{13}C and ^{31}P CP-MAS NMR spectroscopy. The ^{13}C CP-MAS NMR spectrum (Fig. 1b) shows the resonance signals at 166, 155, 135, 128, 122 and 57 ppm corresponding to carbon no. 1, 2, 3, 4, 5 and 6, respectively (Fig. 1b, Table S2, ESI†).[20] The absence of signal at 160 ppm (due to imine linkage) and the observation of the signal at 57 ppm (due to the tertiary carbon) confirm the formation of the aminal linkages in the HNM-1.[20] The observation of a single resonance signal at 9.6 ppm in the ^{31}P CP-MAS spectrum of HNM-1 (Fig. 1c) confirms the incorporation of the cyclophosphazene units in the framework.[7–9]

The aminal linkage in the HNM-1 was further supported by the elemental analysis (Table S3, ESI†). Assuming a fully condensed form having aminal linkage as shown in Scheme 1, the theoretical composition of the HNM-1 would be $C_{78}H_{66}N_{75}O_3P_3$. Thus, it will have 41.77, 46.84, 2.97, and 4.28% of C, N, H and O, respectively. The observed elemental composition for HNM-1 was 40.18, 42.16, 4.46 and 5.25% for C, N, H and O, respectively, which was fairly matching with the theoretical values. The excess O and H observed were mainly due to the terminal functionality and trapped moisture in the nanopores. Further, assuming the imine linkage in HNM-1, the theoretical composition would be $C_{60}H_{30}N_{39}O_6P_3$ with 48.49, 36.76, 2.03 and 6.46% of C, N, H and O, respectively, which was not matching with the experimental results.

The HNM-1 was thermally stable up to a temperature of 623 K in air as evaluated by the TGA/DTG analysis (Fig. S5, ESI†).

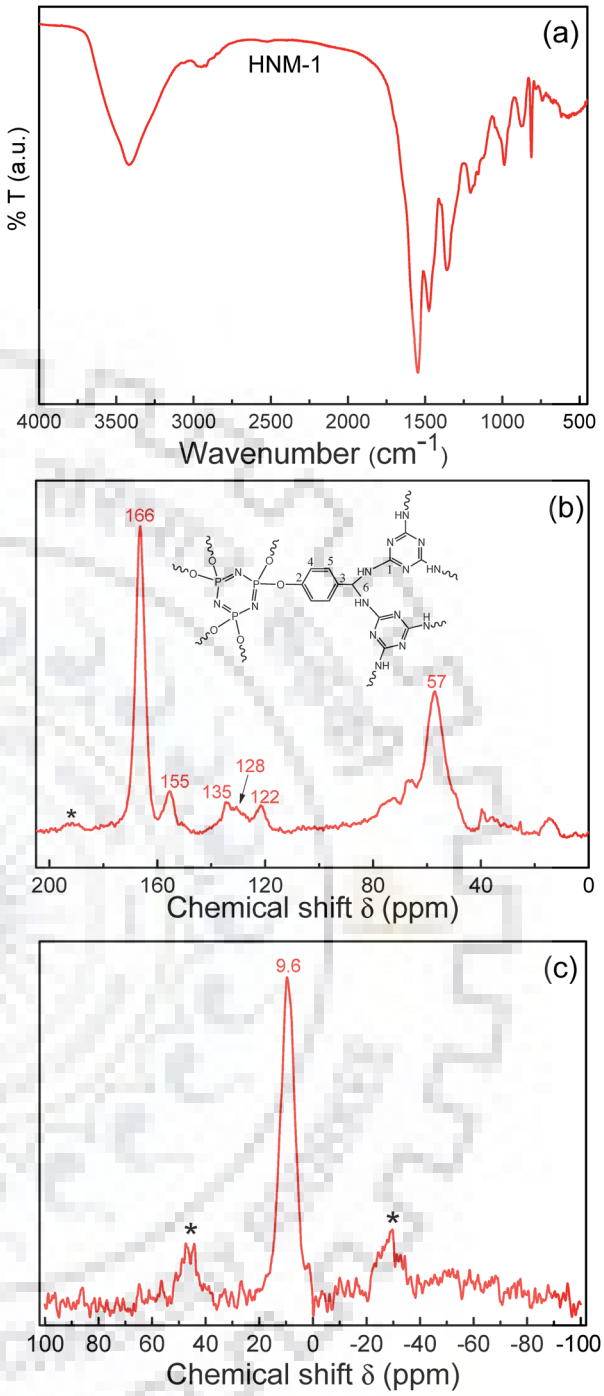

Fig. 1 (a) FT-IR spectrum, (b) ^{13}C CP-MAS NMR spectrum and (c) ^{31}P CP-MAS NMR spectrum of HNM-1.

The HNM-1 was further found to be X-ray amorphous (Fig. S6, ESI†). The particles of size 20 to 50 nm forming the network could be seen from the FESEM and TEM images (Fig. 2). The inter-particulate pores could be seen in the FESEM image (Fig. 2a), however, nanoporous nature of the HNM-1 can be clearly seen with the TEM image (Fig. 2b). The SAED pattern in the inset of Fig. 2b further confirms the amorphous nature of the specimen.

The formation of the aminal frameworks as proposed in the Scheme 1, and the observation of the nanoporous structure in the FESEM and TEM images, has encouraged us to study the textural properties of the HNM-1. Fig. 3a shows the N_2 sorption isotherm of HNM-1 measured at 77 K. A type-I isotherm with steep N_2 uptake at low pressure (below $P/P_0 = 0.01$) and significant multilayer adsorption in intermediate section with narrow hysteresis in the higher pressure range could be seen. The hysteresis at higher pressure could be due to significant N_2 adsorption between the particles of very small size (20–50 nm) and due to the external surface area in the interparticulate voids. The steep N_2 uptake at low pressure indicates the presence of ultra-micropores in the specimen with minor mesopores and macropores. The pore size distribution (PSD) estimated by DFT model (Fig. S9†) shows the average pore diameter of 0.65 nm and majority of the pores were <2 nm in diameters, with some distribution in the higher diameter range. The specific surface area calculated by using BET (S_{BET}) and Langmuir (S_{Lang}) model were found to be to 976 and 1237 m^2 g^{-1}, respectively (Fig. S10†). These values are further comparable with the cumulative surface area (967 m^2 g^{-1}) calculated by DFT & Monte-Carlo analysis. The multilayer adsorption in intermediate section of N_2 isotherm indicated the presence of significant external surface area. The external surface area calculated by the *t*-plot method was found to be 603 m^2 g^{-1}. This further supports the smaller particle size of the sample. Pore volume calculated at relative pressure (P/P_0) 0.90 from the adsorption branch of the isotherm, was found to be 1.07 cm^3 g^{-1} (Table S4, ESI†). The higher specific surface area and pore volume of HNM-1 could be attributed to the unique paddle wheel structure of the cyclophosphazene moieties in the framework, which has been reported earlier.[6–8,10] In order to further understand if the reaction temperature has any profound effect on the textural properties, two more samples have been synthesized at 423 and 393 K (while keeping all other reaction conditions same) designated as HNM-2 and HNM-3, respectively. It was observed that with the decrease in the reaction temperature, there was the decrease in the S_{BET} to 807 and 513 m^2 g^{-1}, in HNM-2 and HNM-3, respectively (Fig. S7, S11–S12, Table S4, ESI†). The pore size distribution calculated by DFT model for HNM-2 and HNM-3 was found to be centred at about 0.64 nm. This could be attributed to the weaker framework condensation at lower temperature. High temperature led to opening of micropore that led to increase of both micropore as well as external surface area of HNM-1 in comparison to HNM-2 and HNM-3 (pl. see ESI, Table S4†). However, there was no substantial difference in the particle size and shape (Fig. S8†) although, the experiments were carried out at three different temperatures. The presence of the ultra-micropores with high S_{BET} and pore volume coupled with the high nitrogen content (>42%) encouraged us to study the CO_2 sorption properties. Fig. 3b shows the CO_2 sorption isotherms of HNM-1 measured at 273 and 298 K. Almost complete reversibility was observed with minor hysteresis. The highest CO_2 uptake was found to be 18.9 and 12.3 wt% at 273 and 298 K, respectively (Table S5, ESI†). The CO_2 uptake of HNM-1 is higher than many of the recently reported materials like TBILP-1,[35] PAF-3 [36] and C-NP[37] (Table S6, ESI†). The HNM-2 and HNM-3 also show noteworthy CO_2 uptake of 13.2 wt% and 9.5 wt%, respectively at 273 K and 1 bar (Fig. S13 and Table S5†). It is, however, important to note that the high nitrogen content is not the only factor that can tune the CO_2 capture capacity. There could be multiple factors that affect the CO_2 capture capacity such as pore size, pore geometries, surface functionalities and kinetics. The role of high nitrogen content is to enhance the Lewis basic nature of framework which helps in the adsorption of Lewis acidic gas like CO_2. The higher CO_2 uptake of HNM-1 in comparison to HNM-2 and HNM-3 could be due to higher surface area and pore volume.

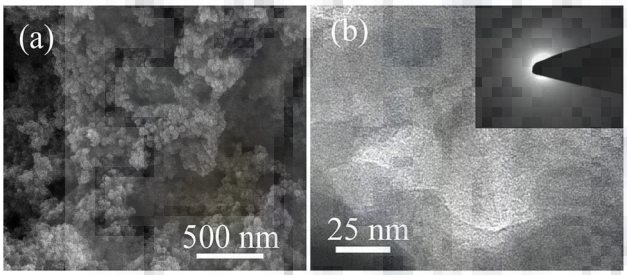

Fig. 2 (a) FESEM and (b) TEM image of HNM-1. SAED pattern in the inset of (b).

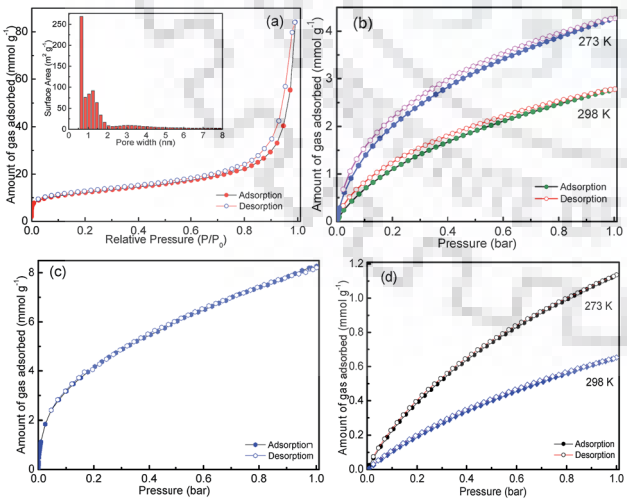

Fig. 3 Gas sorption isotherms of HNM-1. (a) N_2 sorption isotherm measured at 77 K, (b) CO_2 sorption isotherms measured at 273 and 298 K, (c) H_2 sorption isotherm measured at 77 K and (d) CH_4 sorption isotherms measured at 273 and 298 K. The pore size distribution histogram calculated by the DFT model from the N_2 sorption data is given in the inset of (a).

The isosteric heats of adsorption (Q_{st}) of HNMs were further calculated using Clausius–Clapeyron equation (Fig. S14, ESI†). At the onset, the Q_{st} values are 34.7, 35.9 and 33 kJ mol^{-1} for HNM-1, HNM-2 and HNM-3, respectively (Table S5, ESI†). The Q_{st} values of HNMs indicated the interaction between the adsorbent and the adsorbate was neither purely physisorption nor pure chemisorption and was at the cusp of these two.[10]

Furthermore, HNMs were tested for the H_2 and CH_4 storage. The H_2 sorption isotherm as shown in Fig. 3c was completely reversible without hysteresis and the uptake at maximum pressure range for the HNM-1 was 1.63 wt% at 77 K and 1 bar. It is further worth mentioning that the sorption isotherm was not saturated in the measured pressure range indicating a higher uptake could be achieved at higher pressure.[38] The H_2 uptake of HNM-1 surpasses or comparable to various porous organic polymers and nanoporous hybrid materials such as, PSN-3,[31] CTC-COF,[32] PIMs[33] and BLP(2H).[34] The CH_4 uptake of HNM-1 was found to be 1.13 and 0.88 wt% measured at 273 and 298 K, respectively. To understand the feasible application of the synthesized materials for the purpose of post combustion CO_2 capture in coal fired power plants, the selective uptake of CO_2 over CH_4 and N_2 is one of the main criteria. The selectivity of CO_2 with respect to CH_4 and N_2 was estimated by using the Henry's law constant.[10] The selectivity of CO_2 over N_2 and CO_2 over CH_4 for HNM-1 were found to be 62 and 14, respectively, at 273 K (Fig. S16–S21 and Table S5, ESI†). The selective uptake of HNMs is comparable to the recently reported materials like TBILP-1,[35] PECONF-3 [10] and higher than TBILP-2,[35] C-NP,[37] PAN-1,[39] and fl-CTF350 [40] (Table S6, ESI†). The moderate selectivity shown by HNMs despite having very high nitrogen content could be attributed to the fact that CO_2 might not be interacting with all the nitrogen of the framework and it is interacting with only nitrogen present on the surface.

4. Conclusions

In summary, Schiff base condensation has been used for the first time to synthesize aminal linked nanoporous inorganic–organic hybrid materials, which shows relatively high specific surface area and could capture up to 18.9 wt% of CO_2 at 273 K along with 1.63 wt% of H_2 at 77 K. The materials synthesized in this work has a higher nitrogen content (>42%) which is beneficial for exploiting the Lewis basic character needed for several applications. Further, the synthesis method could be extended to make various other cyclophosphazene derived nanoporous hybrid materials.

Acknowledgements

The work was financially supported by DST, Govt. of India with Grant code DST/IS-STAC/CO2-SR-132/12(G).

Notes and references

1 C. Sanchez, P. Belleville, M. Popall and L. Nicole, *Chem. Soc. Rev.*, 2011, **40**, 696–753.
2 D. Wang, W. Yang, S. Feng and H. Liu, *Polym. Chem.*, 2014, **5**, 3634–3642.
3 L. Nicole, C. L. Robert, L. Rozes and C. Sanchez, *Nanoscale*, 2014, **6**, 6267–6292.
4 M. H. Lim and A. Stein, *Chem. Mater.*, 1999, **11**, 3285–3295.
5 P. Pierce, *Structure in Nature is a Strategy for Design*, MIT Press, 1990.
6 P. Rekha, U. Sahoo and P. Mohanty, *RSC Adv.*, 2014, **4**, 34860–34863.
7 P. Rekha, R. Muhammad and P. Mohanty, *RSC Adv.*, 2015, **5**, 67690–67699.
8 P. Rekha, V. Sharma and P. Mohanty, *Microporous Mesoporous Mater.*, 2016, **219**, 93–102.
9 R. Kagit, M. Yildirim, O. Ozay, S. Yesilot and H. Ozay, *Inorg. Chem.*, 2014, **53**, 2144–2151.
10 P. Mohanty, L. D. Kull and K. Landskron, *Nat. Commun.*, 2011, **2**, 401–406.
11 H. R. Allcock, *Chemistry and Applications of Polyphosphazenes*, Wiley, New Jersey, 2002.
12 H. Schiff, *Justus Liebigs Ann. Chem.*, 1864, **131**, 118–119.
13 N. E. Borisova, M. D. Reshetova and Y. A. Ustynyuk, *Chem. Rev.*, 2007, **107**, 46–79.
14 L. S. M. Forlani and P. E. Todesco, *Gazz. Chim. Ital.*, 1986, **116**, 229–232.
15 S. J. Rowan and J. F. Stoddart, *Org. Lett.*, 1999, **1**, 1913–1916.
16 M. Y. Khuhawar, M. A. Mughal and A. H. Channar, *Eur. Polym. J.*, 2004, **40**, 805–809.
17 Y. Xin and J. Yuan, *Polym. Chem.*, 2012, **3**, 3045–3055.
18 F. J. U. Romo, J. R. Hunt, H. Furukawa, C. Klock, M. O'Keeffe and O. M. Yaghi, *J. Am. Chem. Soc.*, 2009, **131**, 4570–4571.
19 P. Pandey, A. P. Katsoulidis, I. Eryazici, Y. Wu, M. G. Kanatzidis and S. T. Nguyen, *Chem. Mater.*, 2010, **22**, 4974–4979.
20 M. G. Schwab, B. Fassbender, H. W. Spiess, A. Thomas, X. Feng and K. Mullen, *J. Am. Chem. Soc.*, 2009, **131**, 7216–7217.
21 W. C. Song, X. K. Xu, Q. Chen, Z. Z. Zhuang and X. H. Bu, *Polym. Chem.*, 2013, **4**, 4690–4696.
22 A. Laybourn, R. Dawson, R. Clowes, J. A. Iggo, A. I. Cooper, Y. Z. Khimyak and D. J. Adams, *Polym. Chem.*, 2012, **3**, 533–537.
23 Y. Zhu, H. Long and W. Zhang, *Chem. Mater.*, 2013, **25**, 1630–1635.
24 R. Gomes, P. Bhanja and A. Bhaumik, *Chem. Commun.*, 2015, **51**, 10050–10053.
25 D. Lee, C. Zhang, C. Wei, B. L. Ashfeld and H. Gao, *J. Mater. Chem. A*, 2013, **1**, 14862–14867.
26 S. D. Kenarsari, D. Yang, G. Jiang, S. Zhang, J. Wang, A. G. Russell, Q. Wei and M. Fan, *RSC Adv.*, 2013, **3**, 22739–22773.
27 W. Lu, J. P. Sculley, D. Yuan, R. Krishna, Z. Wei and H. C. Zhou, *Angew. Chem., Int. Ed.*, 2012, **51**, 7480–7484.
28 G. Li, B. Zhang, J. Yan and Z. Wang, *Chem. Commun.*, 2014, **50**, 1897–1899.
29 N. B. McKeown, P. M. Budd and D. Book, *Macromol. Rapid Commun.*, 2007, **28**, 995–1002.
30 V. Sharma, A. Sahoo, Y. Sharma and P. Mohanty, *RSC Adv.*, 2015, **5**, 45749–45754.

31 G. Li, B. Zhang and Z. Wang, *Macromol. Rapid Commun.*, 2014, **35**, 971–975.
32 J. T. Yu, Z. Chen, J. L. Sun, Z. T. Huang and Q. Y. Zheng, *J. Mater. Chem.*, 2012, **22**, 5369–5373.
33 B. S. Ghanem, K. J. Msayib, N. B. McKeown, K. D. M. Harris, Z. G. Pan, P. M. Budd, A. Butler, J. Selbie, D. Book and A. Walton, *Chem. Commun.*, 2007, **43**, 67–69.
34 K. T. Jackson, T. E. Reich and H. M. El-Kaderi, *Chem. Commun.*, 2012, **48**, 8823–8825.
35 A. K. Sekizkardes, S. Altarawneh, Z. Kahveci, T. İslamoğlu and H. M. El-Kaderi, *Macromolecules*, 2014, **47**, 8328–8334.
36 T. Ben, C. Pei, D. Zhang, J. Xu, F. Deng, X. Jinga and S. Qiu, *Energy Environ. Sci.*, 2011, **4**, 3991–3999.
37 M. Saleh and K. S. Kim, *RSC Adv.*, 2015, **5**, 41745–41750.
38 B. Adeniran and R. Mokaya, *J. Mater. Chem. A*, 2015, **3**, 5148–5161.
39 G. Li, B. Zhang, J. Yan and Z. Wang, *Macromolecules*, 2014, **47**, 6664–6670.
40 S. Hug, M. B. Mesch, H. Oh, N. Popp, M. Hirscher, J. Senker and B. V. Lotsch, *J. Mater. Chem. A*, 2014, **2**, 5928–5936.

LANGMUIR Article
Cite This: Langmuir 2018, 34, 2926−2932
pubs.acs.org/Langmuir

Cyclophosphazene-Based Hybrid Nanoporous Materials as Superior Metal-Free Adsorbents for Gas Sorption Applications

Raeesh Muhammad and Paritosh Mohanty*

Functional Materials Laboratory, Department of Chemistry, IIT Roorkee, Roorkee, Uttarakhand 247667, India

Supporting Information

ABSTRACT: Cyclophosphazene-based inorganic−organic hybrid nanoporous materials (CHNMs) have been synthesized by a facile solvothermal method. The condensation of pyrrole with the reaction product of phosphonitrilic chloride trimer and 4-hydroxybenzaldehyde resulted in the formation of high-surface-area CHNMs. The maximum specific surface area (SA_{BET}) of 1328 m^2 g^{-1} with hierarchical pore structures having micropores centered at 1.18 nm and mesopores in the range of 2.6−3.6 nm was estimated from the N_2 sorption analysis. Observation of high SA_{BET} could be attributed to the synergy effect exerted by the cyclophosphazene moiety owing to its three-dimensional paddle wheel structure. The metal-free adsorbent exhibited a high and reversible CO_2 uptake of 22.8 wt % at 273 K and 1 bar. The performance is on the higher side among the reported metal-free inorganic−organic hybrid nanoporous adsorbents. Moreover, the high H_2 uptake of 2.02 wt % at 77 K and 1 bar is an added advantage. The superior performance of the adsorbents for the gas sorption applications could be attributed to the combined effect of high SA_{BET} and hierarchical pore structure, which has made CHNMs good candidates for energy and environmental applications.

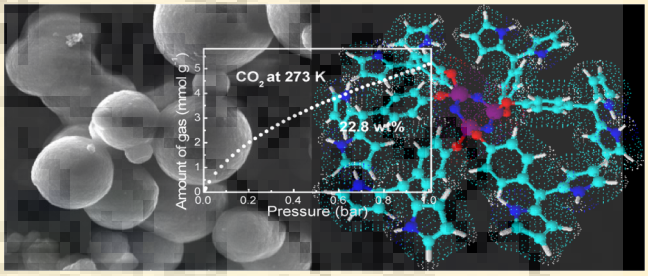

1. INTRODUCTION

The massive consumption of fossil fuel to satisfy the ever-growing energy demand with the rapid population growth has contributed to the dramatic increase in the emission of CO_2 in the atmosphere that crossed 400 ppm in the recent times.[1−3] The uncontrolled CO_2 emission has led to rise in the earth's surface temperature at an unusually rapid rate and has risen by 0.83 °C since preindustrial era.[2,4] If not taken proper care now or in the near future to control the CO_2 emission, several devastating calamities are predicted, for example, submerging of many populous cities due to the rise in the sea level owing to the melting of glaciers.[5−7] Further, the lower albedo would cause a faster melting of the glaciers.[8] Additionally, the increased earth's temperature will cause problems such as drought, downpour, and typhoon.[9]

To reduce the emission of CO_2, several measures have been pursued. Notably, the use of (i) renewable energies such as solar energy, wind energy, hydroelectric energy, and geothermal energy, (ii) carbon-free fuel such as H_2, and (iii) fossil-based energy source without the release of CO_2 into the atmosphere are the leading technologies.[10−14] After rigorous research and development (R&D) activities for decades, the renewable source of energy could reach maximum up to 19.3% in 2015 of the total energy demand so far and could not compete with the conventional fossil fuel.[15,16] The H_2 production and storage technology is yet far from the sustainability.[1,17] Still, the majority of the energy demand lies with the use of fossil fuels.[1] Therefore, using fossil fuels in a greener way by capturing and sequestrating CO_2 could be a potential solution that looks pragmatic. In this regard, liquid organic alkanolamine and its derivatives have been commercially employed for tripping off CO_2 from the flue gas stream, but the high regeneration cost, low thermal stability, and high equipment corrosion rate have limited its wide spread applications.[18−21] Recently, solid adsorbents have emerged as potential alternatives.[4,13,18,22] The interaction between solid adsorbents and CO_2 is governed by weak van der Waal's interaction without forming a permanent chemical bond, owing to the reduced undesired kinetic and thermodynamic barrier.[20,22] This, in turn, facilitates the regeneration, and the process would be less energy intensive.[20] High-surface-area microporous solids have emerged so far, the winner for such applications due to the superior van der Waal's interaction in an ultrasmall confined pore space.[22−24] Various explored microporous adsorbents for the CO_2 capture application include activated carbon,[24−26] amine-grafted silica,[27−29] zeolite imidazole framework,[30−32] metal−organic framework,[33−35] covalent organic framework,[36−38] porous aromatic framework,[39−41] porous electron-rich covalent organonitridic framework (PECONF),[21] porous polymer networks,[42,43] porous hybrid materials,[44] porous azo-linked polymers (ALPs),[45] benzimidazole-linked polymers (BILPs),[46] hybrid nanoporous materials (HNMs), and so forth.[47]

Among the various characteristics that determine the efficiency of an adsorbent for CO_2 capture includes but not

Received: September 16, 2017
Revised: January 8, 2018
Published: February 8, 2018

DOI: 10.1021/acs.langmuir.7b03263
Langmuir 2018, 34, 2926−2932

Scheme 1. Reaction Scheme for the Synthesis of CHNMs

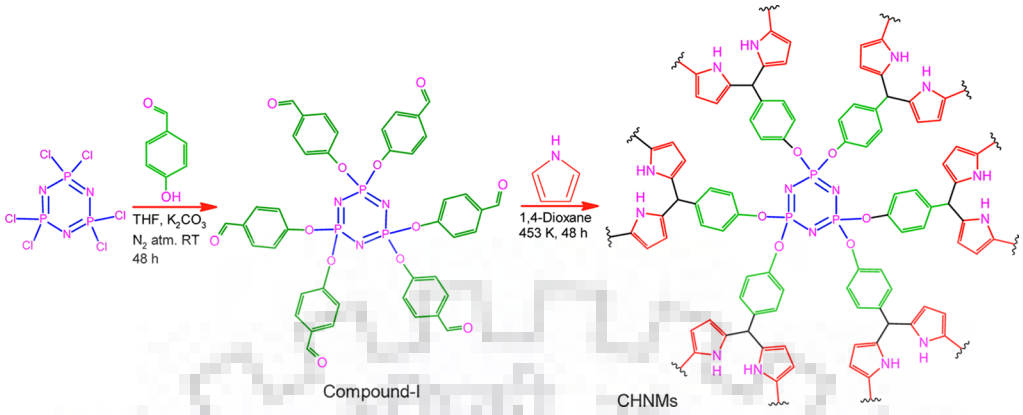

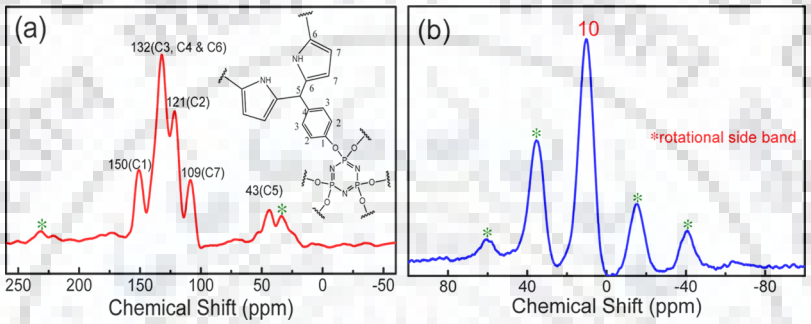

Figure 1. (a) ^{13}C CP-MAS NMR and (b) ^{31}P CP-MAS NMR spectra of CHNM-1.

limited to the high specific surface area, narrow pore size distribution, large pore volume, and basic functionalities in the framework.[47] A continuous effort has been made in the past to improve some of the above characteristics. A combination of few or all of the characteristics could potentially provide an ideal adsorbent. In this regard, our research group has been using cyclophosphazene as an interesting and important metal-free inorganic moiety to synthesize high-surface-area inorganic−organic hybrid materials.[44,47−50] As documented in some of our recent research, the three-dimensional paddle wheel structure of cyclophosphazene has exerted a synergic effect in improving the specific surface area.[44,47−50] This synergic effect was proved with various precursors and different synthetic approaches such as click chemistry, Schiff base condensation, hydrolysis, and polycondensation. Additionally, the N and P present in the framework further facilitate the applications.[44,47] In the present research, high-surface-area nanoporous multifunctional hybrid adsorbents have been made by condensing pyrrole with the cyclophosphazene derivative. These adsorbents have been used for the CO_2 capture and H_2 storage applications. H_2 as a fuel is considered as a green energy source because of its high energy density (33.3 kW h kg^{-1}) in comparison to gasoline (11.1 kW h kg^{-1}) and nonpolluting in nature.[51,52] For practical applications in fuel cells, hydrogen needs to be stored at high densities without much additional weight.[52] This safety issue mainly hindered the use of compressed hydrogen.[17,51,52] Therefore, finding a suitable adsorbent that can store a substantial amount of H_2 could be one of the potential solutions.

2. EXPERIMENTAL SECTION

2.1. Materials. Phosphonitrilic chloride trimer (99%, Sigma-Aldrich), 4-hydroxybenzaldehyde (99%, Sigma-Aldrich), dichloromethane (SRL), methanol (Merck), and potassium carbonate (Himedia) were used as-received without any purification. Pyrrole (99%, SRL) has been distilled; Na_2SO_4 (Himedia), tetrahydrofuran (THF, Fisher Scientific) and 1,4-dioxane (Fisher Scientific) have been dried before their use.

2.2. Synthesis of Compound-I. One of the reactants used for the synthesis of Cyclophosphazene-based inorganic−organic hybrid nanoporous materials (CHNMs), compound-I, has been prepared following our previous report (Schemes 1 and S1).[47] The detailed structural characterization of compound-I by Fourier transform infrared (FT-IR) and NMR spectroscopies is given in Figures S1−S4.

2.3. Synthesis of CHNMs. CHNMs have been synthesized by solvothermal condensation of pyrrole with compound-I at 453 K for 48 h using a Teflon-lined autoclave, as shown in Scheme 1. Prior to the solvothermal treatment, 3.0 mmol freshly distilled pyrrole and 0.5 mmol compound-I dissolved in 5 mL of dry 1,4-dioxane were stirred at 343 K for 1 h in the N_2 atmosphere. A brownish-black monolith was obtained which was collected after cooling to room temperature and washed it repeatedly with THF and methanol. The dried sample (dried in vacuum at 353 K) was designated as CHNM-1. Two more specimens, CHNM-2 and CHNM-3, were prepared by increasing the solvent amount from 5 mL in CHNM-1 to 10 and 15 mL, respectively, keeping all other reaction conditions identical.

2.4. Characterization. The structural and microstructural investigation of the specimens have been carried out using FT-IR (Spectrum Two, PerkinElmer), solid-state cross-polarization magic-angle spinning (CP-MAS) ^{31}P and ^{13}C NMR (JEOL resonance JNM-ECX-400II), powder X-ray diffraction (XRD; Ultima IV, Rigaku), CHNS (varioMICRO), field emission scanning electron microscopy (FESEM; MIRA3, TESCAN), and transmission electron microscopy (TEM; TECNAIG2S-TWIN) instruments. The thermal stability of the specimens has been investigated using an EXSTAR TG/DTA6300 TGA analyzer under air.

The textural properties and gas sorption studies have been investigated by Autosorb iQ2 (Quantachrome Instruments). The N_2 sorption analysis was performed at 77 K using a liquid N_2 bath after

DOI: 10.1021/acs.langmuir.7b03263
Langmuir 2018, 34, 2926−2932

activating the specimen by degassing at 393 K for 6 h under vacuum. Pore size distribution (PSD) was calculated by fitting the N_2 sorption isotherm to the density functional theory (DFT) model with a kernel carbon model (cylindr. pores, QSDFT adsorption branch). The CO_2 uptake has been carried out at 273 and 298 K. The H_2 storage capacity of the specimen was estimated at 77 K. The isosteric heat of adsorption (Q_{st}) for CO_2 was calculated using the Clausius−Clapeyron equation. The CO_2 versus N_2 selectivity was estimated using the initial slope method (Henry's law constant).

3. RESULTS AND DISCUSSION

The proposed structure as shown in Scheme 1 was confirmed by the spectroscopic investigation. Solid-state CP-MAS NMR spectra of a representative sample, CHNM-1, are shown in Figure 1. The observation of the resonance signal at the δ of 43 ppm in the ^{13}C CP-MAS NMR spectrum (Figure 1a) originated due to the presence of methine carbon (C5) in the framework confirms the nucleophilic condensation of pyrrole with the aldehyde functionality of compound-I.[53] The resonance signal at 150 ppm is observed due to deshielded C1 carbon that is directly attached to the electronegative O atom.[47] The resonance signal at 132 ppm originated due to C3 and C4 aromatic carbons and C6 carbon of the pyrrole ring.[47,53,54] The resonance signal of the C2 carbon is observed at 121 ppm.[47] Moreover, the C7 pyrrolic carbon could be seen at the δ of 109 ppm.[53,54] All of the signals from the ^{13}C CP-MAS NMR spectrum could be indexed to different carbons of the proposed structure, confirming the framework formation. Moreover, the absence of a resonance signal at the δ of 170 ppm (due to the carbonyl carbon of compound-I) indicates the completeness of the condensation reaction. Further, the observation of a broad resonance signal at 10 ppm in the ^{31}P CP-MAS NMR spectrum of CHNM-1 (Figure 1b) confirms the inclusion of the cyclophosphazene moieties in the framework.[47,48] Detailed NMR signal assignments are summarized in Table S1a,b.

The FT-IR spectra further corroborated the results obtained from the CP-MAS NMR spectra. The disappearance of the band at 1710 cm^{-1} in the FT-IR spectra (Figure S4, Supporting Information) due to the carbonyl group of compound-I and the observation of the band at 2930 cm^{-1} due to methine linkage confirm the condensation.[47] The band at 3430 cm^{-1} in the FT-IR spectra is revealed because of the −N−H stretching vibrations of pyrrole moieties in the frameworks.[55,56] The band at 1690 cm^{-1} due to C═N stretching present in the pyrrole is also observed in the CHNMs.[57,58] This band should not be mistaken for carbonyl stretching. The presence of bands at 1620, 1420, and 1270 cm^{-1} could be attributed to asymmetric ring, N−H bending, and −C−H in-plane vibrations for the pyrrole ring, respectively.[54−56] The band at 1600 cm^{-1} is attributed to aromatic ring stretching.[40] The observation of bands in the range of 1203 to 1193, 986, and 584 cm^{-1} assigned to ν_{as}(P═N−P), ν_{as}(P−O−C), and δ(P═N−P) vibrations, respectively, confirms the inclusion of the cyclophosphazene units in the frameworks.[44,47−50] Detailed FT-IR band assignments are summarized in Table S1c.

The CHNMs were found to be insoluble in most of the common polar and nonpolar solvents. The elemental compositions of the CHNMs estimated from the CHNS elemental analyzer are given in Table S2. The theoretical and experimental estimation of the elemental compositions matched fairly well with a minor deviation due to the nature of the materials. In general, the experimental elemental compositions of high-surface-area amorphous frameworks have shown a deviation from their respective theoretical values.[47] This could be attributed due to several factors such as the presence of end-group functionality and trapping of solvent, moisture, and small gas molecules inside the pores. This was further observed in the thermogravimetric (TG)/derivative thermogravimetric analysis of CHNMs (Figure S5, Supporting Information). The initial mass loss above 373 K is due to the removal of trapped moisture, atmospheric gases, and solvents used during synthesis and washing. The framework is thermally stable up to a temperature of 500 K, and above this, a gradual decomposition could be seen when the experiment was carried out in the air.

The phase analysis of the CHNMs was carried out by powder XRD. The absence of any sharp diffraction peak and the presence of two broad halos centered around 12 and 20.5° in the 2θ scale in the XRD patterns shown in Figure S6 indicate the amorphous nature of specimens. The microstructure of the specimens has been investigated by FESEM and TEM. The typical FESEM images of CHNM-1, CHNM-2, and CHNM-3 are shown in Figure 2a−c, respectively. CHNM-1 has a different microstructure as compared to the other two samples. It can be seen from Figure 2 that CHNM-2 and CHNM-3 have spherical particles of micrometer sizes connected with each other. The surface of these spherical particles is comparatively smooth. However, small particles with an average diameter around 120 nm with irregular shapes can be observed in the FESEM image of CHNM-1 in Figure 2a. These small particles are agglomerated with each other forming clusters. Interestingly, the TEM analysis of this sample reveals a porous nature of the specimen, as shown in Figure 2d. The pores are of different sizes in the nanometer range forming a hierarchical pore structure. The corresponding selected-area electron diffraction (SAED) pattern shown in the inset of Figure 2d has diffused broad halos further supporting the amorphous nature of CHNM-1 as observed in the XRD patterns.

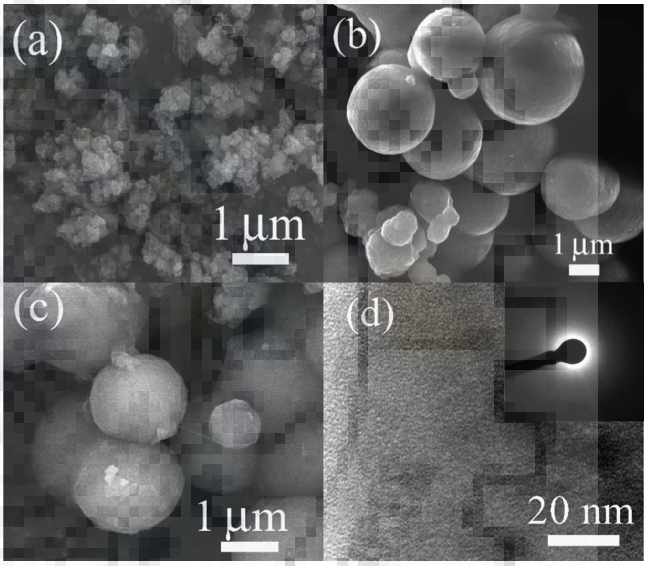

Figure 2. FESEM images: (a) CHNM-1, (b) CHNM-2, and (c) CHNM-3. (d) TEM image of CHNM-1. The SAED pattern of CHNM-1 is given in the inset of (d).

The observation of different microstructures on changing the concentration of the reactants in these CHNMs could be attributed to different kinetics of condensation. At the higher concentration, because of the supersaturation condition, a large

DOI: 10.1021/acs.langmuir.7b03263
Langmuir 2018, 34, 2926−2932

number of nuclei are formed at the beginning of the reaction and for the growth, a fewer number of materials are left in the reaction solution, resulting in the formation of smaller particles with a rough surface. On the other hand, at a higher dilution, a less number of nuclei are formed and these nuclei have got enough materials in the reaction solution for the growth of the particles with larger sizes and comparatively smooth surface.

The observation of the nanoporous structure from the TEM image in Figure 2d has encouraged us to investigate the textural properties of the CHNMs. The N_2 sorption isotherms of CHNMs, as shown in Figure 3a, exhibit a combination of type-I and type-IV isotherm. A sharp uptake at a low relative pressure (P/P_0) of <0.01 represents the type-I isotherm owing to the presence of the micropores. Moreover, a hysteresis above 0.45, which extends up to 0.9, indicates the presence of mesopores in the specimens, thus forming a hierarchical pore structure. This corroborates the TEM observation, which was further confirmed from the PSD analysis that shows the presence of micropores centered around 1.18 nm and mesopores in the region of 2.6 to 3.6 nm (Figure 3b and Table 1) forming a hierarchical pore structure. This is very interesting and important for the materials to be used as adsorbents. The ultrasmall pores help in achieving a higher loading due to the enhanced interaction of the pore surface with the adsorbates owing to the shorter distance between them (thermodynamically favorable processes) in combination with the capillary action, whereas the larger mesopores help in the kinetics of the adsorbate molecules to have a facile mass transfer.[24,59] Such phenomenon has already been reported by our group and other groups.[21,24,46,47] There is a gradual increase in the adsorption that extends throughout the pressure range in CHNM-1, whereas in CHNM-2 and CHNM-3, the adsorption branch of the isotherms is comparatively flat. This may be attributed to the particle size, shape, and the roughness of the particle surfaces. As discussed above with the FESEM images, a comparatively rough surface can be seen in CHNM-1 with smaller particle size. The interparticulate voids could further increase the adsorption at a higher pressure range.[47] It is worth mentioning that the desorption branch of all the specimens has not closed even at a low-pressure range. This could be attributed to the swelling effect.[60,61] Such a swelling effect is commonly observed in high-surface-area nanoporous polymeric materials owing to the access of the ultra-micropores by the probe molecules with some restrictions.[60−63]

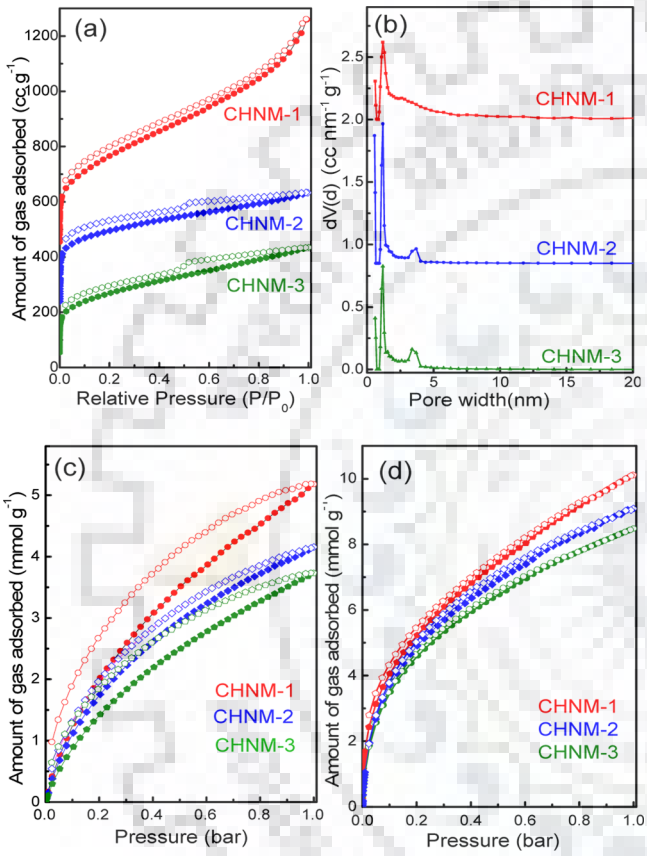

Figure 3. (a) N2 sorption isotherms: CHNM-1 (+400), CHNM-2 (+200), and CHNM-3. (b) pore size distributions; CHNM-1 (+2), CHNM-2 (+0.85), and CHNM-3. (c) CO_2 sorption, and (d) H_2 sorption isotherms.

Table 1. Physicochemical Properties of CHNMs

sample	SA_{BET} (m^2 g^{-1})	pore size (nm)	pore vol. (cm^3 g^{-1})
CHNM-1	1328	1.18 & 2.6	1.30
CHNM-2	1070	1.18 & 3.6	0.67
CHNM-3	960	1.18 & 3.4	0.67

The specific surface area (SA_{BET}) calculated by the Brunauer−Emmett−Teller (BET) method has shown a gradual decrease in the SA_{BET} with an increase in the dilution. CHNM-1 has a maximum SA_{BET} of 1328 m^2 g^{-1} (Figure S7a, Supporting Information). The SA_{BET} of CHNM-2 and CHNM-3 was estimated to be 1070 and 960 m^2 g^{-1}, respectively (Figure S7b,c, Supporting Information). As discussed above, the difference in the SA_{BET} could be attributed to the surface roughness as well as particle sizes. CHNM-1 has a large pore volume of 1.33 cm^3 g^{-1} estimated at a relative pressure (P/P_0) of 0.99. The pore volume of CHNM-2 and CHNM-3 is same (0.67 cm^3 g^{-1}). Detailed textural properties of all these specimens are summarized in Table 1.

The high SA_{BET}, narrow PSD, hierarchical pore structure, and the presence of Lewis basic sites in CHNMs have propelled us to study CO_2 adsorption. The CO_2 sorption isotherm measured at 273 K and 1 bar, given in Figure 3c, shows the CO_2 uptake of 22.8, 18.3, and 16.4 wt % for CHNM-1, CHNM-2, and CHNM-3, respectively. The CO_2 uptake of CHNM-1 is better than many reported high-surface-area solid sorbent such as PECONF-3,[21] MPC-700,[25] PAF-3,[39] HNM-1,[47] HCMP-1,[61] and CZ@PON[62] and comparable to many top-performing reported high-surface-area solid adsorbents such as PPF-1,[40] ALP-1,[45] BILP-4,[64] BILP-6-NH_2,[46] and IBFNP-1[65] (for more details, see Supporting Information, Table S3). At 298 K, as expected, the CO_2 uptake decreases to 14.1, 10.5, and 8.9 wt % for CHNM-1, CHNM-2, and CHNM-3, respectively (Figure S8, Supporting Information). It can further be seen that the desorption branch of the isotherms does not close even at low pressure. This may be attributed to the higher Lewis acid−Lewis base interaction (higher heat of adsorption), smaller pore size, and swelling effect.[60] The isosteric heat of adsorption (Q_{st}) for CO_2 sorption for the CHNMs was estimated using the Clausius−Clapeyron equation. At zero coverage, the Q_{st} of CO_2 with CHNM-1, CHNM-2, and CHNM-3 was estimated to be 31.76, 37.16, and 34.92 kJ mol^{-1}, respectively (Table 2, Figure S9, Supporting Information). The higher Q_{st} for CHNM-2 than those for CHNM-1 and CHNM-3 could be attributed to the higher

DOI: 10.1021/acs.langmuir.7b03263
Langmuir 2018, 34, 2926−2932

Table 2. Gas Sorption Summary of CHNMs

sample	CO_2 uptake (wt %) 273 K	CO_2 uptake (wt %) 298 K	Q_{st} for CO_2 (kJ mol^{-1})	H_2 uptake (wt %) 77 K
CHNM-1	22.8	14.1	31.76	2.02
CHNM-2	18.3	10.5	37.16	1.82
CHNM-3	16.4	8.9	34.92	1.70

nitrogen content, as can be seen in Table S2. However, as the SA_{BET} of CHNM-2 is only 80.6% of CHNM-1, the total CO_2 capture capacity could not exceed. The high CO_2 capture capacity for CHNMs is due to the favorable interactions between the Lewis acidic CO_2 molecules and Lewis basic N-functionality in the porous framework. The Q_{st} of CHNMs falls at the cusp of physisorption and chemisorption. This is because the materials that have basic sites usually display higher affinity toward CO_2 and hence higher Q_{st}. However, as there is no permanent covalent bond formed, the energy input is low enough compared to the chemisorbed surfaces as in the case of primary alkanolamine monoethanolamine, which remains one of the great challenges for its use in current CO_2 capture technologies.

The use of molecular H_2 as a fuel has been considered the best alternative to replace the traditional fossil-based energy system for the automotive application.[1] Hence, we have employed CHNMs for H_2 storage at 77 K and 1 bar (Figure 3d). CHNM-1, CHNM-2, and CHNM-3 have shown reversible H_2 uptake of 2.02, 1.82, and 1.70 wt %, respectively. The H_2 storage capacity of CHNM-1 can be compared with many of the recently reported high-surface-area solid adsorbent materials such as PAF-3,[39] PPF-4,[40] PAF-47,[41] ALP-2,[45] HNM-1,[47] and BILP-4[64] (for more details, see Supporting Information, Table S4). Interestingly, the isotherms are completely reversible in nature which indicates the physisorption reversibility of CHNMs, and do not show saturation up to the measured pressure range of 1 bar. Thus, an elevated pressure could improve the H_2 storage capacity substantially.[66] The detailed gas sorption summary of all these specimens is given in Table 2.

The efficiency of the adsorbent to be used industrially to capture and separate CO_2 from the flue gas stream depends upon several factors, and gas selectivity is one of them. The selectivity of CO_2 versus N_2 is important particularly as N_2 is the major component amounting about 70% in the flue gas.[21] Using Henry's law constant,[21] the selectivity of CO_2 over N_2 was estimated at 273 K to be 66, 77, and 47 for CHNM-1, CHNM-2, and CHNM-3, respectively (Figure S10, Supporting Information). The higher selectivity of CHNM-2 could be resulted due to higher Q_{st}, owing to the higher nitrogen content among these samples. The selectivity can be compared to the recently reported materials such as PECONF-3,[21] BILP-4,[64] and higher than PAF-3,[39] PPF-1,[40] APOP-3,[67] TBILP-1,[68] *fl*-CTF350,[69] and PAN-1[70] (pl. see Supporting Information, Table S3).

4. CONCLUSIONS

The incorporation of cyclophosphazene moieties into the framework of a series of inorganic−organic hybrid nanoporous materials (CHNMs) has played a synergic role in improving the textural properties. A facile solvothermal method was used for the synthesis of the CHNMs which could yield metal-free adsorbents with a specific surface area, SA_{BET}, as high as 1328 m^2 g^{-1}. The hierarchical pore structure and large pore volume are beneficial for CO_2 capture and H_2 storage applications. A maximum CO_2 uptake of 22.8 wt % at 273 K and a maximum H_2 storage of 2.02 wt % at 77 K were realized. The large CO_2 uptake could be attributed to the higher adsorbent−adsorbate affinity because of the presence of Lewis basic functionality on the pore surface. The high H_2 storage was mainly due to the hierarchical pore structure with the presence of pores in the micropore regime. The observed physicochemical properties make these metal-free adsorbent materials front runners for the future generation adsorbents for energy and environmental applications.

■ ASSOCIATED CONTENT

Supporting Information

The Supporting Information is available free of charge on the ACS Publications website at DOI: 10.1021/acs.langmuir.7b03263.

Reaction scheme, NMR and FT-IR spectra, elemental analysis, TGA, XRD pattern, multipoint BET plots, CO_2 sorption isotherms at 298 K, isosteric heat of adsorption, and CO_2/N_2 selectivity (PDF)

■ AUTHOR INFORMATION

Corresponding Author

*E-mail: pmfcy@iitr.ac.in, paritosh75@gmail.com.

ORCID

Raeesh Muhammad: 0000-0003-3448-5846

Paritosh Mohanty: 0000-0003-2765-0129

Notes

The authors declare no competing financial interest.

■ ACKNOWLEDGMENTS

This research was financially supported by DST, Govt. of India with grant no. DST/TDT/TDP-03/2017(G).

■ REFERENCES

(1) Eddaoudi, M.; Barbour, L. J. CO_2 Separation, Capture and Reuse: A Web Themed Issue. *Chem. Commun.* **2015**, *51*, 5554−5555.

(2) https://www.co2.earth/. (accessed August, 2017).

(3) Soleimanisalim, A. H.; Sedghkerdar, M. H.; Karami, D.; Mahinpey, N. Pelletizing and Coating of Synthetic Zirconia Stabilized Calcium-Based Sorbents for Application in Calcium Looping CO_2 Capture. *Ind. Eng. Chem. Res.* **2017**, *56*, 5395−5402.

(4) Patel, H. A.; Byun, J.; Yavuz, C. T. Carbon Dioxide Capture Adsorbents: Chemistry and Methods. *ChemSusChem* **2017**, *10*, 1303−1317.

(5) Feng, Y.; Liu, Y. Scenario Prediction of Emerging Coastal City Using CA Modeling under Different Environmental Conditions: A Case Study of Lingang New City, China. *Environ. Monit. Assess.* **2016**, *188*, 540.

(6) Jevrejeva, S.; Jackson, L. P.; Riva, R. E. M.; Grinsted, A.; Moore, J. C. Coastal Sea Level Rise with Warming Above 2 °C. *Proc. Natl. Acad. Sci. U.S.A.* **2016**, *113*, 13342−13347.

(7) Zuo, J.; Yang, Y.; Zhang, J.; Chen, M.; Xu, Q. Prediction of China's Submerged Coastal Areas by Sea Level Rise due to Climate Change. *J. Ocean Univ. China* **2013**, *12*, 327−334.

(8) Erickson, D. J.; Sulzberger, B.; Zepp, R. G.; Austin, A. T. Effects of Stratospheric Ozone Depletion, Solar UV Radiation, and Climate Change on Biogeochemical Cycling: Interactions and Feedbacks. *Photochem. Photobiol. Sci.* **2015**, *14*, 127−148.

(9) Thornes, J. E.; Pope, F. D. Why do We Need Solutions to Global Warming? *Geoengineering of the Climate System*; RSC: UK, 2014.

DOI: 10.1021/acs.langmuir.7b03263
Langmuir 2018, 34, 2926−2932

(10) Panwar, N. L.; Kaushik, S. C.; Kothari, S. Role of Renewable Energy Sources in Environmental Protection: A Review. *Renew. Sustain. Energy Rev.* **2011**, *15*, 1513−1524.
(11) Alahakoon, S. B.; Thompson, C. M.; Occhialini, G.; Smaldone, R. A. Design Principles for Covalent Organic Frameworks in Energy Storage Applications. *ChemSusChem* **2017**, *10*, 2116−2129.
(12) Dhankhar, S. S.; Nagaraja, C. M. Green Synthesis, Optical and Magnetic Properties of a Mn^{II} Metal−Organic Framework (MOF) that Exhibits High Heat of H_2 Adsorption. *RSC Adv.* **2016**, *6*, 86468−86476.
(13) Nandi, S.; Rother, J.; Chakraborty, D.; Maity, R.; Werner-Zwanziger, U.; Vaidhyanathan, R. Exceptionally Stable Bakelite-type Polymers for Efficient Pre-Combustion CO_2 Capture and H_2 Purification. *J. Mater. Chem. A* **2017**, *5*, 8431−8439.
(14) Wang, Z. G.; Liu, X.; Wang, D.; Jin, J. Trger's Base-Based Copolymers with Intrinsic Microporosity for CO_2 Separation and Effect of Troger's Base on Separation Performance. *Polym. Chem.* **2014**, *5*, 2793−2800.
(15) Lund, H. Renewable Energy Strategies for Sustainable Development. *Energy* **2007**, *32*, 912−919.
(16) *Renewables 2017 Global Status Report, REN21*; 2017, p 30.
(17) Jena, P. Materials for Hydrogen Storage: Past, Present, and Future. *J. Phys. Chem. Lett.* **2011**, *2*, 206−211.
(18) Yang, J.; Tan, H. Y.; Low, Q. X.; Binks, B. P.; Chin, J. M. CO_2 Capture by Dry Alkanolamines and an Efficient Microwave Regeneration Process. *J. Mater. Chem. A* **2015**, *3*, 6440−6446.
(19) Vitillo, J. G.; Smit, B.; Gagliardi, L. Introduction: Carbon Capture and Separation. *Chem. Rev.* **2017**, *117*, 9521−9523.
(20) Zou, L.; Sun, Y.; Che, S.; Yang, X.; Wang, X.; Bosch, M.; Wang, Q.; Li, H.; Smith, M.; Yuan, S.; Perry, Z.; Zhou, H.-C. Porous Organic Polymers for Post-Combustion Carbon Capture. *Adv. Mater.* **2017**, *29*, 1700229.
(21) Mohanty, P.; Kull, L. D.; Landskron, K. Porous Covalent Electron-Rich Organonitridic Frameworks as Highly Selective Sorbents for Methane and Carbon Dioxide. *Nat. Commun* **2011**, *2*, 401.
(22) Samanta, A.; Zhao, A.; Shimizu, G. K. H.; Sarkar, P.; Gupta, R. Post-Combustion CO_2 Capture Using Solid Sorbents: A Review. *Ind. Eng. Chem. Res.* **2012**, *51*, 1438−1463.
(23) Kumar, K. V.; Preuss, K.; Lu, L.; Guo, Z. X.; Titirici, M. M. Effect of Nitrogen Doping on the CO_2 Adsorption Behavior in Nanoporous Carbon Structures: A Molecular Simulation Study. *J. Phys. Chem. C* **2015**, *119*, 22310−22321.
(24) Sevilla, M.; Parra, J. B.; Fuertes, A. B. Assessment of the Role of Micropore Size and N-Doping in CO_2 Capture by Porous Carbons. *ACS Appl. Mater. Interfaces* **2013**, *5*, 6360−6368.
(25) Wang, J.; Liu, Q. An Efficient One-Step Condensation and Activation Strategy to Synthesize Porous Carbons with Optimal Micropore Sizes for Highly Selective CO_2 Adsorption. *Nanoscale* **2014**, *6*, 4148−4156.
(26) Silvestre-Albero, A.; Silvestre-Albero, J.; Martínez-Escandell, M.; Rodríguez-Reinoso, F. Micro/Mesoporous Activated Carbons Derived from Polyaniline: Promising Candidates for CO_2 Adsorption. *Ind. Eng. Chem. Res.* **2014**, *53*, 15398−15405.
(27) Qi, G.; Fu, L.; Giannelis, E. P. Sponges with Covalently Tethered Amines for High-Efficiency Carbon Capture. *Nat. Commun* **2014**, *5*, 5796.
(28) Zhang, G.; Zhao, P.; Xu, Y. Development of Amine-Functionalized Hierarchically Porous Silica for CO_2 Capture. *J. Ind. Eng. Chem.* **2017**, *54*, 59−68.
(29) Chen, C.; Zhang, S.; Row, K. H.; Ahn, W.-S. Amine−silica Composites for CO_2 Capture: A Short Review. *J. Energy Chem.* **2017**, *26*, 868.
(30) Pérez-Pellitero, J.; Amrouche, H.; Siperstein, F. R.; Pirngruber, G.; Nieto-Draghi, C.; Chaplais, G.; Simon-Masseron, A.; Bazer-Bachi, D.; Peralta, D.; Bats, N. Adsorption of CO_2, CH_4, and N_2 on Zeolitic Imidazolate Frameworks: Experiments and Simulations. *Chem.—Eur. J.* **2010**, *16*, 1560−1571.
(31) Cacho-Bailo, F.; Matito-Martos, I.; Perez-Carbajo, J.; Etxeberría-Benavides, M.; Karvan, O.; Sebastián, V.; Calero, S.; Téllez, C.; Coronas, J. On the Molecular Mechanisms for the H_2/CO_2 Separation Performance of Zeolite Imidazolate Framework Two-Layered Membranes. *Chem. Sci.* **2017**, *8*, 325−333.
(32) Russell, B. A.; Migone, A. D. Low Temperature Adsorption Study of CO_2 in ZIF-8. *Microporous Mesoporous Mater.* **2017**, *246*, 178−185.
(33) Doldan, B. P.; Rosnes, M. H.; Dietzel, P. D. C. An In-depth Structural Study of the Carbon Dioxide Adsorption Process in the Porous Metal−Organic Frameworks CPO-27-M. *ChemSusChem* **2017**, *10*, 1710−1719.
(34) Feng, G.; Peng, Y.; Liu, W.; Chang, F.; Dai, Y.; Huang, W. Polar Ketone-Functionalized Metal−Organic Framework Showing a High CO_2 Adsorption Performance. *Inorg. Chem.* **2017**, *56*, 2363−2366.
(35) Liu, Z.; Lv, L.; He, Y.; Feng, Y. An Anionic Metal−Organic Framework Constructed from a Triazole-Functionalized Diisophthalate Featuring Hierarchical Cages for Selective Adsorptive C_2H_2/CH_4 and CO_2/CH_4 Separation. *CrystEngComm* **2017**, *19*, 2795−2801.
(36) Zhai, L.; Huang, N.; Xu, H.; Chen, Q.; Jiang, D. A Backbone Design Principle for Covalent Organic Frameworks: The Impact of Weakly Interacting Units on CO_2 Adsorption. *Chem. Commun.* **2017**, *53*, 4242−4245.
(37) Zeng, Y.; Zou, R.; Zhao, Y. Covalent Organic Frameworks for CO_2 Capture. *Adv. Mater.* **2016**, *28*, 2855−2873.
(38) Huang, N.; Chen, X.; Krishna, R.; Jiang, D. Two-Dimensional Covalent Organic Frameworks for Carbon Dioxide Capture through Channel-Wall Functionalization. *Angew. Chem., Int. Ed.* **2015**, *54*, 2986−2990.
(39) Ben, T.; Pei, C.; Zhang, D.; Xu, J.; Deng, F.; Jing, X.; Qiu, S. Gas Storage in Porous Aromatic Frameworks (PAFs). *Energy Environ. Sci.* **2011**, *4*, 3991−3999.
(40) Zhu, Y.; Long, H.; Zhang, W. Imine-Linked Porous Polymer Frameworks with High Small Gas (H_2, CO_2, CH_4, C_2H_2) Uptake and CO_2/N_2 Selectivity. *Chem. Mater.* **2013**, *25*, 1630−1635.
(41) Li, L.; Cai, K.; Wang, P.; Ren, H.; Zhu, G. Construction of Sole Benzene Ring Porous Aromatic Frameworks and Their High Adsorption Properties. *ACS Appl. Mater. Interfaces* **2015**, *7*, 201−208.
(42) Lu, W.; Verdegaal, W. M.; Yu, J.; Balbuena, P. B.; Jeong, H.-K.; Zhou, H.-C. Building Multiple Adsorption Sites in Porous Polymer Networks for Carbon Capture Applications. *Energy Environ. Sci.* **2013**, *6*, 3559−3564.
(43) Lu, W.; Yuan, D.; Zhao, D.; Schilling, C. I.; Plietzsch, O.; Muller, T.; Bräse, S.; Guenther, J.; Blümel, J.; Krishna, R.; Li, Z.; Zhou, H.-C. Porous Polymer Networks: Synthesis, Porosity, and Applications in Gas Storage/Separation. *Chem. Mater.* **2010**, *22*, 5964−5972.
(44) Rekha, P.; Sahoo, U.; Mohanty, P. Click-Based Porous Inorganic−Organic Hybrid Material (PHM) Containing Cyclophosphazene Unit and Their Application in Carbon Dioxide Capture. *RSC Adv.* **2014**, *4*, 34860−34863.
(45) Arab, P.; Rabbani, M. G.; Sekizkardes, A. K.; İslamoğlu, T.; El-Kaderi, H. M. Copper(I)-Catalyzed Synthesis of Nanoporous Azo-Linked Polymers: Impact of Textural Properties on Gas Storage and Selective Carbon Dioxide Capture. *Chem. Mater.* **2014**, *26*, 1385−1392.
(46) Islamoglu, T.; Behera, S.; Kahveci, Z.; Tessema, T.-D.; Jena, P.; El-Kaderi, H. M. Enhanced Carbon Dioxide Capture from Landfill Gas Using Bifunctionalized Benzimidazole-Linked Polymers. *ACS Appl. Mater. Interfaces* **2016**, *8*, 14648−14655.
(47) Muhammad, R.; Rekha, P.; Mohanty, P. Aminal Linked Inorganic−Organic Hybrid Nanoporous Materials (HNMs) for CO_2 Capture and H_2 Storage Applications. *RSC Adv.* **2016**, *6*, 17100−17105.
(48) Rekha, P.; Muhammad, R.; Mohanty, P. Sonochemical Synthesis of Cyclophosphazene Bridged Mesoporous Organosilicas and Their Application in Methyl Orange, Congo Red and Cr(VI) Removal. *RSC Adv.* **2015**, *5*, 67690−67699.
(49) Rekha, P.; Muhammad, R.; Sharma, V.; Ramteke, M.; Mohanty, P. Unprecedented Adsorptive Removal of $Cr_2O_7^{2-}$ and Methyl Orange

DOI: 10.1021/acs.langmuir.7b03263
Langmuir 2018, 34, 2926−2932

by Using a Low Surface Area Organosilica. *J. Mater. Chem. A* **2016**, *4*, 17866−17874.
(50) Rekha, P.; Sharma, V.; Mohanty, P. Synthesis of Cyclophosphazene Bridged Mesoporous Organosilicas for CO_2 Capture and Cr (VI) Removal. *Microporous Mesoporous Mater.* **2016**, *219*, 93−102.
(51) Basdogan, Y.; Keskin, S. Simulation and Modelling of MOFs for Hydrogen Storage. *CrystEngComm* **2015**, *17*, 261−275.
(52) Suh, M. P.; Park, H. J.; Prasad, T. K.; Lim, D.-W. Hydrogen Storage in Metal−Organic Frameworks. *Chem. Rev.* **2012**, *112*, 782−835.
(53) Katsoulidis, A. P.; Dyar, S. M.; Carmieli, R.; Malliakas, C. D.; Wasielewski, M. R.; Kanatzidis, M. G. Copolymerization of Terephthalaldehyde with Pyrrole, Indole and Carbazole gives Microporous POFs Functionalized with Unpaired Electrons. *J. Mater. Chem. A* **2013**, *1*, 10465−10473.
(54) Melhi, S.; Ding, X.; Liu, Z.-W.; Cao, C.-X.; Han, B.-H. A New Strategy to Microporous Polypyrrole Networks Based on Condensation of Pyrrole and Diketone. *Macromol. Chem. Phys.* **2016**, *217*, 1529−1533.
(55) Lee, S. Y.; Boo, B. H. Molecular Structures and Vibrational Spectra of Pyrrole and Carbazole by Density Functional Theory and Conventional ab Initio Calculations. *J. Phys. Chem.* **1996**, *100*, 15073−15078.
(56) Jang, J.; Yoon, H. Facile Fabrication of Polypyrrole Nanotubes Using Reverse Microemulsion Polymerization. *Chem. Commun.* **2003**, 720−721.
(57) Chougule, M. A.; Pawar, S. G.; Godse, P. R.; Mulik, R. N.; Sen, S.; Patil, V. B. Synthesis and Characterization of Polypyrrole (PPy) Thin Films. *Soft Nanosci. Letter* **2011**, *1*, 6−10.
(58) Arora, K.; Chaubey, A.; Singhal, R.; Singh, R. P.; Pandey, M. K.; Samanta, S. B.; Malhotra, B. D.; Chand, S. Application of Electrochemically Prepared Polypyrrole−Polyvinyl Sulphonate Films to DNA Biosensor. *Biosens. Bioelectron.* **2006**, *21*, 1777−1783.
(59) Lee, G.-Y.; Lee, J.; Vo, H. T.; Kim, S.; Lee, H.; Park, T. Amine-Functionalized Covalent Organic Framework for Efficient SO_2 Capture with High Reversibility. *Sci. Rep.* **2017**, *7*, 557.
(60) Woodward, R. T.; Stevens, L. A.; Dawson, R.; Vijayaraghavan, M.; Hasell, T.; Silverwood, I. P.; Ewing, A. V.; Ratvijitvech, T.; Exley, J. D.; Chong, S. Y.; Blanc, F.; Adams, D. J.; Kazarian, S. G.; Snape, C. E.; Drage, T. C.; Cooper, A. I. Swellable, Water- and Acid-Tolerant Polymer Sponges for Chemoselective Carbon Dioxide Capture. *J. Am. Chem. Soc.* **2014**, *136*, 9028−9035.
(61) Liao, Y.; Weber, J.; Mills, B. M.; Ren, Z.; Faul, C. F. J. Highly Efficient and Reversible Iodine Capture in Hexaphenylbenzene-Based Conjugated Microporous Polymers. *Macromolecules* **2016**, *49*, 6322−6333.
(62) Mondal, S.; Kundu, S. K.; Bhaumik, A. A Facile Approach for the Synthesis of Hydroxyl-Rich Microporous Organic Networks for Efficient CO_2 Capture and H_2 Storage. *Chem. Commun.* **2017**, *53*, 2752−2755.
(63) Tan, L.; Li, B.; Yang, X.; Wang, W.; Tan, B. Knitting Hypercrosslinked Conjugated Microporous Polymers with External Crosslinker. *Polymer* **2015**, *70*, 336−342.
(64) Rabbani, M. G.; El-Kaderi, H. M. Synthesis and Characterization of Porous Benzimidazole-Linked Polymers and Their Performance in Small Gas Storage and Selective Uptake. *Chem. Mater.* **2012**, *24*, 1511−1517.
(65) Muhammad, R.; Rekha, P.; Mohanty, P. Facile Synthesis of a Thermally Stable Imine and Benzimidazole Functionalized Nanoporous Polymer (IBFNP) for CO_2 Capture Application. *Greenhouse Gases: Sci. Technol.* **2016**, *6*, 150−157.
(66) Adeniran, B.; Mokaya, R. Low Temperature Synthesized Carbon Nanotube Superstructures with Superior CO_2 and Hydrogen Storage Capacity. *J. Mater. Chem. A* **2015**, *3*, 5148−5161.
(67) Song, W.-C.; Xu, X.-K.; Chen, Q.; Zhuang, Z.-Z.; Bu, X.-H. Nitrogen-Rich Diaminotriazine-Based Porous Organic Polymers for Small Gas Storage and Selective Uptake. *Polym. Chem.* **2013**, *4*, 4690−4696.
(68) Sekizkardes, A. K.; Altarawneh, S.; Kahveci, Z.; İslamoğlu, T.; El-Kaderi, H. M. Highly Selective CO_2 Capture by Triazine-Based Benzimidazole-Linked Polymers. *Macromolecules* **2014**, *47*, 8328−8334.
(69) Hug, S.; Mesch, M. B.; Oh, H.; Popp, N.; Hirscher, M.; Senker, J.; Lotsch, B. V. A Fluorene Based Covalent Triazine Framework with High CO_2 and H_2 Capture and Storage Capacities. *J. Mater. Chem. A* **2014**, *2*, 5928−5936.
(70) Li, G.; Zhang, B.; Yan, J.; Wang, Z. Tetraphenyladamantane-Based Polyaminals for Highly Efficient Captures of CO_2 and Organic Vapors. *Macromolecules* **2014**, *47*, 6664−6670.

DOI: 10.1021/acs.langmuir.7b03263
Langmuir 2018, 34, 2926−2932

Journal of CO_2 Utilization 25 (2018) 302–309

Contents lists available at ScienceDirect

Journal of CO_2 Utilization

journal homepage: www.elsevier.com/locate/jcou

Harnessing electron-rich framework in cyclophosphazene derived hybrid nanoporous materials for organocatalytic C—C bond formation and gas sorption applications

Raeesh Muhammad, Monika Chaudhary, Paritosh Mohanty*

Functional Materials Laboratory, Department of Chemistry, Indian Institute of Technology Roorkee, Roorkee, Uttarakhand, 247667, India

ARTICLE INFO

Keywords:
Inorganic-Organic hybrid nanoporous materials
Hierarchical pore structure
Carbon dioxide capture
Organocatalysis
C—C bond formation

ABSTRACT

Nanoporous inorganic-organic hybrid materials with estimated specific surface area (SA_{BET}) of 870 $m^2 g^{-1}$ and multimodal hierarchical pore structure centered at 1.64, 3.14 and 6.3 nm have been synthesized. These cyclophosphazene derived metal-free materials have adsorbed 14.8 and 1.61 wt% of CO_2 and H_2 at 273 and 77 K, respectively, at 1 bar. The materials have shown efficient C—C bond formation via the Knoevenagel condensation with a maximum yield of 97% that only reduced marginally to 81% even after five cycles. These electron rich high surface area materials could further be useful for several other energy and environmental applications.

1. Introduction

The current thrust in materials research is directed towards finding suitable materials/methods for reducing the dependence on fossil fuel and simultaneously utilizing non-conventional energy sources without hampering the social and ecological balances [1,2]. To sustain the exponentially rising population driven energy demand and economic growth, the fossil fuel is being used at uncontrolled rate resulting in the emission of 41 billion ton of CO_2 annually into atmosphere [2–5]. This has led to the sharp rise in atmospheric CO_2 level reaching as high as 406.75 ppm in December 2017 [6]. With the scientific consensus about the role of CO_2 in environment deterioration as well as global warming, there is an utmost need to reduce the atmospheric CO_2 emission arising from anthropogenic activities [7–10]. Moreover, there is also an urgent need for development of more energy efficient industrial processes to reduce the energy wastage to cut the consumption of fossil fuels [11].

One way to reduce the CO_2 emission arising from anthropogenic activities is to capture it from the flue gas stream economically. This is considered as one of the best solutions as avoiding the fossil-based energy sources is not feasible at present, although, these are the largest contributor of anthropogenic CO_2 into the atmosphere [9,12]. Commercially, organic liquid amines have been employed in power plants to capture CO_2 from flue gas stream with an unacceptable financial burden [12–15]. Recently, solid high surface area adsorbents such as zeolites [16], activated carbon [17], mesoporous silica [18], metal organic frameworks (MOFs) [19], microporous organic polymer (MOPs) [20–22], benzimidazole-linked polymers (BILPs) [23], porous electron rich covalent organonitridic framework (PECONFs) [15], hybrid nanoporous materials (HNMs) [24], and porous hybrid materials (PHM) [25] etc. have been explored for CO_2 capture application, although, the commercial viability and sustainability is yet to be tested.

Some of the major advancement on finding suitable adsorbents for the CO_2 capture application lies on the control of their textural properties, stability and surface functionalities [16–27]. On this direction, our research group has focused on enriching the framework with electron rich heteroatoms to induce a stronger Lewis base-Lewis acid interaction (CO_2 being the Lewis acidic gas). Towards this, cyclophosphazene moiety has been incorporated into the framework. Moreover, the three-dimensional paddle wheel structure of cyclophosphazene has a synergy effect in controlling the textural properties [24,25,28,29]. Such materials have shown not only the superior CO_2 capture capacity but also storing descent amount of H_2 [24]. The applicability of these high surface area electron rich materials for the metal-free catalysis is a research of prime importance. With the awareness about the negative environmental impact of metal-based catalysts, their limited abundance, and high cost, the use of metal-free catalyst has been in the forefront [30–33]. Small organic molecules have been explored initially, but their separation and recyclability have been the bottleneck for wide scale industrial use [31]. Recently, high surface area polymeric framework materials such as, conjugated microporous polymers [32], microporous polyurethane [33] have been exploited as metal-free heterogeneous catalysts for several important organic conversions. The high surface nanoporous materials show better catalytic activity owing to large number of active sites [34]. In the present research,

* Corresponding author.
E-mail addresses: pmfcy@iitr.ac.in, paritosh75@gmail.com (P. Mohanty).

https://doi.org/10.1016/j.jcou.2018.04.008
Received 23 January 2018; Received in revised form 14 March 2018; Accepted 8 April 2018

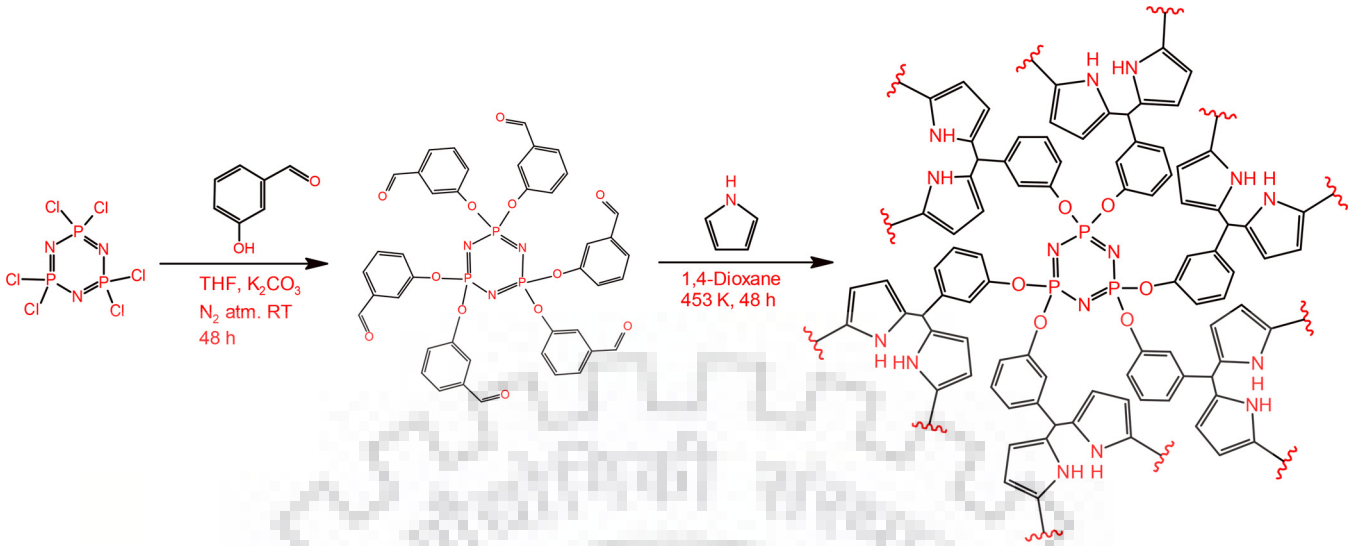

Scheme 1. Reaction scheme for the synthesis of cyclophosphazene derived hybrid nanoporous materials.

cyclophosphazene derived inorganic-organic hybrid nanoporous materials with uniform distribution of electron rich heteroatoms (N, P and O) have been synthesized (Scheme 1). These materials have been utilized for CO_2 sorption, H_2 storage and organocatalytic C—C bond formation.

2. Experimental

2.1. Materials

Phosphonitrilic chloride trimer (PNC) (99%, Sigma Aldrich, India), Pyrrole (99%, SRL, India), 3-hydroxybenzaldehyde (99%, Sigma Aldrich, India), 1,4-dioxane (Fisher Scientific, India), Tetrahydrofuran (THF, Fisher Scientific, India), Methanol (THF, Fisher Scientific, India), Sodium sulphate (Na_2SO_4, Himedia, India), Dichloromethane (DCM, Fisher Scientific, India) and Potassium carbonate (K_2CO_3, Himedia, India) were of analytical grade and used as received else mentioned.

2.2. Synthesis of the precursor

The precursor that has been used for the condensation with pyrrole to synthesize the desired high surface area hybrid nanoporous materials was initially prepared following a similar method reported [24]. As shown in Scheme 1, 10 mmol (3.47 g) of PNC dissolved in 50 ml of dry THF (dried by passing over anhydrous Na_2SO_4) was added drop-wise to a round bottom flask charged with 61 mmol (7.46 g) of 3-hydroxybenzaldehyde dissolved in 100 ml dry THF in presence of 121 mmol (16.698 g) K_2CO_3 under N_2 atmosphere. The reaction was continued for 48 h at RT under stirring condition. The insoluble salt was filtered out and the product was separated from THF under reduced pressure using rotary evaporator. The obtained white product was re-dissolved in DCM and extracted thrice with brine solution and water (50 ml each time), respectively. It was further passed through anhydrous Na_2SO_4 to remove trace amount of water if any. The final product was separated from DCM under reduced pressure by rotary evaporator followed by recrystallization with ethylacetate that yields white crystals. The successful synthesis of the precursor was verified spectroscopically by the ^1H, ^{13}C and ^{31}P NMR, and FTIR as shown in Fig. S1-S4.

2.3. Synthesis of cyclophosphazene derived hybrid nanoporous materials

The cyclophosphazene derived hybrid nanoporous materials were synthesised by the solvothermal condensation of synthesized precursor with pyrrole as shown in Scheme 1. In a typical synthesis, 0.5 mmol of the precursor was condensed with 3 mmol of freshly distilled pyrrole in 5 ml of 1,4-dioxane. The reaction mixture was stirred at 343 K for 1 h in N_2 atmosphere followed by a solvothermal treatment at 453 K for 48 h using a Teflon lined autoclave. A brownish-black monolith was formed. The trapped solvent from the monolith was exchanged by repeated washing with methanol and THF, and dried at 353 K. The specimen is designated as CHNM-1M with the final yield of 78%. In order to investigate the role of dilution on the properties of the synthesized materials, two more samples, designated as CHNM-2M and CHNM-3M, have been synthesized by increasing the 1,4-dioxane content from 5 ml to 10 and 15 ml, respectively.

2.4. Characterization

The ^1H, ^{13}C and ^{31}P NMR spectra and CPMAS ^{13}C and ^{31}P NMR spectra were recorded on JEOL resonance JNM-ECX-400II spectrophotometer. The FT-IR analysis was carried out using PerkinElmer Spectrum Two FT-IR spectrophotometer. Powder XRD patterns were recorded using Rigaku Ultima IV x-ray diffractometer. TESCAN MIRA3 FESEM and TECNAI G^2S-TWIN TEM instruments were employed to study the microstructure of the samples. Elemental analyser, vario MICRO, was used for elemental analysis (C/H/N). The thermal stability of the specimens was investigated by EXSTAR TG/DTA6300 TGA instrument. Textural characterization and gas sorption studies were performed using Autosorb iQ2 gas sorption equipment (Quantachrome Instruments, USA). Before the gas sorption analysis, the specimens were degassed at 393 K for 12 h. N_2 sorption experiments were carried out using liquid N_2 at 77 K. Pore size distribution (PSD) analysis was carried out using density functional theory (DFT) model. Total pore volume was calculated at relative pressure (P/P_0) of 0.90 using adsorption branch. The H_2 storage capacity was measured at 77 K and 1 bar. The isosteric heat of adsorption (Q_{st}) for CO_2 was estimated by fitting the CO_2 sorption data measured at 273 and 298 K in Clausius-Clapeyron equation. The selective uptake of CO_2 vs N_2 was estimated using initial slope method (Henry's law constant).

2.5. Organocatalytic study

In a typical base catalyzed Knoevenagel condensation reaction, 1 mmol of malononitrile was dissolved in 1 ml solvent (1:1 water-ethanol mixture) containing 10 mg catalyst under stirring condition followed by dropwise addition of 1 mmol of aldehydes precursor to it. The stirring was continued for 4 h at RT. The progress of reaction was monitored by TLC at certain interval of time and after 4 h of stirring,

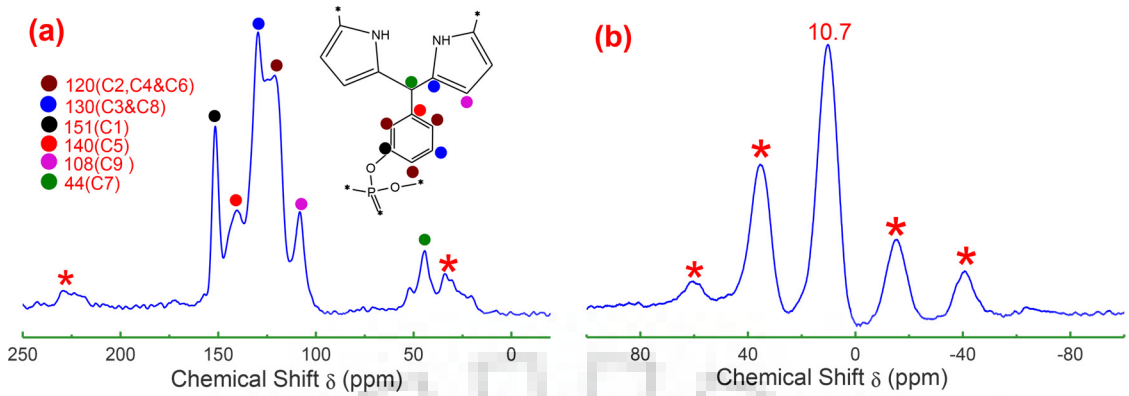

Fig. 1. (a) ^{13}C CP-MAS and (b) ^{31}P CP-MAS NMR spectra of CHNM-1M.

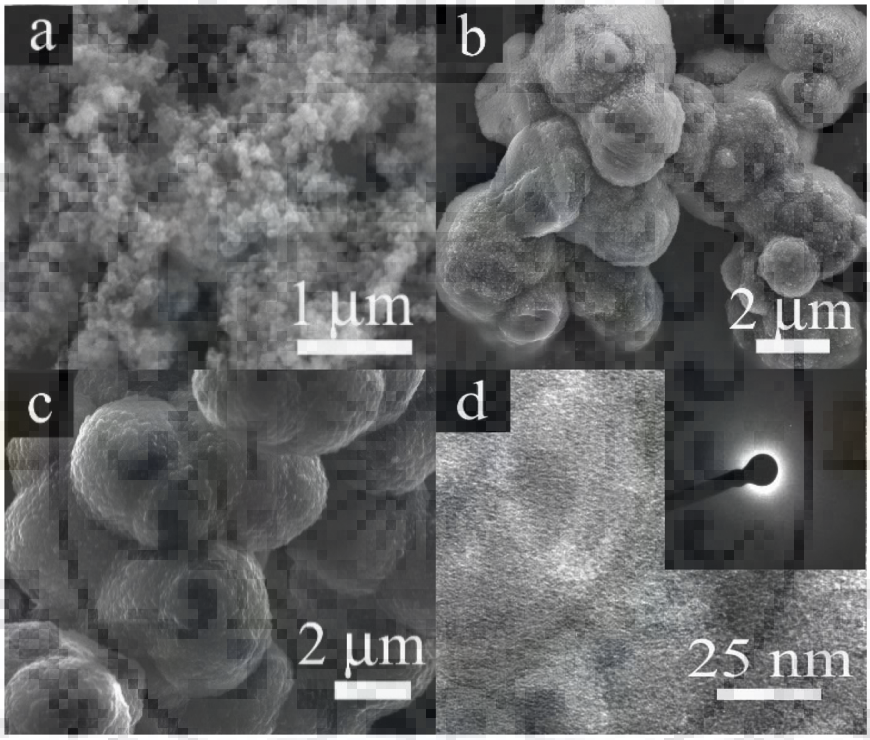

Fig. 2. FESEM images: (a) CHNM-1M, (b) CHNM-2M and (c) CHNM-3M. (d) TEM image of CHNM-1M. The SAED pattern of CHNM-1M is given in the inset of (d).

reaction was found to be completed. After completion of the reaction, almost a solid mass of the products along with the catalyst was obtained. This was dissolved in 5 ml ethanol and the catalyst was separated by filtration, and the final product was obtained by evaporating the solvent naturally at RT. The final product was obtained by recrystallization using ethanol.

3. Results and discussion

The formation of the cyclophosphazene derived hybrid nanoporous materials as shown in Scheme 1 was investigated by CPMAS NMR and FTIR spectroscopies. The observation of a resonance signal at 44 ppm in the ^{13}C CPMAS NMR spectrum given in Fig. 1(a) assigned to the aliphatic methine carbon along with the signals originated from pyrrole moieties and carbons in the precursor confirm the formation of the product as proposed in the Scheme 1 [24,35]. Further, a broad resonance signal at 10.7 ppm in the ^{31}P CPMAS NMR spectrum {Fig. 1(b)} originated from the P of the cyclophosphazene moieties in the synthesized specimen strongly supports the condensation and incorporation of the cyclophosphazene units in the polymeric framework as proposed [24]. The assignment of all other ^{13}C CPMAS NMR signals is shown in the inset of Fig. 1(a) and are consistent with the structure [24,35,36]. Moreover, the absence of the characteristic signals at 170 ppm due to carbonyl carbon in the ^{13}C CPMAS NMR spectrum and the signal at 19 ppm due to the P of PNC in the ^{31}P CPMAS NMR spectrum in Fig. 1 further confirms the complete condensation. A similar conclusion was also drawn from the FT-IR investigation (Fig. S4). The observation of −C−H stretching vibration bands due to −C−H of methine linkage at 2955 cm^{-1} and dis-appearance of carbonyl band at 1705 cm^{-1} confirm the complete condensation of synthesized precursor with pyrrole [24,35]. The band at 3440 and 1690 cm^{-1} could be ascribed to −N−H stretching and −C=N stretching of pyrrole moiety [36–38]. The bands in the range of 1270 to 1130 cm^{-1} due to ν_{as}(P=N−P) and bands at 986 and 555 cm^{-1} due to ν_{as}(P−O−C) and δ(P=N−P) vibrations, respectively, confirm the inclusion of cyclophosphazene moiety [15,24,25,35]. The bands due to benzene ring of synthesized precursor could be seen at 1590 cm^{-1} [24,37]. The pyrrole ring stretching, ring deformation, and N−H bending are observed at 1610, 1480 and 1440 cm^{-1} [36–38]. Detailed assignments of the FT-IR bands is given in the Table S1.

Absence of diffraction peak and the presence of broad halos in powder x-ray diffraction patterns at 8 and 20 in 2θ scale indicate the amorphous nature of the specimens (Fig. S5). Based on the proposed structure of cyclophosphazene derived hybrid nanoporous materials, the theoretical elemental composition can be compared with that of the experimental values with minor aberration (Table S2). Such a deviation in the composition is very common in amorphous polymeric framework materials owing to the presence of a large number of end group functionalities, trapping of the solvents, gases and moisture [39–41]. The specimens show a thermal stability up to 630 K in air as investigated by the TGA (Fig. S6).

The microstructure of the synthesized specimens was investigated by FESEM and TEM. As shown in Fig. 2, small particle size ~30 nm forming an inter-connected network structure can be seen in CHNM-1M, whereas, the microstructure is altogether different in the other two samples. The CHNM-2M and CHNM-3M specimens have much bigger particles of 1–5 μm in size which are in the agglomerated form forming bigger chunks. Unlike CHNM-1M, individual particles can't be separated in both these samples. The variation in microstructure versus dilution could be ascribed to different condensation kinetics. The supersaturation condition at higher concentration led to the formation of large number of nuclei at the beginning of the reaction and growth of these nuclei was restricted due to the less availability of the condensed molecules. This led to the formation of small size particles with rough surface. However, at lower concentration lesser number of nuclei are formed and availability of the enough condensed molecules led to the growth of the particles into larger size and which in-turn form agglomeration. The TEM image shown in Fig. 2(d) revealed the hierarchical pore structure of the specimen. The SAED pattern shown in inset of Fig. 2(d) shows the diffused ring pattern which indicates the amorphous nature of material and further supports the XRD result.

The textural properties of these specimens have been investigated by N_2 sorption analysis. The typical N_2 sorption isotherm of CHNM-1M as shown in Fig. 3(a) exhibits sharp N_2 uptake at low relative pressure (P/P_0) range below 0.01 indicating the presence of the micropores. The desorption branch in the sorption analysis didn't close even at a low pressure range (P/P_0) of 0.025. This open hysteresis could be attributed to the swelling effect which is normally observed in high surface area organic polymeric materials with small confined micropores that are not easily accessible by the probe (N_2) molecule [42–44]. The CHNM-1M exhibited the specific surface area (SA_{BET}) of 870 $m^2 g^{-1}$ (Fig. S7) with the total pore volume of 0.83 $cm^3 g^{-1}$. The PSD estimated from the N_2 sorption analysis has shown a multimodal PSD in Fig. 3(b) with majority of the pores centered at 1.64 nm (micropore) with significant number of pores in mesopore region spread in the range of 3.14 to 8.6 nm. This indicates the formation of a hierarchical pore structure. It can be conceivable that in a flexible framework like in case of organic polymers, the pores that are open for the adsorption due to the thermodynamic criteria may no longer follow the same criteria for the desorption process. Rather a low relative pressure is required for such molecules to get desorbed. The CHNM-2M and CHNM-3M have shown similar nitrogen sorption isotherms with comparatively a lower SA_{BET} of 639 and 548 $m^2 g^{-1}$ (Fig. S7), respectively. The smaller particle size of CHNM-1M as compared to the other two samples has contributed to higher SA_{BET} with a pronounced hysteresis as compared to the other samples. The PSD profile of CHNM-2M and CHNM-3M as shown in Fig. 3(b) is also similar to CHNM-1M. The pore volume for CHNM-2M and CHNM-3M was estimated to be 0.52 and 0.50 $cm^3 g^{-1}$, respectively at relative pressure (P/P_0) of 0.90. Detailed textural properties of these specimens are given in the Table 1.

Table 1
Textural properties of cyclophosphazene derived hybrid nanoporous materials.

Sample	SA_{BET} ($m^2 g^{-1}$)	Pore size distribution (nm)	Pore volume ($cm^3 g^{-1}$)
CHNM-1M	870	1.64, 3.14, 6.3	0.83
CHNM-2M	639	1.64, 3.06, 6.3	0.52
CHNM-3M	548	1.84, 3.06, 6.3	0.50

These specimens were further investigated for the CO_2 sorption studies at 273 and 298 K at 1 bar are shown in Fig. 4(a) and Fig. 4(b) . The isotherms are reversible in nature with minor hysteresis in desorption branch. At the onset, the CO_2 uptake rises sharply in low pressure region up to 0.15 bar and after that show small increase in gas uptake. The sharp rise in CO_2 uptake at low-pressure region could be ascribed to filling of micropores due to enhanced van der Waal's interaction in the confined narrow pores [45,46]. In CHNM-1M, the maximum CO_2 uptake of 14.8 and 9.9 wt% was observed at 273 and 298 K at 1 bar, respectively. The CHNM-2M and CHNM-3M have shown a CO_2 uptake of 13.1 and 9.7 wt%, respectively at 273 K and 1 bar. This can be due to the lower SA_{BET}. Detailed CO_2 sorption properties of these specimens are given in Table S3. The CO_2 uptake of CHNM-1M is comparable to many of the reported solid adsorbents like PECONF-3 [15], HNM-2 [24], PTHB [47], NOP-54 [48], PCTP-3 [49], HCPANI [50], MPOP-C [51], FCBCz [52] and higher than PHM-1 [25], PVVP-10%-pc [53], Fepc–TiO_2 [54], MPOP-0 [55], NETPMO-8 [56], PTPA-3 [57], HCP-9-DMM [58], PSN-3 [59] etc. For detailed comparison with recently reported solid adsorbents, please see Table S4.

To access the nature of interaction of CO_2 with cyclophosphazene derived hybrid nanoporous materials, the isosteric heat of adsorption (Q_{st}) was estimated using Clausius-Clapeyron equation. The Q_{st} value at zero coverage for CHNM-1M, CHNM-2M and CHNM-3M was estimated to be 34.82, 34.58 and 37.05 kJ mol^{-1}, respectively, as shown in Fig. 4(c). The estimated Q_{st} values indicates that the strong physisorption is operating between CO_2 and cyclophosphazene derived hybrid nanoporous materials which help in achieving the higher gas uptake and regeneration will not be energy intensive [60]. The higher Q_{st}

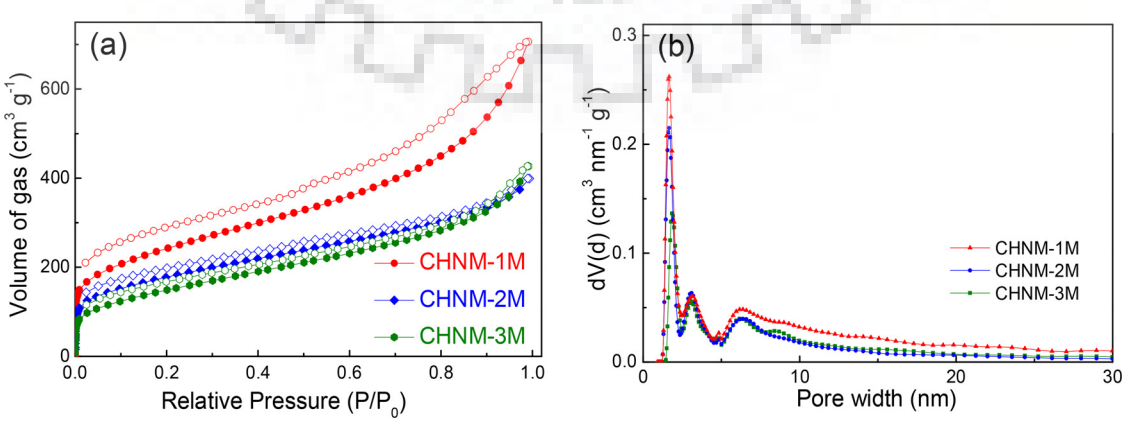

Fig. 3. (a) N_2 sorption analysis of CHNM-1M, CHNM-2M and CHNM-3M. (b) Pore size distribution estimated using DFT model.

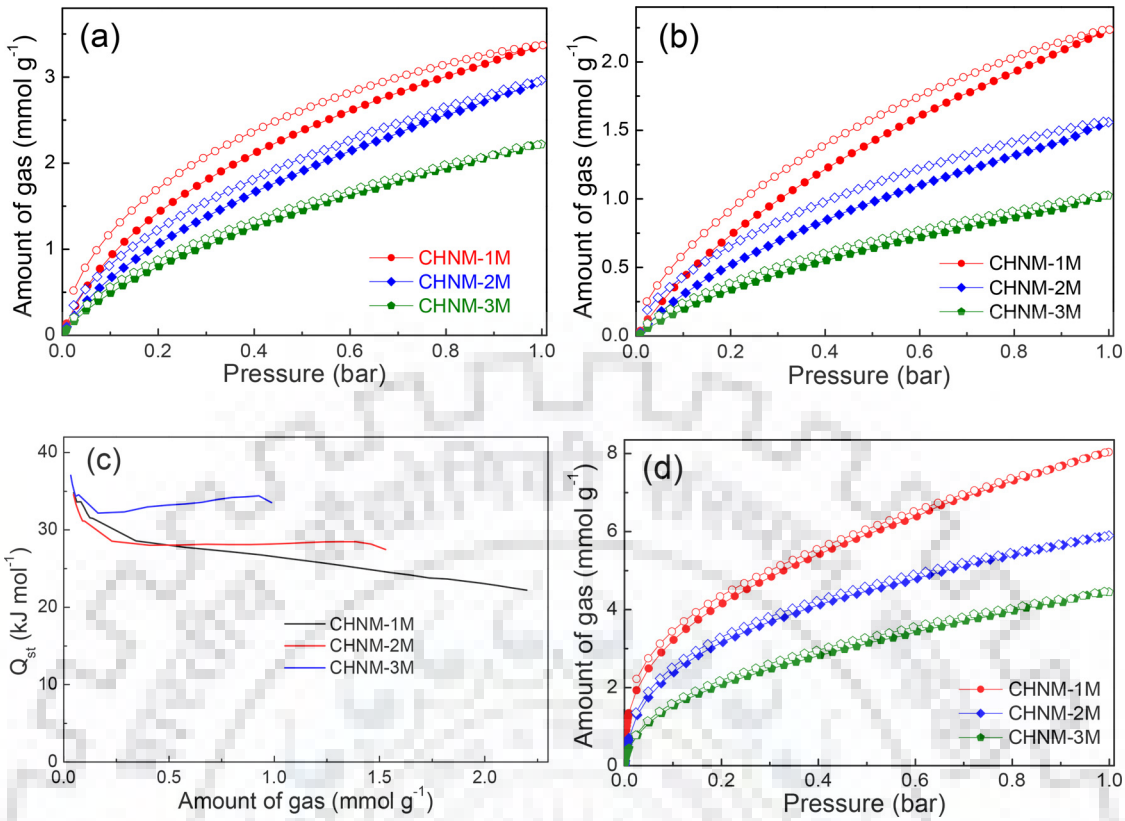

Fig. 4. Gas sorption study of cyclophosphazene derived hybrid nanoporous materials: (a) and (b) CO_2 sorption isotherms measured at 273 and 298 K, respectively, (c) Isosteric heat of adsorption for CO_2, and (d) H_2 sorption isotherms measured at 77 K.

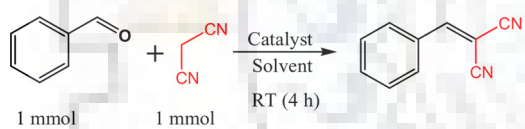

Scheme 2. CHNM-1M catalyzed Knoevenagel condensation reaction between benzaldehyde and malononitrile for the formation of benzylidene malononitrile.

values could be ascribed to higher binding affinity of CO_2 with amine functionality of specimens [61]. Further the selective uptake of CO_2 over N_2 was estimated using initial slope method (Henry's law constant) [15]. It was estimated to be 34, 42 and 44 for CHNM-1M, CHNM-2M and CHNM-3M, respectively at 273 K (Fig. S8). The higher selectivity of CHNM-3M could be ascribed to its higher Q_{st} as compared to CHNM-1M and CHNM-2M.

Considering the environmental friendly nature of H_2 as a fuel, the

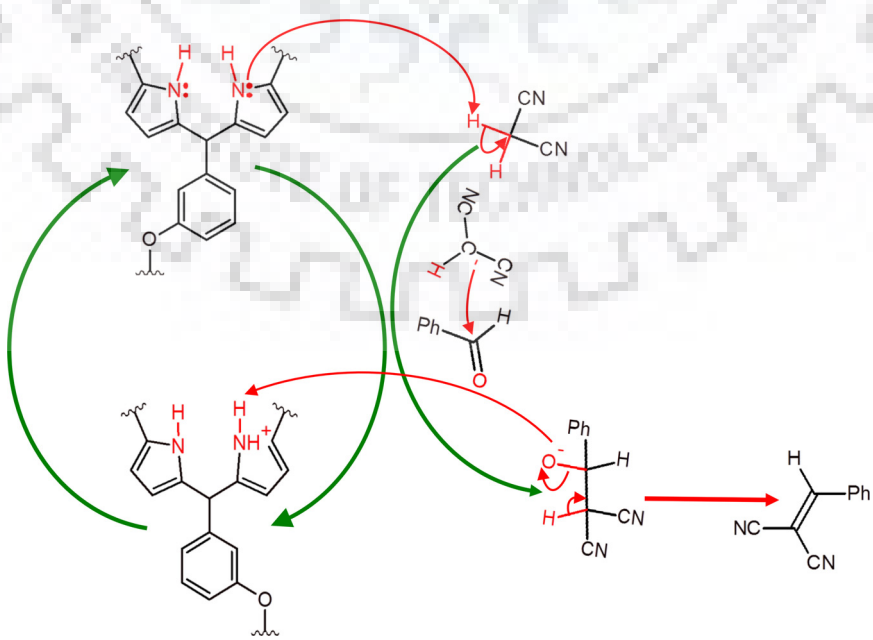

Fig. 5. Possible reaction mechanism of CHNM-1M catalyzed C–C bond formation by Knoevenagel condensation reaction.

Table 2
CHNM-1M catalyzed C—C bond formation between various aldehyde and malononitrile via Knoevenagel condensation.

S. N.	Aldehyde	Product	Yield (%)
1	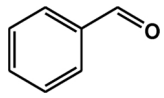	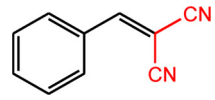	97
2	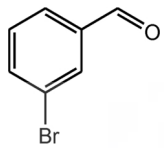	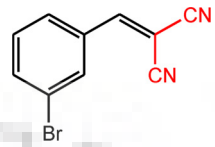	84
3	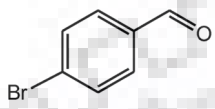	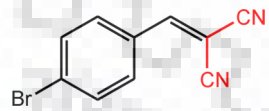	85
4	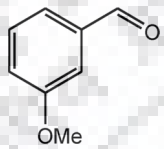	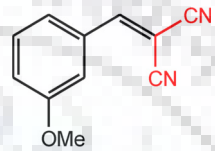	82
5	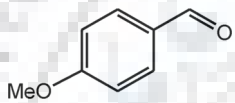	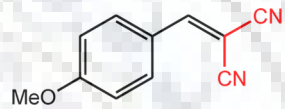	81
6	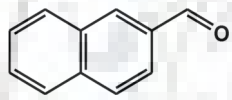	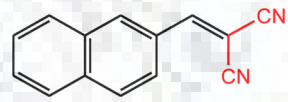	79
7	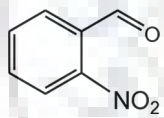	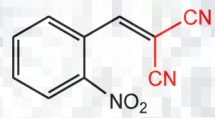	72
8	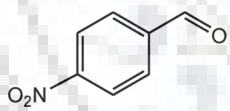	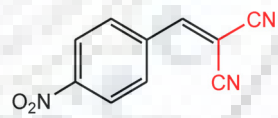	74
9	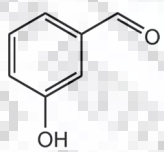	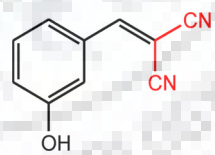	48
10	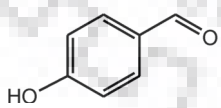	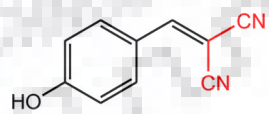	59

General experimental condition: aromatic aldehyde (1 mmol), malononitrile (1 mmol), solvent amount - 1 ml, time - 4 h, temperature - RT.

synthesized specimens were further utilized for H_2 storage application [50,62]. The H_2 sorption isotherm given in Fig. 4(d) are completely reversible in nature with maximum uptake of 1.61, 1.16 and 0.89 wt% at 77 K and 1 bar for CHNM-1M, CHNM-2M and CHNM-3M, respectively. It is noteworthy to mention that the H_2 uptake increases sharply at the onset and has shown no sign of saturation up to measured pressure range. The H_2 uptake of CHNM-1M is comparable to many of the reported nanoporous materials like HNM-1 [24], HCPANI [50], FCBCz [52], PSN-3 [59], CTC-COF [63], IBFNP-1 [64], Trip-PIMs [65], etc. Detailed gas sorption summary of all these specimens has been given in Table S3, and H_2 storage comparison with reported adsorbent is given in Table S5.

Based on the observation of high surface area, hierarchical pore structure and basic nature of cyclophosphazene derived hybrid nanoporous materials, evident from high CO_2 capture capacity, the CHNM-1M was further utilized for organocatalytic C—C bond formation in Knoevenagel condensation. The CHNM-1M was chosen among the three specimens as it has the smallest particle size, highest SA_{BET} and pore volume among the three specimens. The catalytic ability of CHNM-1M was initially accessed with a model reaction using malononitrile 'an active methylene compound' and benzaldehyde, as shown in Scheme 2. The detailed mechanism of CHNM-1M catalyzed C—C bond formation

by Knoevenagel condensation reaction is given in Fig. 5. In a typical Knoevenagel condensation reaction, 1 mmol of benzaldehyde and 1 mmol of malononitrile were condensed in 1 ml of solvent in presence of 10 mg catalyst. The reaction has been performed using different solvents, catalyst amount and varying the reaction time, and its progress was monitored using TLC at regular interval of time. The best catalytic activity can be observed with the maximum yield of 97%, when the reaction was conducted for 4 h at RT in 1:1 ethanol-water mixture by taking 10 mg of the catalyst and 1 mmol each of the benzaldehyde and malononitrile. No trace of the reactants could be seen in NMR spectra (Fig. S9). Further increase of the reaction time didn't result any substantial increase in the yield. The higher yield in ethanol-water mixture could be attributed to better dispersion of solid catalysts and better solubility of precursors and was reported earlier for other catalyst systems [32]. The low catalyst loading produced inferior yield while higher loading didn't show any improvement in the yield. Thus, it was concluded that the reaction time of 4 h, catalyst amount of 10 mg and 1:1 ethanol-water mixture produced the best results. This optimized reaction condition was utilized to test the versatility of catalyst for the reaction of malononitrile with various other aromatic aldehydes with different functional groups towards the C—C bond formation as shown in Table 2. The obtained products were characterized by recording the ^{1}H and ^{13}C NMR spectra (Fig. S10-S18).

The catalytic recycling was also performed to access the performance of CHNM-1M for prolong catalytic usage. The catalytic activity remains intact and a minor loss was observed after five consecutive runs with a maximum yield of 81% (Fig. S19). The catalytic performance of CHNM-1M could be compared to recently reported metal-free organocatalyst like MFCMP-1 [32], MPU [33], JUC-Z12 [66], CN-Mic [31] etc. Thus, based on above observations, the CHNM-1M as metal-free catalyst has shown promising performance towards organocatalytic C—C bond formation via Knoevenagel condensation.

4. Conclusions

The cyclophosphazene derived hybrid nanoporous materials with maximum SA_{BET} of 870 $m^2 g^{-1}$ and hierarchical pore structure having uniform distribution of electron-rich hetero atoms (P, N and O) were synthesized by solvothermal method. The high electron density of the hybrid framework enabled to capture a maximum of 14.8 wt% CO_2 at 273 K and 1.61 wt% of H_2 at 77 K, and 1 bar. The metal-free organocatalytic efficiency of the CHNM-1M have been tested and a yield of 97% could be reported for the C—C bond formation by Knoevenagel condensation. The observation of the multiple applications for the same materials is very important in terms of sustainability and hence, the reported materials have potential to be useful for both environmental and energy applications.

Conflict of interest

The authors declare no competing financial interest.

Acknowledgement

This research was financially supported by DST, Govt. of India with Grant No. DST/TDT/TDP-03/2017(G).

Appendix A. Supplementary data

Supplementary material related to this article can be found, in the online version, at doi:https://doi.org/10.1016/j.jcou.2018.04.008.

References

[1] P. Poizot, F. Dolhem, Clean energy new deal for a sustainable world: from non-CO_2 generating energy sources to greener electrochemical storage devices, Energy Environ. Sci. 4 (2011) 2003–2019.
[2] S. Sorrell, Reducing energy demand: a review of issues, challenges and approaches, Renew. Sustain. Energy Rev. 47 (2015) 74–82.
[3] S. Chu, A. Majumdar, Opportunities and challenges for a sustainable energy future, Nature 488 (2012) 294–303.
[4] D. Day, R.J. Evans, J.W. Lee, D. Reicosky, Economical CO_2, SO_x, and NO_x capture from fossil-fuel utilization with combined renewable hydrogen production and large-scale carbon sequestration, Energy 30 (2005) 2558–2579.
[6] www.co2.earth Accessed January 8 (2018).
[7] J.S. Sawyer, Man-made carbon dioxide and the "greenhouse" effect, Nature 239 (1972) 23–26.
[8] K.S. Lackner, S. Brennan, J.M. Matter, A.-H.A. Park, A. Wright, B. van der Zwaan, The urgency of the development of CO_2 capture from ambient air, Proc. Natl. Acad. Sci. U. S. A. 109 (2012) 13156–13162.
[9] S.K. Kaliyavaradhan, T.-C. Ling, Potential of CO_2 sequestration through construction and demolition (C & D) waste-an overview, J. CO_2 Util. 20 (2017) 234–242.
[10] Y. Fang, Y. Ma, M. Zheng, P. Yang, A.M. Asiri, X. Wang, Metal–organic frameworks for solar energy conversion by photoredox catalysis, Coordin. Chem. Rev. (2017), http://dx.doi.org/10.1016/J.CCR.2017.09.013.
[11] N.A. Madlool, R. Saidur, M.S. Hossain, N.A. Rahim, A critical review on energy use and savings in the cement industries, Renew. Sustain. Energy Rev. 15 (2011) 2042–2060.
[12] L.M. Romeo, D. Catalina, P. Lisbona, Y. Lara, A. Martínez, Reduction of greenhouse gas emissions by integration of cement plants, power plants, and CO_2 capture systems, Greenhouse Gases: Sci. Technol. 1 (2011) 72–82.
[13] J. Yang, H.Y. Tan, Q.X. Low, B.P. Binks, J.M. Chin, CO_2 capture by dry alkanolamines and an efficient microwave regeneration process, J. Mater. Chem. A 3 (2015) 6440–6446.
[14] J.G. Vitillo, B. Smit, L. Gagliardi, Introduction: carbon capture and separation, Chem. Rev. 117 (2017) 9521–9523.
[15] P. Mohanty, L.D. Kull, K. Landskron, Porous covalent electron-rich organonitridic frameworks as highly selective sorbents for methane and carbon dioxide, Nat. Commun. 2 (2011), http://dx.doi.org/10.1038/ncomms1405.
[16] A. Zukal, M. Shamzhy, M. Kubů, J. Čejka, The effect of pore size dimensions in isoreticular zeolites on carbon dioxide adsorption heats, J. CO_2 Util. 24 (2018) 157–163.
[17] J. Wang, Q. Liu, An efficient one-step condensation and activation strategy to synthesize porous carbons with optimal micropore sizes for highly selective CO_2 adsorption, Nanoscale 6 (2014) 4148–4156.
[18] G. Zhang, P. Zhao, Y. Xu, Development of amine-functionalized hierarchically porous silica for CO_2 capture, J. Ind. Eng. Chem. 54 (2017) 59–68.
[19] G. Feng, Y. Peng, W. Liu, F. Chang, Y. Dai, W. Huang, Polar ketone-functionalized metal – organic framework showing a high CO_2 adsorption performance, Inorg. Chem. 56 (2017) 2363–2366.
[20] H. Kim, Y. Kim, M. Yoon, S. Lim, S.M. Park, G. Seo, K. Kim, Highly selective carbon dioxide sorption in an organic molecular porous material, J. Am. Chem. Soc. 132 (2010) 12200–12202.
[21] L. Zhai, N. Huang, H. Xu, Q. Chena, D. Jiang, A backbone design principle for covalent organic frameworks: the impact of weakly interacting units on CO_2 adsorption, Chem. Commun. 53 (2017) 4242–4245.
[22] G. Wang, K. Leus, S. Zhao, P. Van Der Voort, Newly designed covalent triazine framework based on novel N-heteroaromatic building blocks for efficient CO_2 and H_2 capture and storage, ACS Appl. Mater. Interfaces 10 (2018) 1244–1249.
[23] T. Islamoglu, S. Behera, Z. Kahveci, T.D. Tessema, P. Jena, H.M. El-Kaderi, Carbon dioxide capture from landfill gas using bifunctionalized benzimidazole-linked polymers, ACS Appl. Mater. Interfaces 8 (2016) 14648–14655.
[24] R. Muhammad, P. Rekha, P. Mohanty, Aminal linked inorganic–organic hybrid nanoporous materials (HNMs) for CO_2 capture and H_2 storage applications, RSC Adv. 6 (2016) 17100–17105.
[25] P. Rekha, U. Sahoo, P. Mohanty, Click-based porous inorganic–organic hybrid material (PHM) containing cyclophosphazene unit and their application in carbon dioxide capture, RSC Adv. 4 (2014) 34860–34863.
[26] Q. Wang, J. Luo, Z. Zhong, A. Borgna, CO_2 capture by solid adsorbents and their applications: current status and new trends, Energy Environ. Sci. 4 (2011) 42–55.
[27] S. Choi, J.H. Drese, C.W. Jones, Adsorbent materials for carbon dioxide capture from large anthropogenic point sources, ChemSusChem 2 (2009) 796–854.
[28] P. Rekha, R. Muhammad, P. Mohanty, Sonochemical synthesis of cyclophosphazene bridged mesoporous organosilicas and their application in methyl orange, congo red and Cr(vi) removal, RSC Adv. 5 (2015) 67690–67699.
[29] P. Rekha, R. Muhammad, V. Sharma, M. Ramteke, P. Mohanty, Unprecedented adsorptive removal of $Cr_2O_7^{2-}$ and methyl orange by using a low surface area organosilica, J. Mater. Chem. A 4 (2016) 17866–17874.
[30] M. Shaikh, A. Sahu, A.K. Kumar, M. Sahu, S.K. Singh, K.V.S. Ranganath, Metal-free carbon as a catalyst for oxidative coupling: solvent-enhanced poly-coupling with regioselectivity, Green Chem. 19 (2017) 4533–4537.
[31] J. Xu, K. Shen, B. Xue, Y.-X. Li, Microporous carbon nitride as an effective solid base catalyst for Knoevenagel condensation reactions, J. Mol. Catal. A: Chem. 372 (2013) 105–113.
[32] Y. Zhang, A. Sigen, Y. Zou, X. Luo, Z. Li, H. Xia, X. Liu, Y. Mu, Gas uptake, molecular sensing and organocatalytic performances of a multifunctional carbazole-based conjugated microporous polymer, J. Mater. Chem. A 2 (2014) 13422–13430.
[33] S.K. Dey, N.S. Amadeu, C. Janiak, Microporous polyurethane material for size selective heterogeneous catalysis of the Knoevenagel reaction, Chem. Commun. 52 (2016) 7834–7837.
[34] C. Tan, X. Cao, X.-J. Wu, Q. He, J. Yang, X. Zhang, J. Chen, W. Zhao, S. Han, G.-H. Nam, M. Sindoro, H. Zhang, Recent advances in ultrathin two-dimensional

nanomaterials, Chem. Rev. 117 (2017) 6225–6331.
[35] A.P. Katsoulidis, S.M. Dyar, R. Carmieli, C.D. Malliakas, M.R. Wasielewski, M.G. Kanatzidis, Copolymerization of terephthalaldehyde with pyrrole, indole and carbazole gives microporous POFs functionalized with unpaired electrons, J. Mater. Chem. A 1 (2013) 10465–10473.
[36] S. Melhi, X. Ding, Z.W. Liu, C.X. Cao, B.H. Han, A new strategy to microporous polypyrrole networks based on condensation of pyrrole and diketone, Macromol. Chem. Phys. 217 (2016) 1529–1533.
[37] S.Y. Lee, B.H. Boo, Molecular structures and vibrational spectra of pyrrole and carbazole by density functional theory and conventional *ab initio* calculations, J. Phys. Chem. 100 (1996) 15073–15078.
[38] J. Jang, H. Yoon, Facile fabrication of polypyrrole nanotubes using reverse micro-emulsion polymerization, Chem. Commun. (2003) 720–721.
[39] M.G. Rabbani, H.M. El-Kaderi, Synthesis and characterization of porous benzimidazole-linked polymers and their performance in small gas storage and selective uptake, Chem. Mater. 24 (2012) 1511–1517.
[40] K. Wang, H. Huang, D. Liu, C. Wang, J. Li, C. Zhong, Covalent triazine-based frameworks with ultramicropores and high nitrogen contents for highly selective CO_2 capture, Environ. Sci. Technol. 50 (2016) 4869–4876.
[41] S. Dey, A. Bhunia, I. Boldog, C. Janiak, A mixed-linker approach towards improving covalent triazine-based frameworks for CO_2 capture and separation, Micropor. Mesopor. Mater. 241 (2017) 303–315.
[42] R.T. Woodward, L.A. Stevens, R. Dawson, M. Vijayaraghavan, T. Hasell, I.P. Silverwood, A.V. Ewing, T. Ratvijitvech, J.D. Exley, S.Y. Chong, F. Blanc, D.J. Adams, S.G. Kazarian, C.E. Snape, T.C. Drage, A.I. Cooper, Swellable, water- and acid-tolerant polymer sponges for chemoselective carbon dioxide capture, J. Am. Chem. Soc. 136 (2014) 9028–9035.
[43] L. Tan, B. Li, X. Yang, W. Wang, B. Tan, Knitting hypercrosslinked conjugated microporous polymers with external crosslinker, Polymer 70 (2015) 336–342.
[44] Y. Liao, J. Weber, B.M. Mills, Z. Ren, C.F.J. Faul, Highly efficient and reversible iodine capture in hexaphenylbenzene-based conjugated microporous polymers, Macromolecules 49 (2016) 6322–6333.
[45] M. Sevilla, J.B. Parra, A.B. Fuertes, Assessment of the role of micropore size and N-doping in CO_2 capture by porous carbons, ACS Appl. Mater. Interfaces 5 (2013) 6360–6368.
[46] S.J. Gregg, K.S.W. Sing, In Adsorption, Surface Area and Porosity, Academic Press, London, 1991.
[47] Z. Tian, J. Huang, X. Zhang, G. Shao, Q. He, S. Cao, S. Yuan, Ultra-microporous N-doped carbon from polycondensed framework precursor for CO_2 adsorption, Micropor. Mesopor. Mater. 257 (2018) 19–26.
[48] D. Chen, Y. Fu, W. Yu, G. Yu, C. Pan, Versatile adamantane-based porous polymers with enhanced microporosity for efficient CO_2 capture and iodine removal, Chem. Eng. J. 334 (2018) 900–906.
[49] P. Puthiaraj, W.-S. Ahn, Facile synthesis of microporous carbonaceous materials derived from a covalent triazine polymer for CO_2 capture, J. Energy Chem. 26 (2017) 965–971.
[50] V. Sharma, A. Sahoo, Y. Sharma, P. Mohanty, Synthesis of nanoporous hypercrosslinked polyaniline (HCPANI) for gas sorption and electrochemical supercapacitor applications, RSC Adv. 5 (2015) 45749–45754.
[51] R. Dawson, E. Stockel, J.R. Holst, D.J. Adams, A.I. Cooper, Microporous organic polymers for carbon dioxide capture, Energy Environ. Sci. 4 (2011) 4239–4245.
[52] X. Yang, M. Yu, Y. Zhao, C. Zhang, X. Wang, J.-X. Jiang, Hypercrosslinked microporous polymers based on carbazole for gas storage and separation, RSC Adv. 4 (2014) 61051–61055.
[53] L. Shao, M. Liu, J. Huang, Y.-N. Liu, CO_2 capture by nitrogen-doped porous carbons derived from nitrogen containing hyper-cross-linked polymers, J. Colloid Interface Sci. 513 (2018) 304–313.
[54] P.V.R.K. Ramacharyulu, R. Muhammad, J.P. Kumar, G.K. Prasad, P. Mohanty, Iron phthalocyanine modified mesoporous titania nanoparticles for photocatalytic activity and CO_2 capture applications, Phys. Chem. Chem. Phys. 17 (2015) 26456–26462.
[55] N. Zhang, B. Zou, G.-P. Yang, B. Yu, C.-W. Hu, Melamine-based mesoporous organic polymers as metal-free heterogeneous catalyst: effect of hydroxyl on CO_2 capture and conversion, J. CO_2 Util. 22 (2017) 9–14.
[56] R. Muhammad, Jyoti, P. Mohanty, Nitrogen enriched triazine bridged mesoporous organosilicas for CO_2 capture and dye adsorption applications, J. Mol. Liq. 248 (2017) 127–134.
[57] D. Zhang, L. Tao, Q. Wang, T. Wang, A facile synthesis of cost-effective triphenylamine-containing porous organic polymers using different crosslinkers, Polymer 82 (2016) 114–120.
[58] D. Zhang, L. Tao, J. Ju, Y. Wang, Q. Wang, T. Wang, Postmodification of linear poly-p-phenylenes to prepare hyper-crosslinked polymers: tuning the surface areas by the molecular weight, Polymer 60 (2015) 234–240.
[59] G. Li, B. Zhang, Z. Wang, Microporous poly(schiff base) constructed from tetraphenyladamantane units for adsorption of gases and organic vapors, Macromol. Rapid Commun. 35 (2014) 971–975.
[60] M. Oschatz, M. Antonietti, A search for selectivity to enable CO_2 capture with porous adsorbents, Energy Environ. Sci. 11 (2018) 57–70.
[61] S.S. Dhankhar, N. Sharma, S. Kumar, T.J.D. Kumar, C.M. Nagaraja, Rational design of bifunctional, 2-fold interpenetrated Zn(II)-metal-organic framework for selective adsorption of CO_2 and efficient aqueous phase sensing of 2,4,6-trinitrophenol, Chem. Eur. J. 23 (64) (2017) 16204–16212.
[62] T.S. Blankenship, N. Balahmar, R. Mokaya, Oxygen-rich microporous carbons with exceptional hydrogen storage capacity, Nat. Commun. 8 (2017), http://dx.doi.org/10.1038/s41467-017-01633-x.
[63] J.T. Yu, Z. Chen, J.L. Sun, Z.T. Huang, Q.Y. Zheng, Cyclotricatechylene based porous crystalline material: synthesis and applications in gas storage, J. Mater. Chem. 22 (2012) 5369–5373.
[64] R. Muhammad, P. Rekha, P. Mohanty, Facile synthesis of a thermally stable imine and benzimidazole functionalized nanoporous polymer (IBFNP) for CO_2 capture application, Greenhouse Gases: Sci. Technol. 6 (2016) 150–157.
[65] B.S. Ghanem, K.J. Msayib, N.B. McKeown, K.D.M. Harris, Z.G. Pan, P.M. Budd, A. Butler, J. Selbie, D. Book, A. Walton, A triptycene-based polymer of intrinsic microposity that displays enhanced surface area and hydrogen adsorption, Chem. Commun.. 43 (2007) 67–69.
[66] B. Liu, T. Ben, J. Xu, F. Deng, S. Qiu, Hydrogen bonding controlled catalysis of a porous organic framework containing benzimidazole moieties, New J. Chem. 38 (2014) 2292–2299.

Journal of Molecular Liquids 248 (2017) 127–134

Contents lists available at ScienceDirect

Journal of Molecular Liquids

journal homepage: www.elsevier.com/locate/molliq

Nitrogen enriched triazine bridged mesoporous organosilicas for CO_2 capture and dye adsorption applications

Raeesh Muhammad, Jyoti, Paritosh Mohanty *

Functional Materials Laboratory, Department of Chemistry, IIT Roorkee, Roorkee, Uttarakhand 247667, India

ARTICLE INFO

Article history:
Received 15 June 2017
Received in revised form 30 August 2017
Accepted 7 October 2017
Available online 9 October 2017

Keywords:
Triazine bridged mesoporous organosilica
CO_2 capture
Methyl orange adsorption
Mesoporous materials

ABSTRACT

Triazine bridged mesoporous organosilicas with nitrogen content of up to 16.57 wt% have been synthesized by condensation of 3-aminopropyl triethoxysilane and cyanuric chloride followed by hydrolysis and co-condensation with variable amount of tetraethoxyorthosilicate in presence of CTABr. The specific surface area (SA_{BET}) of these materials varies in the range of 232 to 1304 m^2/g depending upon the experimental conditions. The maximum SA_{BET} of 1304 m^2/g was estimated in the sample NEPMO-8 that was synthesized at the APTES to TEOS ratio of 1:8. The CO_2 uptake of 11.6 wt% at 273 K and 1 bar, and methyl orange adsorption capacity of 1262 mg/g at pH = 7 have made this material an important adsorbent.

1. Introduction

The breakthrough work in 1999 on the incorporation of organic moieties into the porous siliceous frameworks, popularly known as periodic mesoporous organosilicas (PMOs), by three research groups independently made the beginning of a new era of porous organo-siliceous materials [1–3]. Inclusion of organic moieties in the inorganic framework created a lot of hope in the research communities especially in catalysis, drug delivery, sensing, chromatography, energy and environment [4–15]. The organic moieties are expected to provide the functionalities, chemical environment, processibility and flexibility, whereas the inorganic moieties would provide the framework its much needed mechanical strength, thermal and hydrothermal stability [16,17]. After the initial invention, where methylene, ethylene and vinylene groups were incorporated, a lot of efforts have been made to incorporate various organic functionalities into the frameworks [1–3,17]. Some of the notable functionalities that provided the room for exploring various applications are diacetylene, amine, amidoxime, porphyrin, vinyl, thiol, carboxylic acid, phosphonic acid and sulphonic acid [12–14,18–23].

A better understanding of the research on PMOs has enabled to control the pore structure and textural properties, such as pore size distribution, pore volume and specific surface area by use of various structure directing agents, salts, swelling agents/pore expander and manipulation of reaction conditions [24–28]. The control over the textural properties like increase in the pore size, has enabled to explore applications such as immobilization and encapsulation of large molecules and functional nanoparticles [24,25,29]. Development of methodologies to control the morphologies such as thin films and monoliths have their specific applications in heavy metal ion sensing, optoelectronics, microelectronics and protein adsorption [10,18,29,30]. The conventional method of polycondensation followed by aging for the synthesis of PMOs, in many instances, have also been replaced by several non-conventional synthesis methods such as microwave and ultrasound assisted methods to save time and energy, without compromising the quality of the products formed [31,32].

Broadly, the incorporation of organic moieties into the PMO could be carried out in two different ways, *i.e.*, post synthesis functionalization and *in-situ* method. Each method has its own strengths and weaknesses. For example, post synthetic modification is a widely used method for the synthesis of PMOs because of its simplicity and versatility. However, this multistep process has limitations in non-homogeneity and lower loading of functionality along with occasional pore blocking that affect the performance of PMOs [33]. Many of these weaknesses of post-synthesis functionalization method can be overcome by the *in-situ* synthesis method, however, finding the right precursor for the specific functionality is always a bottleneck in the *in-situ* synthesis of PMO [33]. Moreover, maintaining the pore ordering in many examples is very difficult because of the incompatibility between the precursor, structure directing agent and solvent used [15,34]. One way to overcome some of the drawbacks of the *in-situ* method is the co-condensation of the organosilica precursor with the silica precursor (TEOS) so that the resultant inorganic-organic hybrid silica could be produced with improved textural properties [35]. Thus, there is always a trade-off between choosing these two methods for any specific need.

Among the many organic moieties incorporated in the PMOs, comparatively less effort was given for the incorporation of the nitrogen enriched moieties in the framework [36–38]. The electron rich nitrogen

* Corresponding author.
E-mail address: pmfcy@iitr.ac.in (P. Mohanty).

https://doi.org/10.1016/j.molliq.2017.10.036
0167-7322/

enriched moieties could be beneficial in several applications such as catalysis, gas adsorption, energy storage and electrocatalysis application [38–42]. Triazine ring with alternative carbon and nitrogen in the hexagonal ring is one of the very important organic moieties owing to its high electron density and aromatic character. Its presence in various high surface area microporous organic polymers with extraordinary properties and applications has made it one of the very important organic moieties to be incorporated in the PMOs to explore the potential applications [40–42]. In this regard, Ibrahim et al. [37], have synthesized triazine incorporated membrane and investigated the water desalination applications. Furthermore, Lin et al. [36] have synthesized triazine bridged polysilsesquioxanes containing lanthanide ions for luminescence application. Further, the triazine incorporated PMO has also been reported by Prasetyanto et al. [38] and Mandal et al. [39], and have shown the catalytic behavior of the materials. However, the specific surface area reported is inferior compared to many of the high surface area PMOs.

In this article, a systematic investigation of the incorporation of the triazine moiety into the organosilica framework by synthesizing nitrogen enriched triazine bridged mesoporous organosilicas (NETPMOs) has been carried out. The synthesized electron enriched high surface area NETPMOs have further been utilized for the carbon dioxide capture and dye removal applications. As it has already been well accepted fact that the CO_2 content in the atmosphere has a primary role in the global warming, capturing it with a feasible and economical way could potentially make the coal fired power plant a greener energy production option. Similarly, the urge for getting the right kind of solid high surface area adsorbents for removal of organic synthetic dyes from the effluent of the textile, paper and paint industries is very high. These dyes are candidates for harsh environment impact leading to carcinogenic and mutagenic effects. Thus, removing these dyes from the waste water could lead to the positive environmental impact.

2. Experimental

2.1. Materials

The reagents and solvents used in this research are of analytical grade and used as received. Cyanuric chloride (CC, Sigma Aldrich), (3-Aminopropyl)triethoxysilane (APTES, Alfa Aesar), Tetraethoxyorthosilicate (TEOS, Sigma Aldrich), Cetyltrimethylammoniumbromide (CTABr, Himedia), Sodium hydroxide (Fisher Scientific), 1,4-Dioxane (Fisher Scientific), Methanol (Rankem), Hydrochloric acid (Himedia), Methyl orange (MO, SRL).

2.2. Synthesis of NETPMOs

The synthesis of NETPMOs was carried out by the condensation of CC and APTES, as shown in Scheme 1, in dioxane in the presence of CTABr as structure directing agent. The synthesis was further extended to synthesize organosilicas by co-condensation of CC and APTES with a variable amount of TEOS. In a typical synthesis, 1 g of CTABr was dissolved in 100 ml of 0.125 M NaOH in 250 ml polypropylene bottle. To it, requisite amount of TEOS was added and the solution was stirred for 1 h. CC (1 mmol) and APTES (3 mmol) were condensed separately in 5 ml dioxane. The resulting condensed solution was added drop-wise to the solution containing TEOS and CTABr followed by stirring for 1 h. The resulting mixture in the polypropylene bottle was placed in an oven at 90 °C for 24 h. The white precipitate formed during this hydrothermal treatment was filtered and dried. The molar composition of reactants in reaction mixture was kept at CC:APTES:TEOS:CTABr:NaOH:H_2O = 0.33:1:x:0.913:4.16:1851.85, where x (x = 0, 2, 4, 6, 8, 10) is the amount of TEOS in mole. CTABr was extracted by refluxing the as-synthesized sample in a mixture of 100 ml methanol and 10 ml 2 M HCl for 72 h. The specimens were designated as NETPMO-x (x = 0, 2, 4, 6, 8, 10).

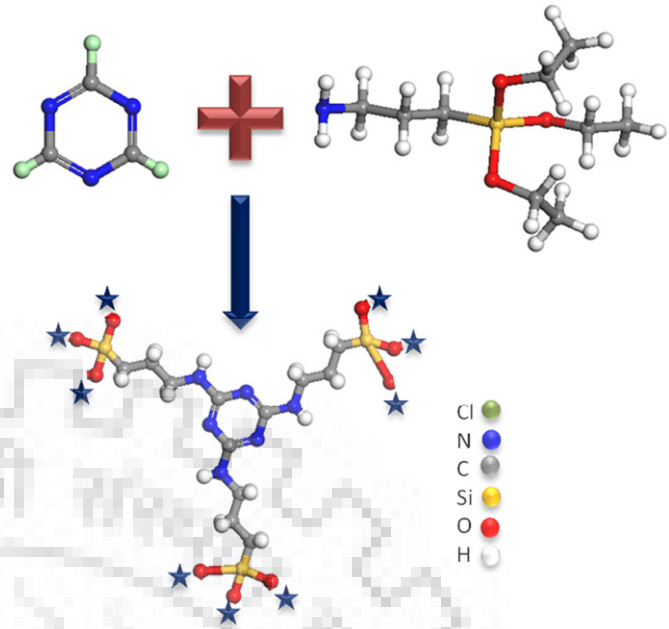

Scheme 1. Reaction scheme for the synthesis of NETPMOs.

2.3. Characterization

Spectroscopic techniques such as NMR and FTIR were used to study the incorporation of organic moieties in the framework. JEOL resonance EXP-400 NMR spectrophotometer was used to record the ^{13}C and ^{29}Si cross polarization magic angle spinning (CPMAS) NMR spectra. The FT-IR spectra in the range of 500 to 4000 cm^{-1} were recorded on the Perkin-Elmer Spectrum Two FT-IR spectrophotometer. Small angle x-ray scattering (SAXS) patterns were obtained using a Rigaku Ultima IV. MIRA3 field emission scanning electron microscope (FE-SEM) and TECNAI G^2S transmission electron microscope (TEM) were used to study the microstructure of the specimens. The TGA/DTG analysis was performed on EXSTAR TG/DTA 6300 with temperature range of 25 to 1000 °C at ramping rate of 10 °C/min under N_2 flow. The Autosorb-iQ2 (Quantachrome Instruments, USA) was used to study the N_2 and CO_2 sorption analysis. Prior to sorption analysis, the samples were activated by degassing at 120 °C for 12 h under vacuum. The quantitative elemental estimation was performed using CHNS/O analyser (Thermo scientific, Flash 2000). The MO concentration was measured using the Shimadzu UV-1800 UV–Vis spectrophotometer.

2.4. Adsorptive removal of methyl orange

Methyl Orange (MO), an organic synthetic dye has been used as a model dye for studying the efficiency of the NETPMO as an adsorbent. The adsorption experiments were carried out in aqueous solutions of the MO at different concentrations (200–2000 mg/l) using batch adsorption experiment. Typically, 10 mg of the NETPMO was used for the experiments that were carried out at RT. The concentration of MO was estimated by plotting calibration curve using the UV–Vis absorption results. The effect of contact time, temperature and pH on adsorption capacity was studied. For recyclability study of the adsorbent, the loaded MO was separated by washing in dil. NaOH followed by dil. HCl solutions. Finally, the adsorbent was washed with copious amount of Millipore water and dried at 60 °C.

The equilibrium adsorption capacity of MO was calculated using below given Eq. (1)

$$q = \frac{(C_0 - C_e)V}{W} \quad (1)$$

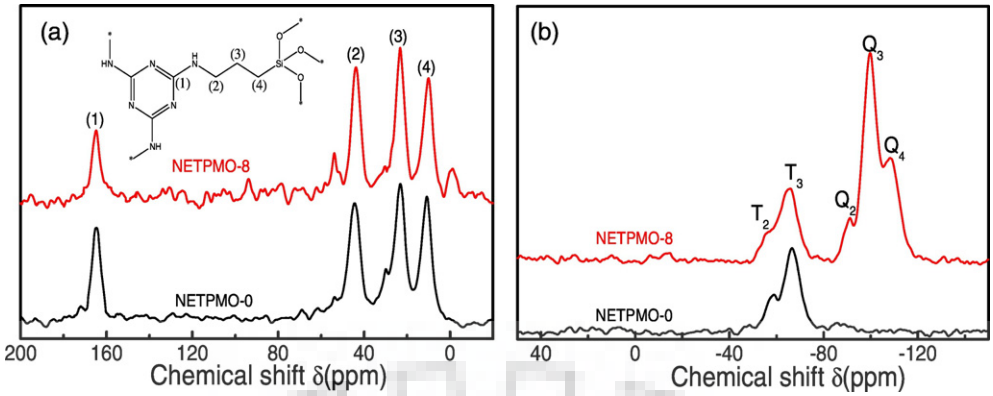

Fig. 1. (a) ^{13}C and (b) ^{29}Si CPMAS NMR spectra of NETPMOs.

where, q is the adsorption capacity (mg/g), C_o and C_e are the initial and equilibrium concentration of adsorbate in the test solution (mg/l), V is the volume of test solution (L) and W is the weight of adsorbent (g).

3. Results and discussion

Incorporation of the triazine moiety into the silica framework by rigid covalent bonding in NETPMOs was carried out by the condensation reaction of cyanuric chloride with three easily removable chloride groups and APTES having amine functionality. This was followed by the hydrolysis of the ethoxy groups attached to the Si of APTES. Co-condensation of APTES with varying amount of TEOS was carried out to manipulate the textural properties. In order to understand the successful condensation of NETPMOs, spectroscopic investigation such as ^{13}C and ^{29}Si CPMAS NMR and FTIR were performed. For example, the presence of triazine moiety in the NETPMO-0 and NETPMO-8 was confirmed by the observation of resonance signal at δ of 165 ppm in ^{13}C CPMAS NMR spectra as shown in Fig. 1a [40,43,44]. Moreover, the additional signals at δ of 44, 23 and 10 ppm could be ascribed to aliphatic carbons of APTES as assigned in the inset of Fig. 1a [14]. The observation of only T sites in the ^{29}Si CPMAS NMR spectrum (Fig. 1b) of NETPMO-0 confirm the absence of any inorganic silica, as no TEOS was used for the condensation [15,34]. This was further supported by the presence of both T and Q sites in ^{29}Si CPMAS NMR spectrum of NETPMO-8, where APTES was co-condense with TEOS (Fig. 1b) [15,34]. Detailed assignment of individual signals is given in Table 1, Fig. 2.

This observation was further corroborated by the FTIR investigation shown in Fig. 2, where three strong bands in the region of 1560 to 1340 cm^{-1} were observed due to stretching vibration of triazine ring in all the samples [40,43,44]. The —C═N-stretching and out-of-plane bending of triazine ring vibration bands were observed at 1270 and 788 cm^{-1}, respectively. Additionally, the presence of stretching vibrations below 3000 cm^{-1} confirms the presence of —CH_2— aliphatic chain originated from APTES [15]. The intensity of this band decreases in accordance with the increasing TEOS content with respect to APTES. Moreover, the absence of band at 850 cm^{-1}, due to —C—Cl stretching further prove the complete condensation of cyanuric chloride in NETPMOs [45]. As expected, the —Si—O—Si-bands were observed in the region of 1210–1036 cm^{-1} [15,34]. The as-synthesized sample displays the sharp band at 2900 cm^{-1} due to aliphatic –C-H stretching of CTABr (Fig. S1). This characteristic band in extracted specimen is attenuated while the other weak band in this region corresponds to —C—H stretching of APTES. Detailed assignment of individual bands is given in Table S1.

Thermogravimetric analysis (TGA) performed in air revealed that NETPMOs are stable up to 350 °C as shown in Figs. 3 and S2. The mass loss below 100 °C could be ascribed to release of adsorbed water, atmospheric gases and organic solvents. The second mass loss beyond 350 °C and up to 450 °C is due to decomposition of incorporated organic moiety —CH_2— and triazine in the framework. When the as-synthesized samples were employed for the TGA (Fig. S3), all the above mentioned mass loss steps are observed in these samples. Additionally, mass loss between 200 and 300 °C was observed and this mass loss step is not seen in the extracted specimens. This mass loss is due to the decomposition of the CTABr template. This further indicates that the procedure adopted in this study to remove the template is effective. As expected, the mass loss of the NETPMOs is a function of TEOS content. With increasing in the TEOS content, there was a regular decrease in the mass loss that further support the incorporation of organic moiety in framework.

The elemental composition (C, N and H %) estimated using CHNS/O analyser has been summarized in Table 2. The wt% of C and N keeps on decreasing with increasing TEOS but their C/N ratio remains about 1.75 similar to their theoretical C/N ratio with minor deviation. This deviation could be ascribed to unhydrolyzed ethoxy group which is well documented [15,46]. With increasing TEOS, the wt% of N and C decreased because Si content is increasing.

The microstructural analysis was carried out by FESEM and TEM. The agglomerated particles of nearly spherical shape with variable sizes in

Table 1
NMR signal description for NETPMOs.

Sample ID	^{13}C				^{29}Si				
	δ for Carbons (ppm)				δ for *T* sites (ppm)		δ for *Q* sites (ppm)		
	(1)	(2)	(3)	(4)	T^2	T^3	Q^2	Q^3	Q^4
NETPMO-0	165	44	23	10	−59	−66	–	–	–
NETPMO-8	165	44	23	10	−57	−65	−90	−100	−110

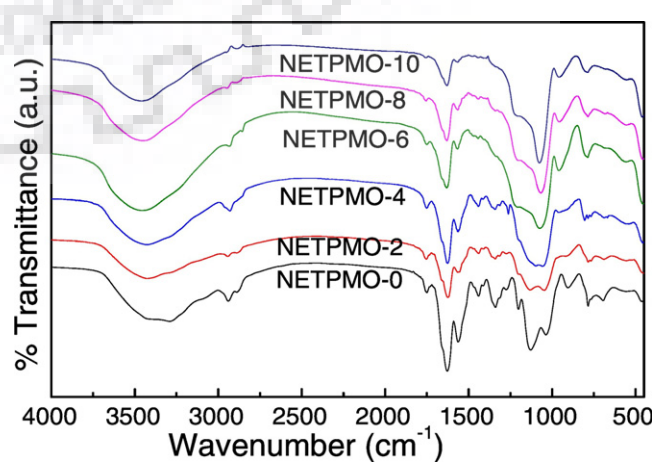

Fig. 2. FTIR spectra for NETPMOs.

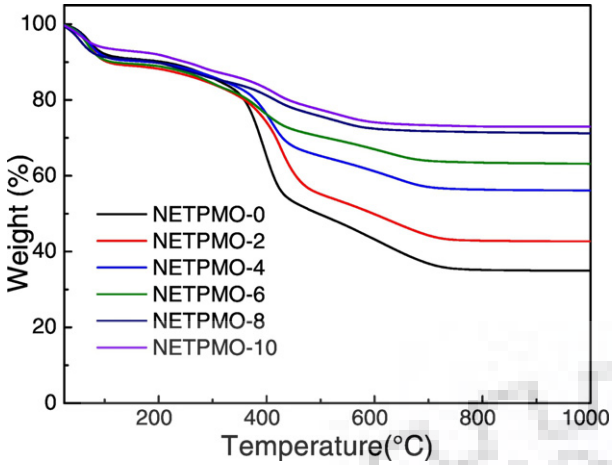

Fig. 3. TGA isotherm for NETPMOs.

Table 2
C, H and N elemental analyses of NETPMOs.

Sample ID	N (wt%)	C (wt%)	H (wt%)	C/N ratio
NETPMO-0	16.57	29.08	6.22	1.75
NETPMO-2	11.13	19.07	5.66	1.71
NETPMO-4	7.34	13.14	6.16	1.79
NETPMO-6	6.14	11.60	5.82	1.88
NETPMO-8	4.95	9.48	5.57	1.91
NETPMO-10	4.48	8.48	4.72	1.89

the range of 500 nm to 1 μm have been observed in FESEM images (Fig. 4). Further, TEM of a representative sample NETPMO-8 revealed that the pores of 2–3 nm diameters could be seen in Fig. 5a. The extended mesoscale ordering in NETPMO could not be observed in TEM image. This was further confirmed from the SAXS patterns as no sharp peak could be seen (Fig. S4). The broad diffused SAED pattern as shown in Fig. 5b indicate the amorphous nature of specimen.

The textural property carried out using N_2 sorption analysis at 77 K as shown in Fig. 6 confirmed the porous nature of NETPMOs. N_2 sorption isotherms are completely reversible in nature. Among all the specimens synthesized in this work, the NETPMO-8 has the maximum specific surface area (SA_{BET}) of 1304 m^2/g. The isotherm is type-IV with small hysteresis that extends from low pressure range to higher pressure range.

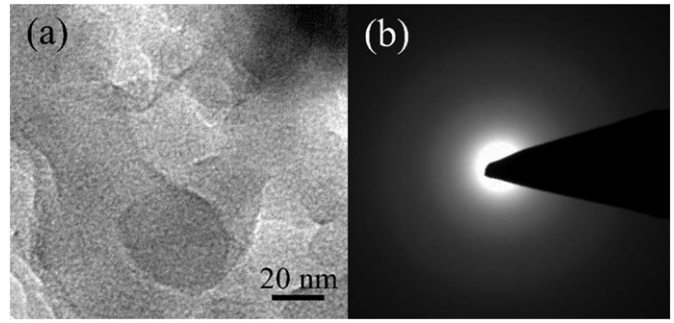

Fig. 5. (a) TEM image and (b) SAED pattern for NETPMO-8.

This indicates that the material has hierarchical pore structure which is mainly due to the combination of the mesopores originated from the structure directing agent along with the inter-particulate pores, which can be seen from the TEM image also. The pore size distribution (PSD) shown in Fig. S5 was performed by density functional theory (DFT). The majority of the pores in these specimens were found to be centred in the range of 2.5 to 3.7 nm with minority of the pores have distributions centred at 8.1 and 9.4 nm (Fig. S5). The observed reduction in pore width with increasing TEOS content could be ascribed to thickening of pore wall [46]. Similarly, all other specimens synthesized in this work have similar isotherm characteristics, with observation of additional microporosity in sample NETPMO-4. Detailed textural properties of all these specimens have been summarized in Table 3. It can be seen that the SA_{BET} of NETPMOs increased from 232 to 1304 m^2/g on increasing the APTES to TEOS ratio up to 1:8, however, on further increasing the ratio to 1:10, there was a decrease in the SA_{BET} (Table 3 & Fig. S6). This phenomenon is commonly observed in the organosilica frameworks synthesized by a similar co-condensation of organosilica precursors with TEOS [15,34]. In such cases, SA_{BET} reduces owing to increase in pore wall thickness [47]. The detailed textural properties of all the specimens are summarized in Table 3.

Further, in order to understand the effect of triazine moiety on textural properties of silica framework, a sample AP-TEOS-8 was synthesized by co-condensing APTES with TEOS at the ratio of 1:8 without using cyanuric chloride. In this sample, the estimated SA_{BET} was only 454 m^2/g (Fig. S7) as against 1304 m^2/g in NETPMO-8. This indicates that the presence of triazine moiety is tuning the textural properties of the synthesized organosilicas by providing a synergy effect. Similar

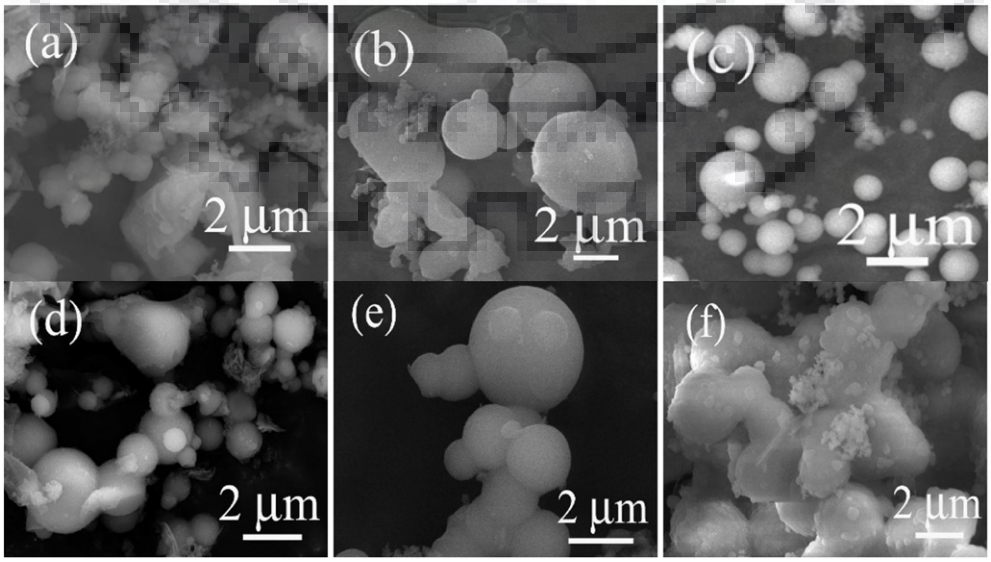

Fig. 4. FESEM images of NETPMOs. (a) NETPMO-0, (b) NETPMO-2, (c) NETPMO-4, (d) NETPMO-6, (e) NETPMO-8 and (f) NETPMO-10.

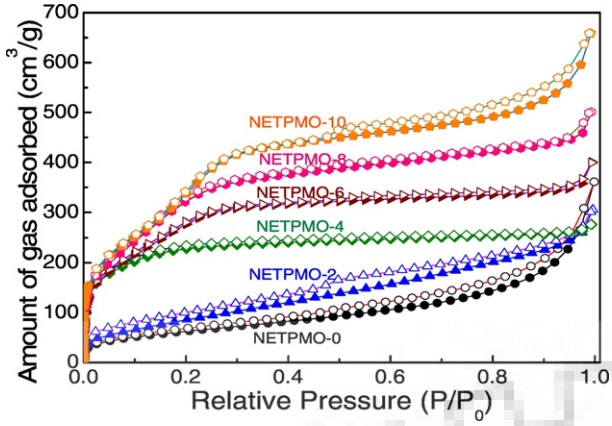

Fig. 6. N_2 adsorption (filled) and desorption (empty) isotherms for NETPMOs measured at 77 K.

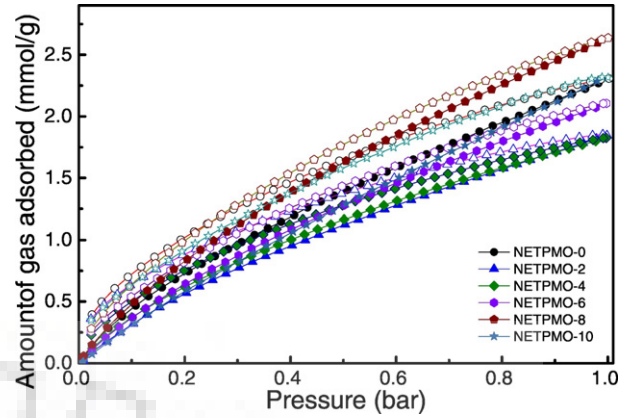

Fig. 7. CO_2 adsorption (filled) and desorption (empty) isotherm of NETPMOs measured at 273 K and 1 bar.

synergy effect in the textural properties of organosilicas have earlier been observed by our group and documented in some of our recent articles [15,34].

3.1. CO_2 adsorption

The presence of amine group attached to the nitrogen rich triazine ring of the NETPMOs framework with substantially high specific surface area has encouraged us to investigate the CO_2 capture behavior of the NETPMOs. The CO_2 sorption of the adsorbents has been studied at 273 K up to 1 bar pressure. The CO_2 sorption isotherms of NETPMOs have been given in Fig. 7. It is important to note that all the isotherms measured at 273 K are reversible in nature with a maximum CO_2 uptake of 11.6 wt% observed in NETPMO-8. It is important to note that the CO_2 adsorption on the surface is a complex phenomenon and depends upon several factors. Some of the important parameters that decide the overall CO_2 capture capacity are; (i) specific surface area, (ii) pore size distribution, (iii) pore volume, and (iv) surface functionality. The higher the surface area the higher will be the adsorption capacity keeping all other parameters identical. The pore size distribution has a complex role in tuning the CO_2 capture capacity. In general, a small PSD especially in the micropore region enhances the CO_2 capture capacity owing to enhanced capillary action and superior van der Walls interaction. However, this is not always true as the kinetic factor limits the accessibility of the active site on many occasions. A higher pore volume holds larger amount of CO_2. The increase in the electron density in the framework by introducing various functionalities in general could improve the CO_2 capture capacity due to the Lewis base-Lewis acid interaction. Thus, as discussed above there is always a trade-off between the kinetics and thermodynamics that ultimately determines the overall CO_2 capture capacity of any adsorbent material.

In the present research, the higher CO_2 uptake of 11.6 wt% by NETPMO-8 could be attributed to the highest SA_{BET} among all these specimens. The CO_2 uptake of 10.2 wt% in NETPMO-0 is marginally lower compared to NETPMO-8, although, the SA_{BET} of NETPMO-0 (232 m^2/g) is 5.6 times lower than NETPMO-8 (1304 m^2/g). This indicates that the higher content of electron rich nitrogen has significant role in CO_2 uptake for NETPMO-0. This was further supported by the fact that all other samples with higher SA_{BET} have lower CO_2 capture capacity as compared to NETPMO-0 (Table 3). However, the CO_2 uptake for NETPMO-4 and NETPMO-6 is lower than NETPMO-8 despite having higher nitrogen content. The presence of micro-porosity in NETPMO-4 evident from N_2 sorption isotherm is not reflecting its effect on CO_2 uptake, which could be due to the pore blockage. Thus, as discussed above, there is a trade-off between surface functionality, specific surface area and PSD that dictates the CO_2 capture capacity. The presence of triazine ring and high amine functionality in framework is the additional advantage which is helpful in enhancing the Lewis basic nature of framework. The CO_2 uptake for NETPMO-8 is better or comparable with some of recently reported siliceous/non-siliceous materials like CPMO-8SR [15], Fepc–TiO_2 [48], GD0 [35], fluorinated Zn^{II} HFMOF [49] and TDCOF-5 [50]. However, CO_2 uptake for NETPMOs is lower than some of the best reported solid adsorbents such as TBILP-1 [51], IBFNP-1 [52], PECONF-1 [53], TPA@PON [54] and SB-TRZ-TPA [55]. For more details, please see Table S2.

The CO_2 capture capacity of the NETPMOs has been further investigated at 298 K to study the capture capacity at higher temperature and also to understand the thermodynamics properties. The isotherms measured at 298 K are shown in Fig. S8. The CO_2 capture capacity of 5.8 wt% was estimated for the NETPMO-8. The CO_2 capture capacity of all the samples are given in Table 3. The CO_2 uptake at 298 K by the NETPMOs are compared with the reported solid adsorbents (Table S2) [56–61]. Further, to access the interaction of CO_2 with NETPMOs, the isosteric heat of adsorption (Q_{st}) was calculated using Clausius–Clapeyron equation. The Q_{st} value of 48.6 kJ/mol for NETPMO-0, was highest among all NETPMOs which further indicate the presence of significantly higher nitrogen content in NETPMO-0 than all other samples (Table 3 and Fig. S9). The Q_{st} values for NETPMOs lies in the range of 24.4 to 48.6 kJ/mol which indicates that the interaction of CO_2 with NETPMOs is physisorption in nature.

Table 3
Textural properties and CO_2 adsorption for NETPMOs.

Sample	APTES:TEOS	SA_{BET} (m^2/g)	Pore size (nm)	Pore Vol. (cm^3/g)	CO_2 (wt%) 273 K	CO_2 (wt%) 298 K	Q_{st} (kJ/mol)
NETPMO-0	1:0	232	3.6	0.55	10.2	5.0	48.6
NETPMO-2	1:2	339	3.7	0.47	8.1	4.3	33.7
NETPMO-4	1:4	625	2.5	0.31	8.0	4.1	31.8
NETPMO-6	1:6	1085	2.9	0.62	9.3	4.7	38.7
NETPMO-8	1:8	1304	2.9	0.78	11.6	5.8	30.7
NETPMO-10	1:10	1131	3.2	1.02	10.1	4.5	24.4

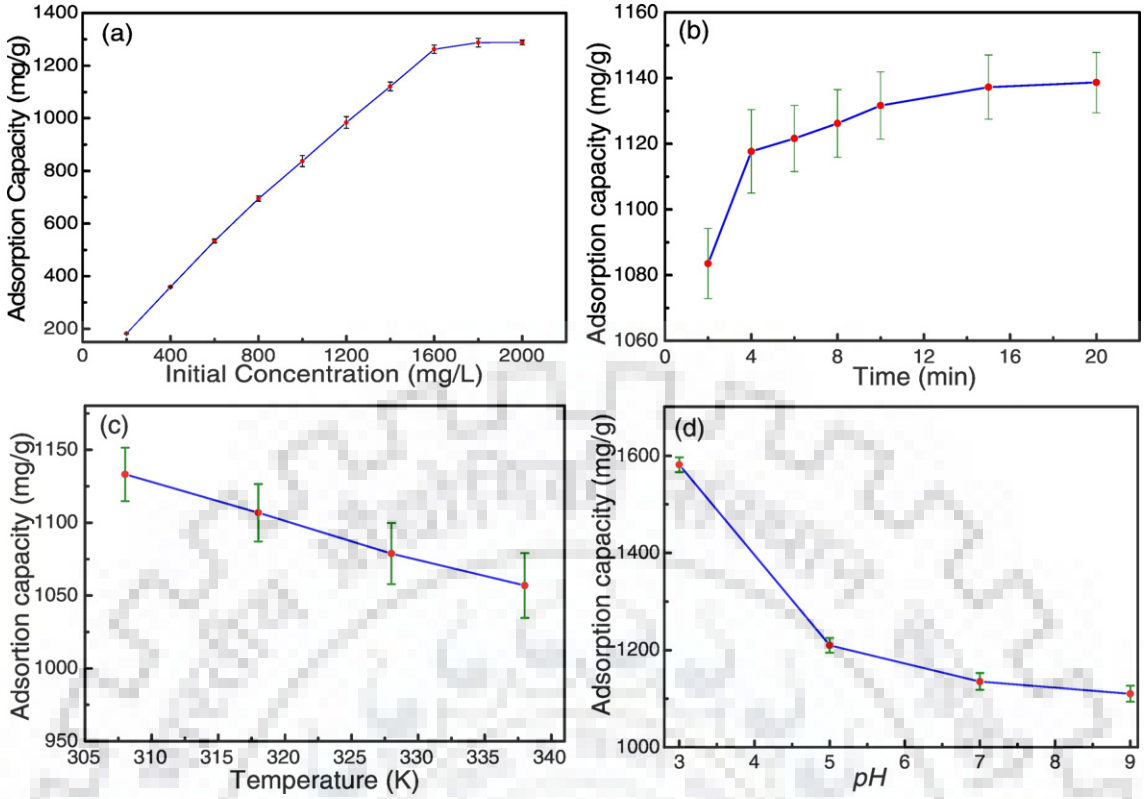

Fig. 8. Variation of adsorption capacity with (a) initial concentration, (b) contact time, (c) temperature and (d) pH for the adsorption of MO by NETPMO-8.

3.2. Dye adsorption studies

Based on the above observation of SA_{BET}, the NETPMO-8 has been chosen as the model adsorbent for studying the kinetics, thermodynamic and adsorption isotherm for adsorptive removal of MO in the aqueous solution. As expected, the adsorption capacity increases linearly up to the MO conc. of 1600 mg/l and a saturation was observed above this value as shown in Fig. 8(a). The adsorption capacity estimated at MO conc. of 1600 mg/l was 1262 mg/g in 60 min. Interestingly, the adsorption takes place very quickly and within only 10 min, adsorption capacity reaches 1132 mg/g (Fig. 8b). On increasing the temp from 308 to 338 K, the adsorption capacity decreases from 1132 to 1057 mg/g as shown in Fig. 8c, indicating the adsorption as an exothermic process. Further, a lower pH favors the adsorption, with a maximum adsorption capacity of 1581 mg/g was observed at the pH of 3 and decreased to 1110 mg/g when pH was raised to 9 as shown in Fig. 8d. This is very important for practical application of the adsorbent where an acidic pH is expected in the industry effluents on many occasions [62]. The higher adsorption capacity at lower pH could be attributed to electrostatic attraction between the positively charged surface of adsorbent and negatively charged MO [63]. The adsorption capacity is comparable or better than reported solid adsorbents such as CPMO-4SR [14], HCPANI [64], Chitosan (non-cross linked) [65], CMK-3 [66], and lower than CPMO-0T [34], Chitosan fiber (cross linked) [67] and TPP [62]. For more details please see Table S3. The recyclability study of NETPMO-8 has shown a gradual decrease in the adsorption capacity and a retention of almost 61% of the initial adsorption capacity could be estimated after 5 cycles (Fig. S10). But it is interesting to see that, the equilibrium time for NETPMO-8 is better than many reported adsorbents [62,63,66].

3.3. Adsorption isotherms

To get the better understanding of adsorption process, the adsorption data were fitted in Langmuir and Freundlich model which are

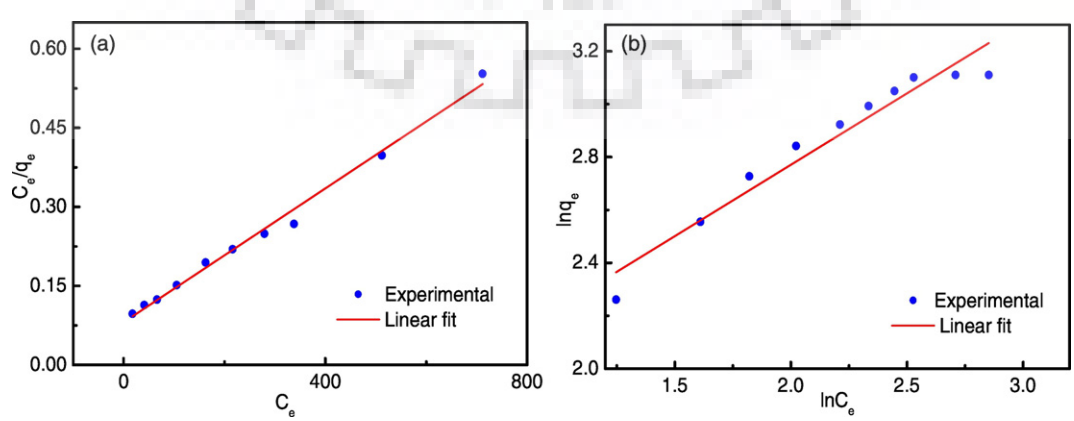

Fig. 9. (a) Langmuir and (b) Freundlich adsorption isotherm of MO removal on NETPMO-8.

Table 4
Adsorption parameters of Langmuir and Freundlich model for adsorption of MO.

Langmuir model			Freundlich model		
R^2	q_{max} (mg/g)	b (L/mg)	R^2	n (L/mg)	K_f (mg/g)
0.990	1574.9	0.0078	0.936	1.85	49.1348

Table 5
Kinetic parameters for pseudo-first order and pseudo-second order kinetics for adsorption of MO.

Pseudo-first order			Pseudo-second order		
R^2	k_1 (min^{-1})	q_e (mg/g)	R^2	k_2 (g/(mg·min))	q_e (mg/g)
0.954	0.226	66.33	0.999	0.00087	1145.98

based on monolayer adsorption with homogeneous binding sites and multilayer adsorption on a heterogeneous site, respectively. The linear form of Langmuir and Freundlich model can be represented in the form of Eqs. (2) and (3), respectively.

$$\frac{C_e}{q_e} = \frac{C_e}{q_{max}} + \frac{1}{q_{max}b} \tag{2}$$

$$logq_e = \frac{logC_e}{n} + logk_f \tag{3}$$

where, q_{max} (mg/g) is the theoretical maximum adsorption capacity, b is the Langmuir constant, K_f is the Freundlich constant, n is the adsorption intensity.

The adsorption data was fitted in the Eqs. (2) and (3) and values for different parameter of both the models were calculated by plotting the graph as shown in Fig. 9(a & b). The correlation coefficient (R^2) for Langmuir model is 0.990 in comparison to 0.936 for Freundlich model, which indicates the presence of homogeneous binding site and formation of single adsorbate layer on adsorbent (Table 4).

3.4. Kinetic study

To predict the adsorption rate, the kinetic parameters were evaluated using the linear form of Pseudo first order and pseudo second order kinetic models given in Eqs. (4) and (5), respectively [68,69].

$$\ln(q_e - q_t) = \ln q_e - k_1 t \tag{4}$$

$$\frac{t}{q_t} = \frac{1}{k_2 q_e^2} + \frac{t}{q_e} \tag{5}$$

where, q_e, q_t, t, k_1 and k_2 are equilibrium adsorption capacity, adsorption capacity at time t, pseudo first order rate constant and pseudo second order rate constant, respectively.

The thermodynamic parameters has been calculated by plotting the graph between $\ln(q_e - q_t)$ *versus* t and t/q_t *versus* t for pseudo first order and pseudo second order, respectively as shown in Fig. 10(a & b) and has been summarized in Table 5. The value of correlation coefficient (R^2) estimated from the graph was closure to unity for pseudo-second order adsorption. Hence, the adsorption of MO on NETPMO-8 follows pseudo-second order adsorption process.

3.5. Thermodynamic study

To have a better insight about the adsorption process, thermodynamics parameters like ΔH and ΔS were calculated using the Eq. (7):

$$k_d = \frac{q_e}{C_e} \tag{6}$$

$$\ln(k_d) = \frac{\Delta S}{R} - \frac{\Delta H}{RT} \tag{7}$$

$$\Delta G = -RT\ln(k_d) \tag{8}$$

where, R, T and k_d are universal gas constant, temperature (K) and distribution coefficient, respectively. k_d was calculated by using Eq. (6).

The ΔH and ΔS values were calculated by using the slope and intercept values of the graph plotted between $\ln(k_d)$ *vs.* 1/T (Fig. 11), respectively. The values for ΔH and ΔS were found to be −6.44 kJ/mol and −13.56 J/mol/K, respectively. The negative ΔH values confirm that adsorption process is exothermic in nature and negative value of ΔS indicate decrease in the randomness at the adsorbate surface. The values of ΔG, calculated by using Eq. (8), were found to be −2.27, −2.14, −1.98 and −1.87 kJ/mol at 308, 318, 328 and 338 K, respectively. The negative values indicate that the adsorption process is spontaneous in nature.

4. Conclusions

The nitrogen enriched triazine bridged mesoporous organosilicas (NETPMOs) synthesized in this work by condensing cyanuric chloride and APTES followed by co-condensation with TEOS has maximum SA_{BET} of 1304 m^2/g in NETPMO-8. The APTES to the TEOS ratios plays an important role in tuning the textural properties of the specimens. The SA_{BET} increases linearly with the increase in the APTES to TEOS ratios from 1:0 to 1:8, and after that decreases in 1:10 sample. The NETPMO-0, which was synthesized without TEOS has SA_{BET} of 232 m^2/g, however, has shown good CO_2 capture capacity of 10.2 wt%. It is interesting to note that the incorporation of triazine ring in the siliceous framework has substantially improved the SA_{BET} from 454 m^2/g (without triazine moiety) to 1304 m^2/g (with triazine moieties). Moreover, NETPMO-8, have also demonstrated very high MO adsorption

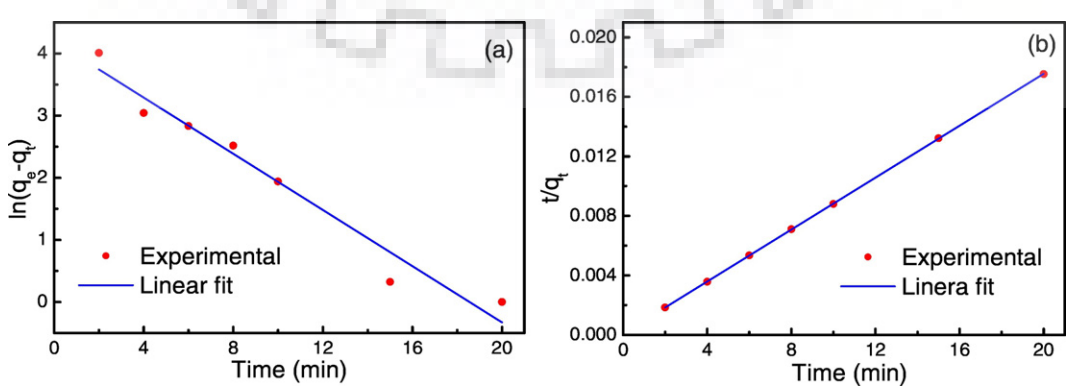

Fig. 10. (a) Pseudo first order and (b) Pseudo second order kinetics for the adsorption of MO.

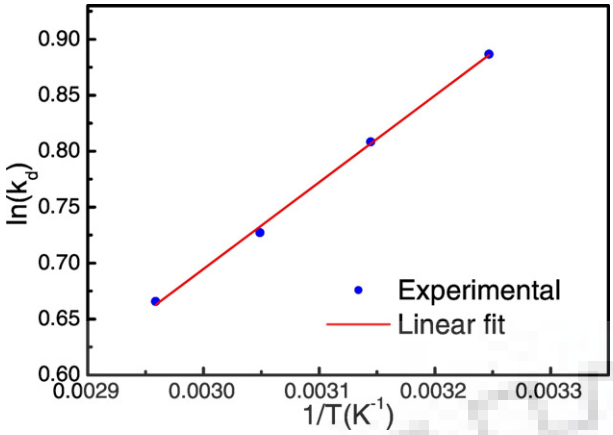

Fig. 11. Plot of $\ln(k_d)$ v/s 1/T for adsorption of MO.

capacity of 1262 mg/g. The adsorption process follows Langmuir adsorption model and pseudo second order kinetic. The negative values of ΔG and ΔH have shown that the adsorption process is highly spontaneous and exothermic in nature. Thus, the NETPMOs reported in this research are good adsorbents for the adsorptive removal of MO from the wastewater and for CO_2 capture applications.

Acknowledgement

The work was financially supported by DST, Govt. of India with Grant code DST/IS-STAC/CO2-SR-132/12(G).

Appendix A. Supplementary data

Supplementary data to this article can be found online at https://doi.org/10.1016/j.molliq.2017.10.036.

References

[1] T. Asefa, M.J. MacLachlan, N. Coombs, G.A. Ozin, Nature 402 (1999) 867–871.
[2] S. Inagaki, S. Guan, Y. Fukushima, T. Ohsuna, O. Terasaki, J. Am. Chem. Soc. 121 (1999) 9611–9614.
[3] B.J. Melde, B.T. Holland, C.F. Blanford, A. Stein, Chem. Mater. 11 (1999) 3302–3308.
[4] P. Borah, X. Ma, K.T. Nguyen, Y. Zhao, Angew. Chem. Int. Ed. 51 (2012) 7756–7761.
[5] A. Modak, J. Mondal, V.K. Aswal, A. Bhaumik, J. Mater. Chem. 20 (2010) 8099–8106.
[6] F. Zhou, X. Hu, M. Gao, T. Cheng, G. Liu, Green Chem. 18 (2016) 5651–5657.
[7] N. Lu, Y. Tian, W. Tian, P. Huang, Y. Liu, Y. Tang, C. Wang, S. Wang, Y. Su, Y. Zhang, J. Pan, Z. Teng, G. Lu, ACS Appl. Mater. Interfaces 8 (2016) 2985–2993.
[8] J. Croissant, X. Cattoën, M.W.C. Man, A. Gallud, L. Raehm, P. Trens, M. Maynadier, J.O. Durand, Adv. Mater. 26 (2014) 6174–6180.
[9] X. Qiu, S. Han, Y. Hu, M. Gao, H. Wanga, J. Mater. Chem. A 2 (2014) 1493–1501.
[10] J. Du, J.C. Wechsler, J.M. Lobez, H.P. Loock, C.M. Crudden, Small 6 (2010) 1168–1172.
[11] V. Rebbin, R. Schmidt, M. Froba, Angew. Chem. Int. Ed. 45 (2006) 5210–5214.
[12] H. Wang, S. Han, Y. Hu, J.J. Dynes, ChemPlusChem (2016)https://doi.org/10.1002/cplu.201600290.
[13] K.M. Li, J.G. Jiang, S.C. Tian, X.J. Chen, F. Yan, J. Phys. Chem. C 118 (2014) 2454–2462.
[14] C. Gunathilake, M. Jaroniec, ACS Appl. Mater. Interfaces 6 (2014) 13069–13078.
[15] P. Rekha, R. Muhammad, P. Mohanty, RSC Adv. 5 (2015) 67690–67699.
[16] S. Fujita, S. Inagaki, Chem. Mater. 20 (2008) 891–908.
[17] N. Mizoshita, T. Tani, S. Inagaki, Chem. Soc. Rev. 40 (2011) 789–800.
[18] Y. Li, F. Auras, F. Löbermann, M. Döblinger, J. Schuster, L. Peter, D. Trauner, T. Bein, J. Am. Chem. Soc. 135 (2013) 18513–18519.
[19] T.S. Deng, J.Y. Zhang, K.T. Zhu, Q.F. Zhang, J.L. Wu, Colloids Surf. A Physicochem. Eng. Asp. 356 (2010) 104–111.
[20] D. Liu, J.H. Lei, L.P. Guo, X.D. Du, K. Zeng, Microporous Mesoporous Mater. 117 (2009) 67–74.
[21] Y.C. Yang, J.R. Deka, C.E. Wu, C.H. Tsai, D. Saikia, H.M. Kao, J. Mater. Sci. 52 (2017) 6322–6340.
[22] O.A. Dudarko, C. Gunathilake, N.P. Wickramaratne, V.V. Sliesarenko, Y.L. Zub, J. Górka, S. Dai, M. Jaroniec, Colloids Surf. A Physicochem. Eng. Asp. 482 (2015) 1–8.
[23] J.G.C. Shen, R.G. Herman, K. Klier, J. Phys. Chem. B 106 (2002) 9975–9978.
[24] X. Wang, Y. Zhang, W. Luo, A.A. Elzatahry, X. Cheng, A. Alghamdi, A.M. Abdullah, Y. Deng, D. Zhao, Chem. Mater. 28 (2016) 2356–2362.
[25] W. Guo, J.Y. Park, M.O. Oh, H.W. Jeong, W.J. Cho, I. Kim, C.S. Ha, Chem. Mater. 15 (2003) 2295–2298.
[26] J. Fan, C. Yu, J. Lei, Q. Zhang, T. Li, B. Tu, W. Zhou, D. Zhao, J. Am. Chem. Soc. 127 (2005) 10794–10795.
[27] M. Kruk, M. Jaroniec, J. Phys. Chem. B 103 (1999) 4590–4598.
[28] A.S. Manchanda, M. Kruk, Microporous Mesoporous Mater. 222 (2016) 153–159.
[29] K. Landskron, B.D. Hatton, D.D. Perovic, G.A. Ozin, Science 302 (2003) 266–269.
[30] Z. Sun, Y. Deng, J. Wei, D. Gu, B. Tu, D. Zhao, Chem. Mater. 23 (2011) 2176–2184.
[31] P. Mohanty, N.M.K. Linn, K. Landskron, Langmuir 26 (2010) 1147–1151.
[32] G. Smeulders, V. Meynen, G.V. Baelen, M. Mertens, O.I. Lebedev, G.V. Tendeloo, B.U.W. Maesc, P. Cool, J. Mater. Chem. 19 (2009) 3042–3048.
[33] F. Hoffmann, M. Cornelius, J. Morell, M. Froba, Angew. Chem. Int. Ed. 45 (2006) 3216–3251.
[34] P. Rekha, R. Muhammad, V. Sharma, M. Ramteke, P. Mohanty, J. Mater. Chem. A 4 (2016) 17866–17874.
[35] Y. Tang, K. Landskron, J. Phys. Chem. C 114 (2010) 2494–2498.
[36] N. Lin, H. Li, Y. Wang, Y. Feng, D. Qin, Q. Gan, S. Chen, Eur. J. Inorg. Chem. (2008) 4781–4785.
[37] S.M. Ibrahim, R. Xu, H. Nagasawa, A. Naka, J. Ohshita, T. Yoshioka, M. Kanezashia, T. Tsuru, RSC Adv. 4 (2014) 23759–23769.
[38] E.A. Prasetyanto, M.B. Ansari, B.H. Min, S.E. Park, Catal. Today 158 (2010) 252–257.
[39] J. Mondal, A. Modak, M. Nandi, H. Uyama, A. Bhaumik, RSC Adv. 2 (2012) 11306–11317.
[40] R. Muhammad, P. Rekha, P. Mohanty, RSC Adv. 6 (2016) 17100–17105.
[41] L. Hao, B. Luo, X. Li, M. Jin, Y. Fang, Z. Tang, Y. Jia, M. Liang, A. Thomas, J. Yang, L. Zhi, Energy Environ. Sci. 5 (2012) 9747–9751.
[42] A. Qu, X. Xu, Y. Zhang, Y. Li, W. Zha, S. Wen, H. Xie, J. Wang, React. Funct. Polym. 102 (2016) 93–100.
[43] M.G. Schwab, B. Fassbender, H.W. Spiess, A. Thomas, X. Feng, K. Mullen, J. Am. Chem. Soc. 131 (2009) 7216–7217.
[44] G. Li, B. Zhang, J. Yan, Z. Wang, Macromolecules 47 (2014) 6664–6670.
[45] H.A. Patel, F. Karadas, A. Canlier, J. Park, E. Deniz, Y. Jung, M. Atilhan, C.T. Yavuz, J. Mater. Chem. 22 (2012) 8431–8437.
[46] K.M. Parida, D. Rath, J. Mol. Catal. A Chem. 310 (2009) 93–100.
[47] F. Kleitz, T.W. Kim, R. Ryoo, Langmuir 22 (2006) 440–445.
[48] P.V.R.K. Ramacharyulu, R. Muhammad, J.P. Kumar, G.K. Prasad, P. Mohanty, Phys. Chem. Chem. Phys. 17 (2015) 26456–26462.
[49] S.S. Dhankhar, M. Kaur, C.M. Nagaraja, Eur. J. Inorg. Chem. 34 (2015) 5669–5676.
[50] Z. Kahveci, T. Islamoglu, G.A. Shar, R. Ding, H.M. El-Kaderi, CrystEngComm 15 (2013) 1524–1527.
[51] A.K. Sekizkardes, S. Altarawneh, Z. Kahveci, T. İslamoğlu, H.M. El-Kaderi, Macromolecules 47 (2014) 8328–8334.
[52] R. Muhammad, P. Rekha, P. Mohanty, Greenhouse Gas Sci. Technol. 6 (2016) 150–157.
[53] P. Mohanty, L.D. Kull, K. Landskron, Nat. Commun. 2 (2011)https://doi.org/10.1038/ncomms1405.
[54] S. Mondal, S.K. Kundub, A. Bhaumik, Chem. Commun. 53 (2017) 2752–2755.
[55] S. Bhuniaa, P. Bhanja, S.K. Das, T. Sen, A. Bhaumik, J. Solid State Chem. 247 (2017) 113–119.
[56] C. Gunathilake, M. Jaroniec, ACS Appl. Mater. Interfaces 6 (2014) 13069–13078.
[57] W. Wang, Y. Yuan, F.X. Sun, Gu.S. Zhu, Chin. Chem. Lett. 25 (2014) 1407–1410.
[58] M. Saleh, K.S. Kim, RSC Adv. 5 (2015) 41745–41750.
[59] C. Gu, Y. Bao, W. Huang, D. Liu, R. Yang, Macromol. Chem. Phys. 217 (2016) 748–756.
[60] D. Zhang, L. Tao, J. Ju, Y. Wang, Q. Wang, T. Wang, Polymer 60 (2015) 234–240.
[61] C. Zhang, T.L. Zhai, J.J. Wang, Z. Wang, J.M. Liu, B. Tan, X.L. Yang, H.B. Xu, Polymer 55 (2014) 3642–3647.
[62] M.S. Chiou, P.Y. Ho, H.Y. Li, Dyes Pigments 60 (2004) 69–84.
[63] Q. Du, J. Sun, Y. Li, X. Yang, X. Wang, Z. Wang, L. Xia, Chem. Eng. J. 245 (2014) 99–106.
[64] V. Sharma, P. Rekha, P. Mohanty, J. Mol. Liq. 222 (2016) 1091–1100.
[65] F.C. Wu, R.L. Tseng, R and S. Juang, J. Hazard. Mater. 73 (2000) 63–75.
[66] N. Mohammadi, H. Khani, V.K. Gupta, E. Amereh, S.J. Agarwal, J. Colloid Interface Sci. 362 (2011) 457–462.
[67] H. Yoshida, A. Okamoto, T. Kataoka, Chem. Eng. Sci. 48 (1993) 2267–2272.
[68] J.K. Bediako, W. Wei, S. Kim, Y.S. Yun, J. Hazard. Mater. 299 (2015) 550–561.
[69] Y.S. Ho, G. McKay, Process Biochem. 34 (1999) 451–465.